

**AD-A274 688**



8

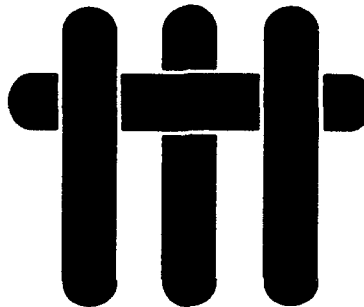
**ANNUAL REPORT**  
**Office of Naval Research**

Contract. No. N00014-93-I-0213

January 1, 1993 - December 31, 1993

**DTIC**  
**ELECTF**  
**JAN 12 1994**  
**S C D**

**M A T E R I A L S**



**BIMATERIAL INTERFACES AND THEIR ROLE  
IN THE MECHANICAL PERFORMANCE  
OF THE IN-SITU COMPOSITES**

by

**A. G. Evans**

Materials Department  
College of Engineering  
University of California  
Santa Barbara, California 93106-5050

**DISTRIBUTION STATEMENT A**  
Approved for public release  
Distribution Unlimited

**94 1 10 174**

**94-01206**

**Best  
Available  
Copy**

REPORT DOCUMENTATION PAGE			Form Approved OMB No. 0705-0188	
1. AGENCY USE ONLY (Leave blank)		2. REPORT DATE 931231	3. REPORT TYPE AND DATES COVERED FINAL REPORT 930101 TO 931231	
4. TITLE AND SUBTITLE Bimaterial Interfaces and Their Role in the Mechanical Performance of the In-Situ Composites			5. FUNDING NUMBERS N00014-93-I-0213	
6. AUTHOR(S) Evans, Anthony G.				
7. PERFORMING ORGANIZATION NAME(S) AND ADDRESS(ES) MATERIALS DEPARTMENT COLLEGE OF ENGINEERING UNIVERSITY OF CALIFORNIA SANTA BARBARA, CA 93106-5050			8. PERFORMING ORGANIZATION REPORT NUMBER	
9. SPONSORING/MONITORING AGENCY NAME(S) AND ADDRESS(ES) OFFICE OF NAVAL RESEARCH MATERIALS DIVISION 800 NORTH QUINCY STREET ARLINGTON, VA 22217-5000			10. SPONSORING/MONITORING AGENCY REPORT NUMBER	
11. SUPPLEMENTARY NOTES				
12A. DISTRIBUTION/AVAILABILITY STATEMENT See Distribution List			12B. DISTRIBUTION CODE	
13. ABSTRACT (Maximum 200 words) The annual report of the Office of Naval Research grant at UCSB on Bimaterial Interfaces and their role in the Mechanical Performance is concerned basically with the mechanical properties of ceramic/metal bonded systems and with establishing criteria for interface decohesion, for sliding and for cracking across interfaces. Please refer to the executive summary for further details.				
14. SUBJECT TERM Bimaterial Interfaces, Mechanical Performance, In-Situ Composites			15. NUMBER OF PAGES 350	
			16. PRICE CODE	
17. SECURITY CLASSIFICATION OF REPORT UNCLASSIFIED	18. SECURITY CLASSIFICATION OF THIS PAGE UNCLASSIFIED	19. SECURITY CLASSIFICATION OF ABSTRACT UNCLASSIFIED	20. LIMITATION OF ABSTRACT	

## **Section 1 EXECUTIVE SUMMARY**

### **Section 2**

	<b><u>TITLE</u></b>	<b><u>AUTHOR</u></b>
Article 1.	Cracking and Stress Redistribution in Ceramic Layered Composites	K.S. Chan M.Y. He J.W. Hutchinson
Article 2.	Fracture Resistance Characteristics of a Metal-Toughened Ceramic	B.D. Flinn C.S. Lo F.W. Zok A.G. Evans
Article 3.	Fiber Coating Concepts for Brittle-Matrix Composites	J.B. Davis J.P.A. Löfvander A.G. Evans E. Bischoff M.L. Emiliani
Article 4.	Cracking and Damage Mechanisms in Ceramic/Metal Multilayers	M.C. Shaw D.B. Marshall M.S. Dadkhah A.G. Evans
Article 5.	Mechanical Properties of an <i>In-Situ</i> Synthesized Nb/Nb <sub>3</sub> Al Layered Composite	H.C. Cao J.P.A. Löfvander A.G. Evans R.G. Rowe D.W. Skelly
Article 6.	A New Procedure For Measuring the Decohesion Energy For Thin Ductile Films on Substrates	A. Bagchi G.E. Lucas Z. Suo A.G. Evans
Article 7.	The Structure and Thermomechanical Properties of Mo/Al <sub>2</sub> O <sub>3</sub> Interfaces	M.R. Turner J.P.A. Löfvander J.B. Davis A.G. Evans
Article 8.	Fatigue Crack Growth and Stress Redistribution at Interfaces	M.C. Shaw D.B. Marshall B.J. Dalgleish M.S. Dadkhah M.Y. He A.G. Evans
Article 9.	Effects of Composite Processing on the Strength of Sapphire Fiber-Reinforced Composites	J.B. Davis J.Y. Yang A.G. Evans



## Section 1: EXECUTIVE SUMMARY

The research is concerned with the mechanical properties of ceramic/metal bonded systems and with establishing criteria for interface decohesion, for sliding and for cracking across interfaces. The research is closely coordinated with other ONR/ARPA programs at UCSB concerned with advanced composites. The research has application to the mechanical performance of biphasic systems, including metal matrix composites, layered materials and refractory metal toughened ceramics. It is also relevant to the adhesion of ceramic coatings on alloy substrates, the joining and brazing of metals to ceramics as well as the mechanical integrity of multilayer capacitors and ceramic packages for electronic devices. A central issue concerns the elucidation of relationships between interface debonding and sliding and the properties and dimensions of the constituents and interphases.

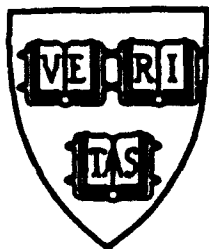
A major focus of the recent research has been on stress redistribution caused by slip and debonding of interfaces. Such redistribution ultimately controls the damage mechanisms that operate in multilayers and hence, their thermostructural performance. The preferred response is one in which damage is spatially distributed rather than localized into a dominant crack. To explore these effects, various calculations and experiments have been performed for multilayers containing cracks in one of the brittle layers. Then, the stresses in the neighboring layers have been ascertained for both slipping and debonding interfaces. The measurements have been made using both Moiré interferometry and fluorescence spectroscopy. The measurements are in good agreement with calculations, which show that debonding is much more effective than slip at reducing stress concentrations, thereby encouraging distributed rather than localized damage.

A complementary activity has been on the cyclic response of interfaces in multilayers, with associated implications for stress redistribution and thermostructural performance. For typical, well-bonded metal/ceramic interfaces, it has been found that fatigue crack growth occurs along the interface, in preference to crack growth through the alloy, whenever the interface is subject to a significant opening mode component (phase angle  $\Psi < 50^\circ$ ). Such fatigue debonding diminishes stress concentrations and enhances the thermostructural response. Conversely, when interface debonds are subject to shear (mode II), fatigue crack growth occurs preferentially through the alloy, leading to degraded structural

performance. The effect of mode mixity on interface fatigue has thus emerged as a critical issue for further study.

The effects of diffusion bonding on the tensile strength has been explored for metal/ceramic systems that do not form reaction products. It has been found that diffusional phenomena occurring at high temperatures cause morphological changes at the interface. Ridges and troughs form in response to surface and interface forces. These features act as flaws that diminish the tensile strength. Such effects are especially prevalent with high strength oxide fibers, which have properties sensitive to small surface flaws. This research has identified phenomena that must be avoided in order to prevent strength degradation in metal/ceramic systems.

Finally, a microelectronics-based method for measuring the debond energy for thin metal films on a substrate has been developed and used to determine the debonding of Cu from SiO<sub>2</sub>. It uses a vapor deposited Cr superlayer, subject to 'intrinsic' tensile stress, to provide the energy release rate for mixed mode decohesion, after deposition. The layer and the film are patterned and severed to establish the critical thickness at which spontaneous decohesion occurs. This critical thickness is explicitly related to  $\Gamma_i$ . The results for Cu/SiO<sub>2</sub> give  $\Gamma_i$  values in the range expected from other studies. The application of this new method to other thin films and multilayers is now being exploited.



MECH-201

# CRACKING AND STRESS REDISTRIBUTION IN CERAMIC LAYERED COMPOSITES

K. S. Chan  
Southwest Research Institute  
San Antonio, TX 78238-5100

M. Y. He  
Materials Department  
University of California, Santa Barbara  
Santa Barbara, CA 93106

and

J. W. Hutchinson  
Division of Applied Sciences  
Harvard University  
Cambridge, MA 02138

DTIC QUALITY INSPECTED 5

Division of Applied Sciences  
HARVARD UNIVERSITY  
Cambridge, Massachusetts 02138

November 1992

Accession For	
NTIS CRA&I	<input checked="checked" type="checkbox"/>
DTIC TAB	<input type="checkbox"/>
Unannounced	<input type="checkbox"/>
Justification	
By	
Distribution /	
Availability Codes	
Dist	Avail and/or Special
A-1	

## **CRACKING AND STRESS REDISTRIBUTION IN CERAMIC LAYERED COMPOSITES**

**K. S. Chan**  
Southwest Research Institute  
San Antonio, TX 78238-5100

**M. Y. He**  
Materials Department  
University of California, Santa Barbara  
Santa Barbara, CA 93106

**and**

**J. W. Hutchinson**  
Division of Applied Sciences  
Harvard University  
Cambridge, MA 02138

### **Abstract**

Several problems are analyzed that have bearing on cracking and survivability in the presence of cracking of layered composite materials comprised of brittle layers joined either by a weak interface or by a thin layer of a well-bonded ductile metal. The problems concern a crack in one brittle layer impinging on the interface with the neighboring brittle layer and either branching, if the interface is weak, or inducing plastic yielding, if a ductile bonding agent is present. For the case of a weak interface, the effect of debonding along the interface is analyzed and results for the stress redistribution in the uncracked layer directly ahead of the crack tip are presented. Debonding lowers the high stress concentration just across the interface, but causes a small increase in the tensile stresses further ahead of the tip in the uncracked layer. A similar stress redistribution occurs when the layers are joined by a very thin ductile layer that undergoes yielding above and below the crack tip, allowing the cracked layer to redistribute its load to the neighboring uncracked layer. The role of debonding and yielding of the interface on 3D tunnel cracking through an individual layer is also discussed and analyzed. Residual stress in the layers is included in the analysis.

## 1. Introduction

When layered, thin sheets of a brittle material may have toughness and strength properties which are far superior to those of the material in bulk form [1-6]. To achieve good strength and toughness, the interface between adjoining layers must stymie the stress concentration effect of any crack that occurs in an individual layer, reducing the likelihood that it will propagate into the next layer. Depending on the nature of the interface, this may occur by debonding, when the interface is brittle and relatively weak, or by yielding and sliding for systems comprised of brittle layers alternating with thin ductile adhesive layers. The latter category is represented by sheets of  $\text{Al}_2\text{O}_3$  joined by thin layers of aluminum [2] and by the model system with sheets of  $\text{Al}_2\text{O}_3$  bonded by epoxy [3]. Some of the issues related to the design of layered brittle materials are similar to those encountered in the design of fiber-reinforced brittle matrix composites, such as the selection of interface toughness to prevent matrix cracks from penetrating the fibers. Other issues are unique to the layered geometry, and this paper addresses a few of them. In particular, the role of yielding or debonding of the interface in defeating cracks in individual layers is analyzed by considering the stress redistribution in the adjoining uncracked layer that accompanies these processes. Results will also be given for the energy release rate of 3D cracks tunneling through an individual layer. This release rate, which is influenced by interface yielding or debonding, provides the essential information needed to predict the onset of widespread layer cracking in terms of the thickness of the brittle layer material and its toughness.

The geometries of the problems to be studied are laid out in Fig. 1. Fig. 1a shows a cracked layer of width  $2w$  with zones of either yielding or debonding in the interface extending a distance  $d$  above and below the crack tips. The interface is taken to be either a very thin ductile layer of an elastic-perfectly plastic material with shear flow stress,  $\tau$ , or a weak plane that debonds and slips under conditions such that the layers remain in contact and exert a friction stress  $\tau$  on each other. The ductile adhesive layer allows slipping of the layers it joins relative to one another by plastic yielding, but it is assumed that debonding does not occur. In this case, the condition  $K_2 = 0$  must be enforced, leading to well-behaved shear stresses at the end of the yielding zone and establishing the zone length  $d$ . In the case where the interface debonds, the interface crack is fully closed for  $d/w > 0.71$  [7]. The mode 2 stress intensity factor  $K_2$  at the end of the slipped zone will be nonzero and must attain the mode 2 toughness of the interface for the debond to spread. Results for  $K_2$  will be given.

Cracks in individual layers spread as 3D tunnel cracks propagating through the layer as depicted in Fig. 2. Once the crack has spread a distance of at least several layer thicknesses in the  $z$ -direction it approaches a steady-state wherein the behavior at the propagating crack front becomes independent of the length of the crack in the  $z$ -direction. Under these steady-state conditions, the

energy release rate of the propagating front can be computed using the plane strain solution associated with the geometry of Fig. 1a (other examples of tunnel cracks are given in the review article [8]). The steady-state energy release rate can be computed in terms of the average of the opening  $\delta(x)$  of the plane strain crack. The zone of yielding or debonding increases the tunneling energy release rate, thereby lowering the overall stress at which widespread layer cracking can occur. Results for the tunneling energy release rate will be given. The role of residual stresses in the layers are readily accounted for, as will be discussed in the final section.

When the interface is weak and debonding occurs, the interface crack is fully open with mixed mode intensity factors when  $d/w < 0.24$  [7]. This case can be well approximated by the asymptotic problem for a semi-infinite crack impinging the interface where the remote field is the K-field associated with the problem in Fig. 1a with  $d=0$ . The stress redistribution in the next layer ahead of the impinging crack tip will be given, along with a correction of previous results for the energy release rate for the doubly-deflected interface crack of [9]. When plastic yielding of a ductile adhesive layer occurs, another asymptotic problem applies when  $\sigma$  is sufficiently small compared to  $\tau$ . Then, the asymptotic problem is that shown in Fig. 1b for a semi-infinite crack loaded remotely by the same K-field. In this case as well, emphasis will be placed on the effect of yielding in the thin adhesive layer on the stress distribution ahead of the crack tip in the uncracked layer.

## 2. Effect of Plastic Yielding on Stress Redistribution.

As discussed above, the thin ductile adhesive layers in Fig. 1a are assumed to be elastic-perfectly plastic with a yield stress in shear of  $\tau$  and are modeled as having zero thickness. The plane strain problem is considered where the central cracked layer has the same elastic properties ( $E, \nu$ ) as the semi-infinite blocks adjoining across the interfaces. Under monotonic increase of the applied remote stress,  $\sigma$ , the zones of yielding of half-height  $d$  spread allowing slip in the form of a tangential displacement discontinuity across the interface in the yielded region. The condition  $\sigma_{xy} = \pm \tau$  is enforced within the yielded zones of the interface. The Dugdale-like condition,  $K_2 = 0$ , at the ends of the yielded zones ensures that the shear stress on the interface falls off continuously just outside the yielded zone, and it determines the relation of  $d/w$  to  $\sigma/\tau$  under the monotonic loading considered. Integral equation methods are employed to solve this problem, as well as the others posed below; a brief outline of the methods used are discussed in the Appendix.

The two most important functional relations needed to solve the 3D tunneling crack problem discussed below are shown in Figures 3 and 4. In Fig. 4,  $\bar{\delta}$  is the average crack opening displacement defined by

$$\bar{\delta} = \frac{1}{2w} \int_{-w}^w \delta(\xi) d\xi \quad (1)$$

The elastic value of  $\bar{\delta}$ , valid when there is no yielding ( $\tau \rightarrow \infty$ ), is  $\bar{\delta}_0 = \pi(1-\nu^2)\sigma w/E$ . Yielding of the adhesive layers begins to make a significant contribution to the average crack opening displacement when  $\sigma/\tau$  exceeds unity. The redistribution of normal stress,  $\sigma_{yy}(x,0)$ , in the block of material across the interface is shown in Fig. 5 for three levels of  $\sigma/\tau$ . The curve shown for  $\sigma/\tau=1.5$  is only very slightly reduced below the elastic distribution ( $\sigma_{yy}(x,0)=(x+1)/(x^2+2x)^{1/2}$ ) for  $x/w > 0.05$ . Reduction of stress ahead of the crack tip begins to be appreciable when  $\sigma/\tau=2.7$ , and is quite significant when  $\sigma/\tau=6.4$ . The drop in stress just across the interface is offset by a slight increase in stress relative to the elastic distribution further away from the interface. This is a feature seen in all the stress redistribution results.

Stress redistribution can be presented in another way when  $d/w$  is sufficiently small using the asymptotic problem depicted in Fig. 1b. As long as  $d/w$  is sufficiently small, the yielding behavior is small scale yielding with the elastic stress intensity factor  $K$  as the controlling load parameter. The remote field imposed on the semi-infinite crack is the elastic  $K$ -field. This asymptotic problem has also been solved with integral equation techniques. The extent of the yield zone in the asymptotic problem is

$$d = 0.052 \left( \frac{K}{\tau} \right)^2 \quad (2)$$

Fig. 6 displays the normal stress directly ahead of the crack tip in the adjoining block normalized by the elastic stress field for the limit  $\tau = \infty$ . The stress ratio in Fig. 6 depends on  $x/d$  but is otherwise independent of  $K$  in the asymptotic problem. Yielding reduces the stress below the elastic level over a region ahead of the crack tip which is a little larger than  $d/10$ . Beyond that region the stresses are slightly elevated above the elastic levels and approach the elastic distribution as  $x/d$  becomes large. The stress redistribution due to debonding which is also presented in Fig. 6 is more dramatic, as will be discussed later in the paper.

### 3. Effect of Plastic Yielding on Tunnel Cracking

As stated earlier, the steady-state energy release rate for a 3D tunneling crack can be computed using the plane strain solution. For the geometry and loading shown in Figs. 1a and 2, the leading edge of the tunneling crack propagating in the  $z$ -direction experiences mode I conditions. Let  $G_{ss}$  denote the energy release rate averaged over the propagating crack front. An energy balance accounting for the release of energy per unit advance of the tunnel crack under steady-state conditions gives that  $2wG_{ss}$  is the work done by the tractions acting across the plane

of the layer crack in the plane strain problem as those tractions are reduced to zero from  $\sigma$ . For the present problems, this is the same as

$$G_{ss} = \int_0^{\sigma} \bar{\delta}(\sigma') d\sigma' \quad (3)$$

where  $\bar{\delta}$  is the average crack opening displacement for the traction-free plane strain crack under monotonically increased remote  $\sigma$ . The elastic result for  $d=0$  (i.e.,  $\tau=\infty$ ) is

$$G_{ss}^0 = \frac{\pi(1-\nu^2)\sigma^2 w}{2E} \quad (4)$$

The ratio of  $G_{ss}$  to  $G_{ss}^0$  can be computed from the data in Fig. 4 using simple numerical integration. The result is plotted in Fig. 7. Increases of the steady-state release rate above the elastic value become important when  $\sigma/\tau$  exceeds unity.

#### 4. Effect of Debonding and Frictionless Slipping on Stress Redistribution

A review of the plane strain interface debonding problem for the geometry of Fig. 1a is as follows for the case where no frictional resistance is exerted across the debonded interfaces (i.e.,  $\tau=0$ ). According to [7], the debonded interface will be fully open when  $d/w < 0.24$ , and the interface crack tip at the end of the debond is subject to mixed mode conditions, as will be discussed further for the asymptotic problem below. For  $0.24 < d/w < 0.71$ , the debond crack tip is closed and therefore in a state of pure mode 2, but a portion of the interface near the main layer crack is still open. For  $d/w > 0.71$ , the interface is fully closed and the interface crack tip is in mode 2. The top curve for the normalized mode 2 stress intensity factor in Fig. 8 applies to the frictionless case. It was computed using the integral equation methods outlined in the Appendix under the constraint that the interface remains closed. The results are strictly correct only for  $d/w > 0.71$  (and are in agreement with the results of [7]), but are only slightly in error for smaller  $d/w$ . The average crack opening displacement,  $\bar{\delta}$ , needed for the tunnel crack calculations is shown in Fig. 9 where the top curve again applies to the frictionless case.

The role of debonding on stress redistribution is seen in Fig. 10, where curves of the stress ahead of the right-hand layer crack tip (normalized by the remote applied stress  $\sigma$ ) are plotted for various levels of debonding, all for the closed interface with  $\tau=0$ . Debonding clearly has a significant effect on lowering the stress on the adjoining material just across the interface, more so than for plastic yielding of a thin ductile layer discussed in connection with Fig. 5. For sufficiently small  $d/w$ , the debonded interface is fully open and, moreover, the asymptotic problem for a semi-infinite crack impinging on the interface applies, as depicted in the insert of Fig. 6. The stress redistribution is plotted in Fig. 6, which shows that the stress ahead of the layer crack tip is



reduced below the level in the absence of debonding over a distance from the interface equal to one-half of the debond length  $d$ . This figure also makes clear that debonding appears to be more effective in protecting the uncracked layer across the interface than plastic yielding of a thin ductile adhesive layer.

As a digression, we record the mode 1 and 2 stress intensity factors for the open interface crack tip for the asymptotic problem of Fig. 6:

$$\frac{K_1}{K} = 0.399 \quad \text{and} \quad \frac{K_2}{K} = 0.322 \quad (5)$$

The associated ratio of the energy release rate of the interface crack tip to that of a mode I crack penetrating straight through the interface without debonding is 0.263 when both the deflected tips and the penetrating tip emerge from the main crack tip at the same applied  $K$ . These results correct results given in [9] which were in error for the case of the doubly-deflected interface crack. A complete set of corrections of this energy release rate ratio for this case over the full range of elastic mismatch across the interface will be included in an upcoming paper [10].

## 5. The Effect of Frictional Slipping on Debonding and Tunnel Cracking

Figs. 8 and 9 contain curves for the normalized mode 2 stress intensity factor and the average crack opening displacement, respectively, in the plane strain problem for several levels of a constant friction stress  $\tau$  relative to  $\sigma$  acting over the bonded interface. A constant friction stress, as opposed, for example, to a Coulomb friction stress, has been used by a number of workers to represent the frictional forces exerted across slipping interfaces in composites. The purpose of the present limited study is to illustrate the effect of friction in establishing the extent of debonding and its associated influence on the 3D tunneling energy release rate. Almost certainly, additional studies will be required before a good understanding is in hand, including studies with other friction laws. Some results for the effect of Coulomb friction on the mode 2 interface stress intensity factor have been presented in [11].

Let  $K_c$  denote the mode 2 toughness of the interface. Attention will be concentrated on the behavior following initiation of interface debonding when the debond length,  $d$ , is sufficiently large (i.e., greater than about  $w/4$ ) such that the debond interface crack tip is in mode 2. Impose the debonding condition,  $K_2=K_c$ , on the solution presented in Figs. 8 and 9. The relationships that result between the applied stress and the debonding length and the average crack opening displacement are plotted in Figs. 11 and 12. The two nondimensional stress parameters in these figures are the applied stress parameter,  $(\sigma\sqrt{w})/K_c$ , and the constant friction stress parameter,  $(\tau\sqrt{w})/K_c$ . (Note that it is necessary to interpolate values between the curves of Figs. 8 and 9 to

arrive at the plots in Figs. 11 and 12, since a constant value of  $(\tau\sqrt{w})/K_c$  does not correspond to a constant value of  $\tau/\sigma$ .) In the range of  $d$  less than about  $w/4$ , the predictions are not expected to be correct since the interface undergoes mixed mode debonding and not mode 2 debonding. Thus, the details in the vicinity of the initiation of debonding are not correct. In particular, the value of  $(\sigma\sqrt{w})/K_c$  at which  $\bar{\delta}$  begins to depart from  $\bar{\delta}_0$  (see Fig. 12) would depend on the mixed mode condition for debond initiation. But once debonding has progressed to the point that the interface crack tip is closed, the mode 2 criterion is appropriate and the curves are accurate.

In the absence of friction the debonding process is unstable, since for a fixed  $\sigma$ ,  $K_2$  has a maximum when  $d \cong w$  and then drops slightly to an asymptote as  $d$  increases further. Under a prescribed  $\sigma$ , the mode 2 debond would advance dynamically after it is initiated. In this sense, the curves shown in Figs. 11 and 12 for  $\tau=0$  represent unstable debonding behavior. Friction stabilizes the debonding process giving rise to a monotonically increasing debond length and average crack opening displacement as the applied stress increases. A nondimensional friction stress on the order of  $(\tau\sqrt{w})/K_c=1/8$  or more is required if friction is to be important.

The steady-state energy release rate for tunnel cracking can be computed from the curves in Fig. 12 using (3). The results of this calculation are plotted in Fig. 13. As before,  $G_{ss}$  is normalized by the value for a layer crack with no debonding given in (4). The remarks made above with respect to accuracy in the vicinity of debond initiation apply to these curves as well. It can be seen from Fig. 13 that debonding can indeed significantly promote tunneling cracking when the nondimensional friction stress is less than about  $(\tau\sqrt{w})/K_c=1/2$ .

## 6. Accounting for Residual Stress in the Cracked Layer

The role of an uniform residual tension,  $\sigma_{yy}=\sigma_R$ , pre-existing in the layer that subsequently undergoes tunnel cracking can be readily taken into account in the various results presented above. For the purpose of discussion, now let  $\sigma_{yy}=\sigma_A$  be the applied stress, replacing the notation for  $\sigma$  in the earlier sections. The results in Figs. 3-4, 7-9 and 11-13 apply as they stand if  $\sigma$  in those figures is identified with  $\sigma_A+\sigma_R$ . The results for stress redistribution shown in Figs. 5 and 10 can also be used with the following modifications. With  $\sigma$  identified with  $\sigma_A+\sigma_R$ , the results in Figs. 5 and 10 are correct for the *change* in  $\sigma_{yy}$  in the layer ahead of the tip due to cracking if the numerical value of the ordinate is reduced by 1. To obtain the total stress  $\sigma_{yy}$  in the layer in question, one must then add together the *change* and the stress  $\sigma_{yy}$  existing in the layer prior to the cracking event.

## **Acknowledgment**

The work of KSC was supported by the Internal Research Program, Southwest Research Institute, San Antonio, Texas. The work of M-YH was supported by the DARPA URI at the University of California, Santa Barbara (ONR Contract N00014-86-K-0753). The work of JWH was supported in part by the DARPA URI (Subagreement P.O.#VB38639-0 with the University of California, Santa Barbara, ONR Prime Contract N00014-86-K-0753) and by the Division of Applied Sciences, Harvard University.

## **References**

1. D.B. Marshall and J.J. Ratto, *J. Am. Ceram. Soc.* 74 (1991) 2979-2987.
2. H.C. Cao and A.G. Evans, *Acta Metall. Mater.*, 39 (1991) 2997.
3. C.A. Folsom, F.W. Zok, F.F. Lange and D.B. Marshall, "The mechanical behavior of a laminar ceramic composite", to be published in *J. Am. Ceram. Soc.*
4. B.J. Dalgleish, K.P. Trumble and A.G. Evans, *Acta Metall. Mater.*, 37 (1989) 1923-1931.
5. M.C. Shaw, D.B. Marshall, M.S. Dadkhah and A.G. Evans, "Cracking and damage mechanisms in ceramic/metal multilayers, to be published in *J. Am. Ceram. Soc.*
6. M.Y. He, F.E. Heredia, D.J. Wissuchek, M.C. Shaw and A.G. Evans, "The mechanics of crack growth in layered materials" to be published in *Acta Metall. Mater.*
7. A. Dollar and P.S. Steif, *J. Appl. Mech.*, 58 (1991) 584-586.
8. J.W. Hutchinson and Z. Suo, "Mixed mode cracking in layered materials", in *Adv. Appl. Mech.*, 29 (1991) 63-191.
9. M.Y. He and J.W. Hutchinson, *Int. J. Solids Structures*, 25 (1989) 1053-1067.
10. M.Y. He and J.W. Hutchinson, "The effect of residual stress on the competition between crack deflection and penetration at an interface", to be published.
11. A. Dollar and P.S. Steif, "Interface blunting of matrix cracks in fiber-reinforced ceramics", to be published in *J. Appl. Mech.*

## **Appendix: Numerical Approaches**

Two integral equation formulations were used in the solution of the problems discussed. Both methods have been used by various authors to solve related plane strain problems and, for this reason, details of the methods will not be given. In some cases, results were generated using both schemes as a check. The methods used for the problems for the closed interface cracks at the ends of the finite length layer crack (see Fig. 1a) will be discussed first.

The integral equations in method 1 are formed by representing both the layer crack and the mode 2 interface cracks by distributions of dislocations. With reference to Fig. 1a, let  $b_0(x) = -d\delta_y/dx$  denote the amplitude of the dislocation opening distribution extending from 0 to  $w$  along  $y=0$ , and let  $b_s(y) = -d\delta_y/dy$  denote the amplitude of the dislocation shearing distribution along  $x=w$  extending from 0 to  $d$ . The condition that  $\sigma_{yy}=0$  along  $y=0$  for  $-w < x < w$  can be written as

$$\int_0^w H_1(x, x') b_0(x') dx' + \int_0^d H_2(x, y) b_s(y) dy = -\sigma \quad (A1)$$

where  $H_1(x, x')$  denotes the stress  $\sigma_{yy}(x)$  along  $y=0$  due to  $b_0(x')$ , with due regard for the symmetry of this distribution with respect to  $x=0$ , and  $H_2(x, y)$  denotes  $\sigma_{yy}(x)$  due to  $b_s(y)$ , with the appropriate four-fold symmetry on this distribution imposed. Similarly, the condition that  $\sigma_{xy} = -\tau$  along  $x=w$  between 0 and  $d$  (with the corresponding shear conditions met along the other three legs of the H-crack) is

$$\int_0^w H_3(y, x') b_0(x') dx' + \int_0^d H_4(y, y') b_s(y') dy' = -\tau \quad (A2)$$

where  $H_3(y, x')$  is  $\sigma_{xy}(y)$  along  $x=w$  due to  $b_0(x')$  and  $H_4(y, y')$  is  $\sigma_{xy}(y)$  due to  $b_s(y')$ .

Method 2 makes use of the solution for the problem of four symmetrically placed dislocations interacting with a traction free crack extending along the  $x$ -axis from  $-w$  to  $w$ . With  $H(y, y')$  denoting the shear stress  $\sigma_{xy}(y)$  along  $x=w$  between 0 and  $d$  due to  $b_s(y')$ , with due regard for the other three symmetrically placed dislocations, the single integral equation for  $b_s$  is

$$\int_0^d H(y, y') b_s(y') dy' = -\sigma_{xy}^0(y) - \tau \quad (A3)$$

where  $\sigma_{xy}^0(y)$  is the shear stress along  $x=w$  due to the remote stress acting on the layer crack in the absence of the interface cracks.

The kernels of the integrals above have Cauchy singularities. The dislocation distributions can be obtained using several well known numerical techniques. Once the distributions are known in either method, they may be used with other integral expressions to compute the stress components at any point in the plane and the mode 2 stress intensity factor at the end of the interface crack. For the cases in which  $K_2$  is nonzero, the distribution  $b_s(y)$  has an inverse square root singularity at  $y=d$ , while it diminishes with the square root of the distance from  $y=d$  for the plastic yielding problems with  $K_2=0$ . The solutions are not overly sensitive to having a precise incorporation of the correct behavior of the dislocation distributions at the corner point at  $x=w$  on  $y=0$ . A number of choices were made, including representations which built-in the correct lowest order functional behavior near this point.

The asymptotic problem for the semi-infinite layer crack and the mode 2 interface cracks (see Fig.1b) was solved using method 2. Now,  $H(y,y')$  is the shear stress along  $x=0$  between 0 and  $d$  due to just two symmetrically placed dislocations on  $x=0$  at  $\pm$  interacting with a traction-free semi-infinite crack, and  $\sigma_{xy}^0(y)$  is the shear stress on  $x=0$  due to the K-field in the absence of the interface cracks. The second asymptotic problem discussed in connection with Fig. 6 in which the interface crack opens is also solved using method 2, but here both shear dislocations and opening dislocations must be used and the problem becomes a set of dual integral equations. In all the cases involving method 2, the kernel functions  $H$  can be obtained in closed form using complex variable methods of elasticity.

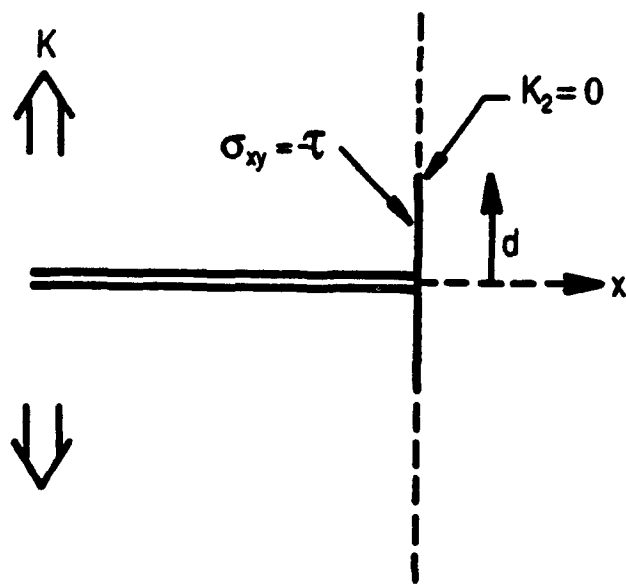
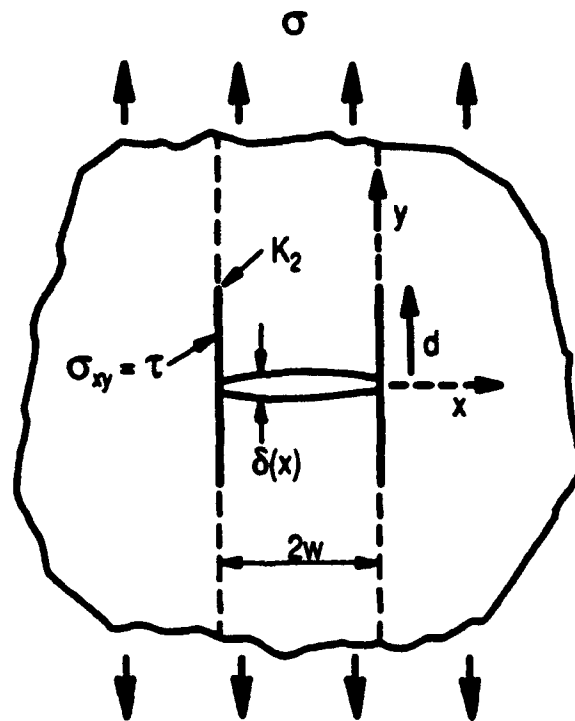


Fig.1 Specification of the plane strain problems. a) Finite layer crack. b) Asymptotic problem.

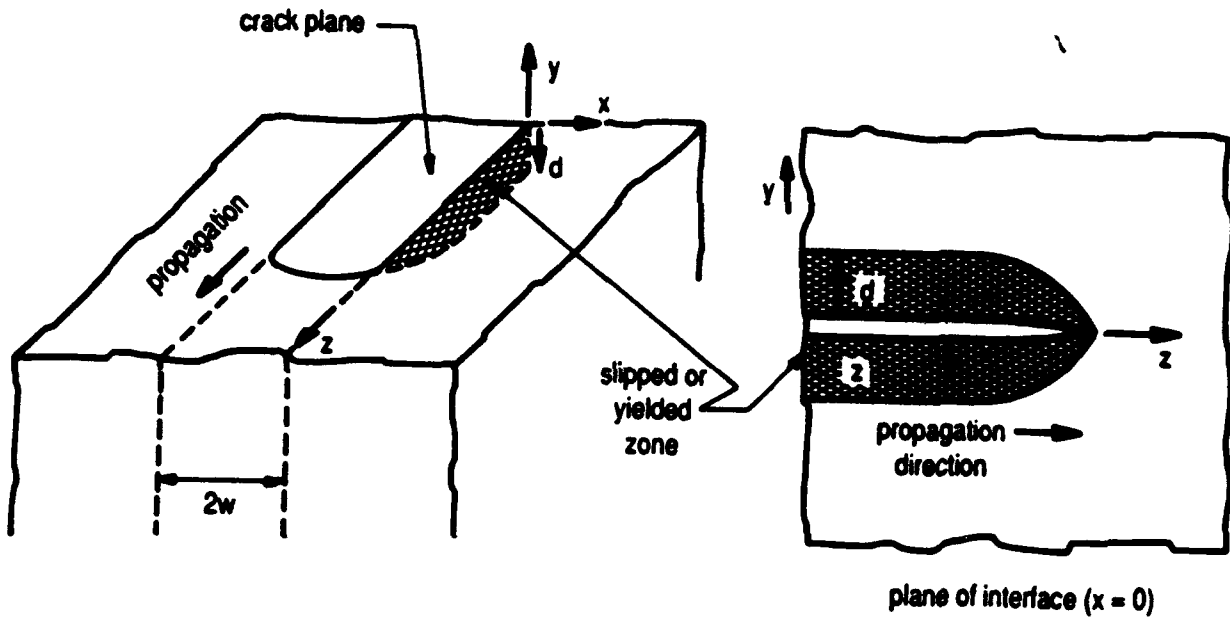


Fig.2 Specification of the 3D tunneling crack problem.

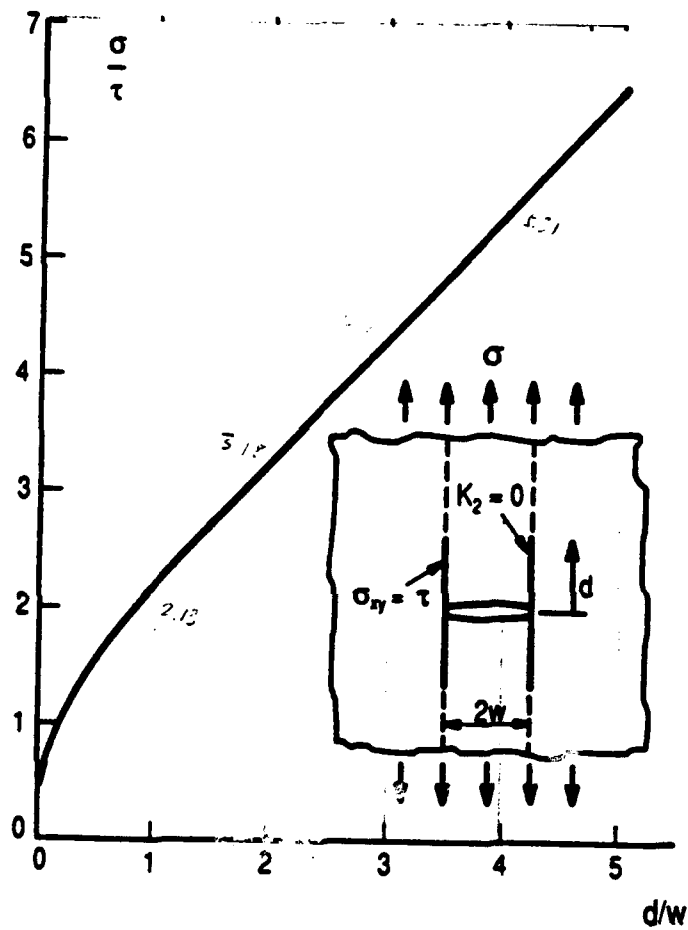


Fig.3 Relation between applied stress and height of the yielding zone in a thin ductile adhesive layer.

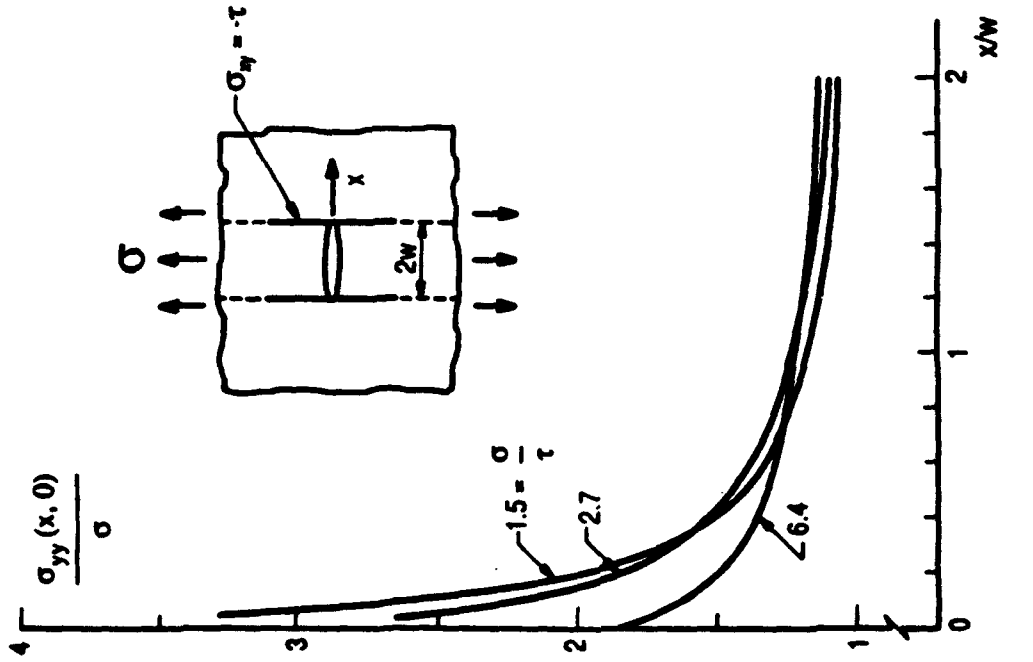


Fig.5 Stress distribution ahead of the crack tip in the uncracked layer at several levels of applied stress to shear yield stress of the thin adhesive layer.

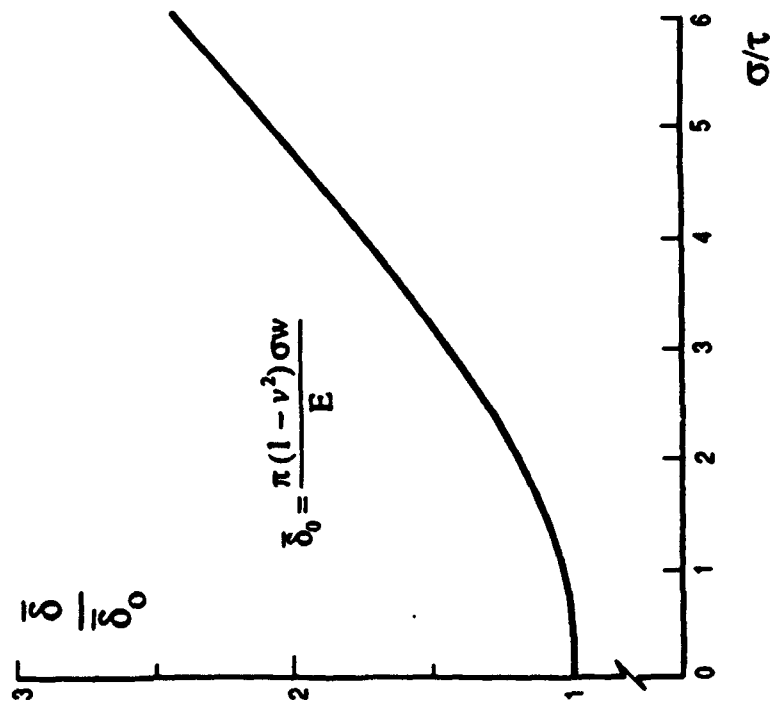


Fig.4 Average crack opening displacement as a function of the ratio of applied stress to shear yield stress of the thin ductile adhesive layer.



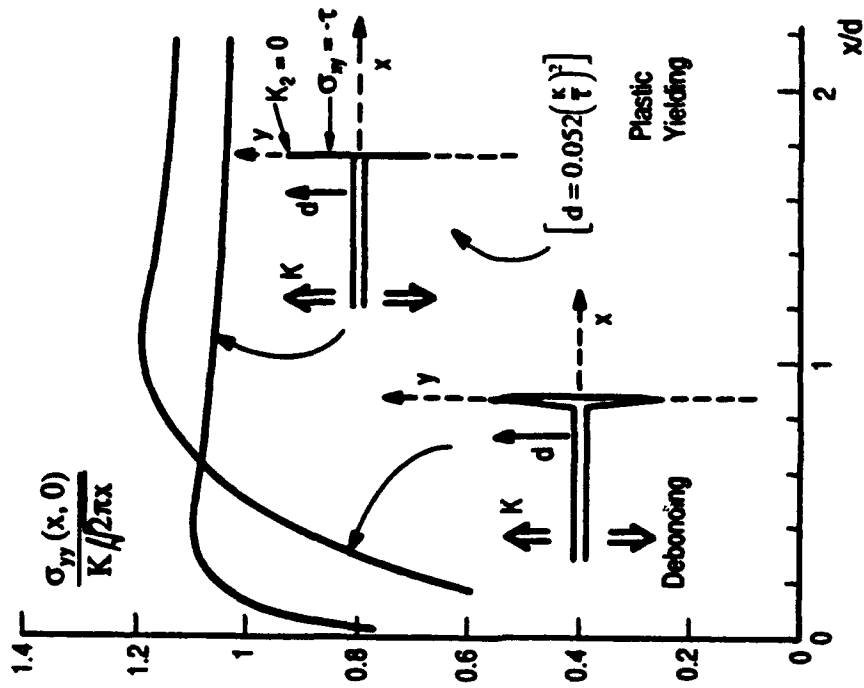


Fig.6 Stress redistribution ahead of the crack tip in the layer across the interface for the two asymptotic problems ( $d \ll w$ ).

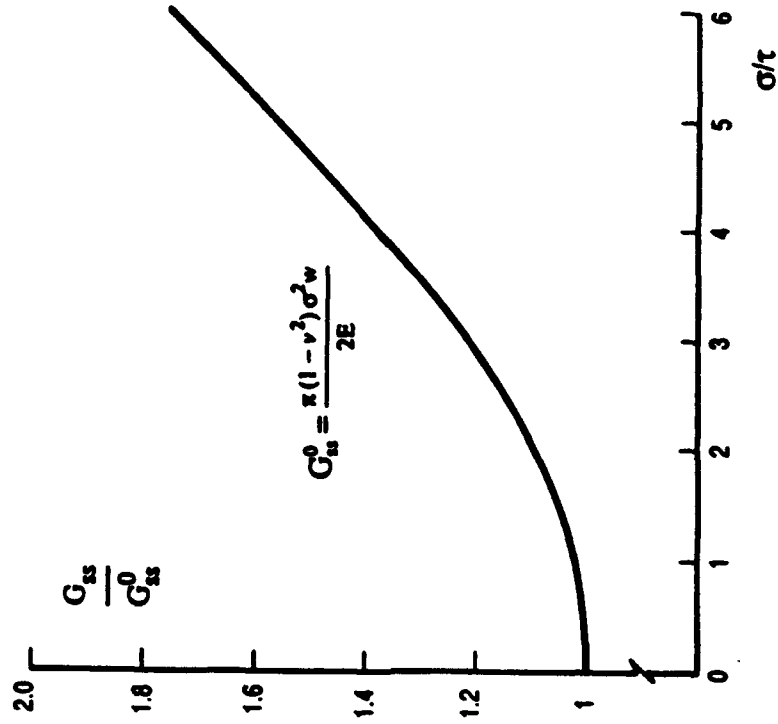


Fig.7 Normalized steady-state energy release rate for the tunneling crack for the case of thin ductile adhesive layers with shear yield stress  $\tau$ .

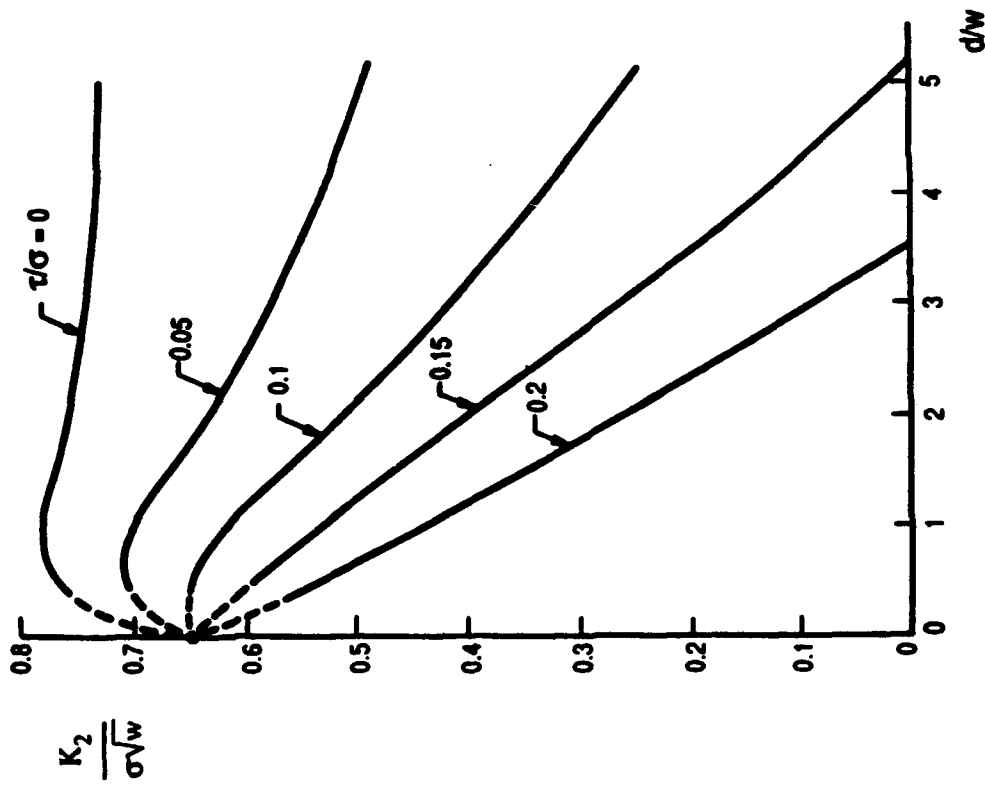


Fig.8 Normalized mode 2 stress intensity factor for the debonding interface crack at several levels of interface friction stress to applied stress.

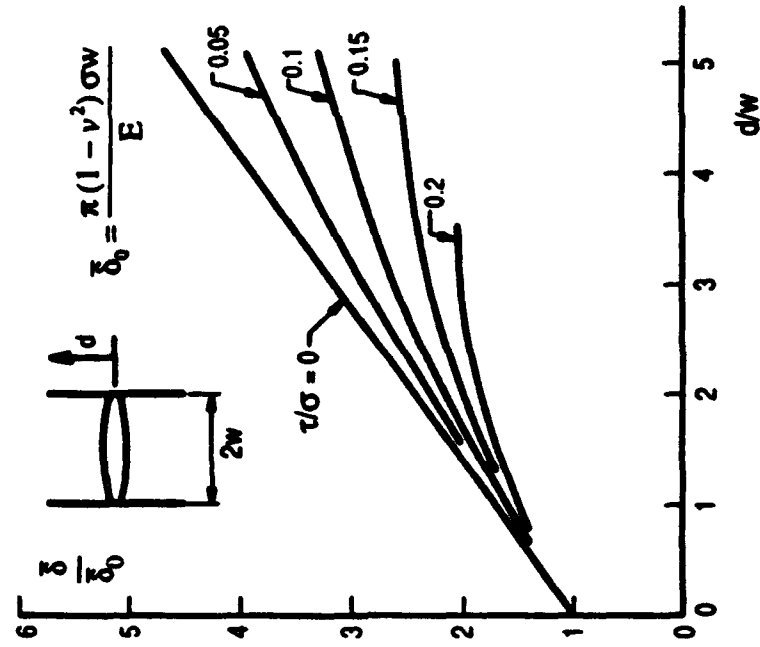


Fig.9 Average crack opening displacement as a function of debond length at several levels of interface friction stress to applied stress.

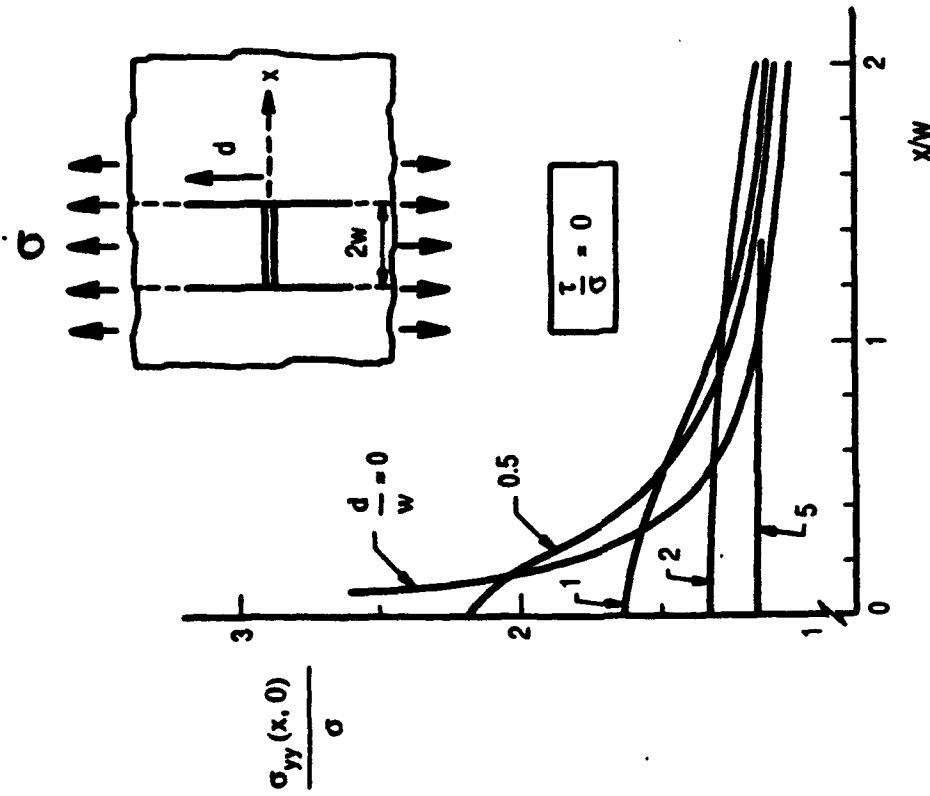


Fig.10 Stress distribution ahead of the crack tip in the uncracked layer across the interface for the case of no interface friction.

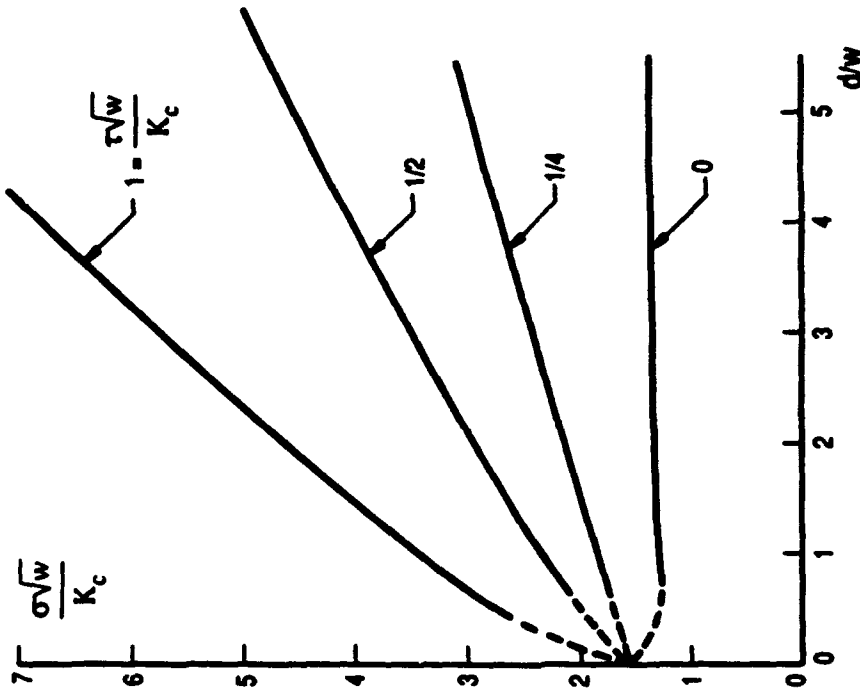


Fig.11 Relation between normalized applied stress and debond height at several levels of the non-dimensional interface friction stress. The condition  $K_2=K_c$  is imposed where  $K_c$  is the mode 2 interface toughness.

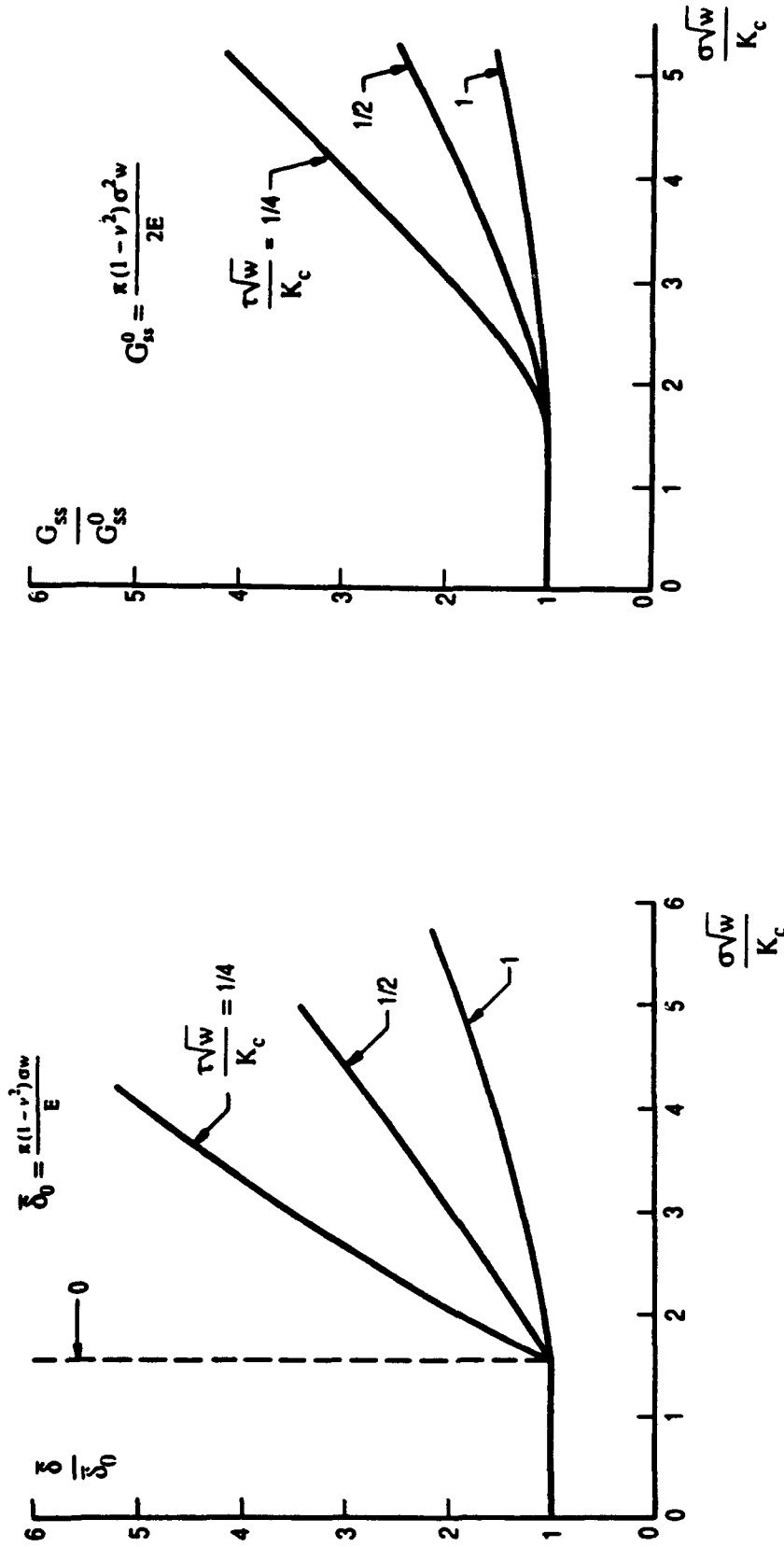


Fig.12 Relation between the average crack opening displacement and normalized applied stress at several levels of the nondimensional interface friction stress. The condition  $K_2=K_c$  has been imposed where  $K_c$  is the mode 2 interface toughness.

Fig.13 Steady-state energy release rate for the tunneling crack. The condition  $K_2=K_c$  has been imposed where  $K_c$  is the mode 2 interface toughness.

# Fracture Resistance Characteristics of a Metal-Toughened Ceramic

Brian D. Flinn, Calvin S. Lo, Frank W. Zok,\* and Anthony G. Evans\*

Materials and Mechanical Engineering Departments, College of Engineering, University of California, Santa Barbara, California 93106-5050

The fracture characteristics of an  $\text{Al}_2\text{O}_3/\text{Al}$  composite are examined. Measurements of resistance curves and work of rupture are compared with predictions of a micromechanical model, incorporating the effects of crack bridging by the Al reinforcements. The bridging traction law is assumed to follow linear softening behavior, characterized by a peak stress,  $\sigma_c$ , and a critical stretch-to-failure,  $u_c$ . The values of  $\sigma_c$  and  $u_c$  inferred from such comparisons are found to be broadly consistent with independent measurements of stretch-to-failure, along with the measured flow characteristics of the Al reinforcement. The importance of large-scale bridging on the fracture resistance behavior of this class of composite is also demonstrated through both the experiments and the simulations.

## 1. Introduction

THE toughening of ceramics and intermetallics by ductile reinforcements has been comprehensively studied,<sup>1-16</sup> and has encompassed the range of materials indicated in Table I. Three key factors regarding such toughening have emerged from these studies as being in need of clarification and further understanding: (i) the partitioning of the plastic dissipation accompanying crack growth between bridging metal ligaments and a process zone; (ii) control of interface debonding and associated relationships with the dissipation occurring within the bridging ligaments; (iii) the incidence and importance of large-scale bridging (LSB)<sup>17</sup> and the resulting relationships between resistance curves, basic constituent properties, and the macroscopic load/deflection response of the composite. This article addresses aspects of each of these issues through experiments and analysis on  $\text{Al}_2\text{O}_3$  toughened with an Al/Mg alloy.

Experimental evidence presented for WC/Co<sup>9</sup> and  $\text{Al}_2\text{O}_3/\text{Al}$ <sup>2</sup> has indicated that both bridging and nonlinear process zones can accompany crack growth and contribute to the crack growth resistance. Trends in these two contributions with microstructure are predicted to be very different.<sup>9</sup> Consequently, it is important to understand and model the separate contributions. Calculations indicate that the dissipation is dominated by the plastically stretching ligaments,<sup>18</sup> provided that the crack surface tractions induced by the ligaments are relatively small compared with the flow strength of the composite material within the process zone. The explicit requirement for ligament dominance is given by the inequality

$$f\sigma_b \approx 3\sigma_f \quad (1)$$

where  $f$  is the volume fraction of the ductile material,  $\sigma_b$  is the average crack surface traction generated by the intact metal ligaments, and  $\sigma_f$  is a measure of the flow strength of the composite. For  $\text{Al}_2\text{O}_3/\text{Al}$  alloy composites with typical values of metal concentration ( $f \approx 0.2$ ),  $\sigma_b$  scales with the uniaxial yield strength of the alloy,<sup>15</sup>  $\sigma_0$ , and is relatively low ( $\sim 100$  MPa),

Table I. Ductile Reinforcement Toughened Ceramics and Intermetallics

Matrix	Reinforcement	Ref
$\text{Al}_2\text{O}_3$	Al	1-4
$\text{B}_2\text{C}$	Al	5
WC	Co	6-9
TiAl	Nb	10
MoSi <sub>2</sub>	Nb	11, 12
NiAl	Mo, Cr	13
AlN	Al	14

whereas  $\sigma_f$ , which is dominated by the elasticity of the matrix,<sup>9</sup> is considerably larger ( $>500$  MPa). Consequently, Eq. (1) predicts that the dissipation should occur *exclusively* in the bridging ligaments. This material system should thus provide a good experimental test of the crack growth predictions based on bridging.

The  $\text{Al}_2\text{O}_3/\text{Al}$  interface is "strong,"<sup>19</sup> but can experience ductile debonding in constrained regions. It should thus be possible in this system to examine the influence of controlled debonding on the fracture resistance. Furthermore, such debonding is expected to result in large-scale bridging. Consequently, this material also provides an experimental model for testing and validating the LSB analyses<sup>20,21</sup> now available for predicting effects of specimen geometry on the nominal fracture resistance.

When fracture resistance is dominated by plastically deforming ligaments, the stress/stretch function associated with these ligaments,  $\sigma_b(u)$ , is the key composite property. A major objective of the present study is the determination of  $\sigma_b(u)$  and its rationalization in terms of the properties of the Al alloy reinforcements, as well as the interface debonding. In general, it has been found that a linear softening traction law has applicability to ductile phase toughened materials,<sup>22</sup> governed by

$$\sigma_b \approx \sigma_c(1 - u/u_c) \quad (2)$$

where  $u$  is the crack opening displacement, and  $\sigma_c$  and  $u_c$  are constants to be determined either by experiment or by calculation. Furthermore,  $\sigma_c$  should be a multiple of the uniaxial yield strength of the reinforcements  $\sigma_0$ . This formulation has led to the following explicit results for the crack growth resistance under small-scale bridging (SSB) conditions: (i) a steady-state toughness ( $\Gamma_{ss}$ ) given by<sup>21</sup>

$$\Gamma_{ss} = \Gamma_m(1 - f) + \sigma_c u_c f/2 \quad (3)$$

where  $\Gamma_m$  is the matrix fracture energy; and (ii) a resistance prior to steady-state ( $\Gamma_R$ ) given by<sup>21</sup>

$$\Gamma_R(\Delta a) \approx \Gamma_m(1 - f) + \sigma_c f u_c [1.6\ell - 0.1\ell^2 + 0.53\ell^3]/4 \quad (4)$$

where  $\ell = \Delta a/L_c$ , with  $\Delta a$  being the crack extension and  $L_c$  the crack growth at the onset of steady-state,

$$L_c = 0.37E u_c / \sigma_c \quad (5)$$

R. Kerans—contributing editor

Manuscript No. 195531. Received July 6, 1992; approved September 10, 1992.

\*Member, American Ceramic Society.

where  $E$  is Young's modulus for the composite. However, as already noted, when large-scale bridging occurs, the nominal resistance may deviate substantially from the SSB predictions. This issue will be a major focus of the present study.

## II. Materials

Composites used in this investigation were fabricated using the method developed by Lange *et al.*<sup>22</sup> In this method, the architecture of the metal is determined by the choice of a pyrolyzable precursor. The precursor (a polymer fiber felt) is packed with a high-purity alumina (Sumitomo AKP-50) slurry by pressure infiltration. After drying, the green body is slowly heated to burn out the precursor and then sintered at 1550°C for 30 min, leaving an interconnected network of channels. The as-sintered  $\text{Al}_2\text{O}_3$  structure is visible on the channel walls. This sintering schedule produces a fine-grained ( $\sim 4\ \mu\text{m}$ ) ceramic preform, with a relatively density  $\geq 99\%$  (exclusive of the channels) (Fig. 1(a)). The preform is then infiltrated with molten Al/4 wt% Mg alloy, by squeeze casting, to produce the composite. The alloy had been heated to 780°C and squeeze cast at a pressure of 170 MPa. The composite billets were typically  $\sim 30$  mm in diameter and  $\sim 5$  mm thick. Microstructural examination of the composite revealed a relatively uniform network of randomly oriented cylindrical aluminum fibers,  $\sim 19\ \mu\text{m}$  in diameter. The metal volume fraction, measured by quantitative metallography, was  $f = 0.28$  (Fig. 1(b)).

The Al channels were devoid of porosity and were bonded to the  $\text{Al}_2\text{O}_3$  matrix. The  $\text{Al}_2\text{O}_3$  grain boundaries appeared devoid of grain boundary phases, as ascertained in the transmission electron microscope (TEM) using dark field, through focus and the EDS X-ray technique. Bright-field TEM indicated no detectable segregation and no interphase formation at the metal/ceramic interface. The aluminum alloy was single phase with magnesium in solid solution.

## III. Measurements and Observations

### (1) Mechanical Testing Procedures

Mechanical test specimens were cut from the composites, surface ground with diamond-impregnated wheels, and notches cut using thin ( $150\ \mu\text{m}$ ) diamond blades. Polished surfaces for crack length measurements were prepared using standard metallographic techniques. Two types of mechanical tests were performed to obtain the fracture resistance curves and the work of rupture. Resistance curve measurements were made upon polished, notched flexure beams ( $3.6\ \text{mm} \times 3.6\ \text{mm} \times 20\ \text{mm}$ ), in accordance with ASTM standards.<sup>23</sup> Specimens were

prepared with notch depths of 0.5, 1.0, and 1.5 mm, representing notch depth to specimen height ratios,  $a/W$ , of 0.14, 0.28, and 0.42. Two flexure test procedures were used: (1) *in situ* inside a scanning electron microscope, and (2) within a stiff servohydraulic test frame (MTS Model 810) using a traveling optical microscope to measure crack lengths. Tests were conducted at a displacement rate of  $0.2\ \mu\text{m/s}$ .

The steady-state fracture properties were characterized using work-of-rupture tests.<sup>22,24</sup> This test involved measurement of the work required to stably propagate a crack across a chevron-notched flexure specimen. To ensure stable crack propagation, the specimen width was twice the specimen height ("double-width specimens").<sup>22,24</sup> Furthermore, a short precrack ( $\sim 100\ \mu\text{m}$ ) was introduced at the notch using a Vickers indenter with a load of 200 N. Corresponding tests were conducted on fully dense  $\text{Al}_2\text{O}_3$  specimens, to allow the toughness enhancement attributable to the metal reinforcements to be evaluated.

The flow properties of the bulk Al/Mg alloy were measured from dog-bone tensile specimens machined from squeeze-cast ingots. Hardness measurements were also made with a nanoindenter on both the bulk Al/Mg alloy and the reinforcements within the composite, in order to compare their flow properties.

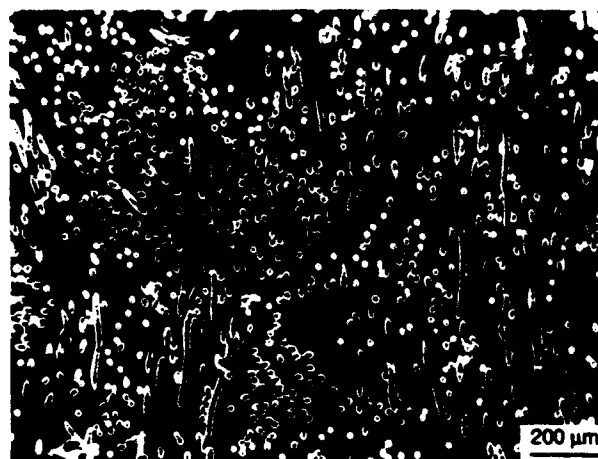
### (2) Fracture Observations

*In situ* and postfracture observations conducted in the SEM provided insight into the crack growth mechanism, as well as the plastic stretching of the Al ligaments. Observations performed *in situ*, shown at four different crack openings in Fig. 2, confirm the existence of a plastic stretching mechanism. Investigation of the resultant fracture surfaces by SEM revealed primarily transgranular cleavage of the  $\text{Al}_2\text{O}_3$  and extensive plastic deformation of the Al. The stretch-to-failure of  $\sim 60$  ligaments was measured using stereo measurements on SEM micrographs. The Al ligament orientation was found to have a strong effect on both the debonding behavior and the plastic stretch-to-failure. Ligaments aligned perpendicular to the crack plane (Fig. 3) exhibited debonding, on the order of the fiber diameter,  $2R$ , and a large plastic stretch-to-failure:  $u_c/R \approx 3.5$ . Inclined ligaments partially debonded (around that segment of the interface experiencing normal tension, Fig. 4(a)) and failed at a relatively small plastic stretch. Ligaments parallel to the crack plane often debonded completely and experienced negligible plastic deformation (Fig. 4(b)). A summary of plastic stretch measurements (Fig. 5) indicates a mean value,  $u_c/R = 2.9$ , with a standard deviation of  $\pm 0.9$ .

Closer examination of the debonded surfaces provided insight into the debond mechanism and the role of matrix microstructure. The  $\text{Al}_2\text{O}_3$  side of the debonded interface (Fig. 6(a)) reveals the presence of a network of Al. The network cell



(a)



(b)

Fig. 1. (a) Ceramic preform, prior to metal infiltration. (b) Composite microstructure, after metal infiltration.

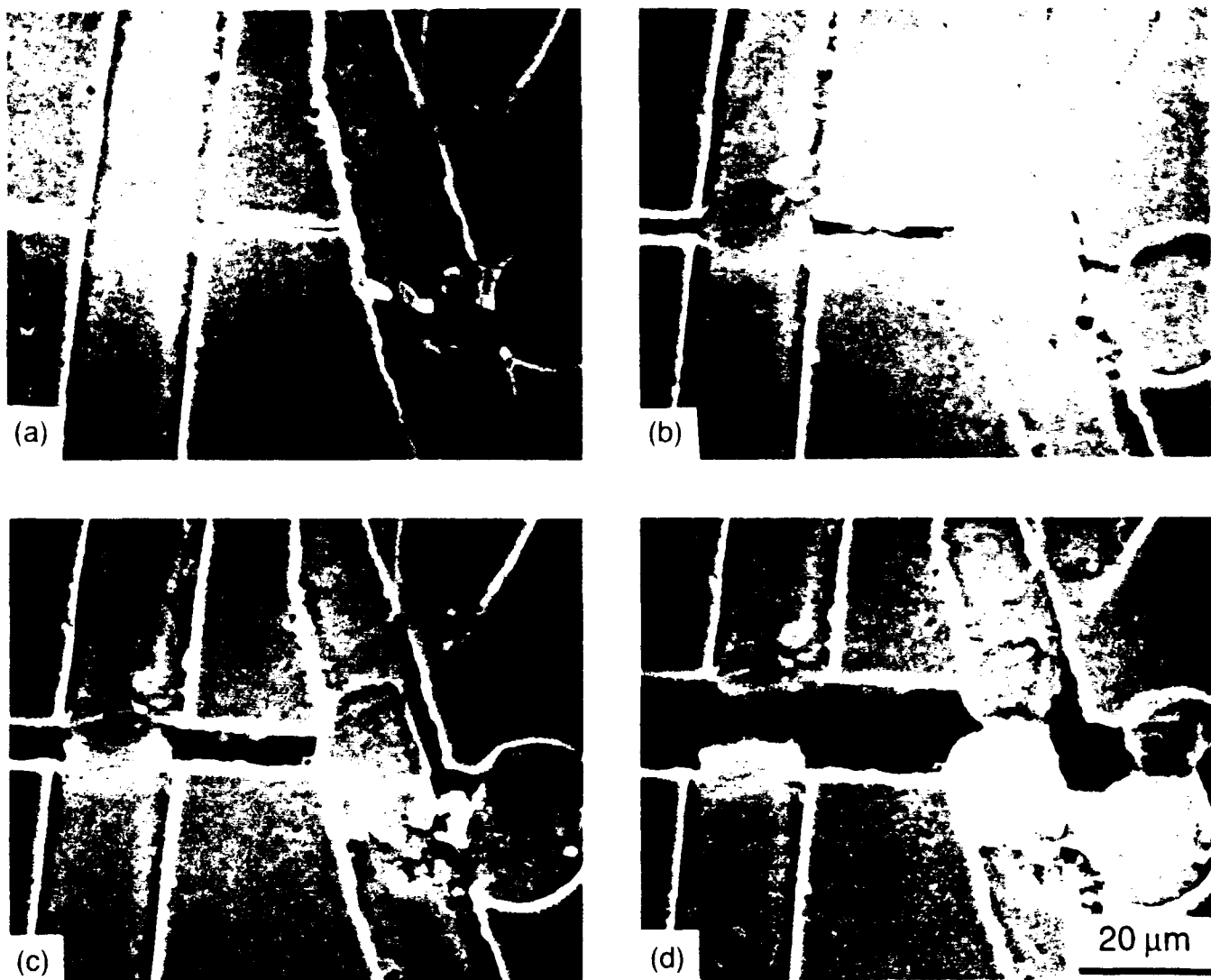


Fig. 2. Bridging Al ligaments in the composite at four different crack openings. Micrographs taken *in situ* under load.

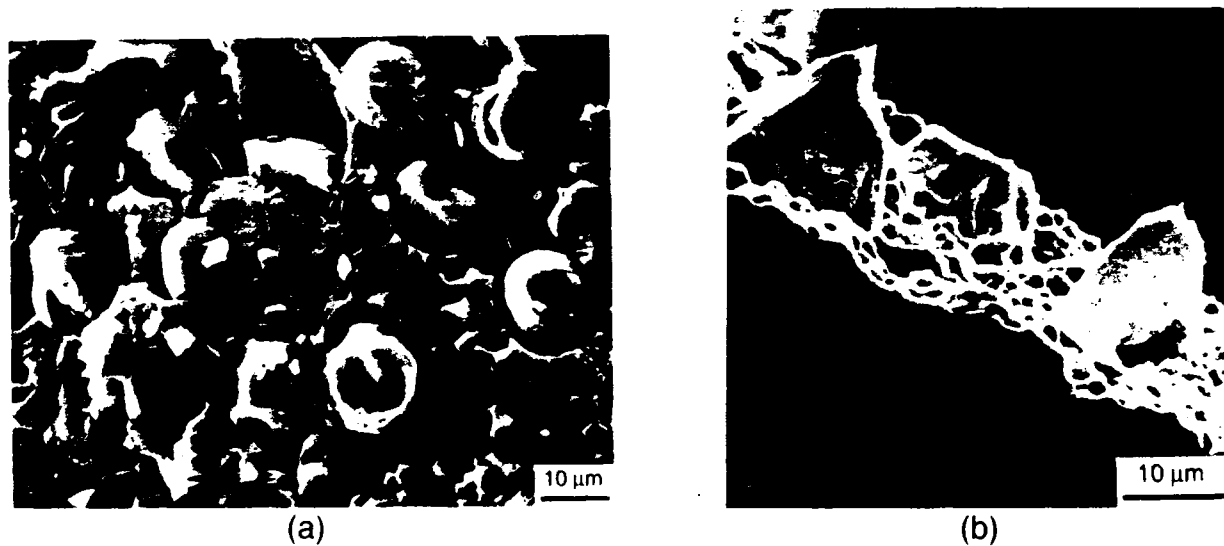


Fig. 3. (a) Composite fracture surface in area where fibers are aligned perpendicular to fracture surface. (b) High-angle (85°) tilt view illustrating plastic stretching of ligaments.

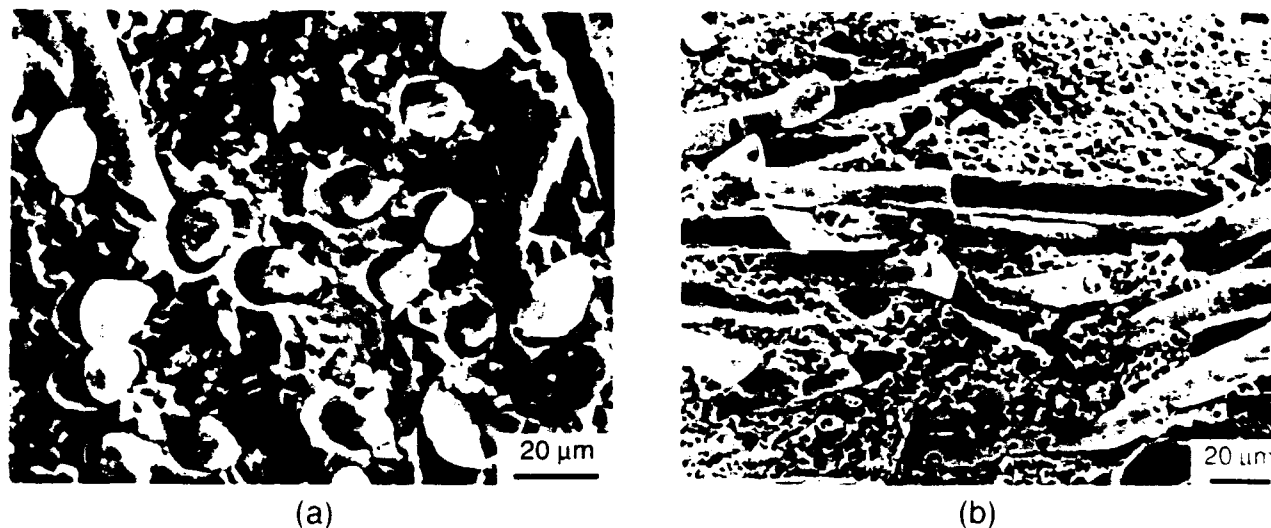


Fig. 4. Composite fracture surface in area where fibers are (a) inclined with respect to crack plane and (b) aligned parallel to the crack plane.

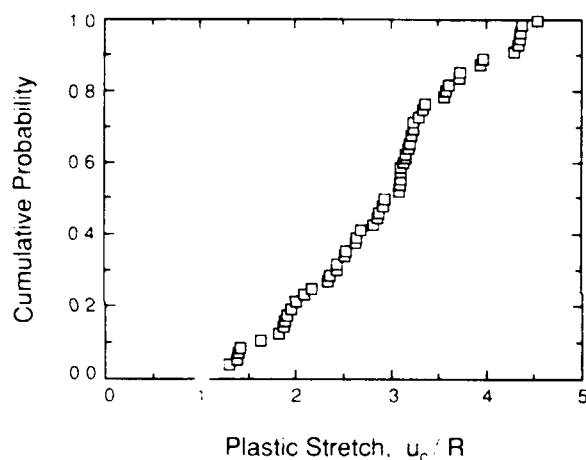


Fig. 5. Cumulative distribution of plastic stretch to failure of Al ligaments.

size is similar to that of the matrix grains and the cell centers are frequently situated at triple-grain junctions on the  $\text{Al}_2\text{O}_3$  surface. The debonded metal exhibited a corresponding, distorted, dimpled surface (e.g., 6(b)). These observations indicate that debonding occurred by a ductile process involving void nucleation at triple-grain junctions of the matrix surface, followed by plastic void growth and coalescence *within the metal*, near the interface. This mechanism of interfacial fracture is consistent with earlier studies which indicate that the  $\text{Al}_2\text{O}_3/\text{Al}$  interface is "strong."<sup>10</sup>

The effect of matrix microstructure on debonding was explored by heat-treating some of the  $\text{Al}_2\text{O}_3$  compacts at  $1600^\circ\text{C}$  for 30 h, to induce substantial grain growth in some regions\* and thus reduce the number of triple-grain junctions at the channel surfaces. After infiltration and fracture, the debonding in these regions was found to be negligible (Fig. 7), whereas the debonding in the fine-grained region was essentially the same as that in the original fine-grained composite (cf. Fig. 3). The plastic stretch of the reinforcements in the coarse-grained region was correspondingly lower,  $u_c/R \approx 1$ .

\*These heat treatments produced a bimodal distribution of grain sizes, a result of abnormal grain growth.

### (3) Properties of Al Alloy

Tensile stress-strain curves for the bulk Al-Mg alloy (Fig. 8) indicated a yield strength of  $\sim 70$  MPa and an ultimate tensile strength of  $\sim 180$  MPa. The reduction in area was approximately 20%. Nanoindentation results at a load of 5 mN indicated similar hardness levels for the bulk aluminum alloy ( $1.1 \pm 0.1$  GPa) and for the reinforcements in the composite ( $1.3 \pm 0.2$  GPa). The relatively large values of hardness (compared to the uniaxial yield strength) reflect the indentation size effect that occurs in the nanometer range.<sup>11</sup>

### (4) Fracture Resistance

The resistance curves for the composite (Fig. 9) have three characteristic features: (i) an initial fracture resistance,  $K_{IC} \approx 3$   $\text{MPa}\cdot\text{m}^{1/2}$ , similar to the fracture toughness of the matrix; (ii) an intermediate region wherein the fracture resistance increases gradually, and (iii) a final region in which the resistance increases rapidly. The latter region commences at smaller crack extensions for specimens with deeper notches. Such behavior is characteristic of large-scale bridging (LSB).

The work of rupture of the composite was  $W_R = 400 \pm 50$   $\text{J}\cdot\text{m}^{-2}$  and that of the fully dense  $\text{Al}_2\text{O}_3$  was  $W_R = 25 \pm 5$   $\text{J}\cdot\text{m}^{-2}$ . The toughness enhancement,  $\Delta W_R$ , attributed to the metal reinforcements, reexpressed in the nondimensional form,<sup>12</sup>

$$\chi = \Delta W_R / (\sigma_u R) \quad (6a)$$

becomes

$$\chi = 2.0 \pm 0.3 \quad (6b)$$

The steady-state fracture resistance,  $K_{IC}$ , of the composite can then be calculated using

$$K_{IC} \approx \sqrt{E W_R} \quad (7)$$

where  $E$  is the composite Young's modulus. Taking  $E = 300$  GPa, Eq. (7) gives the result  $K_{IC} \approx 11$   $\text{MPa}\cdot\text{m}^{1/2}$ , significantly less than the nominal LSB fracture resistance measured at large crack extensions (Fig. 9).

## IV. Modeling

### (1) Bridging Traction

The traction function,  $\sigma_b(u)$ , for the ductile Al ligaments was obtained using two methods. In the first, the function was assumed to obey a linear softening law (Eq. (2)). Selection of

\*Processed similarly and having comparable grain size.



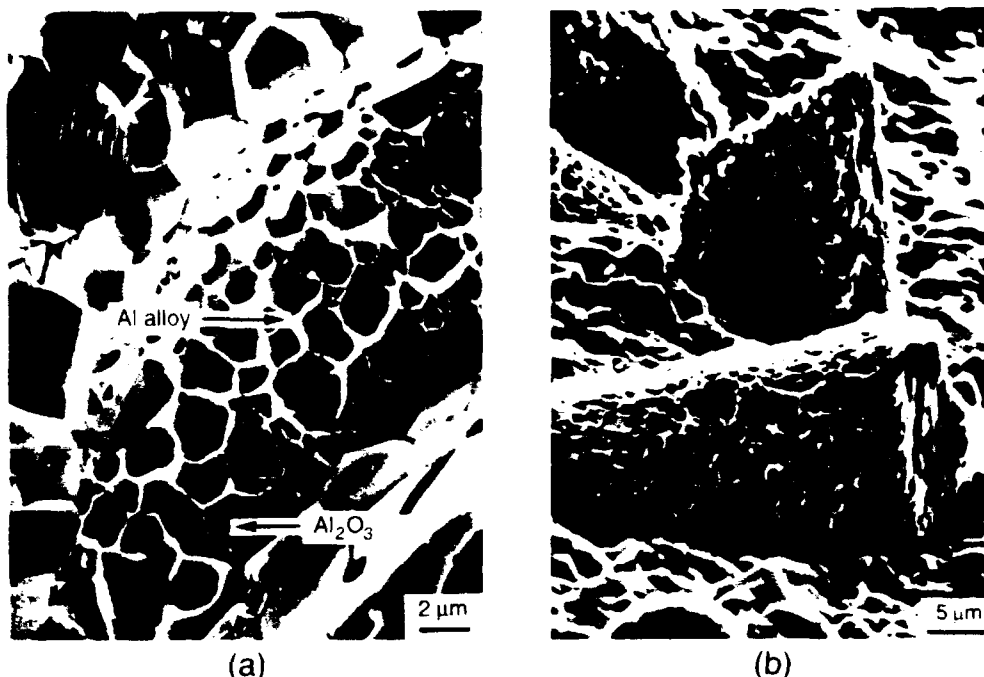


Fig. 6. (a) View of debonded  $\text{Al}_2\text{O}_3$  surface, with cell-like Al network centered around triple-grain junctions. (b) View of debonded Al surface, with ductile dimples corresponding to the  $\text{Al}_2\text{O}_3$  grain size.

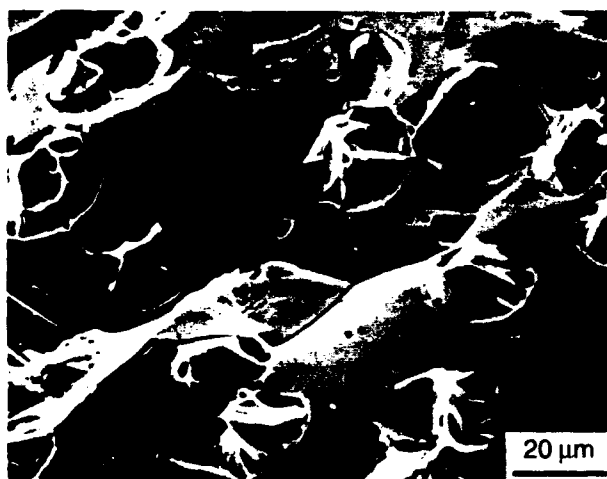


Fig. 7. Fracture surface of composite produced from large-grained  $\text{Al}_2\text{O}_3$  preform. Note the absence of debonding and the reduction in plastic stretch.

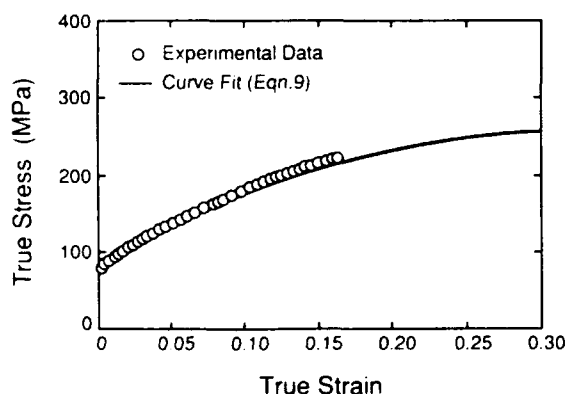


Fig. 8. True stress/strain curves from experimental data and calculated using the Voce law.<sup>11</sup>

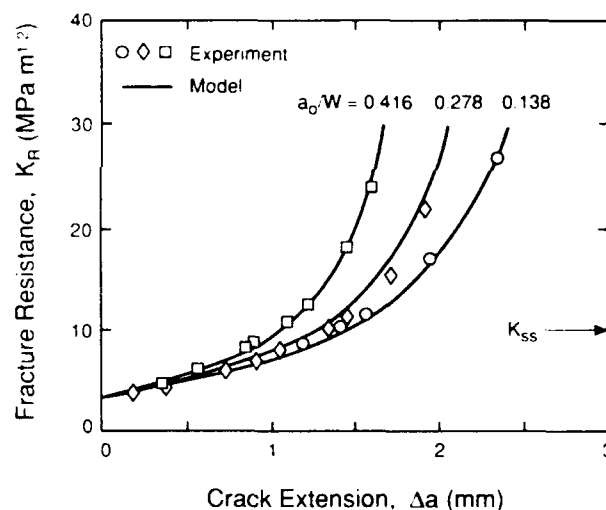


Fig. 9. Comparison of measured and computed fracture resistance curves for three notch depths,  $a_0/w$ .

the peak stress parameter,  $\sigma_p$ , and the stretch-to-failure,  $u_f$ , was based on the following procedure: (i) The stretch-to-failure was made to coincide closely with the SEM measurements ( $u_f/R = 2$ ). (ii) The maximum stress was then selected such that the computed  $R$ -curve (described in Section IV(2)) for one of the specimen geometries was in good agreement with the experimental data. This fit specifies both  $\sigma_p$  and  $u_f$  in Eq. (2). (iii) The  $R$ -curves for the other geometries were computed and compared with the experiments. As an additional consistency check, the area under the normalized  $\sigma_p(u)$  curve was evaluated and compared with the value of  $\chi$  obtained from the work-of-rupture tests (Eq. (6b)).

In the second method, the traction function was computed using a geometric necking model<sup>20</sup> by assuming cylindrical bridging ligaments oriented perpendicular to the crack plane (Appendix). The shape of the ligaments during deformation was taken to be a paraboloid of revolution, with the nominal stress computed from Bridgman's solution<sup>21</sup> for a necking bar.

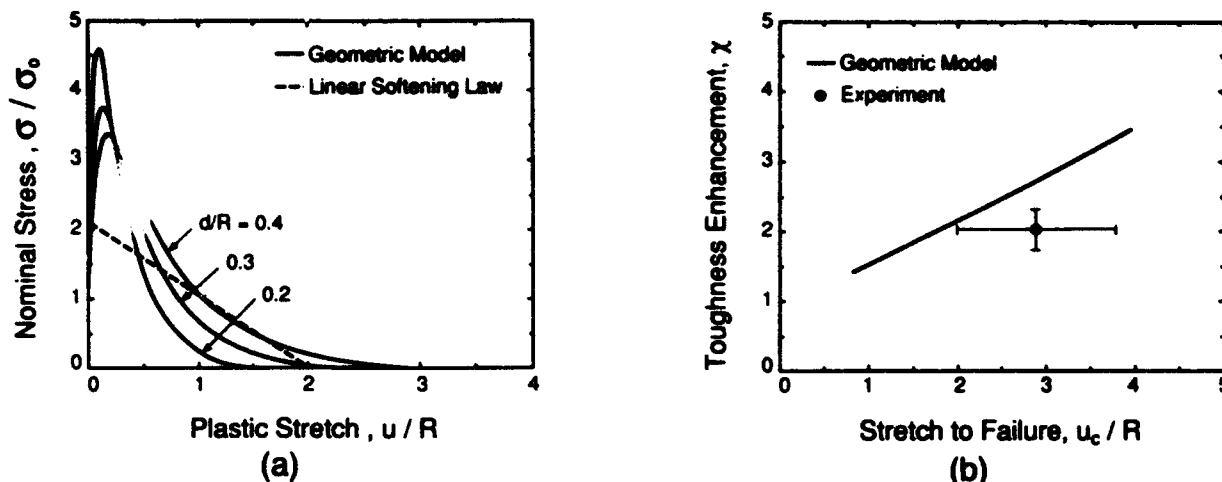


Fig. 10. (a) Linear softening stress/stretch relationships used in modeling of resistance curves and predictions of the geometric necking model for various debond lengths. (b) Comparison of steady-state toughness enhancement from the geometric model and the experimental measurements.

This calculation requires a flow law for the Al ligaments applicable at the large plastic strains that occur during rupture. The commonly used Ramberg–Osgood law typically overestimates the flow stress at large strains, because hardening is limited by the development of a stable dislocation cell structure.<sup>31</sup> Consequently, a more appropriate flow law at large strains is<sup>32</sup>

$$\sigma = \sigma_s(1 - me^{-nu}) \quad (8)$$

where  $\sigma_s$  is the saturation strength, with  $m$  and  $n$  being coefficients that reflect the hardening. A fit of Eq. (8) to the data from Fig. 8 gives the parameters  $\sigma_s = 300$  MPa,  $m = 0.75$ , and  $n = 5.8$ . The stress/stretch relationships for various debond lengths and their influence on the toughness enhancement, predicted using Eq. (8) in the geometric necking model (Appendix), are shown in Fig. 10.

## (2) Fracture Resistance

A cohesive crack model with linear softening has been used (Eq. (2)) and solved by an integral equation method.<sup>20,21</sup> The relevant geometric parameters are shown in Fig. 11. The model considers a matrix crack of length  $a$ , growing from a notch of length  $a_0$  in a flexure specimen of width  $w$ . The bridging tractions are denoted  $f\sigma_b(x)$ , where  $x$  is the distance from the tensile face of the beam. The applied load is represented by the stress,  $\sigma_a(x)$ , that would exist on the fracture plane in the absence of the crack, represented by

$$\sigma_a(x) = 6M(1 - 2x/w)/w^2b \quad (9)$$

where  $b$  is the specimen depth and  $M$  is the bending moment. The net tractions  $p(u)$  acting on the crack face are assumed to follow a linear softening law of the form

$$p(u) = f\sigma_c(1 - u/u_c) \quad (10)$$

Thereafter, the crack opening profile can be related to the applied load by an integral equation,<sup>20,21</sup> which leads to an expression for the stress intensity factor at the crack tip,

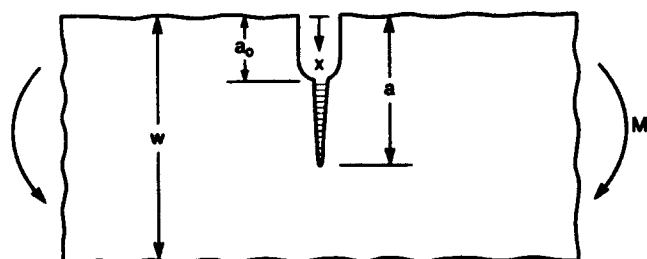


Fig. 11. Schematic representation of specimen geometry.

$$K_{IIP} = \frac{2}{\sqrt{\pi a}} \int_0^a \frac{H(x/a, a/w)}{\sqrt{1 - (x/a)^2}} [\sigma_s(x) - p(u(x))] dx \quad (11)$$

where  $H$  is a weight function defined in Refs. 20 and 21. Using the criterion for matrix crack propagation,  $K_{IIP} = K_0$  (the matrix toughness), the crack growth resistance has been simulated by solving the integral equation for  $K_{IIP}$ , as elaborated below.

## (3) Comparison between Theory and Experiment

Initially, the experimentally measured resistance curve for a notch depth,  $a_0/w = 0.28$ , was compared with predictions for a range of  $\sigma_c/\sigma_0$ . Coincidence was obtained for  $\sigma_c/\sigma_0 = 2.12$  (Fig. 9). Further comparisons for other notch geometries ( $a_0/w = 0.14$  and  $0.42$ ), made using the same value of  $\sigma_c/\sigma_0$ , indicate good agreement over the entire range of crack extension (Fig. 9). In addition, the steady-state toughness enhancement calculated from the linear softening traction law ( $\chi = 2.1$ ) is in accord with the value measured from the work-of-rupture tests ( $\chi = 2.0 \pm 0.3$ ). The consistency between the various measurements and predictions provides confidence in the utility of the linear softening traction law, as well as the key material parameters,  $\sigma_c$  and  $u_c$ .

A discrepancy that arises from the comparison between measurement and calculation is concerned with the predictions of the geometric necking model. The model predicts a peak stress and a toughness enhancement consistently higher than those found by experiment for debond lengths that give the appropriate range of  $u_c/R$  (Fig. 10). Notably, the peak stress should not be lower than the (unconstrained) ultimate tensile strength of the Al alloy ( $\sigma_c \approx 2.6\sigma_0$ ). Yet, a lower value of the peak stress is inferred from the resistance curves ( $\sigma_c \approx 2.1\sigma_0$ ). The discrepancy is believed to be attributable to the random orientation of the ligaments, which significantly lowers the limit load.<sup>32</sup> This effect, in turn, reduces the steady-state toughness enhancement associated with the metal reinforcements.

## V. Conclusion

The close comparison between theory and experiment revealed by the present study has several implications. The primary mechanism of toughening by ductile reinforcements can now be confidently attributed to plastic dissipation by stretching between the crack surfaces. Consequently, the important microstructural variables can be defined and evaluated, especially the requirement for controlled debonding.

The importance of large-scale bridging in metal/ceramic composites has been vividly demonstrated. A major implication of LSB is that the very large specimens required to satisfy semi-infinite specimen geometry assumptions are impractical

and would hinder the development of new materials. Furthermore, it is anticipated that applications for these composites will be in small, complex components, for which the fracture resistance measured from semi-infinite specimens would be of little use. The approach outlined here demonstrates a practical alternative wherein determination of the stress/stretch relationship of the ductile reinforcements from tests conducted on small, simple specimens combined with computer modeling allows the prediction of fracture resistance behavior of finite-sized components.

Finally, it is apparent that a traction law applicable to composites reinforced with randomly oriented metal channels cannot be simulated using simple geometric models of necking ligaments. Experimental evaluation of this law is preferred.

## APPENDIX

The effect of debond length on the stress/stretch relationship for a bridging ligament is estimated using the geometric model described by Mataga.<sup>29</sup> Here, the ligaments are taken to be cylindrical in shape and oriented perpendicular to the crack plane. Debonding is assumed to occur instantaneously (at  $u = 0$ ), such that the debond length,  $d$ , remains fixed during stretching. The profile of the ligament is assumed to be described by a paraboloid of revolution. The minimum ligament diameter,  $2r$ , and the local radius of a curvature are then evaluated in terms of the crack opening displacement by requiring the volume of the ligament to remain constant. This leads to an expression for the crack opening in terms of the current ligament geometry,

$$u/R = 2(d/R)[(1 - 4\rho/3 + 8\rho^2/15)^{-1} - 1] \quad (\text{A-1})$$

where

$$\rho = 1 - r/R \quad (\text{A-2})$$

The nominal stress depends on the current load-bearing area of the ligament (as manifest in the parameter  $\rho$ ), the work hardening behavior of the metal, and the plastic constraint resulting from the ligament profile. Utilizing Bridgman's solution<sup>30</sup> for the average nominal stress in a necking bar leads to the result

$$\sigma/\sigma_0 = (1 - \rho^2)[1 + h^2/R^2\rho(1 - \rho)] \times \ln [1 + \rho(1 - \rho)R^2/h^2] \quad (\text{A-3})$$

where  $2h$  is the current "gauge length" of the ligament,

$$2h = 2d + u \quad (\text{A-4})$$

Combining these results with the flow law for the Al alloy (Eq. (8) in the text) gives the  $\sigma_h(u)$  predictions plotted in Fig. 10(a).

## References

- <sup>1</sup>B. D. Flinn, M. Rühle, and A. G. Evans, "Toughening in Composites of  $\text{Al}_2\text{O}_3$  Reinforced with Al," *Acta Metall.*, **37**, 3001-3006 (1989).
- <sup>2</sup>B. D. Flinn, F. W. Zok, F. F. Lange, and A. G. Evans, "Processing and Properties of  $\text{Al}_2\text{O}_3$  Reinforced with Al Alloys," *Mater. Sci. Eng.*, **A144**, 153-57 (1991).
- <sup>3</sup>M. S. Newkirk, A. W. Urquhart, and H. R. Zwickler, "Formation of Lanxide™ Ceramic Composite Materials," *J. Mater. Res.*, **1**, 81 (1986).
- <sup>4</sup>M. K. Aghajanian, N. H. MacMillan, C. R. Kennedy, S. J. Luszez, and R. Roy, "Properties of Microstructure of Lanxide™  $\text{Al}_2\text{O}_3$ -Al Ceramic Composite Materials," *J. Mater. Sci.*, **24**, 658-70 (1989).
- <sup>5</sup>M. Yasrebi, G. H. Kim, K. E. Gunnison, M. Sarikaya, and I. A. Aksay, "Biomimetic Processing of Ceramics and Ceramic-Metal Composites," pp. 625-35 in *MRS Symposium Proceedings*, Vol. 180. Materials Research Society, Pittsburgh, PA, 1990.
- <sup>6</sup>L. S. Sigl and H. E. Exner, "Experimental Study of the Mechanics of Fracture in WC-Co Alloys," *Met. Trans.*, **18A**, 1299-308 (1987).
- <sup>7</sup>L. S. Sigl and H. F. Fischmeister, "On the Fracture Toughness of Cemented Carbides," *Acta Metall.*, **36**, 887-97 (1988).
- <sup>8</sup>L. S. Sigl, P. A. Mataga, B. J. Dalgleish, R. M. McMeeking, and A. G. Evans, "On the Toughness of Brittle Materials Reinforced with a Ductile Phase," *Acta Metall.*, **36**, 945 (1988).
- <sup>9</sup>D. B. Marshall, W. S. Morris, B. N. Cox, and M. S. Dadkhah, "Toughening Mechanisms in Cemented Carbides," *J. Am. Ceram. Soc.*, **73**, 2938-43 (1990).
- <sup>10</sup>C. K. Elliot, G. R. Odette, G. E. Lucas, and J. W. Sheckherd, "Toughening Mechanisms in Intermetallic  $\gamma$ -TiAl Alloys Containing Ductile Phases," *Mater. Res. Soc. Symp. Proc.*, **120**, 95 (1988).
- <sup>11</sup>T. C. Lu, A. G. Evans, R. J. Hecht, and R. Mehrabian, "Toughening of  $\text{MoSi}_2$  with a Ductile (Niobium) Reinforcement," *Acta Metall. Mater.*, **35**, 1853-62 (1991).
- <sup>12</sup>D. H. Carter and P. L. Martin, "Ta and Nb Reinforced  $\text{MoSi}_2$ ," pp. 131-38 in *MRS Symposium Proceedings*, Vol. 194. Materials Research Society, Pittsburgh, PA, 1990.
- <sup>13</sup>P. R. Subramanian, M. G. Mendiratta, D. B. Miracle, and D. M. Dimiduk, "Microstructure and Mechanical Properties of  $\text{NiSi} + \text{Mo}$  *In Situ* Eutectic Composites," pp. 147-54 in *MRS Symposium Proceedings*, Vol. 194. Materials Research Society, Pittsburgh, PA, 1990.
- <sup>14</sup>C. Troy and W. D. Scott, "Ceramic-Metal Composites Produced by Melt Infiltration," *J. Am. Ceram. Soc.*, **73**, 97-101 (1990).
- <sup>15</sup>M. F. Ashby, F. J. Blunt, and M. Bannister, "Flow Characteristics of Highly Constrained Metal Wires," *Acta Metall.*, **37**, 1947-57 (1989).
- <sup>16</sup>V. D. Krstic, P. S. Nicholson, and R. G. Hoagland, "Toughening of Glasses by Metallic Particles," *J. Am. Ceram. Soc.*, **64**, 499 (1981).
- <sup>17</sup>F. W. Zok and C. L. Hom, "Large-Scale Bridging in Brittle Matrix Composites," *Acta Metall. Mater.*, **38**, 1895-904 (1990).
- <sup>18</sup>V. Tvergaard and J. W. Hutchinson, "Relation Between Crack Growth Resistance and Fracture Process Parameters in Elastic/Plastic Solids," *J. Mech. Phys. Solids*, in press.
- <sup>19</sup>B. J. Dalgleish, K. P. Trumble, and A. G. Evans, "The Strength and Fracture of Alumina Bonded to Aluminum Alloys," *Acta Metall.*, **37**, 1923 (1988).
- <sup>20</sup>B. N. Cox, "Stable and Unstable Solutions for Bridged Cracks in Various Specimens," *Acta Metall. Mater.*, **39**, 1189-201 (1991).
- <sup>21</sup>B. N. Cox and C. S. Lo, "Load Ratio, Notch, and Scale Effects for Bridged Cracks in Fibrous Composites," *Acta Metall. Mater.*, **40**, 69-80 (1992).
- <sup>22</sup>G. Bao and C. Y. Hui, "Effects of Interface Debonding on the Toughness of Ductile-Particle Reinforced Ceramics," *Int. J. Solids Struct.*, **26**, 631-42 (1990).
- <sup>23</sup>F. F. Lange, B. V. Velamakanni, and A. G. Evans, "Method for Processing Metal-Reinforced Ceramic Composites," *J. Am. Ceram. Soc.*, **73**, 388-93 (1988).
- <sup>24</sup>ASTM E399-83, "Plane Strain Fracture Toughness Testing of Metallic Materials," *Annual Book of ASTM Standards*. American Society for Testing and Materials, Philadelphia, PA, 1988.
- <sup>25</sup>H. G. Tattersall and G. Tappin, "The Work of Fracture and Its Measurement in Metals, Ceramics and Other Materials," *J. Mater. Sci.*, **1**, 296-301 (1966).
- <sup>26</sup>J. I. Bluhm, "Slice Synthesis of a Three-Dimensional 'Work of Fracture' Specimen," *Eng. Fract. Mech.*, **7**, 593-604 (1975).
- <sup>27</sup>A. G. Varias, Z. Suo, and C. F. Shih, "Ductile Failure of a Constrained Metal Foil," *J. Mech. Phys. Solids*, **39**, 963 (1991).
- <sup>28</sup>D. Tabor, "Indentation Hardness and Its Measurement: Some Cautionary Comments," pp. 129-59 in *ASTM Special Technical Publication 889*. Edited by P. J. Blau and B. R. Lawn. American Society for Testing and Materials, Philadelphia, PA, 1986.
- <sup>29</sup>P. A. Mataga, "Deformation of Crack-Bridging Ductile Reinforcements in Tough Brittle Materials," *Acta Metall.*, **37**, 3349-59 (1989).
- <sup>30</sup>P. W. Bridgman, *Studies in Large Plastic Flow and Fracture*, pp. 9-32. McGraw-Hill, New York, 1952.
- <sup>31</sup>G. E. Dieter, *Mechanical Metallurgy*, Ch. 15. McGraw-Hill, New York, 1976.
- <sup>32</sup>J. Chakrabarty, *Theory of Plasticity*, Ch. 1. McGraw-Hill, New York, 1987.

# Fiber Coating Concepts for Brittle-Matrix Composites

Janet B. Davis,\* Jan P. A. Löfvander, and Anthony G. Evans\*

Materials Department, College of Engineering, University of California, Santa Barbara, California 93106-5050

Ewald Bischoff

Max-Planck-Institut für Metallforschung, D-7000 Stuttgart 1, Germany

Mario L. Emiliani

Pratt and Whitney, Materials Engineering, West Palm Beach, Florida 33410

The current interest in tough, high-temperature materials has motivated fiber coating development for brittle-matrix composites with brittle reinforcements. Such coatings are needed for controlled interface debonding and frictional sliding. The system investigated in this study was sapphire fiber-reinforced alumina. This system is thermochemically stable for severe use conditions, exhibits little thermal expansion mismatch, and utilizes the excellent strength and creep resistance of sapphire reinforcements. Porous oxide and refractory metal coatings which satisfy requirements for toughness improvement in these composites were identified by employing a variety of newly developed mechanical testing techniques for determining the interfacial fracture energies and sliding resistances.

## I. Introduction

THE mechanical requirements for fiber coatings in brittle-matrix composites are reflected in two properties:<sup>1-3</sup> debonding and sliding. These properties are manifest as an interface debond energy,  $\Gamma_i$ , and a stress to cause sliding along the debonded interface,  $\tau$ . A prerequisite for good composite strength and toughness is that a debond criterion be satisfied, wherein the debond energy relative to the fiber fracture energy,  $\Gamma_f$ , satisfy  $\Gamma_i/\Gamma_f < 1/4$ .<sup>4</sup> Control of sliding is needed to ensure a notch-resistant material, such that  $\tau \approx 100$  MPa. Larger values result in high stress concentrations on fibers around notches and lead to notch-sensitive materials.<sup>5</sup> Coatings of C and BN meet these criteria, but both are susceptible to oxidation. Consequently, when SiC fibers are used, and when matrix cracks are present, oxidation embrittlement is encountered because the fiber oxidizes to form a silicate layer that violates debonding requirements.<sup>6</sup> Other coatings are thus desirable for high-temperature applications. The present study examines some alternative fiber coating concepts, with emphasis on coatings for oxide fibers, such as sapphire, which are not subject to the above oxidation problem.

Debonding of sapphire fibers\* requires coatings with a debond energy  $\Gamma_i \approx 5 \text{ J}\cdot\text{m}^{-2}$ . Few high-temperature materials have intrinsic fracture energies small enough to satisfy such a

requirement. Potential options are oriented micas,<sup>7</sup> some amorphous oxides,<sup>8</sup> and fugitive coatings which are removed after composite consolidation.<sup>10</sup> However, the amorphous coatings have limitations governed by viscous flow at elevated temperatures, plus reaction with  $\text{Al}_2\text{O}_3$ . Two alternative concepts are explored in this article: (i) porous oxide coatings and (ii) coatings that form "weak" interfaces with  $\text{Al}_2\text{O}_3$ . The first concept recognizes that porosity generally decreases the fracture energy of brittle materials, such as oxides.<sup>11</sup> Consequently, certain porous oxide coatings may be able to satisfy debonding requirements for sapphire fibers, by allowing debonding within the coating itself. The second concept is based on the expectation that certain nonoxide coatings may allow interface debonding.<sup>5</sup> While most such interfaces have relatively high fracture energies ( $\Gamma_i > 10 \text{ J}\cdot\text{m}^{-2}$ ),<sup>5,12,13</sup> larger than that required for the debonding of sapphire fibers, preliminary evidence has suggested that certain refractory metals provide suitably low values.<sup>5</sup>

An effective coating should have the attribute that it does not degrade the strength of the fibers. Consequently, coatings that either react with or dissolve the fibers are usually unacceptable. This thermochemical requirement further limits the potential set of coating materials. Various refractory materials that exhibit known thermochemical compatibility with  $\text{Al}_2\text{O}_3$  at  $1500^\circ\text{C}$  have been evaluated (Table I), plus C,  $\text{Y}_2\text{O}_3$ , and the refractory metals, Mo, W, Cr, and Zr. The latter are still susceptible to oxidation, but in conjunction with oxide fibers, it is hoped that the composite system would have good durability in oxidizing atmospheres, superior to either C or BN coatings on SiC fibers.

## II. Approach

The overall approach used to identify viable fiber coating concepts is illustrated in Fig. 1. Planar geometries readily amenable to processing and testing are used to screen candidate coating materials. The associated test procedures include a Hertzian indentation technique<sup>14</sup> and a mixed-mode flexure test<sup>15</sup> (Figs. 1(a) and (b)). For coatings that exhibit debonding,

\*This concept is being explored at Corning Incorporated, by K. Chyung.

R. J. Kerans—contributing editor

Manuscript No. 195645. Received May 22, 1992; approved January 29, 1993.  
Presented at the 94th Annual Meeting of the American Ceramic Society, Minneapolis, MN, April 16, 1992 (Symposium on Ceramic Matrix Composites, Paper No. 74-SII-92).

Supported by the Defense Advanced Research Projects Agency under Contract No. MDA 972-90-K-001.

\*Member, American Ceramic Society.

\* $\Gamma_f \approx 12\text{--}20 \text{ J}\cdot\text{m}^{-2}$ , depending on the fracture plane.<sup>7</sup>

Table I. Some Materials Thermochemically Stable with  $\text{Al}_2\text{O}_3$  at  $1500^\circ\text{C}$

Material	Ref.	Remarks
$\gamma\text{-TiAl}$	29	$\text{Al}_2\text{O}_3$ dissolves
Nb	30	$\text{Al}_2\text{O}_3$ dissolves
NiAl	31	
$\text{ZrO}_2$	32	

the fracture energy,  $\Gamma$ , may also be determined from these tests. The subset of coating materials that satisfy fiber debonding requirements is then used to address composite performance. For this purpose, sapphire fibers are coated and incorporated into a brittle matrix. Beam specimens are cut from the consolidated plate (Fig. 1(c)), with the fibers oriented along the beam axis. Tensile and/or flexural tests are then used to assess the interaction of a crack with the coated fibers and to obtain information about the sliding stress,  $\tau$ . The magnitude of  $\tau$  is ascertained from a measurement of the crack opening displacement as a function of the applied load.<sup>16</sup> Such tests also permit measurement of the fiber pull-out length,  $h$ , and the fiber fracture mirror radii.<sup>17–19</sup> The latter yield a direct estimate of the *in situ* strengths of fibers,  $S$ .<sup>19</sup> The magnitudes of  $S$  and  $h$ , in turn, give another estimate of  $\tau$ , and thus provide a useful consistency check. In addition,  $\tau$  can be obtained from fiber push-through tests (Fig. 1(d)).<sup>20–22</sup> In the present study, a combination of the above tests is used to assess coating concepts for sapphire fibers in polycrystalline  $\text{Al}_2\text{O}_3$ .

### III. Experimental Procedure

#### (1) Processing

The coatings were deposited either by evaporation, sputtering, chemical vapor deposition, or sol-gel methods. For the *planar geometry*, coatings were deposited on two surfaces, each representing either the fiber or matrix component of the composite. Bonding was then conducted by hot pressing at homologous temperatures (for the coating material) in the range  $0.4 < T/T_m < 0.7$ . Consequently, the system experienced a thermal cycle analogous to that expected for composite processing. *Specimens containing fibers* were produced by sputter or evaporation coating sapphire fibers and incorporating them into powder matrices, using hot pressing to achieve consolidation.

(A) *Coating Deposition:* Oxide "sol-gel" coatings were produced from liquid precursor materials. A spin coating apparatus was used to deposit the coatings onto the planar substrates used for diffusion bonding. The coated substrates were then heat-treated in air to temperatures suitable for pyrolysis of the precursor, typically below 1000°C. During pyrolysis, the film is converted to an oxide. Subsequent iterations were used to increase the thickness of the coating.

Sputtered coatings were deposited onto sapphire *disks* and *fibers* (Saphikon single-crystal sapphire fibers) in an rf diode sputtering unit. The sputtering targets used in most cases were high purity ( $\geq 99.9\%$ ); only the W target had a lower purity ( $\sim 99.5\%$ ). Oxide coatings were deposited by reactive sputtering using a 50%–50% mixture of research-grade argon and oxygen at a total working gas pressure of 6 mtorr. The intermetallic compounds were produced from dual opposed targets of the pure elements. Both the refractory metal and intermetallic coatings were deposited in an atmosphere comprised of research-grade argon at 6 mtorr working gas pressure. The top and bottom target voltages were maintained at 3 and 0.5 kV, respectively. Fibers were rotated during coating at  $\sim 1$  rpm.

Submicrometer-thick Mo coatings were deposited onto sapphire fibers using an electron beam evaporator and a high-purity target. A glow discharge cleaning procedure was used prior to coating the fibers. Deposition was carried out at relatively high vacuum ( $< 10^{-6}$  torr), with the fibers rotated at  $\sim 10$  rpm.

The carbon coatings were produced by a low-pressure chemical vapor deposition technique in which methane was mixed with research-grade argon carrier gas in a tube furnace. Flow rates of 10  $\text{cm}^3/\text{min}$ , for the methane, and 100  $\text{cm}^3/\text{min}$ , for the argon, were used. Throughout deposition, the furnace temperature was maintained at 1200° to 1300°C.

(B) *Bonding and Consolidation:* For experiments to be conducted with planar configurations, three different  $\text{Al}_2\text{O}_3$  materials were used: (i) (0001) sapphire; (ii) a high-purity poly-

crystalline material; and (iii) a low-purity material (Coors AD-995 and Coors AD-96 substrates, respectively). The test specimens were produced by diffusion bonding, using a procedure described elsewhere.<sup>12</sup> Bonding at  $T/T_m \approx 0.5$  allowed coatings to be produced with relative density levels in the range 0.65 to 1.

Tests on coated sapphire fibers were conducted after incorporating into a high-purity (99.9%) polycrystalline  $\text{Al}_2\text{O}_3$  matrix. For this purpose, submicrometer  $\text{Al}_2\text{O}_3$  powder (AKP-50 with a particle size of  $\sim 0.2$   $\mu\text{m}$  obtained from Sumitomo Chemical Co., Ltd.) was isostatically cold-pressed into two thin disks  $\sim 5$  cm in diameter. These disks were then sintered in air at 1500°C for 2 h. A row of coated fibers and loose powder were placed between the disks, the assembly inserted between dies and vacuum hot-pressed at 1500°C for 2 h subject to an axial pressure of  $\sim 2$  MPa. These consolidation conditions resulted in an essentially fully dense matrix.

#### (2) Testing and Analysis

(A) *Mechanical Behavior:* The Hertzian indentation and mixed-mode flexure testing procedures used with planar specimens have been described elsewhere.<sup>14,15</sup> The flexural tests required precracking. This step was conducted in three-point flexure, using a row of Knoop indentations along the tensile surface to control the crack pop-in load and, hence, the extent of the precrack along the interface.

The tests used with the specimens containing fibers have been performed using a combination of fiber push-out and pull-out techniques. The fiber push-out technique has been described previously.<sup>20</sup> The fiber pull-out tests required that chevron notches be machined into beams containing single fibers (Fig. 1(c)). This notch geometry ensured stable crack growth through the beam upon flexural loading. The crack was grown until the crack front passed below the fiber. This occurred with a small crack opening, which induced some fiber debonding and sliding. After precracking, the beam was supported and the remaining matrix ligament mechanically removed. This procedure created a specimen consisting of two blocks of matrix material bridged by a single fiber, amenable to tensile testing. Tests were conducted *in situ* in a Hitachi 2100 scanning electron microscope (SEM) to permit measurement of the crack opening displacement and the corresponding tensile loads. These measurements may be used to evaluate the sliding resistance,  $\tau$ .<sup>16</sup>

(B) *Analytical Techniques:* Specimens for scanning electron microscopy were prepared using standard metallographic techniques. Carbon-coated samples were examined in a JEOL SM 840 SEM in secondary mode. The microscope was equipped with a Tracor Northern TN 5500 system. Samples for transmission electron microscopy (TEM) were prepared by grinding wafers to a final thickness of approximately 100  $\mu\text{m}$  before cutting 3-mm-diameter specimens. These were subsequently dimple-ground and ion milled to electron transparency with Ar at 5 kV and 1 mA at 14° incidence angle. The samples were examined at 200 kV in a JEOL 2000FX TEM equipped with a LINK eXL high take-off angle energy dispersive spectroscopy system. Computer simulations and indexing of selected area diffraction (SAD) patterns were facilitated by the Diffract software package (Microdev Software, Hillsboro, OR 97124).

### IV. Coating Characterization

#### (1) Oxides

For the oxide coatings, a range of porosities was generated, as illustrated in Fig. 2. At the equivalent bonding cycle, the thinner, sol-gel coatings had lower *intercoating* porosity than the sputtered coatings, whereas the porosity at the interface was similar for both. In all cases, the grain size was about equal to the coating thickness. The most notable features found by TEM

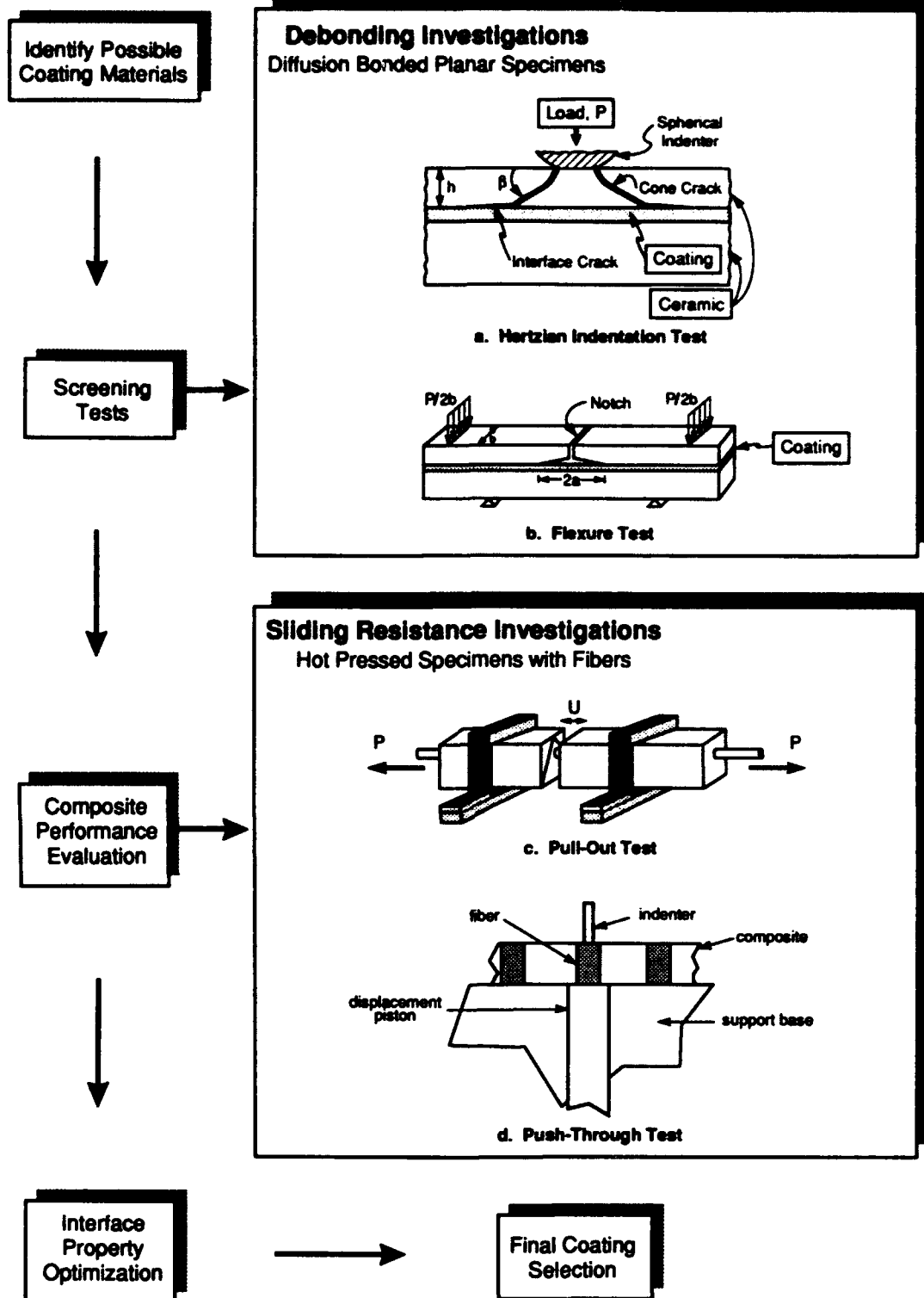


Fig. 1. Approach adopted to identify viable fiber coating concepts for brittle-matrix composites, consisting of developing testing procedures to evaluate the debonding and sliding propensities of various coatings on sapphire.

were bend contours in the sapphire caused by residual strains<sup>21</sup> (Fig. 3). For unstabilized  $\text{ZrO}_2$  coatings, extensive straining in the sapphire was apparent, as well as microcracks within the coating (Fig. 3(A)). This effect diminished with decreasing coating thickness (Fig. 3(B)). Selected area diffraction indicated that the  $\text{ZrO}_2$  was monoclinic and the strains are attributed to the tetragonal-to-monoclinic phase transformation. For  $\text{ZrO}_2$  coatings partially stabilized with 3 mol%  $\text{Y}_2\text{O}_3$ , the tetragonal phase was retained and the intensity of the strain contours diminished (Fig. 3(C)). However, some residual strain persisted, attributed to the thermal expansion mismatch between

$\text{ZrO}_2$  and  $\text{Al}_2\text{O}_3$ . Such strains appear to be an inherent problem with oxide coatings, potentially leading to fiber strength degradation (Appendix).

## (2) Refractory Metals

For the refractory metal coatings, thin foil cross sections for TEM were difficult to produce, because of debonding. However, for Mo, results have been obtained in two cases: (a) a thin ( $0.7 \mu\text{m}$ ) evaporated coating with the high-purity  $\text{Al}_2\text{O}_3$  matrix and (b) a thicker ( $>3 \mu\text{m}$ ) sputtered coating with the lower-purity  $\text{Al}_2\text{O}_3$  matrix. For the former, the coating appeared to

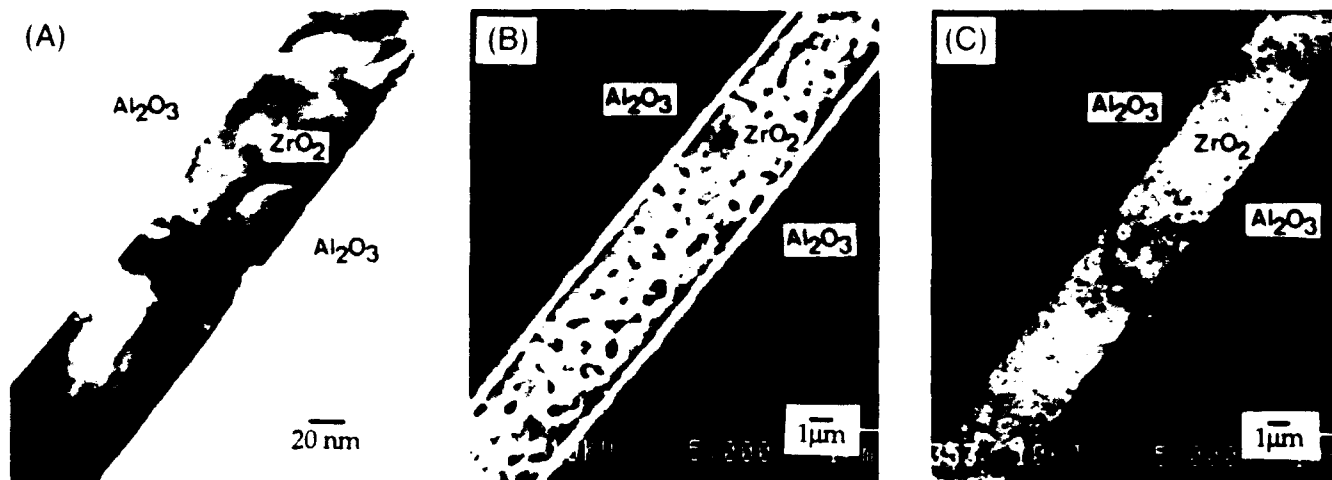


Fig. 2. ZrO<sub>2</sub> coating sapphire interfaces produced by the following diffusion bonding schedules: (A) sol-gel coating diffusion bonded at 1300°C for 12 h with an applied load of  $\sim 1$  MPa; (B) sputtered coating diffusion bonded at 1300°C for 12 h with an applied load of  $\sim 1$  MPa; (C) sputtered coating diffusion bonded at 1300°C for 48 h with an applied load of  $\sim 3$  MPa.

have some discontinuity (Fig. 4(A)), but otherwise survived the consolidation. These discontinuities, which are induced by diffusion, are typical for thin, polycrystalline films.<sup>12</sup> EDS analysis was unable to detect either Mo in the Al<sub>2</sub>O<sub>3</sub> or Al in the Mo. For the latter, a relatively thick ( $\sim 300$  nm) dense polycrystalline MoO<sub>3</sub> phase was found at the sapphire interface (Fig. 4(B)). In addition, an amorphous silicate phase was observed at the MoO<sub>3</sub>/Mo interface that presumably resulted from viscous flow of the silicate from the polycrystalline Al<sub>2</sub>O<sub>3</sub> into porosity at this interface.

The Mo coatings were also investigated by SEM, after debonding. For sputtered coatings, oxide particles (identified as MoO<sub>3</sub>) were found to be attached to the sapphire in regions where debonding occurred between the Mo and sapphire. X-ray diffraction of the debond surface confirmed the presence of MoO<sub>3</sub> on the sapphire. Shallow ridges were also apparent on the sapphire side of the debond surface, having spacings comparable to the grain size in the metal (Fig. 5(A)). These ridges are believed to form at grain boundaries, by diffusion during the bonding process, as equilibrium dihedral angles are established. Small impressions were evident on the Mo side of the debonded surface between Mo and the higher-purity Al<sub>2</sub>O<sub>3</sub> (Fig. 6), having dimensions which coincide with the Al<sub>2</sub>O<sub>3</sub> grain size. These are believed to have formed by deformation of the Mo during diffusion bonding.

The sputtered Cr coatings exhibited similar features. A thin polycrystalline chromium oxide ( $\sim 200$  nm thick) was attached to the sapphire (Fig. 7), with the remainder of the coating being Cr. Analysis by EDS indicated no Cr in the Al<sub>2</sub>O<sub>3</sub>, and only trace amounts of Al in the chromium oxide. Selected area diffraction patterns established that the chromium oxide was Cr<sub>2</sub>O<sub>3</sub>, and significant porosity existed at the metal/oxide interface. Debonding was evident, occurring between the metal and its oxide layer.

The sputtered W coatings on sapphire exhibited pronounced ridges on the sapphire side of the debond surface (Fig. 5(B)). These have been associated with Fe- and Cr-rich grain boundary impurity phases, originating in the sputtering target. The resulting degradation of the sapphire, evident in Fig. 5(B), illustrates the importance of selecting chemically stable coatings. Similar features were observed at C/Al<sub>2</sub>O<sub>3</sub> interfaces diffusion bonded at high temperatures ( $>1400^\circ\text{C}$ ) under high vacuum ( $<10^{-6}$  torr). For this system, the ridges are attributed to the formation of an Al<sub>4</sub>C<sub>3</sub> reaction product.

Studies of the as-sputtered Mo and Cr films, using WDS and X-ray diffraction, revealed an oxide surface layer. In addition, there was an oxide layer adjacent to the sapphire, identified by peeling the coating from the substrate. These findings indicate

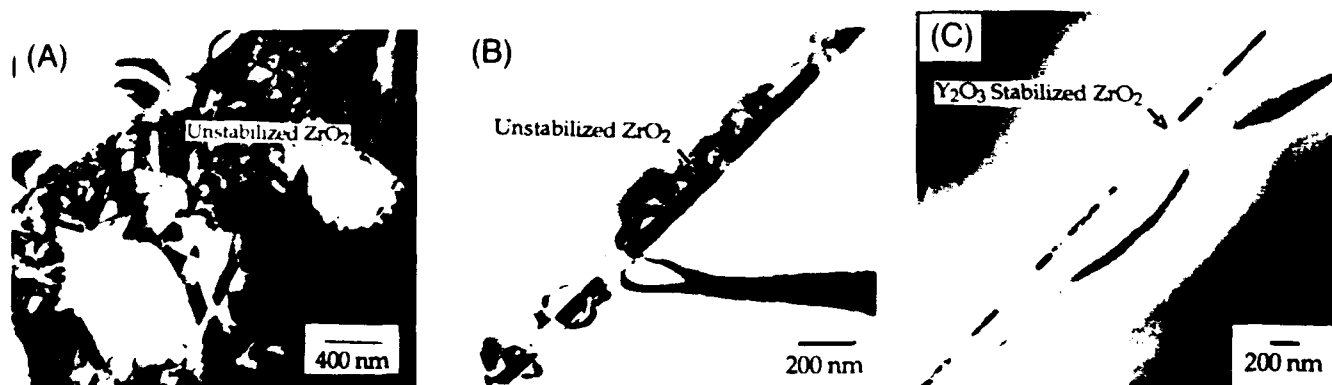


Fig. 3. (A) Extensive bend contours in the sapphire when unstabilized ZrO<sub>2</sub> sputtered coatings were used. It is believed that the contours result from strain in the fiber due to the  $t\text{-}m\text{-ZrO}_2$  phase transformation. (B) The bend contours in the sapphire decrease with coating thickness for the unstabilized sol-gel ZrO<sub>2</sub> coating. (C) The extent of bend contours was further reduced when thin stabilized sol-gel ZrO<sub>2</sub> coatings were used. The remaining stresses are believed to result from CTE mismatch across the well-bonded interface.

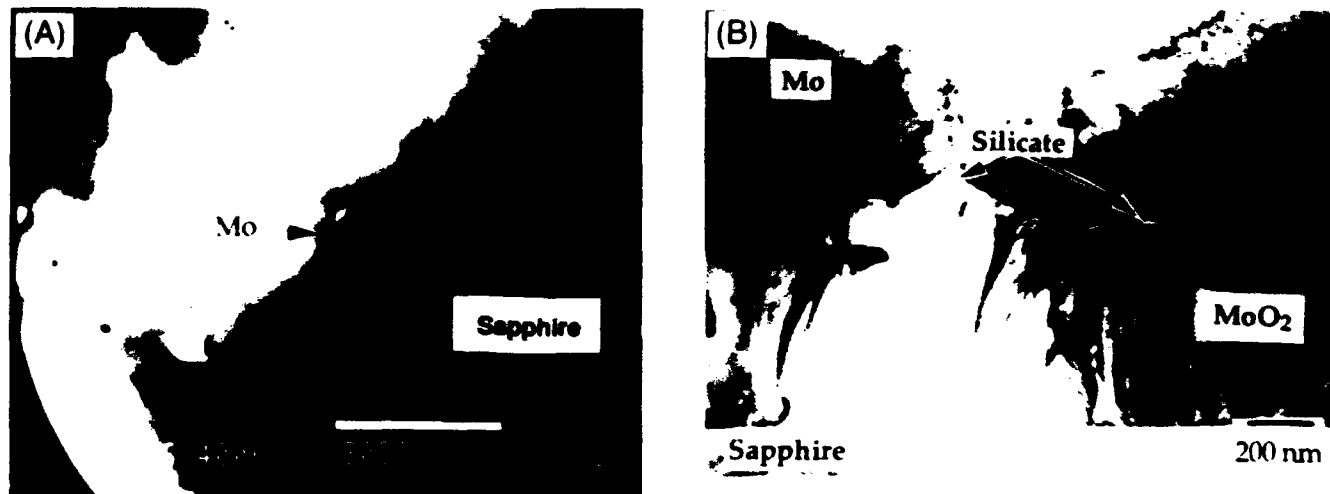


Fig. 4. (A) TEM micrograph showing the discontinuous submicrometer Mo coating on a sapphire fiber in the high-purity  $\text{Al}_2\text{O}_3$  matrix. (B) TEM micrographs of a diffusion bonded Mo/sapphire interface with the lower-purity  $\text{Al}_2\text{O}_3$ . A continuous  $\text{MoO}_3$  phase occurs adjacent to the sapphire and an amorphous silicate phase exists within the interfacial pores between Mo and the  $\text{MoO}_3$  phase.

that the oxide phase is initially deposited on the sapphire substrate during sputtering and that a surface oxide forms subsequent to deposition, prior to diffusion bonding.

## V. Mechanical Measurements

### (1) Debonding

Preliminary experiments conducted on planar specimens with a spherical indenter provided information about the incidence of debonding at a  $30^\circ$  crack inclination to the interface. From such experiments, it was established that most diffusion-bonded coatings formed high fracture energy interfaces. Only the coatings consisting of Mo, W, Cr, Zr, and C debonded consistently. Coatings of  $\text{ZrO}_2$  and  $\text{Y}_2\text{Al}_2\text{O}_7$  were found to exhibit variable debonding tendencies. Coatings of Nb,  $\gamma\text{-TiAl}$ , and  $\text{NiAl}$  did not debond. Furthermore, from the list of promising coating materials, several were observed to chemically react with the sapphire during diffusion bonding. The only coating materials from this set which were found to be *chemically stable* with sapphire above  $1300^\circ\text{C}$  and to *reliably debond* were

Mo, Cr, porous  $\text{ZrO}_2$ , and porous  $\text{Al}_2\text{O}_3$ . Further studies were confined to these materials. The refractory metals would obviously oxidize during service. The effects of oxide formation on coating performance would need to be further studied. In at least one instance, for Mo, coating oxidation can be beneficial, as discussed in Section V(2).

The debonding propensity of the *refractory metal* coatings was observed to vary with the purity of the  $\text{Al}_2\text{O}_3$ . When either sapphire or sapphire plus *high-purity* polycrystalline  $\text{Al}_2\text{O}_3$  was used, debonding occurred consistently with  $\Gamma_i \approx 4 \text{ J}\cdot\text{m}^{-2}$  for Mo and  $2\text{--}3 \text{ J}\cdot\text{m}^{-2}$  for Cr. Furthermore, as already noted, the debonding occurred at the interfaces between either Mo/ $\text{Al}_2\text{O}_3$  or Mo/ $\text{MoO}_3$  and Cr/ $\text{Cr}_2\text{O}_3$ . Conversely, when the *impure*  $\text{Al}_2\text{O}_3$  was used, debonding was not observed in the Hertzian indentation test, implying a *lower bound* for  $\Gamma_i$  of  $\sim 16 \text{ J}\cdot\text{m}^{-2}$ .<sup>3</sup> This behavior is attributed to the silicate phase found at the Mo/ $\text{MoO}_3$  interface, which seemingly forms a strong bond<sup>25,26</sup> and increases  $\Gamma_i$  for that interface. In addition, as already noted,  $\text{MoO}_3$  appears to bond well with sapphire.

<sup>3</sup>Formed by chemical reaction during bonding with  $\text{Y}_2\text{O}_3$  coatings.

<sup>3</sup>This lower bound is  $\Gamma_i = 0.8\Gamma_c$ , corresponding to a crack/interface inclination of  $30^\circ$ , with  $\Gamma_c = 20 \text{ J}\cdot\text{m}^{-2}$ .

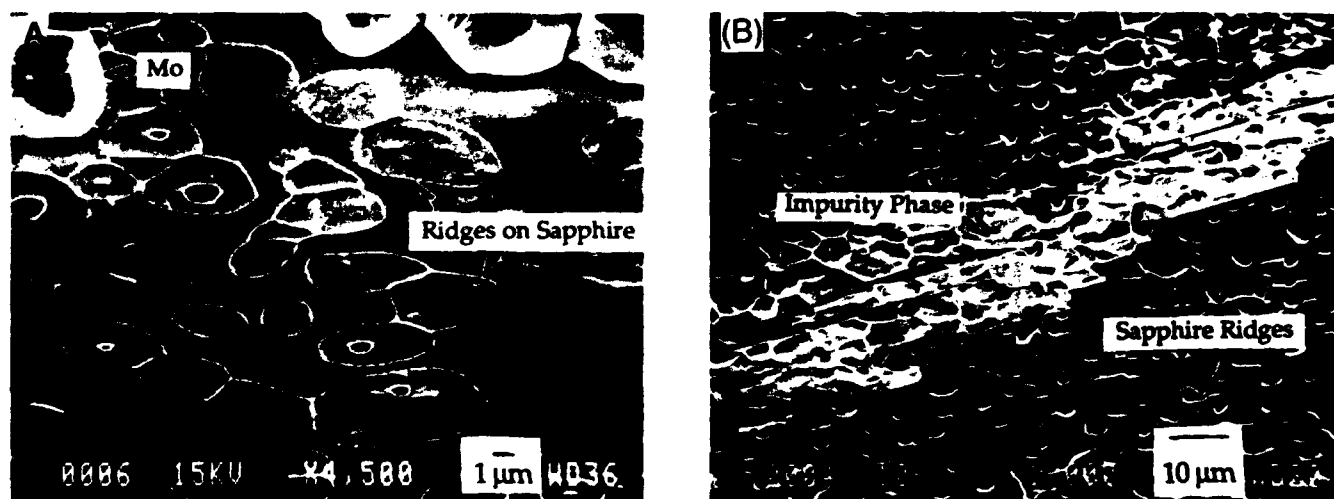


Fig. 5. (A) Shallow ridges observed on the sapphire surface of a Mo/sapphire diffusion couple upon debonding. (B) Pronounced ridges on the debonded sapphire surface when an impure W coating was used. The grain boundary impurity phase is composed of Fe and Cr.



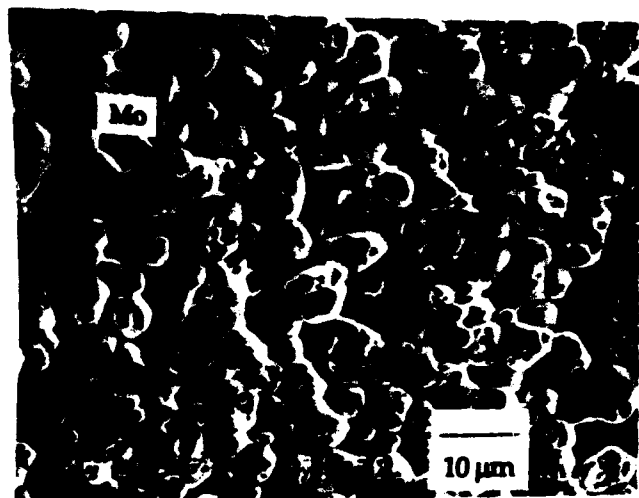


Fig. 6. Mo coating conforming to the surface features of a high-purity polycrystalline Al<sub>2</sub>O<sub>3</sub> substrate during diffusion bonding.

The results for the *oxide coatings* were found to be sensitive to the coating porosity. The *dense* coatings, which have a relatively high interfacial fracture energy, debond along the *interface*. But debonding only occurred when the crack approached the interface at a shallow inclination. Conversely, the coatings having the *lowest relative density* ( $\rho \approx 0.65$ ), exhibited a relatively low interfacial fracture energy,  $\Gamma_i \approx 5 \text{ J} \cdot \text{m}^{-2}$ , and debonded *within the coating*, at all crack inclinations. Such debonds exhibit fracture surface features typical of those for porous ceramics.<sup>11</sup> These debonding tendencies are rationalized by using the coating density,  $\rho$ , as a plotting variable against the ratio of the interfacial fracture energy to sapphire fracture energy  $\Gamma_i/\Gamma_r$  (Fig. 8(A)).

The debonding results obtained for all of the above coatings can be displayed on a debond diagram, relevant to sapphire fiber-reinforced brittle-matrix composites (Fig. 8(B)).

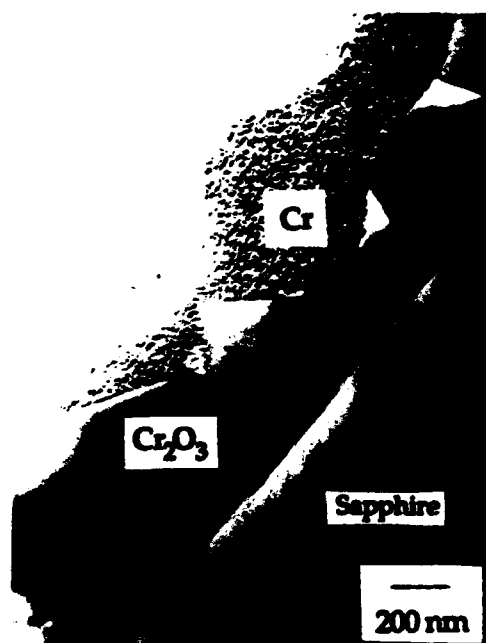
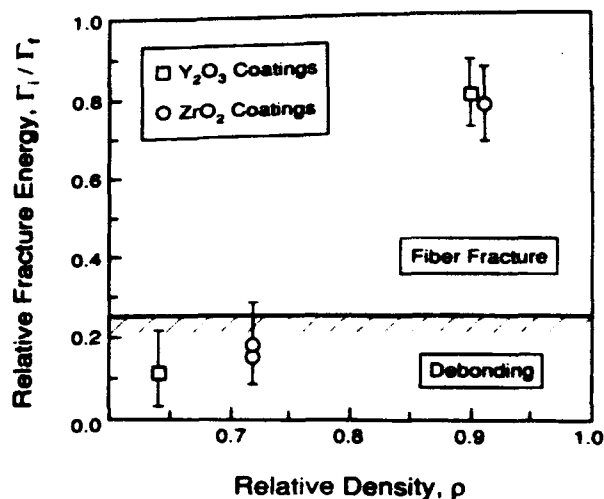
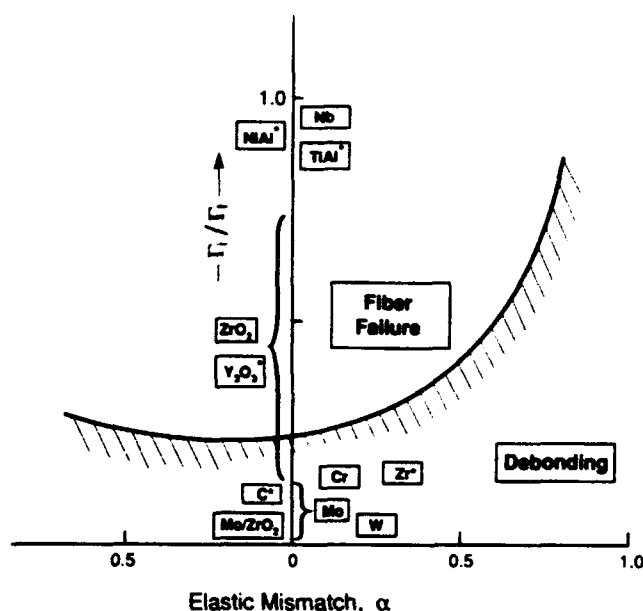


Fig. 7. Cr/sapphire diffusion bond containing a Cr<sub>2</sub>O<sub>3</sub> phase adjacent to the interface.



(A)



(B)

Fig. 8. (A) The relative density of oxide coatings plotted as a function of  $\Gamma_i/\Gamma_r$  clarifies the role of coating porosity in the debonding process. (B) A summary of the interfacial fracture energy measurements for various coatings on sapphire is presented on a "debond map." Coatings which fall within the fiber debonding regime of the map have some potential for sapphire fibers. However, coatings denoted by  $\star$  were found to chemically react with sapphire; these were precluded from further consideration.

## (2) Sliding Resistance

For *porous oxide coatings* on sapphire fibers in a polycrystalline Al<sub>2</sub>O<sub>3</sub> matrix, single-fiber tests revealed small fiber pull-out (Fig. 9). Debonding resulted in a monolayer of the oxide particles attached to the fiber that remained throughout the sliding process (Fig. 9). These particles are believed to act as asperities that resist sliding, resulting in a relatively large sliding stress,  $\tau$ . This stress was estimated from the pull-out length and the fracture<sup>16-18</sup> mirror radius to be  $\sim 140 \text{ MPa}$  (Table II). A similar value was obtained from fiber push-out measurements. This value of  $\tau$  is larger than that required for optimum composite strength and toughness.

The refractory oxides debond readily during single-fiber pull-out tests, but the coating is plastically deformed. This deformation occurs because the coating conforms to both the matrix and the fiber during consolidation and results in prohibitively high sliding resistances, such that little fiber pull-out

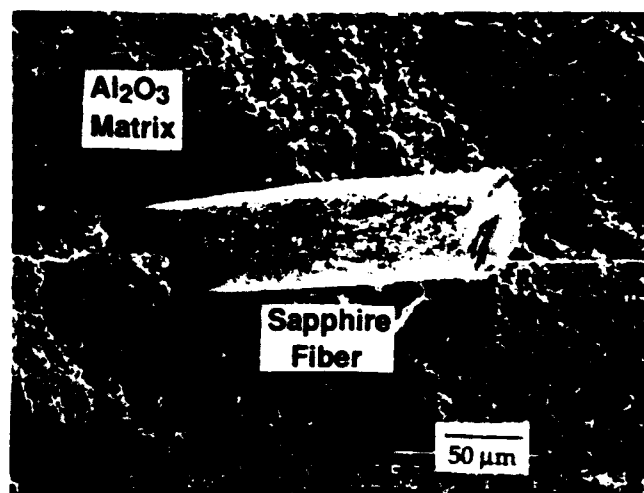


Fig. 9. A porous oxide interface led to fiber pull-out of a few fiber diameters. Oxide particles were observed to sinter to the sapphire fiber and remained attached during pull-out. The fracture mirror on the fiber is also visible.

occurs (Fig. 10). Similar behavior is found during push-out tests (Fig. 11(A)), which also indicate a high sliding resistance,  $\tau \approx 120$  MPa (Fig. 13).

A reduction in the sliding resistance for Mo-coated fibers has been achieved by removing the coating, after composite consolidation, to leave a gap between the fiber and the matrix. This has been accomplished by heating the composite in air\* (1000°C for 2 h). The surface roughness of the fiber and the matrix then provide the sliding resistance. For coatings somewhat thicker than the asperity amplitude on the fiber ( $\sim 1$   $\mu\text{m}$ ), the sliding resistance obtained from crack opening displacement measurements in single-fiber pull-out tests is found to be small ( $\tau < 1$  MPa), with large associated pull-out lengths (Fig. 12). This sliding resistance is too low for the requisite combination of strength and toughness in the composite. For thinner ( $\sim 0.7$   $\mu\text{m}$ ) coatings, push-out tests indicate a sliding resistance within the requisite range,  $\tau \approx 20$  MPa (Fig. 13), with no evidence of wear mechanisms on the fiber surface (Fig. 11(B)).

## VI. Concluding Remarks

The debonding and sliding properties of various coating materials on sapphire fibers have been evaluated. In general, most materials bonded well to sapphire. The notable exceptions were certain refractory metals (such as Mo, Cr, and W) which formed low fracture energy interfaces with sapphire. Several factors may be responsible for the low debond energies: porosity at the interfaces, oxygen dissolved in the metal (that suppresses plastic dissipation),<sup>11</sup> and the formation of a metal oxide

(MoO<sub>3</sub> or Cr<sub>2</sub>O<sub>3</sub>).<sup>22,23</sup> A systematic study would be needed to identify the critical factor(s).

Oxide coatings, which form strong interfaces with sapphire, can also be useful debond coatings, provided that they contain a significant amount of porosity subsequent to composite consolidation. The porosity in these coatings provides a low fracture energy path causing debonding within the coating. The practical problem of ensuring coating porosity may be approached by incorporating a second phase material, such as colloidal graphite, into the coating and removing it after the composite is consolidated.<sup>22</sup>

The sliding characteristics of the various interfaces were also investigated. The sliding resistance obtained on interfaces produced with refractory metal coatings is apparently too high for significant fiber pull-out, because the coating deforms during sliding. However, for coatings such as Mo, which form volatile oxides, the interfacial sliding resistance can be significantly reduced through coating removal by heat treatment in air. Fugitive carbon coatings also have this attribute,<sup>10</sup> but were not used in this study because the carbon reacted with the sapphire in the diffusion bonding experiments. It is recognized, however, that altering the processing conditions could eliminate this problem. Once the coating has been removed, the fiber surface and matrix roughness provide the sliding resistance needed for load transfer. The resultant system is also oxidatively stable. The coating thickness relative to the fiber and matrix roughness amplitude is now a key parameter.<sup>22</sup> An optimization study is in progress.

The sliding resistances of oxide coatings examined in this study were also unacceptably high, because of the undulating debond trajectory. It is believed that  $\tau$  can be reduced if the grain size and porosity of the coating are carefully controlled. Further studies of the effect of debond surface irregularities on the sliding behavior are needed to address this issue.

Fiber strength degradation is another concern for oxide coatings. When reaction products with the fiber coating are avoided, potential sources of fiber strength degradation persist, including residual strain (Fig. 3) and undulations produced on the fiber surface by diffusion (Fig. 5). Some basic characteristics are amenable to analysis (Appendix). The predictions (Fig. 14) indicate that *m*-ZrO<sub>2</sub> coatings are unacceptable because, for typical coating thicknesses ( $h \approx 0.1$ – $1$   $\mu\text{m}$ ), the large mismatch stresses caused by the transformation lead to fiber strengths below the acceptable limit for high-performance applications ( $S < 1$  GPa). Furthermore, coatings such as YAG with a mismatch governed by thermal expansion are also predicted to cause an unacceptably low fiber strength ( $S < 2$  GPa), unless the coatings are thin ( $h < 3$   $\mu\text{m}$ ). A general implication is that

\*Because Mo forms volatile oxides.

Table II. Sliding Stress with Porous Alumina Interface

Fracture mirror radius, $a_m$ ( $\mu\text{m}$ )	In situ fiber strength, $S^*$ (GPa)	Pullout length, $h$ ( $\mu\text{m}$ )	Sliding stress, $\tau$ (MPa)
27	1.68	193	142

\* $S = 3.5 (K/\sqrt{a_m})$ , where  $K$  is the fiber toughness ( $\approx 2.5$  MPa $\sqrt{\text{m}}$ ).<sup>11</sup>  $\tau = S(r/2h)$ , where  $r$  is the sapphire fiber radius.<sup>11</sup>

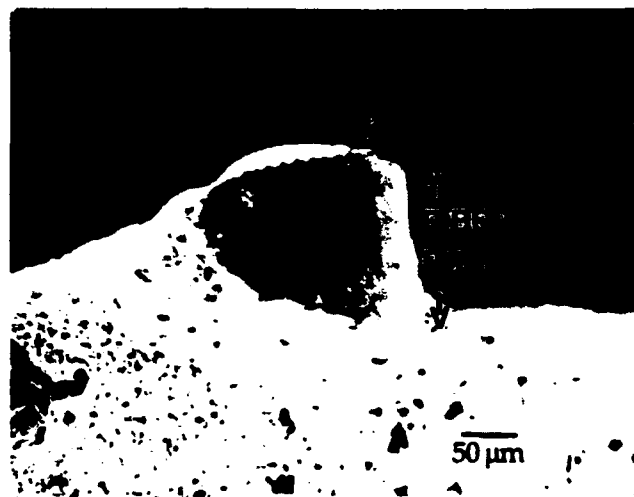


Fig. 10. Short fiber pull-out lengths were observed when Mo coatings were used.

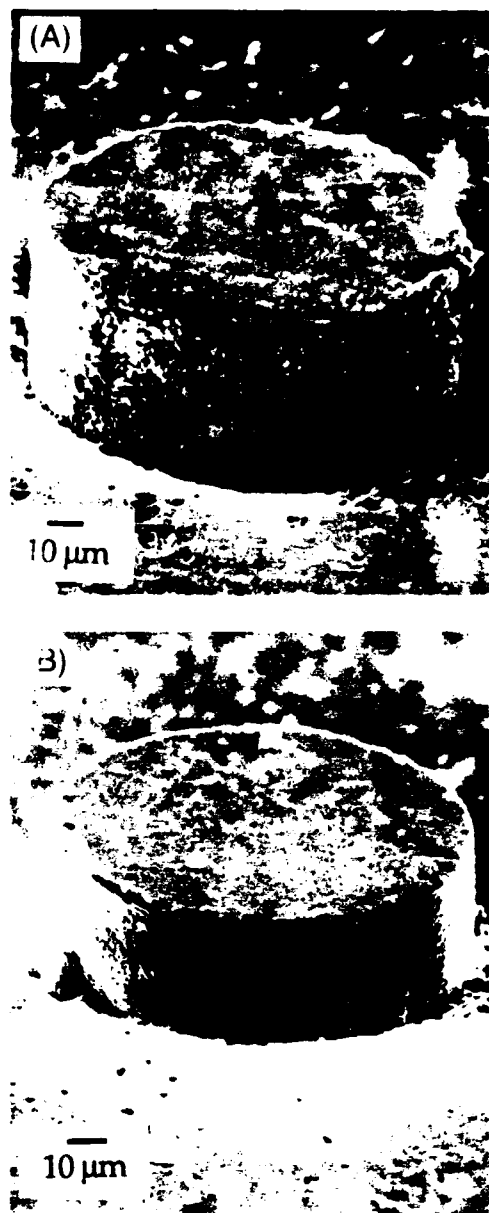


Fig. 11. The surface morphology of the pushed-out sapphire fibers was found to change when the Mo coating was removed by oxidation: (A) as-hot-pressed condition; (B) heat-treated condition.

oxide coatings, which typically bond well to sapphire, are a possible source of fiber strength degradation. The extent of degradation is diminished by thin coatings and small thermal expansion mismatch. Also, porosity in the coating tends to alleviate the degradation problem.

## APPENDIX

### Fiber Degradation

When the coating is in residual tension caused by thermal expansion misfit, the coating cracks before fiber failure and may cause a degradation in fiber strength. When this crack penetrates into the fiber, the stress intensity factor,  $K_R$ , for a crack of depth  $a$  associated with the residual field from the coating is<sup>14</sup>

$$K_R = 1.1E_f h' \sqrt{\pi a} (1 - \nu) \quad (A-1)$$

$$\approx 1.1\sigma_0 h' \sqrt{\pi a}$$

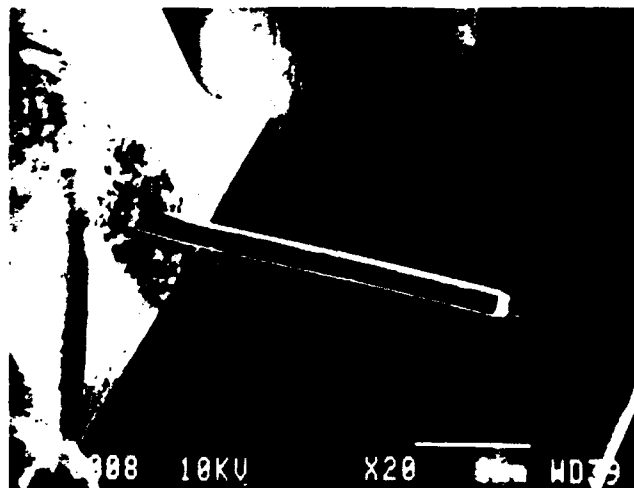


Fig. 12. Long fiber pull-out can result when thick ( $\sim 6 \mu\text{m}$ ) Mo coatings are removed by oxidation.

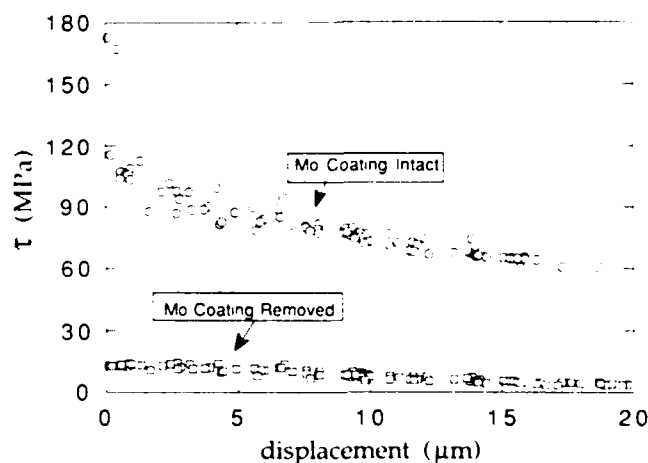


Fig. 13. Fiber push-out curves reveal that the interfacial sliding resistance was decreased to an acceptable level by removing the submicrometer thick ( $0.7 \mu\text{m}$ ) Mo coating from the interface.

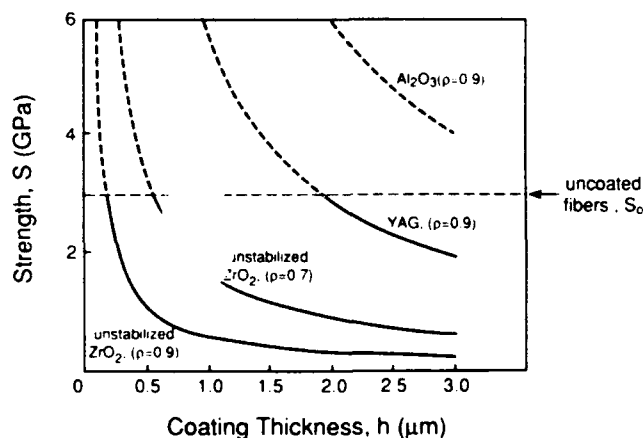


Fig. 14. The predicted influence of oxide coatings on the strength of sapphire fiber:  $\rho$  is the coating density. It is assumed that the uncoated fibers have a strength  $S_0 = 2.5 \text{ GPa}$ .

where  $\epsilon_f$  is the misfit strain,  $h$  the coating thickness,  $E_f$  its Young's modulus,  $\nu$  its Poisson's ratio, and  $\sigma_f$  the misfit stress. The applied stress  $\sigma$  also induces a stress intensity<sup>14</sup>

$$K = 1.1\sigma\sqrt{\pi a} \quad (\text{A-2})$$

By adding the  $K$ 's and equating to the fracture resistance of the fiber, the stress/crack length relation becomes

$$\sigma = 0.9\sqrt{\frac{E_f\Gamma_f}{\pi a}} - \frac{\sigma_f h}{\pi a} \quad (\text{A-3})$$

Differentiating Eq. (A-3) and setting  $d\sigma/da = 0$  for the maximum,  $\sigma_{\max}$ , gives a fiber strength,

$$S \equiv \sigma_{\max} = 0.2(E_f\Gamma_f/\sigma_f h) \quad (\text{A-4})$$

This result applies when  $S$  is smaller than the strength  $S_0$  of the uncoated fibers. Fiber strengths as a function of coating thickness for a range of dense and porous oxide coatings are plotted in Fig. 14.

**Acknowledgment:** We wish to acknowledge Dr. M. De Graef for helpful discussions and the TEM micrograph shown in Fig. 4(A).

## References

- <sup>1</sup>J. Aveston, G. A. Cooper, and A. Kelly, *Properties of Fibre Composites*, IPC Science and Technology Press, London, U.K., 1971.
- <sup>2</sup>D. B. Marshall and A. G. Evans, Overview No. 85, "The Mechanical Behavior of Ceramic Matrix Composites," *Acta Metall. Mater.*, **37** [10] 2567-83 (1989).
- <sup>3</sup>D. B. Marshall, B. N. Cox, and A. G. Evans, "The Mechanics of Matrix Cracking in Brittle-Matrix Fiber Composites," *Acta Metall. Mater.*, **33** [11] 2013-21 (1985).
- <sup>4</sup>M. Y. He and J. W. Hutchinson, "Crack Deflection at an Interface Between Dissimilar Materials," *Int. J. Solids Struct.*, **25**, 1053-67 (1989).
- <sup>5</sup>A. G. Evans, F. W. Zok, and J. B. Davis, "The Role of Interfaces in Fiber-Reinforced Brittle Matrix Composites," *Compos. Sci. Technol.*, **42**, 3-24 (1991).
- <sup>6</sup>H. C. Cao, E. Bischoff, O. Sbaizero, M. Rühle, A. G. Evans, D. B. Marshall, and J. J. Brennan, "Effect of Interfaces on the Properties of Fiber-Reinforced Ceramics," *J. Am. Ceram. Soc.*, **73**, 1691 (1990).
- <sup>7</sup>S. M. Wiederhorn, "Fracture of Sapphire," *J. Am. Ceram. Soc.*, **52**, 485 (1969).
- <sup>8</sup>D. H. Roach, S. Lathabai, and B. R. Lawn, "Interfacial Layers in Brittle Cracks," *J. Am. Ceram. Soc.*, **71** [2] 97-105 (1988).
- <sup>9</sup>S. M. Wiederhorn, *Fracture Mechanics of Ceramics*, Vol. 2; p. 20. Edited by R. C. Bradt *et al.* Plenum Press, New York, 1974.
- <sup>10</sup>T. Mah, K. Keller, T. A. Parthasarathy, and J. Guth, "Fugitive Interface Coating in Oxide-Oxide Composites: A Viability Study," *Ceram. Eng. Sci. Proc.*, **12** [9-10] 1802-15 (1991).
- <sup>11</sup>R. W. Rice, "Effects of Inhomogeneous Porosity on Elastic Properties of Ceramics," *J. Am. Ceram. Soc.*, **58** [9-10] 458-59 (1975).
- <sup>12</sup>M. Rühle and A. G. Evans, "Structure and Chemistry of Metal/Ceramic Interfaces," *Mater. Res. Soc. Symp. Proc.*, **120**, 293-311 (1988).
- <sup>13</sup>A. G. Evans and B. J. Dalgleish, "The Fracture Resistance of Metal-Ceramic Interfaces," p. 295 in *Proceedings of the International Symposium of Metal-Ceramic Interfaces*, Pergamon Press, Oxford, U.K., 1992.
- <sup>14</sup>J. B. Davis, H. C. Cao, G. Bao, and A. G. Evans, "The Fracture Energy of Interfaces: An Elastic Indentation Technique," *Acta Metall. Mater.*, **39** [5] 1019-24 (1991).
- <sup>15</sup>P. G. Charalambides, H. C. Cao, J. Lund, and A. G. Evans, "Development of a Test Method for Measuring the Mixed Mode Fracture Resistance of Bimaterial Interfaces," *Mech. Mater.*, **8**, 269-83 (1990).
- <sup>16</sup>D. B. Marshall, M. C. Shaw, and W. L. Morris, "Measurement of Interfacial Debonding and Sliding Resistance in Fiber Reinforced Intermetallics," *Acta Metall. Mater.*, **40** [3] 443-54 (1992).
- <sup>17</sup>M. D. Thouless, O. Sbaizero, L. S. Sigl, and A. G. Evans, "Effect of Interface Mechanical Properties on Pullout in a SiC-Fiber-Reinforced Lithium Aluminum Silicate Glass Ceramic," *J. Am. Ceram. Soc.*, **72** [4] 525-32 (1989).
- <sup>18</sup>F. E. Heredia, S. M. Spearing, A. G. Evans, P. Mosher, and W. A. Curtin, "Mechanical Properties of Continuous-Fiber-Reinforced Carbon Matrix Composites and Relationships to Constituent Properties," *J. Am. Ceram. Soc.*, **75** [1] 3017-25 (1992).
- <sup>19</sup>W. A. Curtin, "Theory of Mechanical Properties of Ceramic-Matrix Composites," *J. Am. Ceram. Soc.*, **74** [11] 2837-45 (1991).
- <sup>20</sup>D. B. Marshall and W. C. Oliver, "Measurement of Interfacial Mechanical Properties in Fiber-Reinforced Ceramic Composites," *J. Am. Ceram. Soc.*, **70** [8] 542-48 (1987).
- <sup>21</sup>P. D. Jero and R. J. Kerans, "The Contribution of Interfacial Roughness to Sliding Friction of Ceramic Fibers in a Glass Matrix," *Scr. Metall. Mater.*, **24**, 2315-18 (1990).
- <sup>22</sup>T. J. Mackin, P. D. Warren, and A. G. Evans, "The Effects of Fiber Roughness on Interface Sliding in Composites," *Acta Metall. Mater.*, **40** [6] 1251-57 (1992).
- <sup>23</sup>J. B. Davis, E. Bischoff, and A. G. Evans, "Zirconia Coatings for Sapphire Fiber-Reinforced Composites," pp. 631-38 in *Advanced Composite Materials*, Edited by M. D. Sacks, American Ceramic Society, Westerville, OH, 1991.
- <sup>24</sup>K. T. Miller, F. F. Lange, and D. B. Marshall, "The Instability of Polycrystalline Thin Films: Experiment and Theory," *Mater. Res. Soc. Symp. Proc. Ultrast. Proc.*, **121** [3] 823-30 (1988); *J. Mater. Res.*, **1** [5] 151-60 (1990).
- <sup>25</sup>S. S. Cole, Jr., and G. Sommer, "Glass-Migration Mechanism of Ceramic-to-Metal Seal Adherence," *J. Am. Ceram. Soc.*, **44** [6] 265-71 (1961).
- <sup>26</sup>E. Samuel and P. Hrma, "MoO<sub>3</sub> Diffusion in Aluminosilicate Glass," *J. Am. Ceram. Soc.*, **72** [6] 1091-92 (1989).
- <sup>27</sup>*The Metal Molybdenum*, Proceedings of a Symposium sponsored by the Office of Naval Research, Edited by J. Harwood, American Society for Metals, Metals Park, OH, 1958.
- <sup>28</sup>*Ductile Chromium and Its Alloys*, Proceedings of a Conference sponsored by the Office of Ordnance Research, American Society for Metals, Metals Park, OH, 1957.
- <sup>29</sup>H. E. Dève, A. G. Evans, G. R. Odette, R. Mehrabian, M. L. Emiliani, and R. J. Hecht, "Ductile Reinforcement Toughening of  $\gamma$ -TiAl: Effect of Debonding and Ductility," *Acta Metall. Mater.*, **37**, 853-90 (1989).
- <sup>30</sup>M. Rühle, K. Burger, W. Mader, and A. G. Evans, "Some Aspects of Structures and Mechanical Properties of Metal/Ceramic Bonded Systems," pp. 43-70 in *Fundamentals of Diffusion Bonding*, Edited by Y. Ishida, Elsevier, New York, 1987.
- <sup>31</sup>K. P. Trumble and M. Rühle, "The Thermodynamics of Spinel Interphase Formation of Diffusion-Bonded Ni/Al<sub>2</sub>O<sub>3</sub> Interfaces," *Acta Metall. Mater.*, **39** [8] 1915-24 (1991).
- <sup>32</sup>M. Rühle, A. Strecker, D. Waidelich, and B. Kraus, "In Situ Observations of Stress-Induced Phase Transformations in ZrO<sub>2</sub>-Containing Ceramics," pp. 256-74 in *Advances in Ceramics*, Vol. 12, *Science and Technology of Zirconia II*, Edited by N. Claussen, M. Rühle and A. H. Heuer, American Ceramic Society, Columbus, OH, 1984.
- <sup>33</sup>T. J. Mackin, J. Yang, C. G. Levi, and A. G. Evans, "Environmentally Compatible Double Coating Concepts for Sapphire Fiber-Reinforced  $\gamma$ -TiAl," *Mater. Sci. Eng. A*, in press.
- <sup>34</sup>H. Tada, P. C. Paris, and C. R. Irwin, *The Stress Analysis of Cracks Handbook*, Del Research Corp., St. Louis, MO, 1973, 1985. □

## CRACKING AND DAMAGE MECHANISMS IN CERAMIC/METAL MULTILAYERS

M. C. SHAW<sup>1,2</sup>, D. B. MARSHALL<sup>2</sup>, M. S. DADKHAH<sup>2</sup> and A. G. EVANS<sup>1</sup>

<sup>1</sup>Materials Department, College of Engineering, University of California, Santa Barbara, CA 93106-5050  
and <sup>2</sup>Rockwell International Science Center, 1049 Camino Dos Rios, Thousand Oaks, CA 91360, U.S.A.

(Received 10 November 1992)

**Abstract**—Investigations of cracking in multilayered ceramic/metal composites are presented. Two aspects are considered: crack renucleation across intact single metal layers and subsequent crack extension. Crack renucleation criteria are determined and compared with predictions. High-resolution strain-mapping techniques are employed to determine the surface strain fields surrounding cracks. Good agreement is found between these experimental measurements and the predictions of a small-scale yielding model. Subsequent crack progression occurs either by the extension of a dominant, nearly planar crack or by the formation of a zone of periodically spaced cracks. Both patterns are analyzed. The dominant cracking behavior is found to depend on the volume fraction and yield strength of the metal.

### 1. INTRODUCTION

The macroscopic mechanical properties of layered metal/ceramic composites are governed by the mechanisms of deformation and damage that occur upon loading [1–6]. Especially important is the manner in which cracks that first form in brittle layers communicate further damage to the neighboring layers. Two limiting responses have been identified: global and local load sharing [1]. When global load sharing applies, the stress redistribution caused by a crack results in a uniformly increased stress in all of the remaining uncracked layers. Consequently, a straightforward stochastic approach can be used to characterize the mechanical properties, leading to a damage mechanics representation. Conversely, local load sharing results in a stress concentration around an initial crack formed within one layer, which causes damage to progress laterally, often as a dominant mode I crack. In this case, large-scale bridging mechanics is appropriate. As yet, there is no fundamental understanding of the properties of the layers and of the interfaces that govern the occurrence of these extreme behaviors (or of intermediate mechanisms). The present article addresses the criterion that governs this fracture mechanism transition.

A previous study provided some understanding of the stress fields around a crack within a ductile–brittle layered composite [2]. For a crack located in a brittle layer with its tip incident upon a ductile layer (as illustrated in Fig. 1), two limits were identified: (i) a small-scale yielding (SSY) limit, wherein the plastic zone extends completely through the ductile

layer but only a small distance (compared with the crack length) along the layer and (ii) a large-scale yielding (LSY), or shear lag (SL) limit, characterized by the plastic zone extending a relatively large distance normal to the crack. The SSY limit exhibits relatively large stress concentrations and is expected to result in local load sharing. The LSY limit is typified by much smaller stress concentrations and may allow global load sharing. Investigation of these stress fields (including their relationship with the cracking sequence) should provide insight into the transition in mechanism. The present study describes experimental approaches for measuring the stress and displacement fields around such cracks, and compares the results with calculated stress fields.

### 2. EXPERIMENTAL

#### 2.1. Materials

Metal/ceramic multilayers were produced by vacuum diffusion bonding precleaned metal and ceramic sheets. Bonding was conducted at homologous temperatures for the metal,  $T/T_m \sim 0.9$ , for  $\sim 24$  h, with an applied compression  $\sim 2$  MPa, in a vacuum ( $\sim 10^{-6}$  torr). The composites were prepared from two grades of aluminum oxide,† one of higher strength than the other, bonded to high purity aluminum or copper. These systems have strongly bonded interfaces [3]. The properties of the constituents are summarized in Table 1. The thicknesses of the layers, as well as the ratios of the metal thickness,  $h_m$ , to the ceramic thickness,  $h_c$ , were varied, but in all cases, a total multilayer thickness of 4–8 mm was used. The range of systems and diffusion bonding conditions are summarized in Table 2. Some specimens with relatively thick (2 mm)  $Al_2O_3$  outer layers were used

†Coors ADS-995, which is relatively pure and has high flexural strength, and Coors ADS-96, which is less pure and has lower strength.

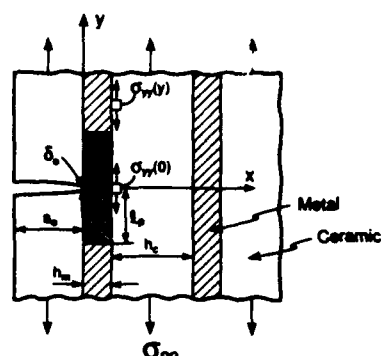


Fig. 1. Schematic illustrating the crack geometry and the parameters measured in the experiments.

in order to establish a well-developed crack prior to testing [Fig. 2(a)].

## 2.2. Measurements

*In situ* observations of crack growth in the multilayered composites were obtained on beam specimens with notches cut to a depth of ~50% of the thickness of the outer ceramic layer with a diamond saw. The specimens were polished optically flat on one face to allow observations of crack growth. Cracks were initiated from the root of the notch and then extended stably to the interface using a loading fixture attached to the stage of an optical microscope [Fig. 2(a)]. Most tests were done in ambient air. However, to examine environmental susceptibility, a few tests on the  $\text{Al}_2\text{O}_3/\text{Al}$  materials were done in dry  $\text{N}_2$ . High magnification micrographs were obtained from the crack tip region during loading. In all cases, cracks were oriented with the crack plane perpendicular to the layers (Figs 1 and 2) and the loads were applied in four-point flexure. Typical specimen dimensions were  $1 \times 8 \times 30$  mm, with the inner and outer loading point separations being 10 and 25 mm. The nominal mode I stress intensity factors  $K_I$  were evaluated from the measured loads, crack lengths and specimen

dimensions by using the calibration for an elastically homogeneous beam (Section 4.1) [7].

Optical micrographs of the crack tip region were analyzed to determine the opening displacement,  $\delta_o$ , of the cracked ceramic layer adjacent to the metal, the strain,  $\epsilon_{yy}$ , in the neighboring ceramic layer, and the plastic zone size,  $l_p$  (Fig. 1). This was achieved by measuring *differential* displacements of corresponding image features in pairs of micrographs: one taken at zero load (the reference) and the other obtained under load. Two image analysis techniques were used: stereo viewing of pairs of micrographs [8] and a computerized image comparison procedure [9] (HASM-AP-High Accuracy Strain MAPing). The latter technique determines full-field maps of in-plane displacements, which can be differentiated to produce the in-plane strain fields. Since both methods measure differential displacements, their sensitivity is much greater than the point-to-point resolution of the micrographs.†

Strain distributions were also measured using microscopic high-resolution moiré interferometry. The procedure involved depositing a diffraction grating on the specimen surface and forming a moiré interference pattern between the specimen grating and a fixed reference grating during loading of the specimen [10, 11]. The moiré image consists of fringes which define contours of constant displacement, with the increment between fringes being equal to one-half of the grating period. A fringe multiplication technique was used [10] to increase the differential displacement resolution to 36 nm/fringe. Interferographs were obtained in two orthogonal directions,  $x$  or  $y$  (Fig. 1), by using two interpenetrating diffraction gratings oriented at  $90^\circ$ . The strains  $\epsilon_{yy}$  were determined by measuring fringe spacings along a line within the ceramic layer,  $5 \mu\text{m}$  from the interface. The  $\sigma_{yy}(y)$  stress was then estimated using the plane stress relation [12]

$$(1 - \nu^2)\sigma_{yy}(y) = E[\epsilon_{yy}(y) + \nu\epsilon_{xx}(y)] \quad (1)$$

where  $\nu$  is Poisson's ratio and  $E$  is Young's modulus of the  $\text{Al}_2\text{O}_3$ .

†Displacement resolution of 10 nm is achieved from optical micrographs.

Table 1. Properties of constituents

Constituent	Thermal expansion coefficient $\alpha (\times 10^{-6} \text{ } ^\circ\text{C}^{-1})$	Young's modulus $E$ (GPa)	Uniaxial yield strength $\sigma_o$ (MPa)	Work hardening coefficient $n$
$\text{Al}_2\text{O}_3$	8	380	—	—
Al	25	70	50	0.2
Cu	17	120	70	0.3

Table 2. Summary of diffusion bonding conditions

Multilayer	Bonding temperature ( $^\circ\text{C}$ )	Bonding pressure (MPa)	Bonding time (h)	$\text{Al}_2\text{O}_3$ thickness ( $\mu\text{m}$ )	Metal thickness ( $\mu\text{m}$ )
	620	1.5	20	45	250
A/ $\text{Al}_2\text{O}_3$	655	2.6	20	680 125	8, 25, 50, 100, 250 250
Cu/ $\text{Al}_2\text{O}_3$	940	1	24	480	8, 25, 100, 250 25, 130

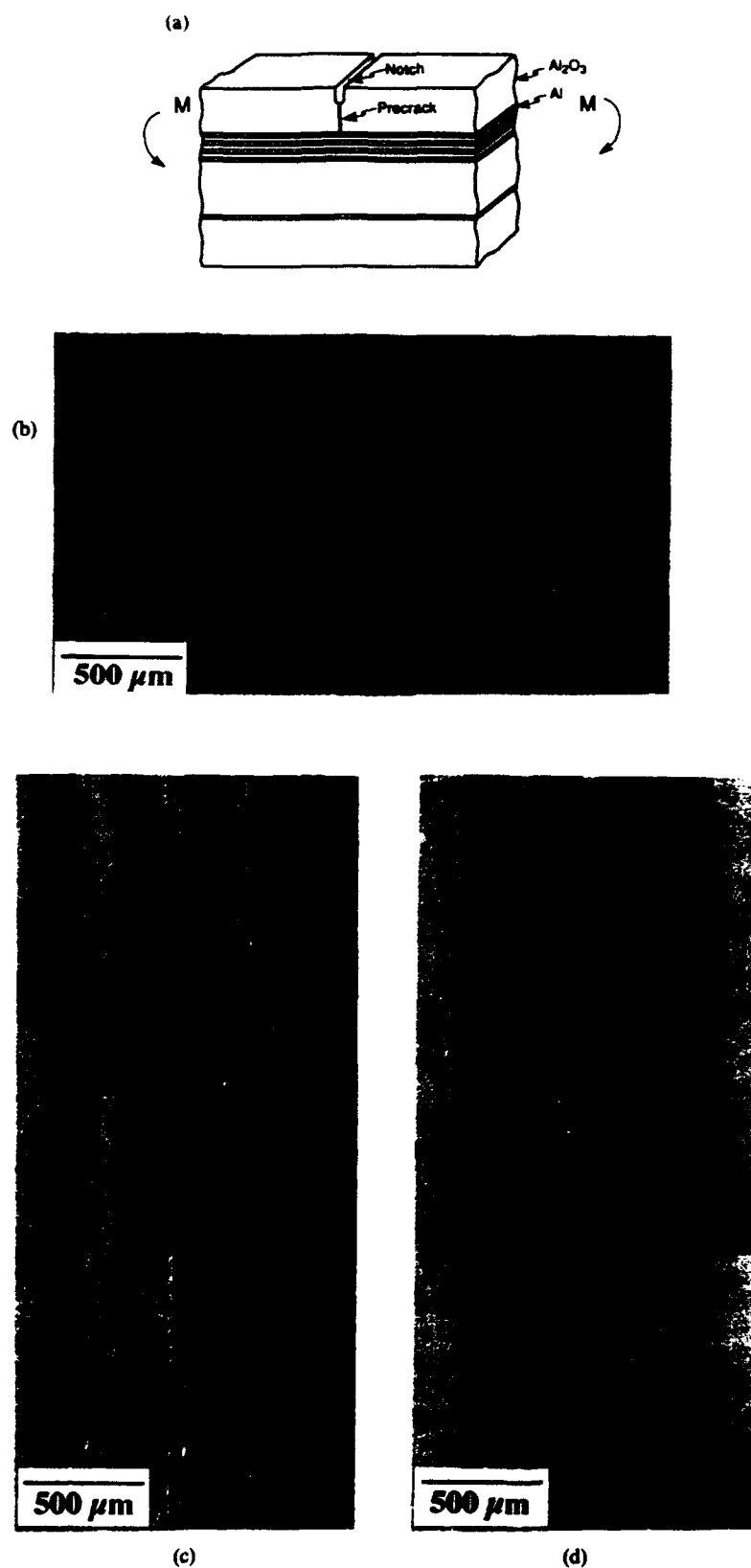


Fig. 2. (a) Schematic illustrating the specimen type and loading geometry where  $M$  is the applied bending moment. (b, c, d) Cracking patterns determined by optical microscopy: (b) single crack in a system with Al/480  $\mu\text{m}$   $\text{Al}_2\text{O}_3$ , (c) multiple cracking in composites with Al/125  $\mu\text{m}$   $\text{Al}_2\text{O}_3$  and (d) Al/45  $\mu\text{m}$   $\text{Al}_2\text{O}_3$ . Arrows indicate the crack locations. All three composites contained 250  $\mu\text{m}$  thick Al layers.

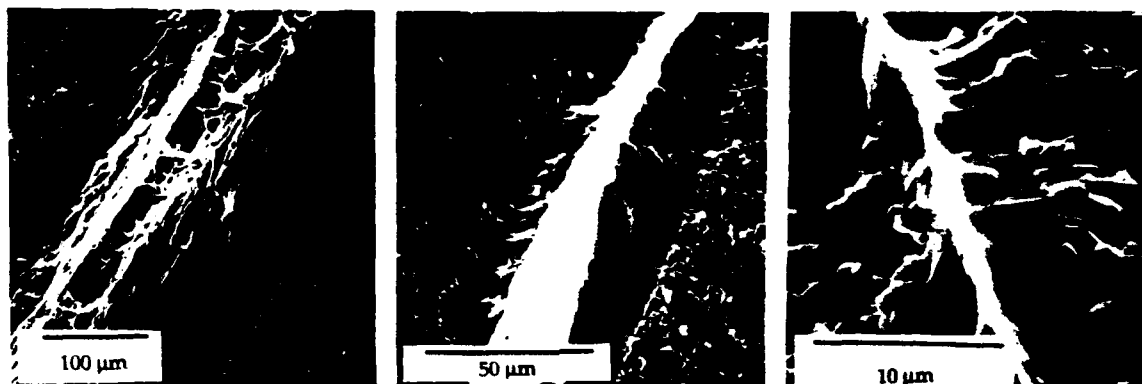


Fig. 3 Scanning electron micrographs of fracture surfaces of  $\text{Al}_2\text{O}_3$  multilayers, showing a single aluminum layer sandwiched between two alumina layers.

In materials with relatively thick  $\text{Al}_2\text{O}_3$  layers ( $>480 \mu\text{m}$ ), average strains,  $\bar{\epsilon}_{11}$ , were measured with strain gauge over an area  $\approx 0.6 \times 0.25 \text{ mm}$ .

The strength distribution of the higher strength alumina was measured using four-point flexural loading of specimens cut from as-received plates ( $680 \mu\text{m}$  thick) and from plates that had been surface-ground to reduce their thickness to  $450 \mu\text{m}$ . The strength distribution of the lower strength alumina was also measured using four-point flexural loading of specimens cut from as-received plates ( $2 \text{ mm}$  thick). The cumulative probability of failure,  $\Phi(S)$ , was determined (using order statistics) as a function of the nominal strength,  $S$ , for both types of alumina, by using the volume flaw solution (see Section 3) [13]

$$-\ln[1 - \Phi(S)] = (S/S_0)^m (Lhw/V_0) \times (m+2)/4(m+1)^2 \quad (2)$$

where  $L$  is the test span,  $w$  is the specimen width and  $h$  is the specimen thickness, with  $V_0$  being a reference volume (taken to be  $1 \text{ m}^3$ ) and  $S_0$  and  $m$  the reference strength and shape parameters.

### 3. RESULTS

#### 3.1. Crack growth

In multilayered composites with low volume fractions of metal ( $f_m < 0.3$ ), a single crack formed in each ceramic layer ahead of the notch during fracture of precracked beams [Fig. 2(b)]. No interfacial debonding occurred in any of the composites, during either crack renucleation or subsequent fracture, despite extensive plastic stretching of the metal layers (Fig. 3). Furthermore, the cracks renucleated sequentially in adjoining layers on nearly the same plane as the notch. The damage is thus viewed as a dominant mode I crack, with the crack tip taken to be the edge of the furthest cracked ceramic layer. A nominal stress intensity factor  $K_I$  can then be defined as the loading parameter.

The growth of mode I cracks in systems containing ceramic layers of thickness greater than that of the

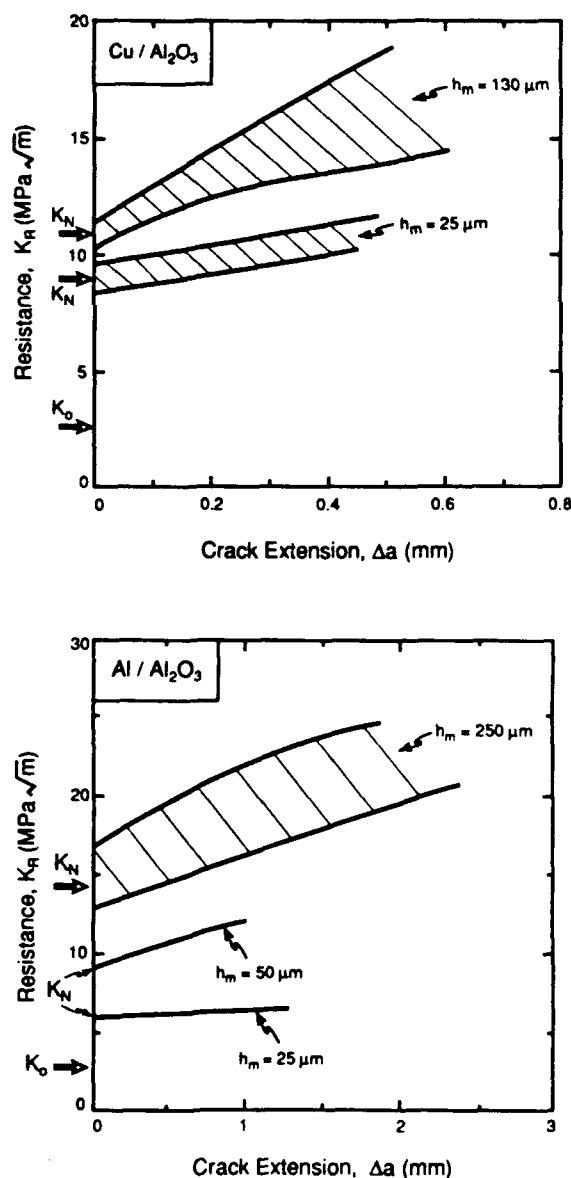


Fig. 4. Measured crack growth resistance,  $K_R$ , as a function of crack extension,  $\Delta a$ , for several multilayered composites.



metal layers ( $h_c = 450\text{--}680\text{ }\mu\text{m}$ ,  $h_m = 8\text{--}250\text{ }\mu\text{m}$ ) may be represented by resistance curves (Fig. 4). Two values of the stress intensity factor characterize crack growth: (i) that needed for initial crack renucleation across intact metal layers,  $K_N$ , and (ii) that needed for subsequent crack growth,  $K_R$ . Initial crack growth is controlled by crack renucleation in the ceramic layer ahead of the crack tip, whereas  $K_R$  increases during

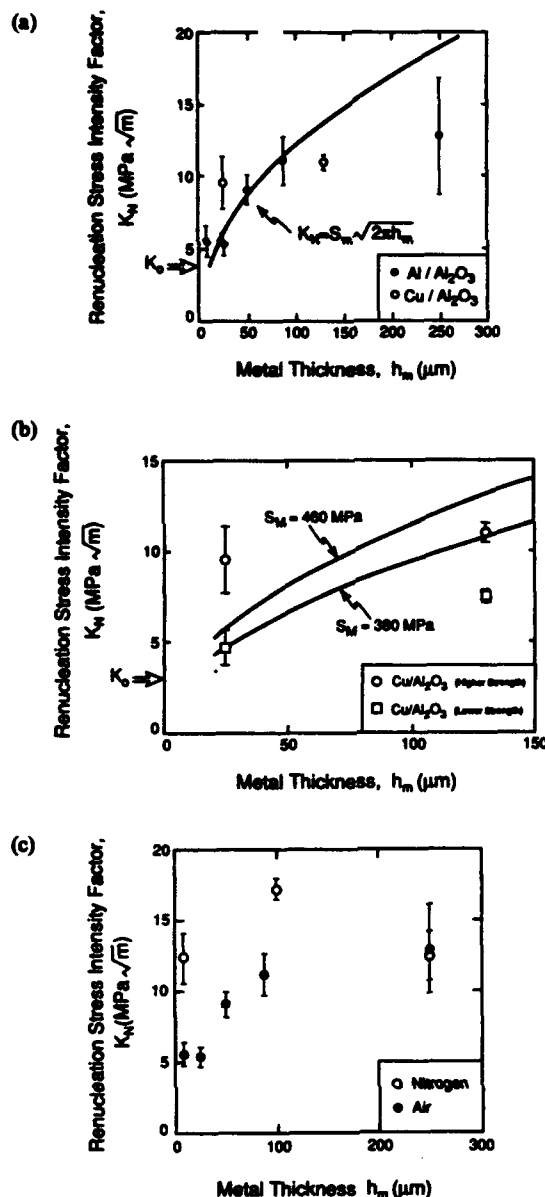


Fig. 5. (a) Crack renucleation stress intensity factor,  $K_N$ , as a function of metal layer thickness,  $h_m$ , for (a) composites fabricated from the higher strength alumina and tested in an air environment. Also shown is the SSY prediction for a median ceramic strength,  $S_m = 460\text{ MPa}$ . (b)  $K_N$  for copper/alumina composites fabricated from either the higher strength or lower strength alumina and tested in an air environment. Also shown are the SSY predictions for  $K_N$  for median ceramic strengths of  $S_m = 460\text{ MPa}$  and  $S_m = 380\text{ MPa}$ . (c)  $K_N$  for aluminum/alumina multilayers fabricated from the higher strength alumina tested in air and dry nitrogen.

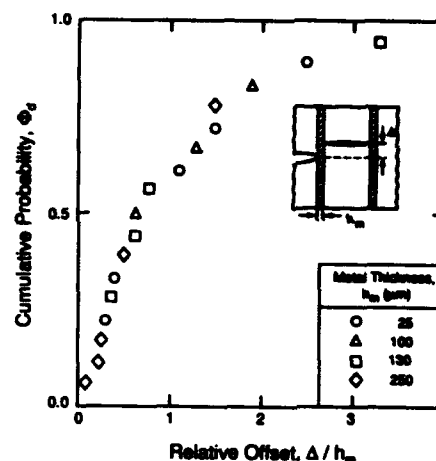


Fig. 6. Cumulative distribution,  $\Phi_d$ , of the offset,  $\Delta$ , in crack renucleation location normalized by the metal layer thickness,  $h_m$ , for multilayers with a range of metal layer thicknesses.

subsequent crack growth because of the bridging effect of intact metal layers in the crack wake. For a given material combination and environment (Fig. 5), the renucleation resistance increased with the thickness of the metal layers. The values of  $K_N$  ranged between 5 and 17 MPa  $\sqrt{\text{m}}$ , in all cases, higher than the fracture toughness of alumina [14] ( $K_0 \sim 3.5$  to 4 MPa  $\sqrt{\text{m}}$ ) [Fig. 5(a)]. The values of  $K_N$  were also systematically higher in Cu/Al<sub>2</sub>O<sub>3</sub> composites containing the higher strength Al<sub>2</sub>O<sub>3</sub> than in equivalent composites with the lower strength Al<sub>2</sub>O<sub>3</sub> [Fig. 5(b)]. Testing of the Al/Al<sub>2</sub>O<sub>3</sub> composites in air resulted in lower values of  $K_N$  than testing in dry N<sub>2</sub>, implying a sensitivity of crack renucleation to moisture [Fig. 5(c)].

Finally, the locations at which the cracks renucleated were usually offset from the crack plane in the previously cracked Al<sub>2</sub>O<sub>3</sub> layer. The offset distances,  $\Delta$ , measured for composites with metal layers of various thicknesses are shown in Fig. 6 as a single probability distribution, plotted as a function of  $\Delta$  normalized by the thickness,  $h_m$ , of the metal layers. The results indicate that  $\Delta$  scales with  $h_m$ .

### 3.2. Crack tip opening displacements

The stationary crack tip opening displacements,  $\delta_0$ , were determined by stereoscopy from *in situ* optical micrographs obtained before cracks renucleated in the ceramic layer ahead of the precrack. For each specimen,  $\delta_0$  was found to increase with increasing  $K_I$ , following the proportionality,  $\delta_0 \propto K_I^2$  [Fig. 7(a)]. This proportionality suggests that the data may be compared with the solution for a homogeneous metal in the small scale yielding limit, given by [15, 16]

$$\delta_0 \equiv \frac{HK_I^2}{E_m \sigma_0}, \quad (3)$$

where  $E_m$  and  $\sigma_0$  are the Young's modulus and uniaxial yield strength of the metal and  $H$  is a

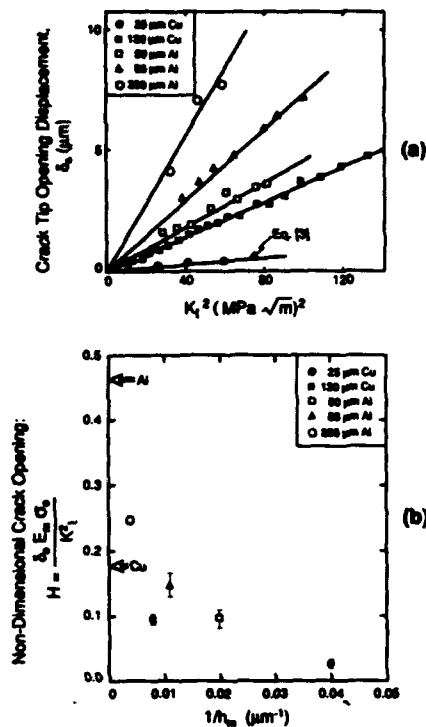


Fig. 7. (a) Crack tip opening displacements,  $\delta_0$ , as a function of the square of the applied stress intensity factor,  $K_I^2$ , for several multilayer systems. Also shown is the prediction [equation (3)]. (b) The non-dimensional parameter,  $H = \delta_0 E_m \sigma_0 / K_I^2$  as a function of inverse metal layer thickness for several different multilayer systems.

non-dimensional parameter. For homogeneous metals,  $H$  depends only on the work hardening coefficient, and typically has values of 0.48 for aluminum and 0.18 for copper [16, 17]. It is apparent from Fig. 7(b) that smaller values of  $H$  obtain for all of the layered materials. Moreover, the magnitude of  $H$  decreases with decreasing metal layer thickness [Fig. 7(b)] and, at given layer thickness, is lower for the multilayers containing copper than for those containing aluminum, consistent with the trend in  $H$  for the homogeneous metals.

### 3.3. Strain measurements

The average strains,  $\epsilon_{yy}$ , measured using strain gauges in the  $Al_2O_3$  layers directly opposite the precrack increased with increasing  $K_I$  (Fig. 8). Both the magnitude of the strain and the rate of increase in strain, at given  $K_I$ , increased with decreasing metal layer thickness.

A moiré interference micrograph showing fringes of constant displacement in the vertical ( $y$ ) direction, obtained from the region surrounding a crack tip in a multilayered Cu/ $Al_2O_3$  composite, is shown in Fig. 9. The stresses,  $\sigma_{yy}$ , along the edge of the  $Al_2O_3$  layer ahead of the crack tip, evaluated from the micrographs [by using equation (1)] are plotted in Fig. 10, along with theoretical predictions to be discussed in the following section. The data obtained

at each of three values of the applied stress intensity factor indicate that local stress concentrations exist ahead of the crack tip, with peaks offset symmetrically by approximately 50 μm from the crack plane. The magnitude of the peak stress increases linearly with  $K_I$ . The strains,  $\epsilon_{yy}$ , in the metal layer displayed a similar distribution as those in the intact ceramic layer, but were much larger in magnitude with a plastic zone that extended beyond the field of view ( $\pm 350$  μm).

The distribution of shear strains (as determined by HASMAP) around a crack in another Cu/ $Al_2O_3$  multilayered composite with thicker copper layers (130 μm) is shown in Fig. 11. A zone of localized plastic strain within the copper layer ahead of the crack tip is evident. The zone extends to the side of the crack to a distance approximately 7 times the metal layer thickness ( $l_p \approx 1$  mm).

### 3.4. Multiple cracking

In composites with larger volume fractions of metal ( $f_m > 0.7$ ), multiple cracks formed within the  $Al_2O_3$  layers [Fig. 2(c, d)] after initial renucleation from the precrack. Furthermore, in multilayers with the highest metal volume fraction [ $f_m = 0.85$ , Fig. 2(d)], lateral spreading of multiple cracks within the same brittle layer often occurred in preference to forward progression of the main crack. In all cases, the crack density eventually saturated within a damage zone  $\sim 2$  mm in total width [approximately twice the width of the region of the specimen containing the thin ceramic layers, Fig. 2(a)], with the distribution,  $\Phi_m$ , of crack spacings shown in Fig. 12. It is evident that the mean crack spacing at saturation,  $l_s$ , increases as the alumina layer thickness increases.

### 3.5. Alumina strengths

The strength distributions measured on the as-sintered and surface-ground specimens of the higher strength  $Al_2O_3$  were indistinguishable [Fig. 13(a)],

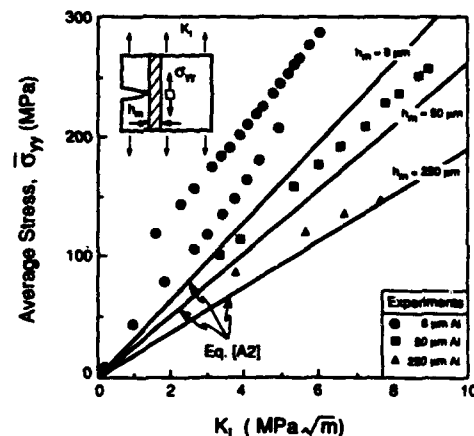


Fig. 8. Average stresses,  $\sigma_{yy}$ , in ceramic layers directly opposite the crack determined with a strain gauge, for several multilayers. Also shown are the predictions for  $\sigma_{yy}$  from equation (A2).

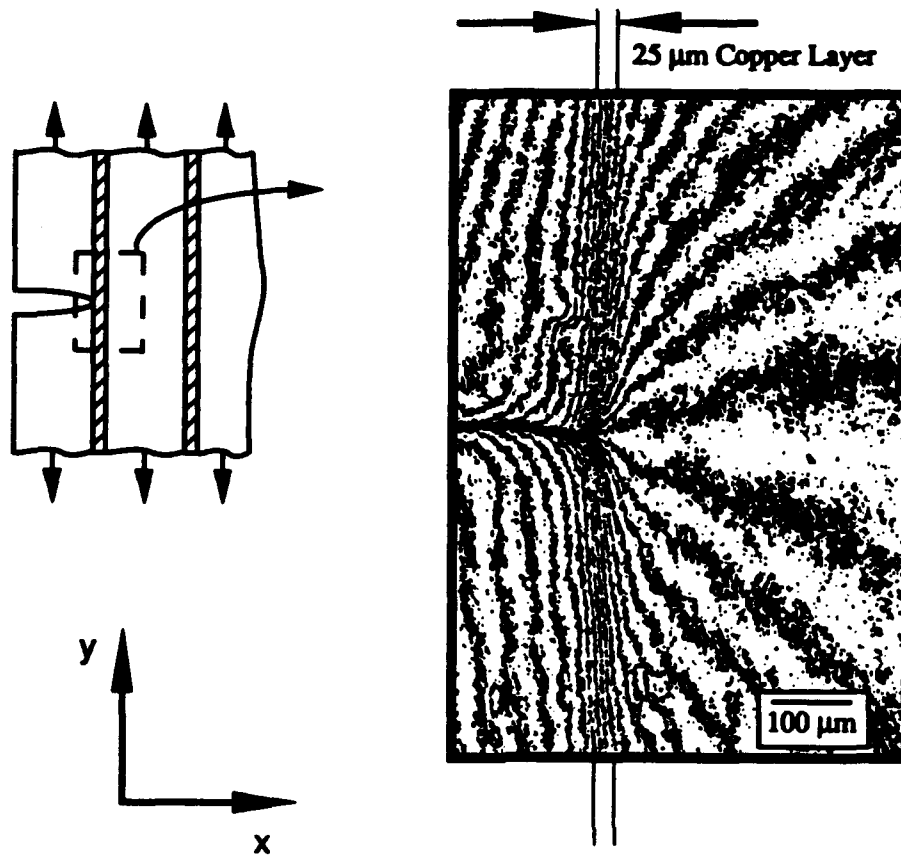


Fig. 9. High-resolution moiré interferograph of the crack tip region in a Cu/Al<sub>2</sub>O<sub>3</sub> multilayer when subjected to an applied stress intensity factor of  $K_I = 7.7 \text{ MPa}\sqrt{\text{m}}$ . Each fringe represents a contour of constant differential displacement of 36 nm in the vertical direction ( $y$ -direction).

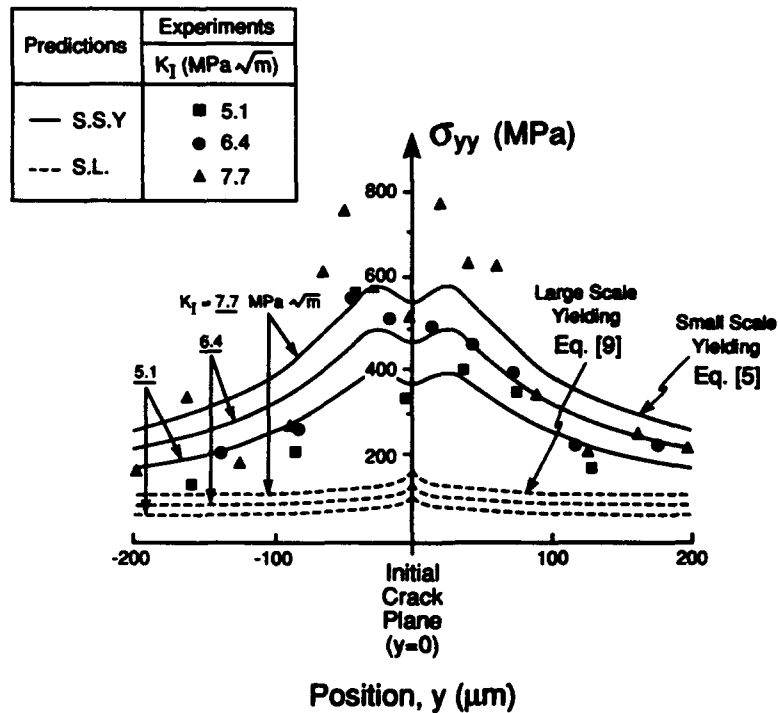


Fig. 10. Stress distributions,  $\sigma_{yy}(y)$ , obtained by moiré interferometry at three loads ( $K_I = 5.1, 6.4$  and  $7.7 \text{ MPa}\sqrt{\text{m}}$ ). Comparisons with SSY and LSY predictions are also shown.

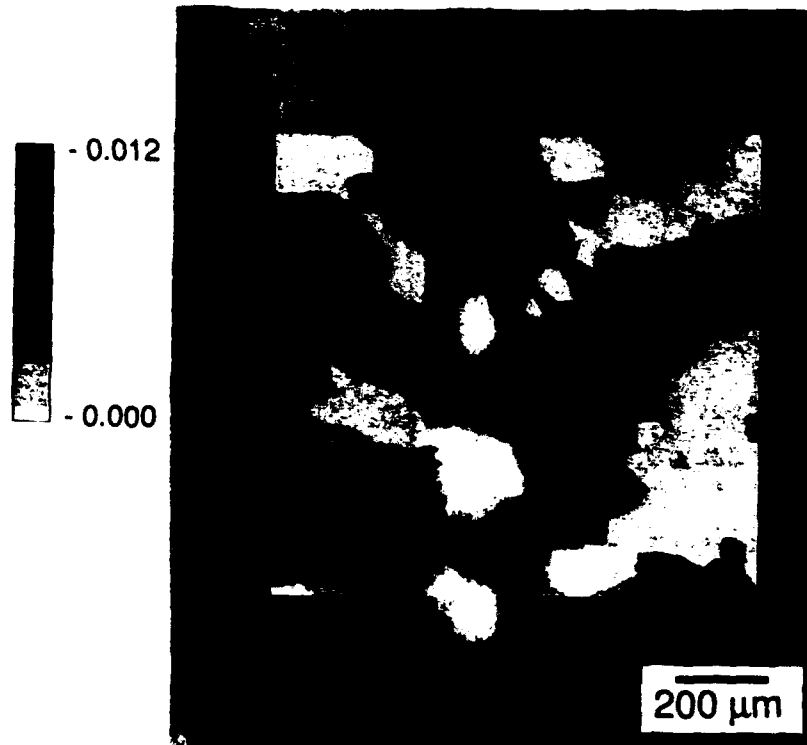


Fig. 11. Contour map of the in-plane shear strain distribution,  $\epsilon_{11}$ , measured by HASMAP just before crack renucleation in a copper alumina multilayer. The contour intervals represent a strain of  $6 \times 10^{-4}$ .

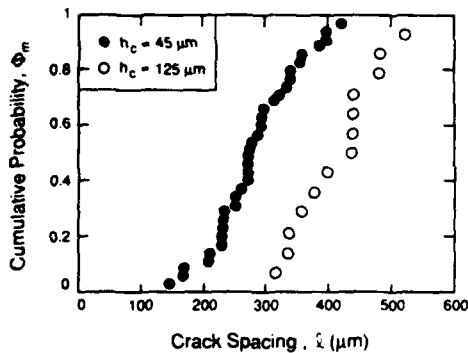


Fig. 12. Distribution,  $\Phi_m$ , of crack spacings, at saturation, from several multiply cracked aluminum/alumina specimens containing 45 and 125  $\mu\text{m}$  thick alumina layers with 250  $\mu\text{m}$  thick aluminum layers.

suggesting that the strength is controlled by volume flaws.<sup>†</sup> The data from both types of specimens were combined, and the magnitudes of the shape parameter,  $m$ , and the reference strength,  $S_0$ , were ascertained by fitting equation (2) to the data, giving  $V_0 S_0^m = 2.9 \times 10^{11} \text{ MPa}^m \cdot \text{m}^3$ . The corresponding median strength is,  $S_m = 460 \text{ MPa}$ . For the lower strength  $\text{Al}_2\text{O}_3$  (as-sintered),  $V_0 S_0^m = 1.2 \times 10^9 \text{ MPa}^m \cdot \text{m}^3$  and the median strength is,  $S_m = 380 \text{ MPa}$  [Fig. 13(b)].

<sup>†</sup>Although it is possible that the surface flaw distributions were the same within the measurement accuracy, it is considered unlikely.

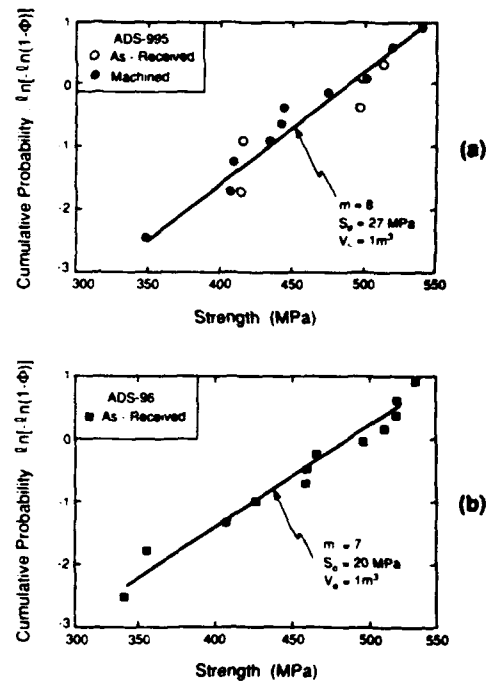


Fig. 13. Cumulative failure probabilities (a) for plates of the higher strength  $\text{Al}_2\text{O}_3$  in the as-received and machined conditions, and (b) plates of the lower strength alumina in the as-received condition.

## 4. COMPARISON WITH MODELS

## 4.1. Crack tip stresses

Two limiting solutions have been identified for the stresses,  $\sigma_{yy}(x, y)$ , within intact brittle layers ahead of the crack tip in layered metal/ceramic composites. In the small-scale yielding (SSY) limit, the stresses along the crack plane closely approximate the elastic solution [2]

$$\sigma_{yy}(x, 0) \approx K_I / \sqrt{2\pi x} \quad (x \geq h_m) \quad (4)$$

where  $K_I$  is computed for an elastically homogeneous medium. This result holds even when the plastic zone extends both through the metal layer and laterally up to a distance several times the metal layer thickness. The corresponding stresses in the intact ceramic layer alongside the metal/ceramic interface ( $x = h_m$ ) are given by [18]

$$\sigma_{ij} = \frac{K_I}{\sqrt{2\pi r}} f_{ij}(\theta), \quad (5)$$

with

$$\sigma_{yy}(r, \theta) = \frac{K_I}{\sqrt{2\pi r}} \left( \cos\left(\frac{\theta}{2}\right) \left[ 1 + \sin\left(\frac{\theta}{2}\right) \sin\left(\frac{3\theta}{2}\right) \right] \right)$$

where  $r$  and  $\theta$  are the radial and angular coordinates from the crack tip (Fig. 1)

$$r = \sqrt{h_m^2 + y^2} \\ \theta = \arctan\left(\frac{y}{h_m}\right). \quad (6)$$

An estimate of the size of the slip zone, obtained by equating  $\sigma_{yy}$  to the shear yield strength of the metal [with  $K_I = \sigma_\infty \sqrt{\pi a_0}$  in equation (5)], is [2]

$$l_p/a_0 \approx 0.38(\sigma_\infty/\sigma_0)^2 \quad (7)$$

where  $\sigma_\infty$  is the applied tensile stress and  $a_0$  is the length of the precrack. For larger slip lengths, corresponding to large-scale yielding (LSY), a finite element analysis has been used to evaluate the stresses [2]. The peak stress in the ceramic layer is [2]

$$\sigma_{yy}(h_m, 0) \approx \sigma_\infty \left[ 1 + \frac{5.8}{\ln(l_p/h_m)} \right]. \quad (8)$$

The distribution of  $\sigma_{yy}$  stresses in the intact ceramic layer for  $0.05 \geq (y/l_p) \geq 1$  is [2]

$$\sigma_{yy}(h_m, y) \approx \sigma_\infty \left[ 1 - 5.8 \left( \frac{a_0}{w} \right) Q \frac{\ln(y/l_p)}{\ln(l_p/h_m)} \right] \quad (9)$$

where  $Q$  is a dimensionless parameter and  $w$  is the specimen width [2]. The corresponding slip length is

$$l_p/a_0 = \sqrt{3}\sigma_\infty/\sigma_0. \quad (10)$$

The predicted stresses, given by equations (5) and (9), are compared with the moiré interferometry data

in Fig. 10. The SSY predictions agree reasonably well with the experimental results, including the locations of the peak stress which are offset from the crack plane. Conversely, the LSY solution substantially underestimates the magnitudes of the stresses and fails to predict the location of maximum stress. Additionally, the SSY predictions are compared with the strain gauge measurements, made over a range of loads (Fig. 8; Appendix A). Again, the SSY predictions agree reasonably well with the data.

The stress distributions at  $x = h_m$  in the ceramic layer ahead of the crack tip can be used in conjunction with the measured strength of the ceramic to predict failure of the ceramic layer and thus, the renucleation stress intensity factor,  $K_N$ . A simple estimate is obtained by equating the stress (at  $x = h_m, y = 0$ ) from equation (5) to the median strength,  $S_m$ , of the  $\text{Al}_2\text{O}_3$  layers.<sup>†</sup> For small-scale yielding, this gives

$$K_N = S_m \sqrt{2\pi h_m}. \quad (11)$$

The prediction of equation (11), with  $S_m = 460$  MPa (from Fig. 13), agrees reasonably well with measured values of  $K_N$  for materials with metal layers of various thicknesses [Fig. 5(a)]. Furthermore, the decrease in  $K_N$  in multilayers fabricated from the lower strength alumina [Fig. 5(b)] also is consistent with the predicted decrease in  $K_N$  resulting from a lower  $S_m$ . These correlations with the SSY predictions apply even though the normalized plastic zone size extends up to  $l_p/a_0 \approx 2$  (Fig. 11). Consequently, the SSY stresses seemingly apply over a wider range of plastic zone sizes than had been expected [2], although these findings are consistent with recent calculations [19].

## 4.2. Multiple cracking

**4.2.1. Transition from single to multiple cracking.** The criterion for the transition from single to multiple cracking is a key design parameter for this class of multilayered composites. Since the present experiments indicate that SSY conditions dominate, this transition does not appear to be related to the onset of LSY conditions. Instead, it is suggested that the transition occurs when new cracks are formed in the  $\text{Al}_2\text{O}_3$  layers in the crack wake. For wake cracking to occur preferentially, the local stresses in the wake must exceed those ahead of the crack, as well as reach the fracture strength of the ceramic layers. These stresses are influenced by two contributions: the K-field of the main crack tip and the bridging tractions exerted by the intact, but plastically stretched, metal layers. The stresses associated with the K-field are always smaller in the wake than ahead of the crack tip. However, the contribution from the bridging tractions can be sufficient to make the wake stress larger than the tip stress. This contribution depends on the magnitude of the bridging tractions,  $T$ , the relative area over which the tractions are applied (the volume fraction of the metal) and the absolute thicknesses of the individual layers. The

<sup>†</sup>A more rigorous analysis would entail statistical analysis of fracture, using the measured strength distribution of the  $\text{Al}_2\text{O}_3$  layers and the nonuniform stress field of Eqn. (5). Preliminary calculations indicate that the present simplification does not result in significant error.

magnitude of  $T$  is known to depend on the metal yield strength and the local crack opening [20, 21].

A simple model for wake cracking, involving a primary crack traversing three ceramic layers and partially bridged by two intact metal layers, is analyzed in Appendix B (Fig. B1). Approximate analytical solutions for the wake stresses as a function of distance from the crack plane, for this particular geometry (Fig. B2), indicate that the stress increases from zero at the crack faces to a maximum at a characteristic distance from the crack plane, and then decreases. The characteristic distance could dictate the crack spacing within the zone of multiple cracking. The analysis reveals that as the volume fraction of metal increases, the location of the larger peak stress changes from the brittle layer ahead of the crack tip to the crack wake, provided that the metal flow strength is sufficiently high (Fig. B2). This trend is qualitatively constant with the observations in Section 3.

**4.2.2. Multiple crack density.** An important measure of the extent of crack damage relevant to a damage mechanics formulation is the crack density,  $\rho$ . No attempt is made here to understand the evolution of  $\rho$ . However, some appreciation for the applicability of damage mechanics may be gained by comparing the measured crack spacings with values predicted by fragment length analysis [1]. Stochastic analysis of multiple cracking in bimaterial systems with sliding interfaces [1] indicates that the crack density saturates and that the saturation density,  $\rho_s$ , is related to the interfacial shear stress,  $\tau$ , as well as a characteristic ceramic layer strength,  $S_c$ , through the relationship

$$\rho_s = \lambda(m)\tau/(h_c S_c) \quad (12)$$

where  $\lambda$  is a dimensionless coefficient of order unity [1], and, for a well-bonded interface,  $\tau$  is the shear flow strength of the metal ( $\tau \approx \sigma_0/\sqrt{3}$ ). The characteristic strength,  $S_c$  (Appendix C), is [1]

$$S_c = (\lambda\tau V_0 S_0^m / h_c^2 w)^{1/(m+1)}. \quad (13)$$

Therefore, equation (12) can be written

$$\rho_s = \left( \frac{\lambda^m \tau^m h_c^{(1-m)w}}{V_0 S_0^m} \right)^{1/(m+1)}. \quad (14)$$

With the relevant parameters for the  $\text{Al}_2\text{O}_3/\text{Al}$  system [ $V_0 S_0^m = 2.9 \times 10^{11} \text{ MPa}^m \cdot \text{m}^3$ ,  $\tau \approx 30 \text{ MPa}$ ,  $\lambda(m=8) \approx 1.6$ ], the saturation crack spacings for multilayered specimens with  $45 \mu\text{m}$  and  $125 \mu\text{m}$  thickness alumina layers are predicted from equation (14) to be  $\sim 0.8 \text{ mm}$  and  $\sim 1.7 \text{ mm}$ , respectively. Although these are larger than the measured spacings, they are in the same range and they scale correctly (Fig. 12). A damage approach based on the stochastics of the brittle layers, coupled with interfacial slip, thus appears to be a potentially viable procedure for characterizing the properties associated with multiple cracking.

## 5. CONCLUSIONS

Crack growth and damage accumulation in strongly bonded ceramic/metal multilayers have been investigated, with particular emphasis on the criterion for crack advance, as well as on crack extension patterns. Crack renucleation beyond intervening metal layers is found to be governed by the small-scale yielding stress field. Plastic flow within the metal layers exerts a minimal influence, despite clear evidence of plasticity in the metal layers prior to crack renucleation. The metal layers therefore act simply to separate the intact ceramic layer from the crack tip by a distance corresponding to the metal layer thickness. This behavior leads to a simple inverse-square root dependence of the crack renucleation resistance,  $K_{IN}$ , on the metal layer thickness,  $h_m$ . These conclusions establish that crack renucleation results from a significant stress concentration associated with cracks in adjacent brittle layers.

Damage develops either as a dominant crack, or as periodic cracks, depending on the volume fraction, layer thickness and yield strength of the metal. As the volume fraction of metal increases, at constant ceramic layer thickness, the stresses in the crack wake increase, whereas the stresses in the intact layer ahead of the crack tip decrease. This trend in stress leads to a transition in cracking mechanism with increasing volume fraction of metal, whenever the metal layers have sufficiently high yield strength. Specifically, for low metal volume fractions, mode I extension of a primary crack occurs, whereas for high metal volume fractions, periodic multiple cracking occurs.

When multiple cracking dominates, a damage mechanics approach for characterizing properties appears to be viable. To assess the validity of such an approach, a simple model has been used to relate the saturation crack density,  $\rho_s$ , to the intrinsic flow properties of the metal, the strength characteristics of the brittle layers and the geometry of the multilayers. The predictions of the model are qualitatively consistent with the measured trends.

**Acknowledgements**—The authors gratefully acknowledge the assistance of Dr B. J. Dalgleish in preparation of the copper/alumina multilayers, and for many valuable discussions. This work was supported by Rockwell International Research and Development funding and by the Office of Naval Research, Contract No. N00014-90-J-1300.

## REFERENCES

1. W. A. Curtin, *J. Mater. Sci.* **26**, 5239 (1991).
2. H. C. Cao and A. G. Evans, *Acta metall. mater.* **39**, 2997 (1991).
3. B. J. Dalgleish, K. P. Trumble and A. G. Evans, *Acta metall.* **37**, 1923 (1989).
4. M. S. Hu and A. G. Evans, *Acta metall.* **37**, 917 (1989).
5. D. C. Agrawal and R. Raj, *Acta metall.* **37**, 1265 (1989).
6. F. S. Shieu, R. Raj and S. L. Sass, *Acta metall.* **38**, 2215 (1990).

7. H. Tada, P. C. Paris and G. R. Irwin, *The Stress Analysis of Cracks Handbook*. Paris Productions, St Louis, MO (1985).
8. D. R. Williams, D. L. Davidson and J. Lankford, *Exp. Mech.* 4 (1980).
9. M. R. James, W. L. Morris and B. N. Cox, *Exp. Mech.* 30, 60 (1990).
10. B. Han, *Optical Engng* 31, 1517 (1992).
11. M. S. Dadkhah, B. Han and M. C. Shaw, to be published.
12. S. P. Timoshenko and J. N. Goodier, *Theory of Elasticity*. McGraw-Hill, New York (1934).
13. N. A. Weil and I. M. Daniel, *J. Am. Ceram. Soc.* 47, 268 (1964).
14. L. A. Simpson and G. J. Merrett, *J. Mater. Sci. Lett.* 9, 685 (1974).
15. J. R. Rice and M. A. Johnson, *Inelastic Behavior of Solids* (edited by M. F. Kanninen, W. F. Adler, A. R. Rosenfield and W. F. Jaffee), pp. 641-672. McGraw-Hill, New York (1969).
16. J. W. Hutchinson, Dept. Solid Mechanics, Technical Univ. of Denmark (1979).
17. R. A. Hertzberg, *Deformation and Fracture Mechanics of Engineering Materials*. Wiley, New York (1983).
18. B. R. Lawn and T. Wilshaw, *Fracture of Brittle Solids*. Cambridge Univ. Press (1975).
19. K. S. Chan, M. Y. He and J. W. Hutchinson, *Mater. Sci. Engng*. In press.
20. D. B. Marshall, B. N. Cox and A. G. Evans, *Acta metall.* 33, 3013 (1985).
21. A. G. Evans and R. M. McMeeking, *Acta metall.* 34, 2435 (1986).
22. T. J. Roark, *Formulas for Stress and Strain*. McGraw-Hill, New York (1954).

## APPENDIX A

### Comparison of Predicted Stresses with Strain Gauge Measurements

The strain gauge data provide a measure of the average stress,  $\bar{\sigma}_{yy}$ , within the region bounded by the strain gauge, i.e.  $h_m < x < h_m + d$ , where  $d$  is the width of the strain gauge. For the stress field given by the small-scale yielding limit [2]

$$\bar{\sigma}_{yy} = \frac{1}{d} \int_{h_m}^{h_m+d} \frac{K}{\sqrt{2\pi x}} dx. \quad (A1)$$

Integration gives

$$\bar{\sigma}_{yy} = \sqrt{\frac{2}{\pi}} \frac{K}{\sqrt{d}} \left( \sqrt{\frac{h_m}{d} + 1} - \sqrt{\frac{h_m}{d}} \right) \equiv \frac{K}{\sqrt{2\pi d}}. \quad (A2)$$

where

$$d = \left[ \frac{d}{2[\sqrt{h_m + d} - \sqrt{h_m}]} \right]^2. \quad (A3)$$

Equation (A2) is compared with measurements for materials with aluminum layers of different thickness in Fig. 8.

## APPENDIX B

### Multiple Cracking Analysis

The mode of damage evolution (single or multiple cracking) depends on the relative magnitudes of the stresses in the ceramic layers ahead of and behind the crack tip. These depend, in turn, on the thickness of the metal and ceramic layers, the crack length, the strength distribution of the ceramic, and the flow properties of the metal. To assess the effect of changing the volume fraction of metal, these stresses are estimated for the specific composite geometry shown in Fig. B1.

The stresses were estimated by regarding the effect of the intact metal bridging ligaments as crack closure tractions,  $T$ , acting on the crack faces (Fig. B1). In general, the magnitude of  $T$  depends on the local crack opening, the flow properties of the metal and interfacial debonding. However, for the purpose of illustrating the transition in behavior,  $T$  is taken to be a constant ( $T = 1.5\sigma_\infty$ ) in the present analysis. Assuming that the stress concentration due to the crack tip is given by a  $K$  field, and assuming elastic homogeneity, the crack tip stresses are [18]

$$\sigma_{\theta\theta} = \frac{K_{\theta\theta}}{\sqrt{2\pi r}} f(\theta) \quad (B1)$$

where  $K_{\theta\theta}$  is the local stress intensity factor given by [20]

$$K_{\theta\theta} = 2 \sqrt{\frac{a}{\pi}} \int_0^1 \frac{[\sigma_\infty - T(X)] dX}{\sqrt{1-X^2}} \quad (B2)$$

where  $X = 1 + x/a$  (Fig. B1). The stresses in the crack wake along the line normal to the crack at  $x = -(h_m + h_c)$  are given by the superposition of two components, one due to the crack tip stress concentration, equation (B1), and the other due to the traction  $T$  [18, 22]

$$\sigma_{\theta\theta} = \frac{K_{\theta\theta}}{\sqrt{2\pi r}} f(\theta) + g(f_m, r, \theta, T) \quad (B3)$$

where  $f(\theta)$  is given by equation (5) and the function  $g(f_m, r, \theta, T)$  accounts for the wake stresses arising from the crack bridging tractions applied to the surface of an elastic half space over the intervals,  $-2(h_c + h_m) < x < -(2h_c + h_m)$ , and  $-(h_c + h_m) < x < -h_c$  [22],

$$g(f_m, r, \theta, T) = T(\alpha_1 + \alpha_2 + \sin \alpha_1 + \sin \alpha_2)/\pi \quad (B4)$$

with

$$\alpha_1 = \arctan\left(\frac{h_m}{y}\right)$$

$$\alpha_2 = \arctan\left(\frac{h_m + h_c}{y}\right) - \arctan\left(\frac{h_c}{y}\right)$$

with  $h_m$ ,  $h_c$ , and  $y$  defined in Fig. 1.

The stresses in the ceramic layers ahead of the crack tip ( $\sigma_A$ ) and in the crack wake ( $\sigma_B$ ) are plotted as a function of distance from the crack plane in Fig. B2 for various values of  $f_m$ . The stress distributions at both locations pass through a maximum at a distance from the crack plane of several times  $h_c$ . At small values of  $f_m$ , the maximum stress is larger ahead of the crack than in the wake, thus favoring growth

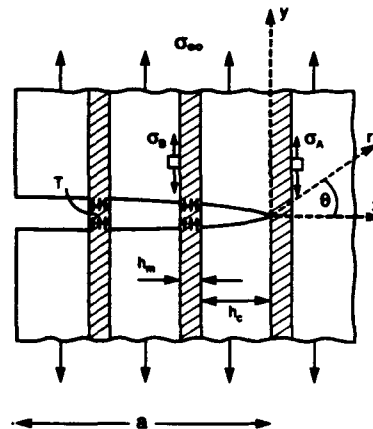


Fig. B1. Schematic of the crack configuration analyzed in Appendix B.

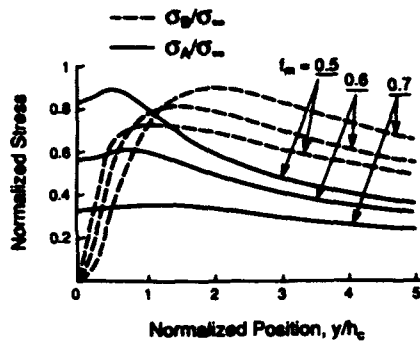


Fig. B2. Approximate analytical solutions for crack tip and crack wake stresses for the crack geometry shown in Fig. B1 with various volume fractions of metal,  $f_m$ , and with bridging tractions taken to be  $T = 1.5\sigma_m$ .

of a single crack. Conversely, at large  $f_m$ , the maximum stress is larger in the wake, leading to multiple cracking. The transition occurs at  $f_m \approx 0.6$ , for the particular value of  $T$  and the crack and layer geometries chosen here, for illustrative purposes.

## APPENDIX C

### Characteristic Ceramic Layer Strength

For a power law strength distribution in the brittle layers, the fraction,  $P$ , of flaws that can cause failure at stress  $S$  in a volume  $V$  is given by

$$P(V, S) = \frac{V}{V_0} (S/S_0)^m. \quad (C1)$$

At the point of crack saturation [1],  $S = S_c$ ,

$$P(V_c, S_c) = \frac{V_c}{V_0} (S_c/S_0)^m = 1 \quad (C2)$$

where  $V_c$  is the volume of material between the cracks. Using equation (12),  $V_c$  can be reexpressed as

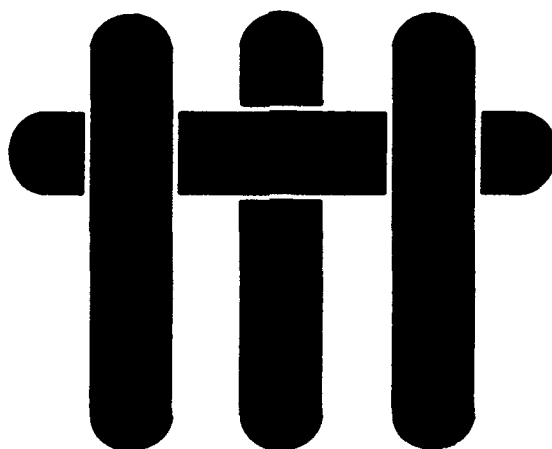
$$V_c = \frac{h_c^2 S_c w}{\lambda \tau}. \quad (C3)$$

Combining equations (C2) and (C3) yields

$$S_c = \left( \frac{\lambda \tau V_0 S_0^m}{h_c^2 w} \right)^{1/(m+1)}. \quad (C4)$$



# M A T E R I A L S



## **MECHANICAL PROPERTIES OF AN IN-SITU SYNTHESIZED Nb/Nb<sub>3</sub>Al LAYERED COMPOSITE**

by

Hengchu Cao, Jan P.A. Löfvander, A. G. Evans, R. Grant Rowe\* and D.W. Skelly

Materials Department  
College of Engineering  
University of California  
Santa Barbara, California 93106-5050

\*GE Corporate Research & Development  
General Electric Company  
Schenectady, NY 12309

## ABSTRACT

A layered metal/intermetallic, consisting of Nb and Nb<sub>3</sub>Al, has been synthesized using a high-rate magnetron sputtering technique. The microstructure and various mechanical properties have been explored. It is demonstrated that the Nb phase contributes substantially to the toughness, through plastic dissipation, combined with frictional sliding at contacting surfaces. However, the toughness is sub-optimal, because of the small layer thickness, which limits the width of the plastic zone. The tensile strength is also relatively low, because of growth defects. Some concepts for improving the strength and fracture resistance by tailoring the constituent and interface properties are suggested.

## 1. INTRODUCTION

High temperature intermetallic systems can exhibit high strength and creep resistance at temperatures above 1000°C.<sup>1</sup> However, these materials are often brittle at lower temperatures. This deficiency has inhibited their use in critical structural components. One approach that enhances the fracture resistance, while retaining high temperature strength, involves the incorporation of a refractory, ductile metal. For example, it has been demonstrated that, by incorporating niobium into TiAl, the fracture resistance could be enhanced by a factor of three.<sup>2-5</sup> Moreover, it now appears feasible to tailor the *overall* mechanical properties by using dual-phase systems. One dual-phase morphology that has demonstrated particular potential, consists of *alternating layers* of intermetallic and metal.<sup>6-8</sup> In this case, the fracture resistance exceeds that of the intermetallic, because ligaments of the ductile phase plastically stretch to failure during crack extension and thereby, dissipate energy.<sup>2-4, 7-10</sup> Moreover, the intermetallic is expected to provide good creep strength, by supporting the loads imposed at elevated temperature.<sup>11</sup> One potential problem is the sensitivity of such materials to fatigue.<sup>12</sup>

The present work describes the microstructure and mechanical properties of a layered material made by high-rate magnetron sputtering. Toughening and strengthening mechanisms responsible for the properties are explored using a micromechanics approach. Furthermore, ways for improving the mechanical performance of the composite through microstructure optimization are suggested.

## 2. SYNTHESIS

Vapor phase deposition by high rate magnetron sputtering<sup>13</sup> is a means for producing layered materials with low interstitial content. The method also provides the

freedom to independently control the ductile and intermetallic phase compositions, volume fractions and dimensions. A schematic of the physical set-up (Fig. 1)\* illustrates the two sputtering targets within a chamber, filled with argon. One target contains pure niobium, while the other comprises segments of aluminum inserted with niobium. The target composition may be adjusted by changing the relative width of the aluminum segments. A stainless steel substrate which traverses between the targets may be preheated, using a bias current, in order to control diffusion during deposition. A tri-layer (titanium-copper-titanium) release coating was deposited before sputtering. This procedure was used to deposit Nb/Nb<sub>3</sub>Al microlaminates onto polished stainless steel substrates.<sup>14</sup>

The Nb/Nb<sub>3</sub>Al system was chosen, after inspecting the phase diagram (Fig. 2), because the two phases are compatible<sup>15</sup> and have melting temperatures above 2000°C. The properties of these constituents are summarized in Table I. The equilibrium phase of Nb has a bcc unit cell with lattice constant,  $a = 0.33$  nm. The Nb<sub>3</sub>Al phase has the A15 (space group Pm $\bar{3}$ n) structure, in equilibrium, with lattice constant,  $a = 0.5183$  nm. However, Nb<sub>3</sub>Al has a tendency to form a metastable bcc structure if the atomic mobility is limited.

The level of oxygen contamination had to be carefully controlled because oxygen affects the ductility of the metal phase.<sup>16</sup> The oxygen content depends on the residual oxygen vapor pressure in the system (in the form of H<sub>2</sub>O and CO) as well as the rate of deposition. At the deposition rate chosen for this study (58 Å/s), an oxygen partial pressure  $< 5 \times 10^{-7}$  torr was required to ensure an oxygen content in the multilayers below the delectability level for Auger electron spectroscopy ( $< 0.5$  at. %).

---

\* An MRC 603 magnetron sputtering system, with Inset magnetron cathodes.

### 3. MICROSTRUCTURE

The composite consisted of 34 layers of Nb and 33 layers of Nb<sub>3</sub>Al, having a total thickness of 145  $\mu\text{m}$ . The microstructure of the as-deposited composite was examined by both scanning electron microscopy (SEM) and transmission electron microscopy (TEM). The SEM images were highlighted by using the back-scatter mode in order to enhance phase contrast (Fig. 3). In this manner, the thicknesses of the Nb and Nb<sub>3</sub>Al layers were found to be 1.6 and 2.4  $\mu\text{m}$ , respectively. The interface appeared convoluted, but continuous, without apparent interfacial porosity.\*

Electron transparent samples suitable for TEM examination were prepared by laminating several 3 mm wide layers of the composite in epoxy, as described elsewhere.<sup>16</sup> Standard dimpling and ion milling were used to produce specimens that were examined in a JEOL 200FX microscope operated at 200 kV equipped with a Link Analytical eXL EDS (energy dispersive X-ray) system. The TEM images revealed a columnar grain structure over the entire electron transparent region (Fig. 4). The interfaces consisted of well-defined facets (Fig. 5c), with facet planes being {110}, in the Nb, as well as the Nb<sub>3</sub>Al. Diffraction patterns along [011] (Fig. 5b) indicate that the Nb is in the equilibrium bcc state. However, the Nb<sub>3</sub>Al is completely disordered, consistent with the deposition temperature being substantially below the T<sub>0</sub> curve (Fig. 2). Moreover, the limited mobility of both Nb and Al atoms, at the deposition temperature, ensures relatively high stability of the metastable phase and is also consistent with the Nb layers having no detectable Al (Fig. 5c).

---

\* The voids observed in the Nb phases are caused by polishing because the Nb phase is much softer and prone to abrasion.

## 4. MECHANICAL BEHAVIOR

### 4.1 Specimen Preparation

For initial evaluation, flexural testing was performed, with the material still attached to the substrate. For this purpose, beams with nominal dimensions  $30 \times 1 \times 2.5$  mm were prepared from the panel by using a low-speed diamond saw. The side and top faces were polished to  $1 \mu\text{m}$  in order to reveal the microstructure and to facilitate observation of damage evolution during testing. The beams were tested in face and edge orientations (Fig. 6a). In the first, the layer planes were located on the tensile face of the beam. In this case, the material experiences a relatively uniform tensile stress, because of the small thickness ratio of the layered material to the substrate (Fig. 6b). In some of these specimens, a groove ( $\sim 10 \mu\text{m}$  deep) was introduced by sliding a Knoop indenter across the tensile face, subject to a load of 2N. In the second orientation (Fig. 6b), the layers were located on the side face. This test arrangement allowed crack extension to occur *stably*, due to the decreasing tensile strain, as the crack approaches the neutral axis.

Other test procedures required that the layered material be removed from the substrate. This was achieved by using nitric acid within an ultrasonic device to dissolve the buffer layer. Three types of tensile specimen were prepared (Fig. 6c). Standard dog-bone specimens were used to characterize the elastic properties and the fracture strength. Edge-notched and center-notched specimens were used to measure the fracture resistance properties, as well as to study the failure mechanisms. In all cases, in order to facilitate gripping, tabs were bonded to the specimen ends.

### 4.2 Results

Three-point flexure tests *with the substrate attached* were conducted *in situ* in the SEM, at low strain rates ( $\leq 10^{-4} \text{ s}^{-1}$ ). At various stress levels, the side faces were

comprehensively inspected. The load was then incrementally increased until failure occurred. Load/displacement curves indicated nonlinearity at  $\sim 350$  MPa, associated with the plastic yielding of the stainless steel substrate. The final rupture, which was unstable, coincided with failure of the layered material at  $\sim 370$  MPa, followed by decohesion of the layered material from the substrate. Similar tests on scratched beams gave identical load-deflection curves. Failure did not occur from the flaw introduced by scratching. Tension tests (Table II) gave strengths significantly lower than those obtained in flexure.

In the second flexural configuration, stable crack extension was evident on the bevelled sections (Fig. 7a). Crack propagation occurred predominantly along the grain boundaries in both phases, resulting in an irregular crack path. Crack surface contacts were evident at some locations (Fig. 7b).

Tension testing on notched specimens was produced by introducing a fatigue precrack. This was achieved by subjecting the specimen to a cyclic load with nominal stress intensity range,  $\Delta K_I = 5 \text{ MPa}\sqrt{\text{m}}$ , and load ratio,  $R = 0.1$ . After a precrack had extended  $\sim 0.5$  mm, the specimen was subjected to a monotonically increasing load and crack growth monitored with an optical microscope. Initial crack extension was found to be stable and a resistance curve recorded for the edge orientation (Fig. 8).

In order to estimate the flow strength of the Nb in the layered materials,  $\sigma_0$ , a Nb layer  $\sim 25 \mu\text{m}$  thick was deposited onto a substrate with exactly the same conditions used to prepare the laminate. Microhardness tests were performed with indentation loads ranging between 20 and 50 mN. These loads ensured that the penetration depth of the indenter was small compared with the layer thickness. These measurements gave a hardness  $H_v \sim 590$  MPa, indicative of a flow strength,<sup>17</sup>  $\sigma_0 \sim H_v/3 \sim 200$  MPa.

## 5. POST-TEST OBSERVATIONS

A study of the fracture surfaces using scanning electron microscopy revealed large processing flaws at the failure origins. These had conical morphology and were  $\sim 200 \mu\text{m}$  in diameter (Fig. 9). Higher resolution images indicated brittle fracture in the  $\text{Nb}_3\text{Al}$  phase and ductile rupture of the Nb (Fig. 10). In the  $\text{Nb}_3\text{Al}$ , crack growth occurred along the columnar grain boundaries, because these boundaries contain voids, which diminish their crack growth resistance. Moreover, the disordered state of the  $\text{Nb}_3\text{Al}$  probably results in enhanced brittleness.

Ductile failure of the Nb involved microvoid coalescence. These voids had a morphological connection with the columnar grain boundaries. Consequently, the plastic stretch depended on the specimen orientation. When the crack extended normal to the grain growth direction, the plastic stretch was relatively large, with  $u_c \sim 1.3 \mu\text{m}$ . Conversely, when the crack extended along the grain direction, the Nb failed with reduced stretch,  $u_c \sim 0.6 \mu\text{m}$ .

## 6. ANALYSIS

### 6.1 Crack Growth Resistance

The preceding observations suggest the mechanisms of dissipation in these layered materials, upon crack growth. One involves the plastic stretching of the ductile Nb phase (Fig. 10). The other relates to friction at contacts along the crack surface (Fig. 7). Contributions to the crack growth resistance from both mechanisms will be considered. The contribution from plastic stretching of the metal layers is known to occur in accordance with a resistance curve. For a well-bonded interface, representative of the present system (Fig. 10), the resistance has the following characteristics. The steady-state toughening is; 2-4,7-10



$$\Delta\Gamma_c = \chi f_m \sigma_o t_m \quad (1)$$

where  $\sigma_o$  is the uniaxial yield strength,  $t_m$  the ductile layer thickness,  $f_m$  the metal concentration and  $\chi$  the work of rupture coefficient. For a well-bonded interface,  $\chi = 2.7$ .<sup>4,7,10</sup> This toughening level arises after a crack extension<sup>10</sup>

$$L_c = 0.03\pi u_c E/\sigma_o \quad (2)$$

Such toughening superposes onto an initiation toughness,  $\Gamma_o$ .<sup>3,6,8</sup> The magnitude of  $\Gamma_o$  depends on the crack orientation.<sup>3</sup> For the edge orientation, the toughness of the intermetallic dictates  $\Gamma_o$ . For the face orientation,  $\Gamma_o$  is larger.<sup>6,8</sup> It is assumed that Nb<sub>3</sub>Al has a toughness similar to other brittle aluminides<sup>3,8</sup> (Table I). Consequently, in the edge orientation, the resistance behavior for the layered material can be predicted from Eqns. (1) and (2). For this purpose,  $u_c$  is given by the experimental measurements and  $\sigma_o$  inferred from the hardness measurements. The simulated resistance curves (Fig. 8) are found to be consistent with the experimental data, for crack extensions up to ~ 100  $\mu\text{m}$ . The subsequently, continually rising, portion of the resistance curve reflects the tractions occurring at crack face contacts<sup>19</sup> (Fig. 7). These occur at larger crack extensions and operate over a substantial spatial range.

## 6.2 Strengths

By using the measured fracture resistance (Fig. 8) in conjunction with an initial flaw size related to the growth faults (Fig. 9), a tensile strength may be predicted using the formulae summarized on Table III. For a flaw size,  $a_o \cong 100 \mu\text{m}$ , the predicted strength,  $S = 600 \text{ MPa}$ . This is appreciably larger than the measured value (Table II). This discrepancy suggests either that there are residual tensile stresses induced around

the growth flaws or that the initial crack growth resistance of the material around these flaws is less than that found by introducing a precrack. Further study would be needed to distinguish these possibilities.

## **7. CONCLUDING REMARKS**

The mechanical properties of the present material are limited by growth flaws. The relatively small length scale, which controls plastic dissipation during crack growth, may also limit the fracture resistance. Both phenomena can be addressed by controlling the deposition and by changing the constituent characteristics. Enhanced plastic dissipation could be accomplished in several ways. One involves the use of periodic, thick ( $\sim 10 \mu\text{m}$ ) Nb layers interspersed among the  $\sim 1 \mu\text{m}$  thick layers. The dissipation within this thicker layer should scale with the increased layer thickness (Eqn. 1). Additional non-linear mechanisms may also be found. Alternately, thin ( $\sim 0.1 \mu\text{m}$ ) interphases might be introduced that induce debonding, in order to spread the dissipation.<sup>3,4,8</sup> Alloying of the Nb to increase its yield strength without degrading its ductility would also be beneficial to the toughness. Experimental study of these concepts is in progress.

## **ACKNOWLEDGEMENTS**

Financial support for this work is provided by Wright Research and Development Center, under contract number 33615-91-C-5613. Work of JL and AGE is supported by ONR Contract No. N00014-93-I-0213.

**TABLE I**  
**Properties of Constituents**

Material Properties	Nb	Nb <sub>3</sub> Al
Young's modulus (in-plane), E (GPa)	105	135
Poisson's ratio, $\nu$	0.4	0.25
Yield strength, $\sigma_0$ (MPa)	195	650
Fracture toughness, $K_{IC}$ (MPa $\sqrt{m}$ )	—	~ 4 <sup>‡</sup>
Melting temperature, $T_m$ (°C)	2469	1940
Thermal expansion coefficient, $\alpha$ (°C <sup>-1</sup> )	$7 \times 10^{-6}$	
Crystal structure	bcc (A2)	A15 <sup>**</sup>
Lattice constant, a (nm)	0.33002	0.5183

<sup>‡</sup> Typical value for brittle intermetallics.<sup>8</sup>

<sup>\*\*</sup> Nb<sub>3</sub>Al has an A15 cubic structure as its equilibrium phase. However, Nb<sub>3</sub>Al can also be in a metastable phase, having a partially ordered bcc structure,<sup>14</sup> as is observed in this study.

**TABLE II****Strength Properties of Composites**

<b>Material Properties</b>	<b>Tensile</b>	<b>Flexure</b>
Young's modulus (in-plane), E (GPa)	126	124
Poisson's ratio, $\nu$	0.27	—
Ultimate strength, S (MPa)	250	350

**TABLE III**

**Formulae Needed to Predict Strength**

$$K = \sqrt{EG} = (2/\sqrt{\pi}) \sigma \sqrt{a_0 + \Delta a} \quad (1)$$

$$K = K_R = \sqrt{E\Gamma_R} \quad (2)$$

$$dK/da = dK_R/d\Delta a \quad (3)$$

$$a = a_0 + \Delta a \quad (4)$$

## REFERENCES

- [1] R.L. Fleischer, "Mechanical Properties Of Diverse High Temperature Compounds—Thermal Variation Of Microhardness and Crack Formation," *Mat. Res. Soc. Symp. Proc.*, **133**, 305–10 (1989).
- [2] H.E. Dève, A.G. Evans, G.R. Odette, R. Mehrabian, M.L. Emiliani and R.J. Hecht, "Ductile Reinforcement Toughening and Gamma-TiAl: Effects of Debonding and Ductility," *Acta Metall. Mater.*, **38**, 1491–502 (1990).
- [3] G.R. Odette, B.L. Chao, J.W. Sheckherd and G.E. Lucas, *Acta Metall. Mater.*, **40** (1992) 2381.
- [4] H.C. Cao, B.J. Dalgleish, H.E. Dève, C.K. Elliot, A.G. Evans, R. Mehrabian and G.R. Odette, "A Test Procedure for Characterizing the Toughening of Brittle Intermetallics by Ductile Reinforcements," *Acta Metall.*, **37** [11] 2969–77 (1989).
- [5] D.L. Anton and D.M. Shah, "Ductile Phase Toughening of Brittle Intermetallics," *Mat. Res. Soc. Symp. Proc.*, **194**, 45–52 (1990).
- [6] H.C. Cao and A.G. Evans, "On Crack Extension in Ductile/Brittle Laminates," *Acta Metall. Mater.*, **39**, 2997–3005 (1991).
- [7] M. Bannister and M.F. Ashby, "The Deformation and Fracture of Constrained Metal Sheets," *Acta Metall. Mater.*, **39**, 2575–82 (1991).
- [8] F.E. Heredia, M.Y. He, G.E. Lucas, A.G. Evans and D. Konitser, *Acta Metall. Mater.*, **41** (1993) 505.
- [9] L.S. Sigl, P.A. Mataga, B.J. Dalgleish, R.M. McMeeking and A.G. Evans, "On the Toughness of Brittle Materials Reinforced with a Ductile Phase," *Acta Metall. Mater.*, **36**, 945–53 (1988).
- [10] G. Bao and C. Hui, *Intl. Jnl. Solids Structures*, **26**, 631 (1990).
- [11] P.L. Martin, D.H. Carter, R.M. Aikin and L. Christodoulou, *Creep and Fracture of Engineering Material* (ed. B. Wilshire and R.W. Evans) Institute of Metals, London (1990) pp. 265–76.
- [12] K.T. Rao, R.O. Ritchie and G.R. Odette, *Acta Metall. Mater.*, **40** (1992) 353.
- [13] R.S. Bhattacharya, A.K. Rai and M.G. Mendiratta, "Tailored Microstructures of Niobium-Niobium Silicides by Physical Vapor Deposition," *Mat. Res. Soc. Symp. Proc.*, **194**, 71–78 (1990).
- [14] R.G. Rowe and D.W. Skelly, "The Synthesis and Evaluation of Nb<sub>3</sub>Al/Nb Laminated Composites," *Mat. Res. Soc. Proc.*, Vol. 273 (1992) in press.

- [15] D.L. Anton and D.M. Shah, "Ductile Phase Toughening Of Brittle Intermetallics," *MRS Symp. Proc.* 194, 45-52 (1990).
- [16] H. Conrad, "Effect of Interstitial Solutes on the Strength and Ductility of Titanium," *Progress in Materials Science*, 26, 123-403 (1981).
- [17] M. De Graef, M.R. Turner, B.J. Dalgleish and A.G. Evans, *Acta Metall. Mater.*, 40 (1992) S333.
- [18] R.F. Bishop, R. Hill and N.F. Mott, *Proc. Phys. Soc.*, 42 (1945) 147.
- [19] G. Vekinis, P.W.R. Beaumont and M.F. Ashby, *Acta Metall. Mater.*, 38 (1990) 1151.

## FIGURE CAPTIONS

- Fig. 1. Schematic of the magnetron sputtering apparatus.
- Fig. 2. Phase diagram for the Nb-Al system.
- Fig. 3. SEM back-scatter cross-sectional micrograph reveals the layered microstructure, Nb/Nb<sub>3</sub>Al.
- Fig. 4. Low magnification TEM micrograph shows the columnar grain structure continually grown through both the Nb and Nb<sub>3</sub>Al layers (interface indicated by the arrows).
- Fig. 5. a) Bright field image indicates epitaxial grain growth across the metal/intermetallic interface.  
b) Diffraction patterns of two areas indicated on the TEM picture.  
c) EDS spectra of the two areas adjacent to the interface.
- Fig. 6. a) Typical loading modes.  
b) Three-point flexure specimen configurations.  
c) Tensile specimen.
- Fig. 7 a) Crack path after stable crack extension.  
b) Crack surface contact.
- Fig. 8. Fracture resistance obtained using a center-notch tensile specimen. Also shown are the resistance curves predicted for plastic stretching of the Nb.
- Fig. 9. Flaws revealed on the fracture surface by SEM.
- Fig. 10. a) SEM of a typical fracture surface after quasi-static fracture (arrow indicates crack propagation direction).  
b) Failure mechanisms in Nb ductile layer showing ductile tearing and ductile dimples in the Nb phase.  
c) Reduced plastic stretch in Nb layers when grain boundary porosity is present.



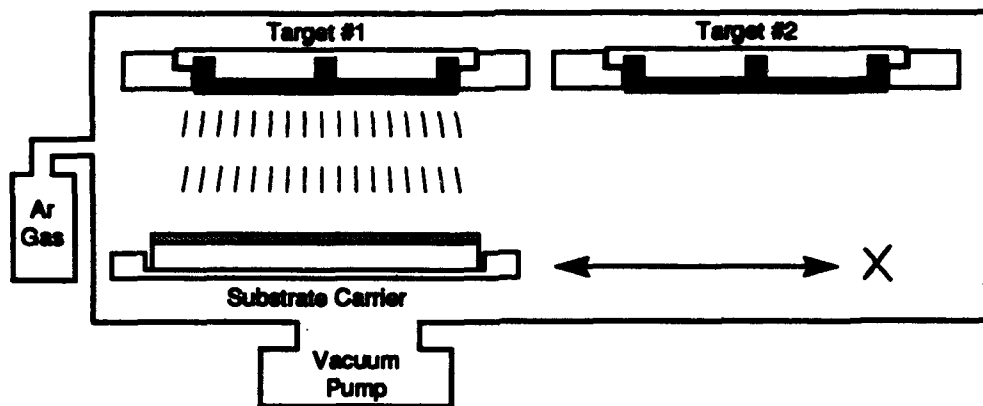


Figure 1. Schematic of system for synthesizing laminated metal - intermetallic composites by alternate sputtering from two targets.

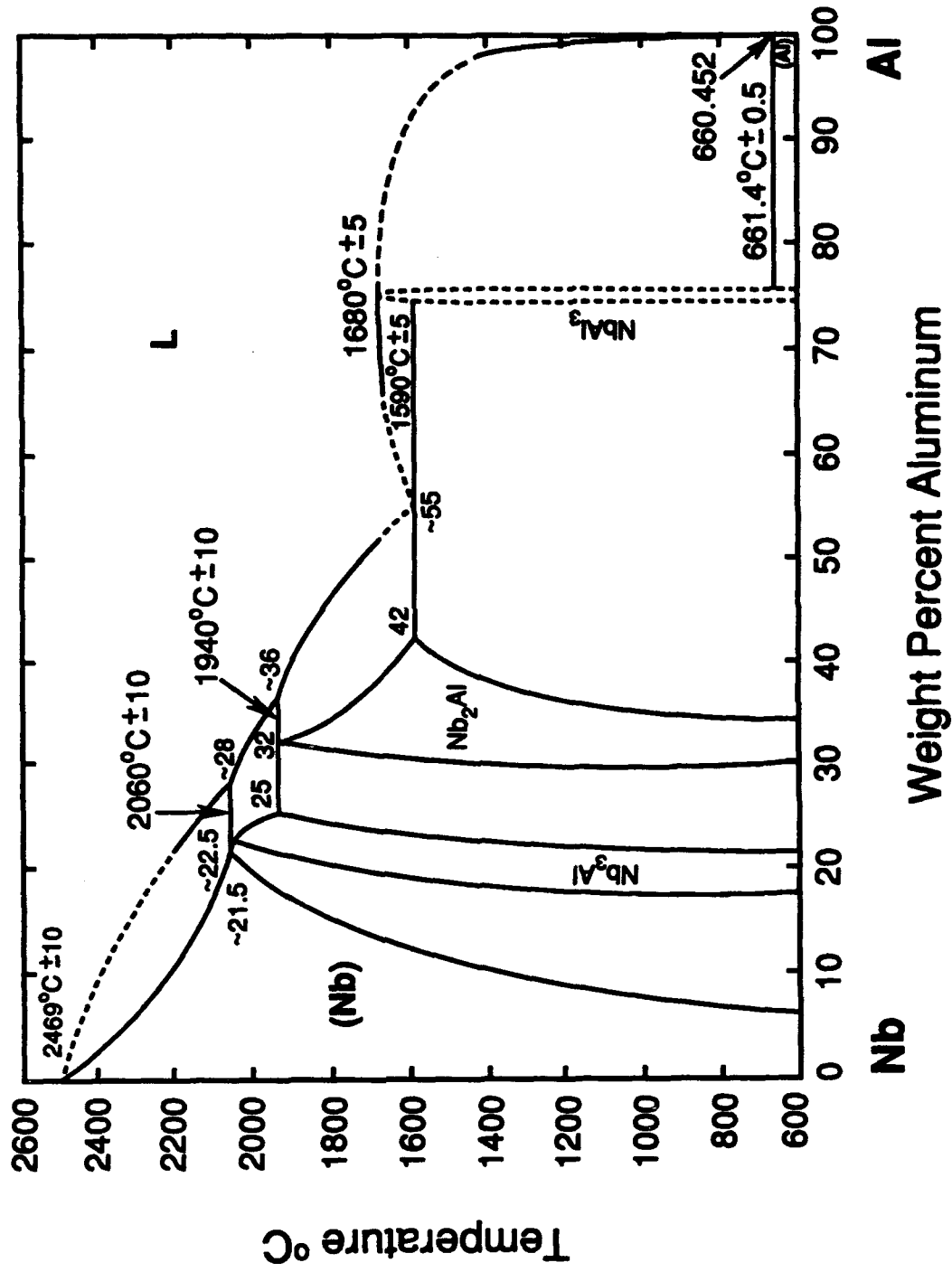


Figure 2. Phase diagram for the Nb-Al system.

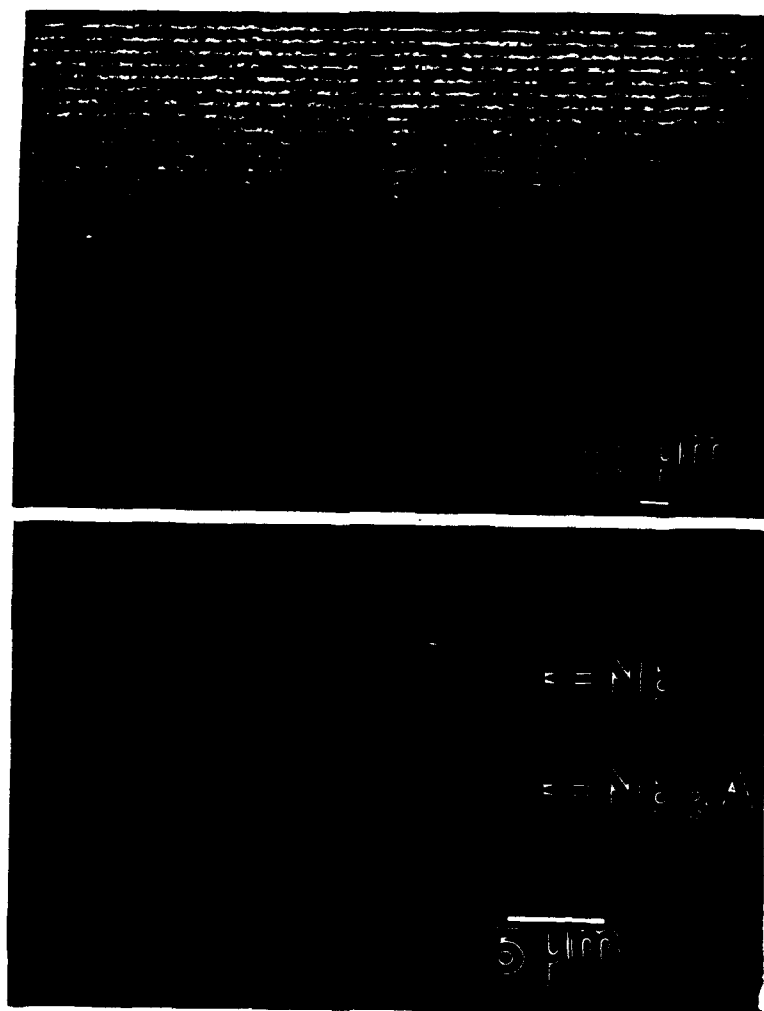
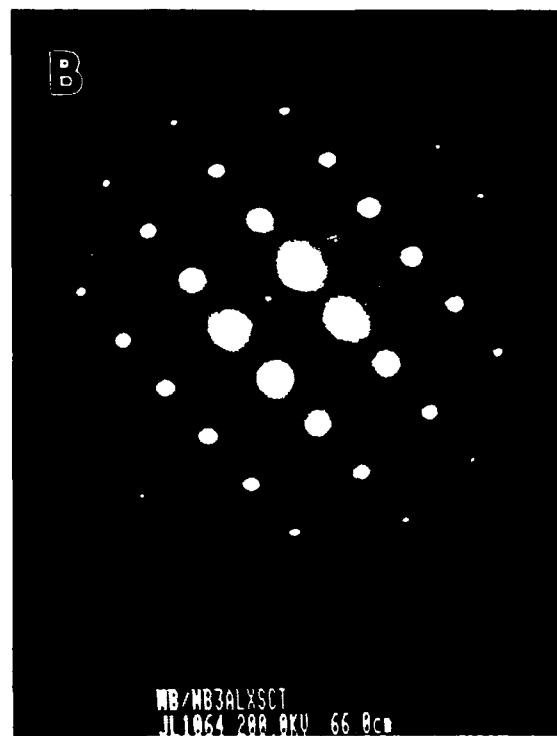
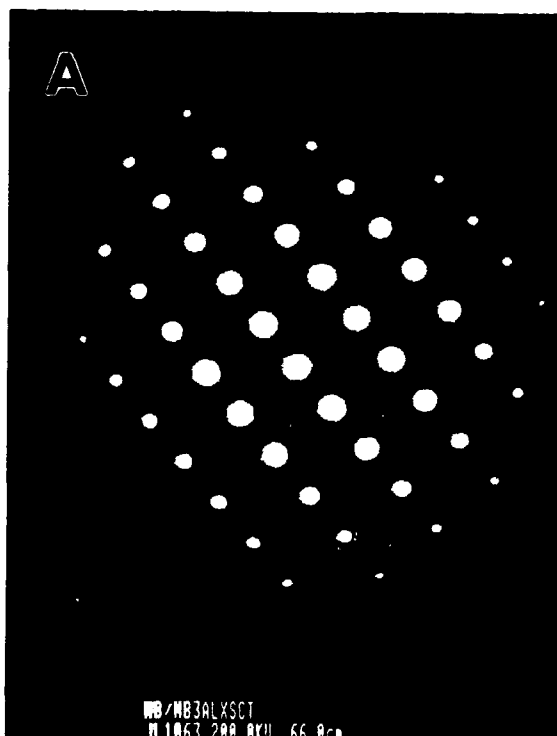
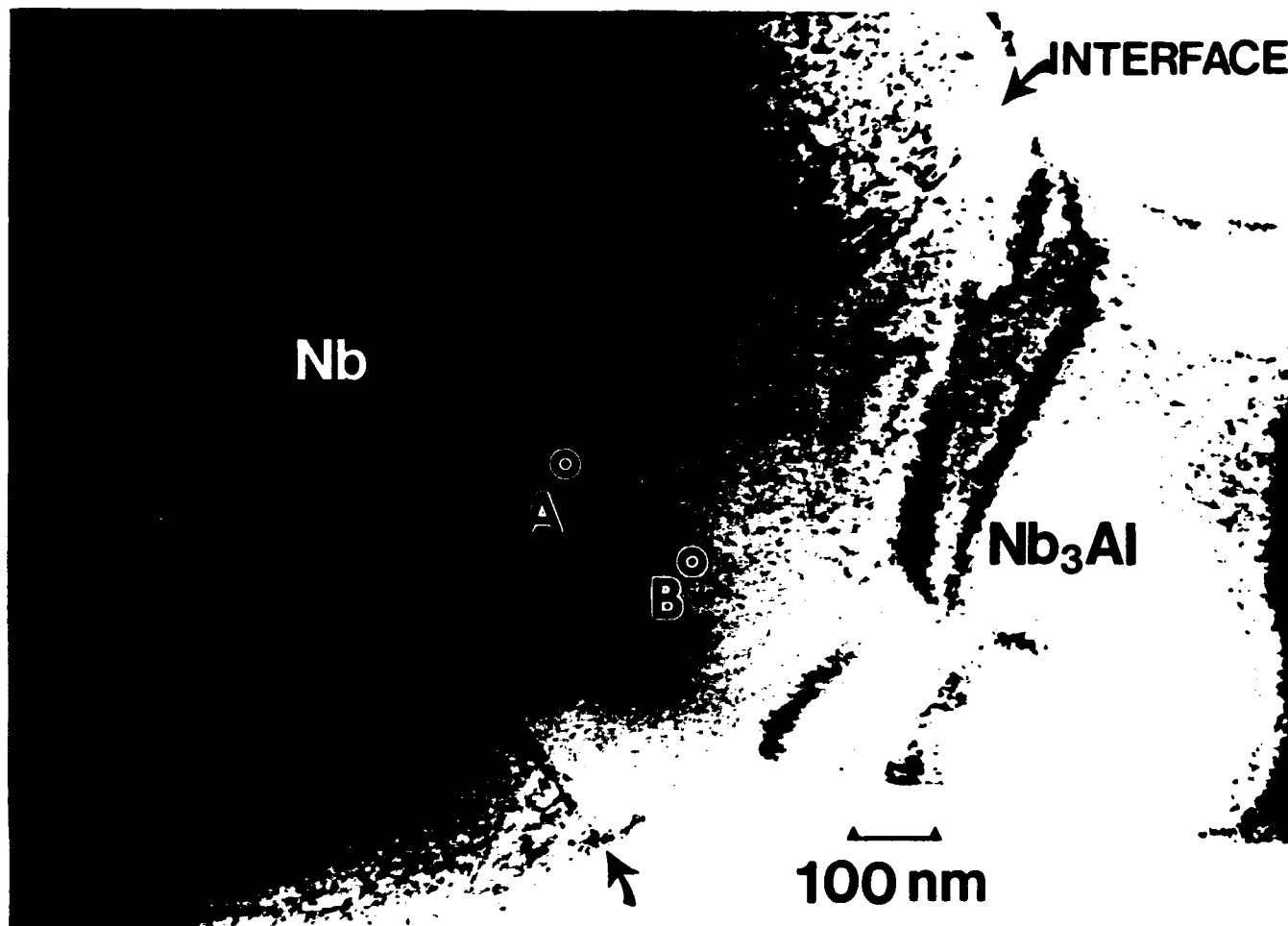


Figure 3. SEM back-scatter cross-sectional micrograph reveals the layered microstructure, Nb/Nb<sub>3</sub>Al.



Figure 4. Low magnification TEM micrograph shows the columnar grain structure continually grown through both the Nb and Nb<sub>3</sub>Al layers (interface indicated by the arrows).

Figure 5. a) Bright field image indicates epitaxial grain growth across the metal/intermetallic interface.  
b) Diffraction patterns of two areas indicated on the TEM picture.



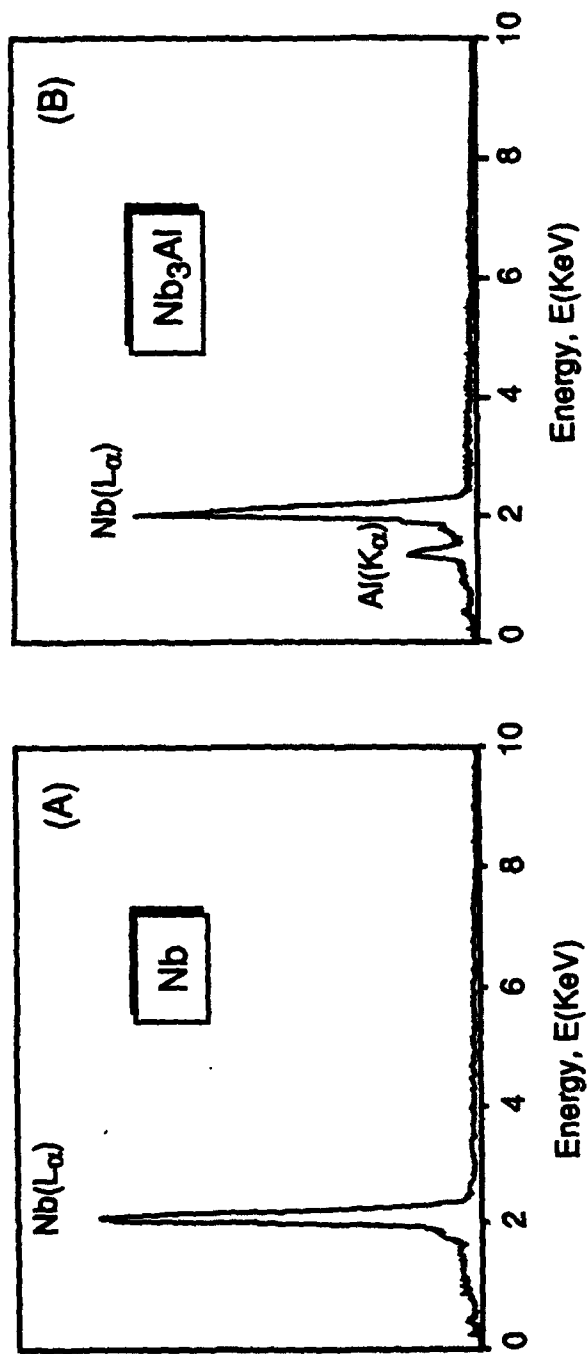
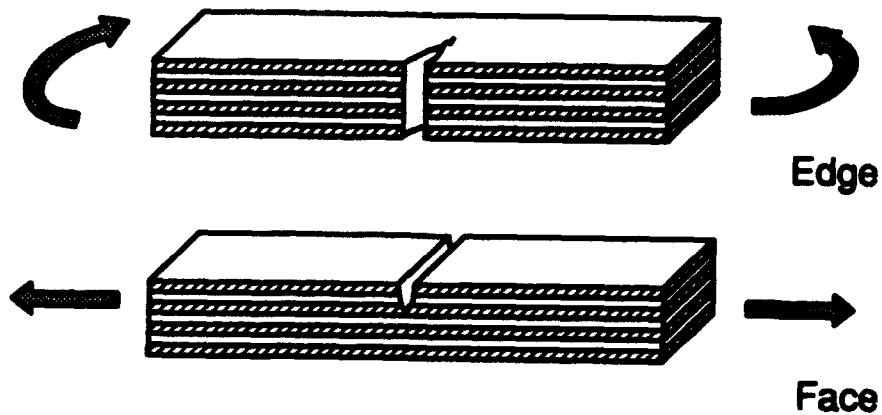
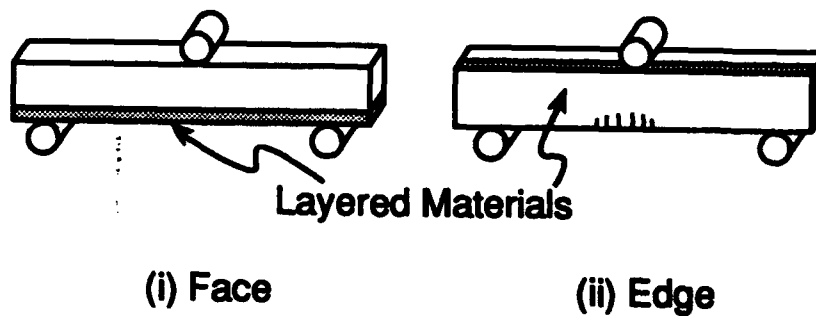


Figure 5 c) EDS spectra of the two areas adjacent to the interface

a) Loading Modes



b) Flexure



c) Tension

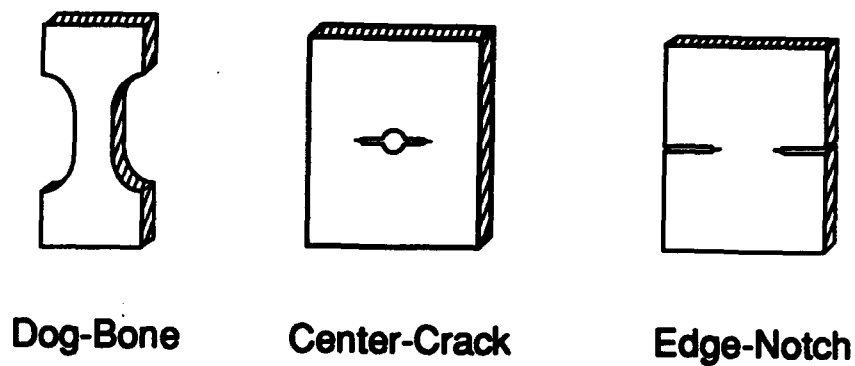


Figure 6. a) Typical loading modes.  
b) Three-point flexure specimen configurations.  
c) Tensile specimen.

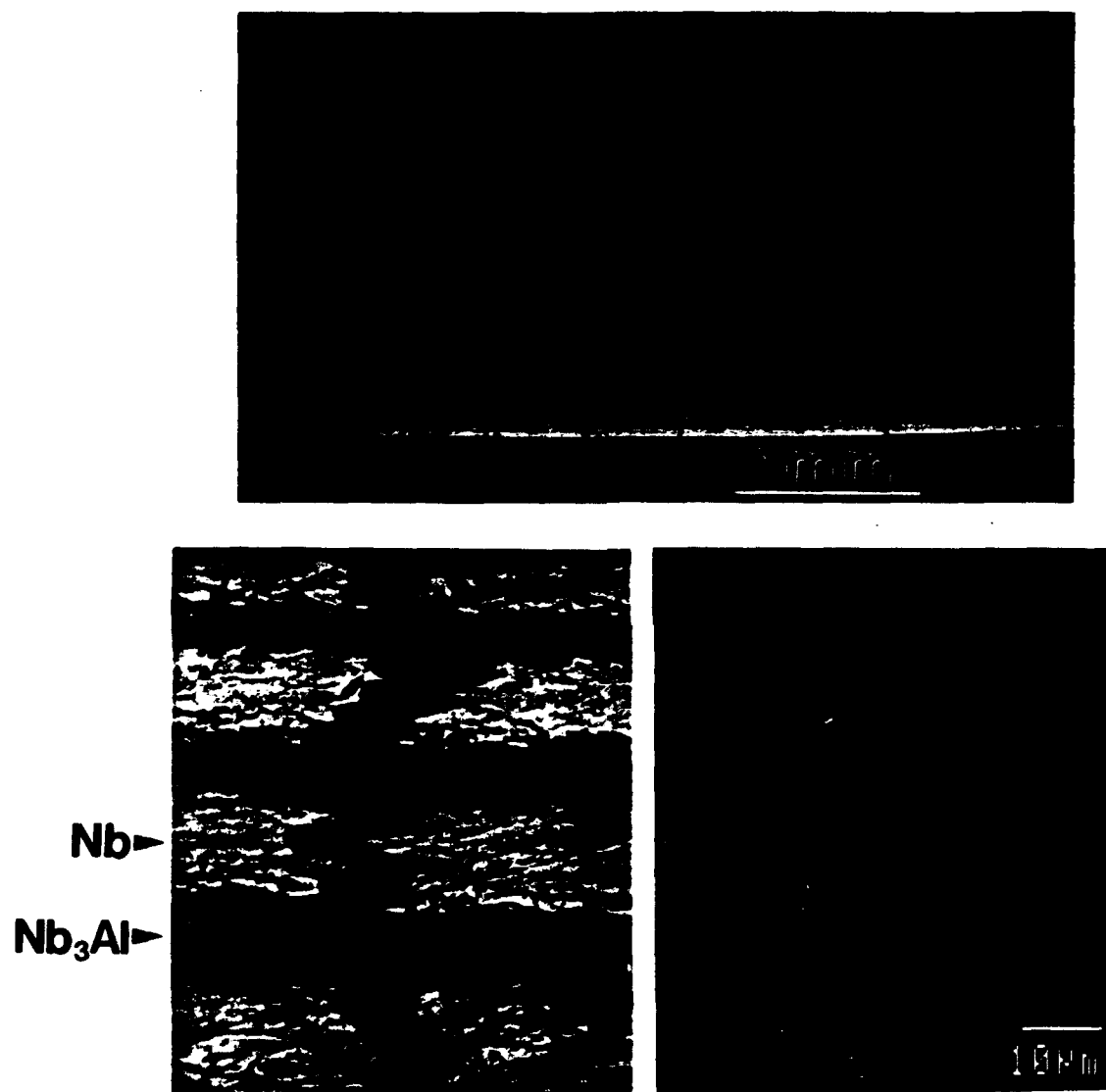


Figure 7. a) Crack path after stable crack extension.  
b) Crack surface contact.



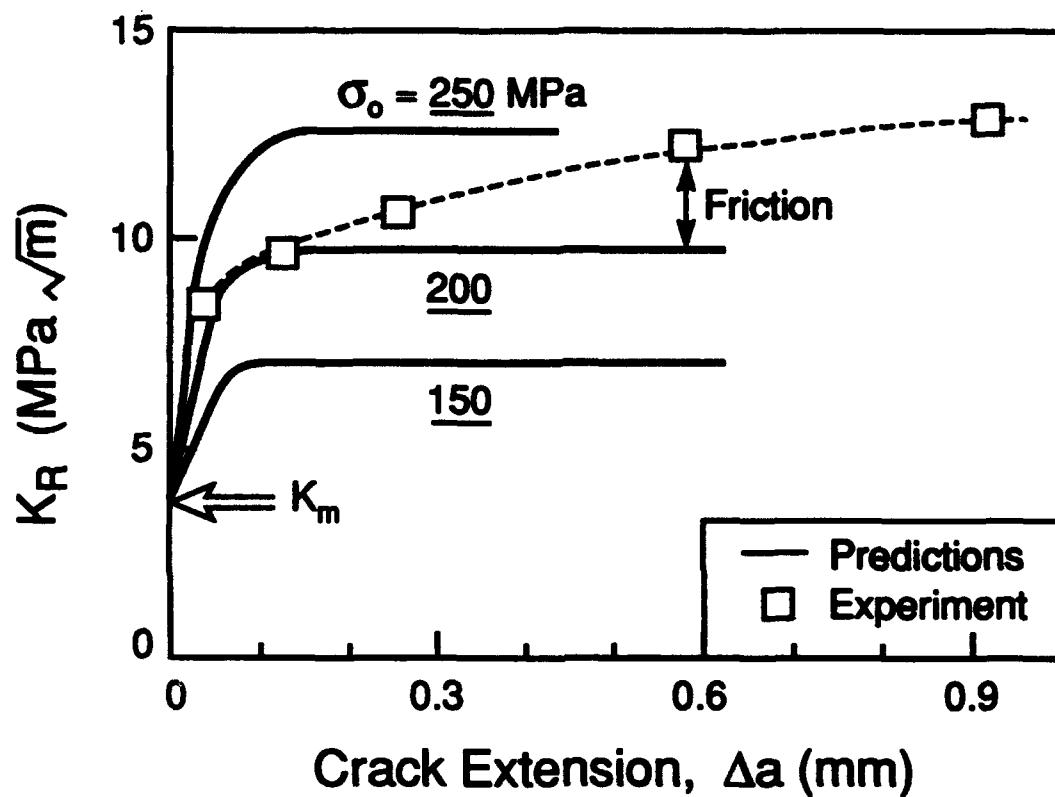


Figure 8. Fracture resistance obtained using a center-notch tensile specimen. Also shown are the resistance curves predicted for plastic stretching of the Nb.

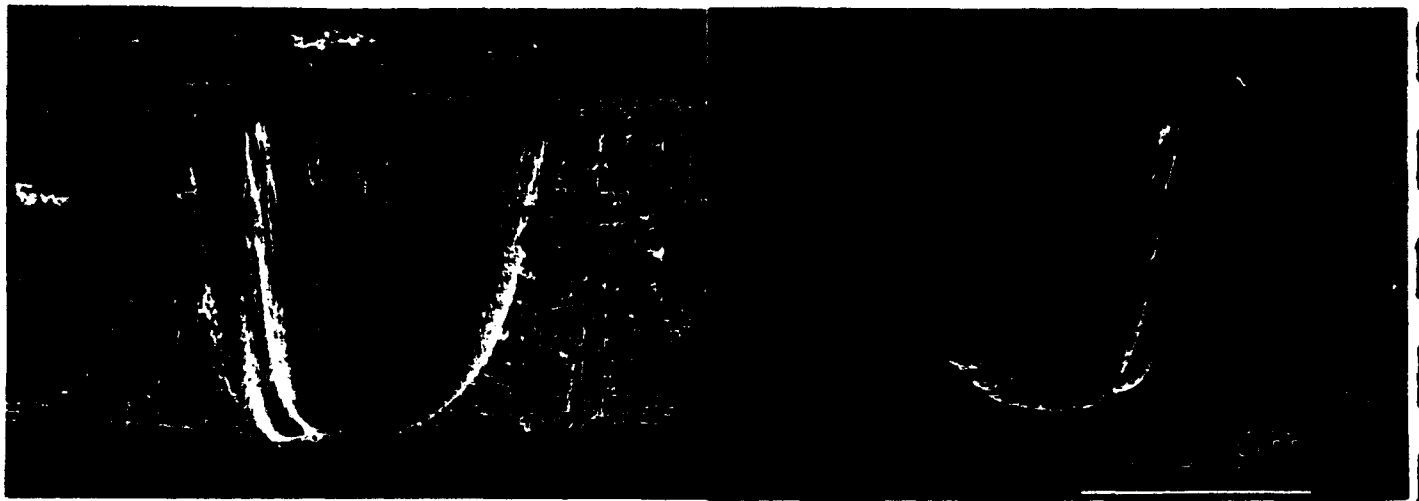


Figure 9. Flaws revealed on the fracture surface by SEM.

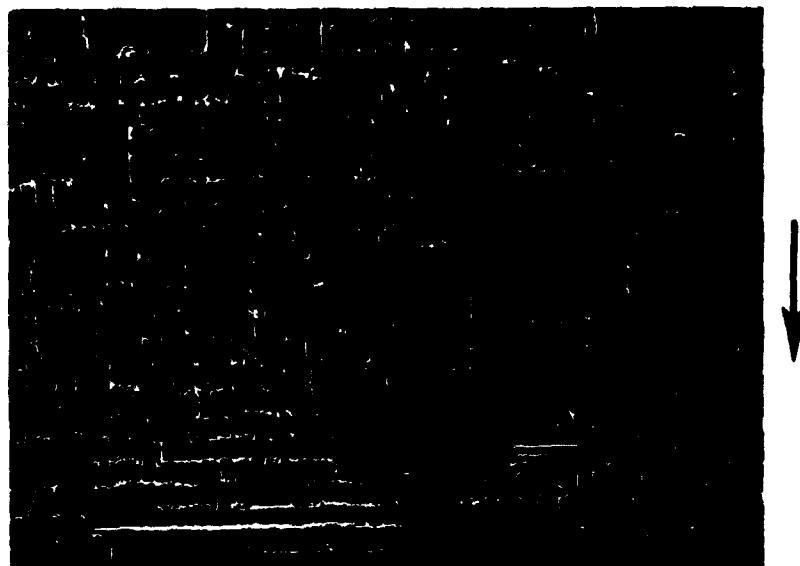
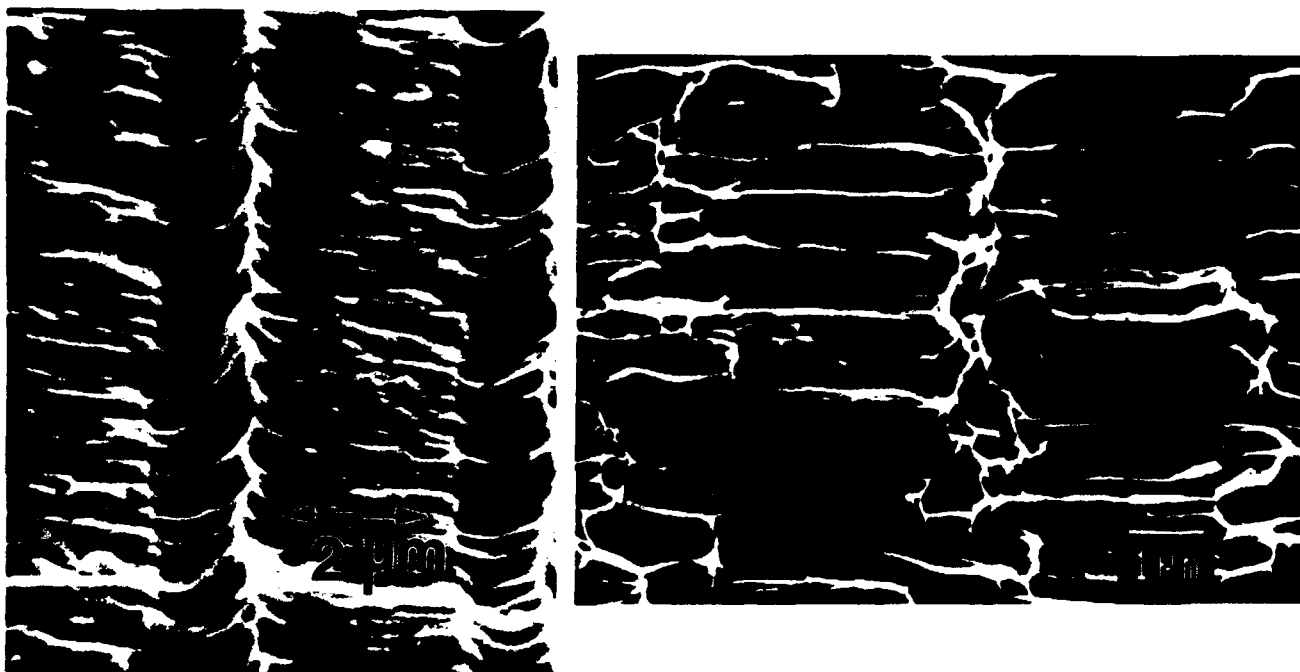
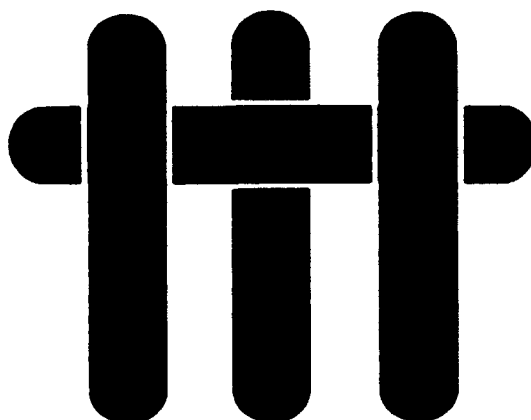


Figure 10. a) SEM of a typical fracture surface after quasi-static fracture (arrow indicates crack propagation direction).



**Figure 10**    **b) Failure mechanisms in Nb ductile layer showing ductile tearing and ductile dimples in the Nb phase.**  
                 **c) Reduced plastic stretch in Nb layers when grain boundary porosity is present.**

# M A T E R I A L S



## **A NEW PROCEDURE FOR MEASURING THE DECOHESION ENERGY FOR THIN DUCTILE FILMS ON SUBSTRATES**

by

A. Bagchi, G.E. Lucas, Z. Suo and A.G. Evans

Materials Department  
College of Engineering  
University of California  
Santa Barbara, California 93106-5050

## ABSTRACT

A novel testing technique has been developed capable of measuring the interfacial fracture resistance,  $\Gamma_i$ , of thin ductile films on substrates. In this technique, the thin film on the substrate is stressed by depositing onto the film a second superlayer of material, having a large intrinsic stress, such as Cr. Subsequent processing defines a pre-crack at the interface between the film and the substrate. The strain energy available for driving the debond crack is modulated by varying the thickness of the Cr superlayer. Spontaneous decohesion occurs for superlayers exceeding a critical thickness. The latter is used to obtain  $\Gamma_i$  from elasticity solutions for residually stressed thin films. The technique has been demonstrated for Cu thin films on silica substrates.

## 1. INTRODUCTION

The decohesion of interfaces between metals and non-metals is a critically important technological issue.<sup>1,2</sup> Many of the basic phenomena have been identified, particularly the role of the interface debond energy,  $\Gamma_i$ , and its dependence on the loading mixity,  $\psi$  (Fig. 1).<sup>3,4</sup> The latter is a measure of the relative shear to tensile opening of the interface crack surfaces near the tip. Methods for measuring  $\Gamma_i$  have also been devised and calibrated (Fig. 2).<sup>4-7</sup> However, these methods typically require specimens made by using a high homologous temperature ( $T/T_m$ ) processing step, such as the diffusion bonding of sandwich specimens, where  $T$  and  $T_m$  denote the processing temperature and the metal melting point respectively (Fig. 2). Decohesion energy measurement methods for interfaces that have only experienced low temperature upon fabrication are subject to ambiguity in interpretation. For example, in peel tests, there is a complex convolution of the plastic dissipation associated with film deformation and the actual decohesion energy for the interface,  $\Gamma_i$ .<sup>7</sup> Moreover, the mode mixity is not representative of that for most situations of practical concern, such as thin film decohesion.

The present article addresses several of the current deficiencies by devising a new test that has the following attributes. The method can be used for ductile thin films deposited onto substrates at low  $T/T_m$ . It has a mode mixity typical of that associated with thin film decohesion ( $\psi \approx 50^\circ$ ). The procedure can be implemented in a conventional microelectronics fabrication facility.

Interface decohesion occurs subject to several dissipation mechanisms.<sup>8-10</sup> The fundamental mechanism involves the work of adhesion,  $W_{ad}$ , which represents the basic separation energy for the bonds across the interface. In general, plastic dissipation  $W_{pl}$  also occurs within a plastic zone in the metal, as the decohesion extends along the interface (Fig. 1). This contribution scales with  $W_{ad}$ .<sup>9,10</sup> It also varies with crack

extention,  $\Delta a$ , leading to a resistance curve.<sup>10</sup> This curve, in turn, depends on the ratio of the peak decohesion stress  $\hat{\sigma}$  to the yield strength of the metal,  $\sigma_0$  (Fig. 3). Moreover,  $W_{pl}$  may increase as the film thickness becomes larger and as the mode mixity angle increases (Fig. 1). In some cases, when the interface is non-planar, frictional effects can also contribute to  $\Gamma_i$ .<sup>3</sup> The new test method has been devised with the intent of systematically exploring these effects for metal thin films on non-metallic substrates.

## 2. SOME BACKGROUND MECHANICS

The relevant mechanics of thin film decohesion considers a thin film subject to residual tension,  $\sigma_f$ , on a thick substrate (Fig. 4). The energy release rate associated with an interface decohesion, originating from an edge (or discontinuity) attains a steady-state value,  $G_{ss}$ , provided that the decohesion length,  $a_0$ , exceeds the film thickness. Moreover, since all of the stress in the film above the decohesion is released, the non-dimensional energy release rate for a thin strip is<sup>3,12</sup>

$$G_{ss} E_f / \sigma_f^2 h_f = 1/2 \quad (1)$$

where  $E_f$  is the Young's modulus for the film and  $h_f$  is the film thickness. The corresponding mode mixity is,  $\psi = 52^\circ$ . The thin film test method should duplicate this mode mixity. For a wide strip (width  $w > h_f$ ), the residual stresses are biaxial and the revised steady-state energy release rate is<sup>3</sup>

$$G_{ss} E_f / \sigma_f^2 h_f = 1 - \nu_f \quad (2)$$



where  $\nu_f$  is the Poisson's ratio of the film. At smaller decohesion lengths ( $a_0 < h_f$ ), the energy release rates depend on the details of the edge.<sup>3,12</sup> *The preferred test method should avoid these edge problems by only using decohesion precracks within the steady-state range.*

For a bilayer film, interface decohesion leads to bending, whereupon some energy is stored in the film above the decohesion. Consequently, the steady-state energy release rate is reduced. The new value, as derived in the Appendix, is

$$G_{ss} = \sum_i \frac{\sigma_i^2 h_i}{E_i} - \sum_i \frac{1}{E_i} \left[ \frac{P}{h_i} + \frac{12M_i}{h_i^3} \right] \quad (3)$$

where  $i = 1,2$  refers to the two materials in the bilayer. The load  $P$  associated with the residual tension  $\sigma_i$  in each layer (Fig. 4) can be expressed in terms of the curvature of the decohered bilayer,  $\kappa$ , the film thickness,  $h_i$ , and the biaxial elastic moduli,  $E_i' = E_i / (1 - \nu_i)$ , as<sup>13</sup>

$$P = \left[ \frac{E_1' h_1^3 + E_2' h_2^3}{6(h_1 + h_2)} \right] \kappa \quad (4)$$

with  $\kappa$  given by

$$\kappa = \frac{6(h_1 + h_2)(\epsilon_1 - \epsilon_2)}{\left[ h_1^2 + E_2' h_2^3 / E_1' h_1 + E_1' h_1^3 / E_2' h_2 + h_2^2 + 3(h_1 + h_2)^2 \right]} \quad (5)$$

where,  $\epsilon_i = \sigma_i / E_i'$ . The bending moment,  $M_i$  (Fig. 4), is given by

$$M_i = E_i' I_i \kappa \quad (6)$$

where  $I_i$  is the moment of inertia,  $I_i = h_i^3 / 12$ .

### 3. THE METHOD

A key consideration for development of a method concerns the mode mixity,  $\psi$ . In order to maintain  $\psi$  in the requisite range, there are few options for loading the system. Among these, the only approach that appears to be straightforward involves the use of a *residual stress* which essentially duplicates the problem of interest. However, for typical thin films ( $h_f < 1 \mu\text{m}$ ), and representative residual stress levels ( $\sigma_f^R < 100\text{MPa}$ ), the residual stress induced energy release rate is small (Eqn. 1), of the order,  $G_{ss} \approx 0.1 \text{ Jm}^{-2}$ . Most interfaces with practical interest would have a debond energy substantially larger than this.<sup>8</sup> Consequently, decohesion would not be induced. The preferred test method must identify a procedure that substantially *increases*  $G_{ss}$ , without changing  $\psi$ , while also preserving the structure and microstructure of the interface.

A method that increases the energy release rate, at essentially constant  $\psi$ , involves deposition of an *additional material layer* onto the film. This *superlayer* increases the total film thickness and also elevates the residual stress without changing the interface. In order to accomplish this, the additional layer must be deposited in accordance with the following three characteristics. Deposition must be conducted at ambient temperature. The layer must not react with the existing film. The layer must have a large residual tension, upon deposition. A Cr film, deposited by electron beam evaporation, meets all three criteria.<sup>11</sup>

The new test method has the following three features. (i) A decohesion precrack is created, with length  $a_0 > h_f$ . (ii) The film is patterned to form narrow strips. (iii) The Cr film thickness is varied in order to produce a range of energy release rates. In order to provide these features, a thin strip of carbon is first deposited. This layer is the source of the interface precrack (Fig. 5). The film of interest is then deposited. Subsequently, a Cr layer with the requisite thickness is deposited onto the film. Thereafter, the bilayer is

patterned to form strips orthogonal to the carbon lines. Finally, the strips are severed above the C. The latter step creates the edge needed to induce an energy release rate (Fig. 5). The half-width of the carbon line,  $a_0$ , defines the pre-crack length. When the strips decohere after severing, the energy release rate exceeds the debond energy, i.e.,  $G_{ss} > \Gamma_i$ . Conversely, when the film remains attached,  $G_{ss} < \Gamma_i$ . Consequently,  $\Gamma_i$  is determined from the critical Cr layer thickness above which decohesion always occurs, designated  $h_c$ . The bilayer solution (Eqn. 3) then relates  $\Gamma_i$  to the critical Cr thickness by using the equalities:  $G_{ss} = \Gamma_i$  and  $h_1 = h_c$ .

#### 4. EXPERIMENTAL PROCEDURE

A flow chart of the overall procedure is presented on Fig. 6. Deposition and photolithography are conducted in a clean room facility. Residual stresses are measured from beam deflections. Then, film severing above the precrack is conducted. The films are inspected to assess the critical thickness,  $h_c$ . Finally, this critical thickness is used to determine  $\Gamma_i$ .

##### 4.1 Deposition and Patterning

Preliminary experiments have been carried out by using evaporated copper films and glass substrates. The choice of copper is particularly attractive due to its emerging importance as an interconnect material. It is expected to replace aluminum for deep sub-micron metal line widths, because of its superior conductivity and higher resistance to electromigration.<sup>14</sup> All processing steps are carried out in Class 100 and Class 10,000 clean room facilities. Careful substrate cleaning is essential. For this purpose, the glass substrates (Corning 0211) are solvent cleaned in trichloroethylene, acetone and isopropyl alcohol in order to remove organic contaminants. Then, they are water cleaned, followed by etch-cleaning in buffered hydrofluoric acid, in order to remove all

inorganic contaminants. Finally, they are rinsed in deionized water and dried. The carbon release layer is thermally evaporated (thickness  $\sim 200\text{\AA}$ ) onto the substrate and patterned to the desired geometry (Fig. 5) by using a bilayer photolithography technique. Pure copper (99.999%) is then deposited by electron beam evaporation at a background pressure  $\approx 8 \times 10^{-7}$  torr. Thereafter, the chromium superstructure layer (99.9% pure) is evaporated. An *in situ* quartz monitor is used to control the deposition rate (Cu  $\sim 10\text{\AA}/\text{s}$ , Cr  $\sim 1\text{\AA}/\text{s}$ ) and the film thickness. Subsequent lift-off defines the metal line geometry. Finally, a through cut is made in the metal bilayer by wet etching. An optical micrograph of a processed test specimen is shown in Fig. 7.

#### 4.2 Residual Stress Measurement

The residual stress is measured by using a standard procedure which relies on curvature determination on the film/substrate system.<sup>15</sup> For this purpose, a profilometer is used to measure substrate curvature.<sup>16</sup> The profilometer uses a metallic stylus, which is horizontally scanned while its vertical movement is converted to an electrical signal. The substrate often has an initial curvature. Therefore, two scans are made in order to measure the bending deflection of the substrate. These are made both with ( $\delta_1$ ) and without ( $\delta_2$ ) the film attached. The residual stress in the film is related to these displacements by,

$$\sigma^R = \frac{4E_s(\delta_1 - \delta_2)h_s^2}{3(1 - \nu_s)L^2 h_f} \quad (7)$$

where  $L$  is the length of the profilometer scan,  $h_s$  is the substrate thickness and  $E_s, \nu_s$  are the substrate Young's modulus and Poisson's ratio, respectively. This procedure is used to evaluate the residual stress in the Cu and then the residual stress in the Cr deposited onto the Cu.

## 5. RESULTS

### 5.1 Residual Stress

Residual stress measurements have been performed on a batch of four samples with the same nominal Cu thickness (4425Å) and with four Cr thicknesses: 220Å, 445Å, 660Å and 900Å. On each sample, five profilometer scans were made before and after removing the film from the substrate. A least square regression fitting to the data gives the deflections ( $\delta_1$  and  $\delta_2$ ) and their respective standard deviations. The film thickness is also obtained from the scans. The substrate thickness is measured with a digital micrometer. The stresses obtained in this manner are plotted on Fig. 8, which indicates that the residual stresses in the Cu and Cr layers are 50 MPa and 1575 MPa, respectively, while the standard deviations are ~ 3%.

### 5.2 Interfacial Fracture Energy

For a glass substrate with a 0.44µm thick Cu film, the results are summarised on Fig. 9. When the Cr superlayer was either 22nm or 45nm thick, the bilayer remained attached to the substrate (Fig. 10). Conversely, when the Cr layer was 90nm thick, decohesion occurred followed by curling of the film (Fig. 10). Consequently,  $h_c$  is between 45nm and 90nm. By introducing these values into the energy release rate formula for the bilayer (equation 3), bounds are placed on the interface fracture energy. For this purpose, the elastic modulus of the film is needed. Generally, polycrystalline thin films can have a lower modulus than the bulk material, because of porosity at the boundaries of the columnar grains. Consequently, for completeness, independent measurement of  $E_f$  would be needed. Such measurement has yet to be performed in this study. Instead, literature values of polycrystalline Cu and Cr thin films are used ( $E_f$  = 120 GPa<sup>17</sup> and 93 GPa<sup>18</sup> respectively). With these choices for  $E_f$ , the bounds on the interface fracture energy are,  $0.3 \leq \Gamma_i \leq 0.8 \text{ Jm}^{-2}$ . Earlier study of Cu/Glass interfaces,

produced by diffusion bonding and annealing, indicated that  $\Gamma_i$  usually ranged between 0.14 to 4 Jm<sup>-2</sup> (the highest being 8 Jm<sup>-2</sup>).<sup>19</sup> The scatter was attributed to surface contaminants, which influenced the bonding. The present results are at the lower end of this range. Such results are consistent with the absence of an annealing step, in the present study, leading to a more pronounced influence of minor contaminants. These, in turn, reduce the potential for a contribution to  $\Gamma_i$  from plastic dissipation in the Cu. Furthermore, the present values are compatible with the work of adhesion ( $W_{ad} = 0.5 \text{ Jm}^{-2}$ ) for liquid Cu on SiO<sub>2</sub>.<sup>20</sup>

## 6 CONCLUDING REMARKS

A new test procedure for measuring the interface decohesion energy  $\Gamma_i$  of metallic thin films on non-metallic substrates has been devised, analyzed and demonstrated. The procedure duplicates the conditions found upon decohesion induced by residual stress. The measured values of  $\Gamma_i$  may thus be used directly, in conjunction with the mechanics of thin films in order to predict such factors as the critical film thickness. Moreover, the method allows a systematic study of trends in  $\Gamma_i$  with the key deposition and post-deposition variables. These include the effect of contaminants, of active metal layers, of annealing, electric fields, etc. Studies are now in progress which will apply the new method to these basic issues.

Finally, since the value of  $\Gamma_i$  obtained from these tests are subjected to knowledge of the elastic properties of the bilayer film, simple acoustic procedures for measuring these properties are being implemented.

## ACKNOWLEDGMENTS

Financial support was provided by the Office of Naval Research under ONR contract N00014-93-I-0213.

## REFERENCES

- <sup>1</sup>P.S. Ho, *Appl. Surf. Sci.* **41-42**, 559 (1989).
- <sup>2</sup>M.D. Thouless, *J. Vac. Sci. Technol.* **A9**, 2510 (1991).
- <sup>3</sup>J.W. Hutchinson and Z. Suo, *Adv. Appl. Mech.* **29**, 63 (1992).
- <sup>4</sup>A.G. Evans, M. Ruhle, B.J. Dalgleish, and P.G. Charalambides, *Met. Trans.* **21A**, 2419 (1990).
- <sup>5</sup>P.G. Charalambides, J. Lund, A.G. Evans, and R.M. McMeeking, *J. Appl. Mech.* **56**, 77 (1989).
- <sup>6</sup>J.S. Wang and Z. Suo, *Acta Metall. Mater.* **38**, 1279 (1990).
- <sup>7</sup>K.S. Kim and N. Aravas, *Int. J. Solids Struct.* **24**, 417 (1988).
- <sup>8</sup>A.G. Evans and B.J. Dalgleish, *Acta Metall. Mater.* **40** Suppl., S295 (1992).
- <sup>9</sup>M.L. Joki, V. Vitek, and C.J. McMahon Jr., *Acta Metall. Mater.* **28**, 1479 (1980).
- <sup>10</sup>V. Tvergaard and J.W. Hutchinson, *Harvard Applied Sciences Report*, MECH 193 (1992).
- <sup>11</sup>M.S. Hu and A.G. Evans, *Acta Metall. Mater.* **37**, 917 (1989).
- <sup>12</sup>M.D. Drory, M.D. Thouless, and A.G. Evans, *Acta Metall. Mater.* **36**, 2019 (1988).
- <sup>13</sup>S. Timoshenko, *J. Opt. Soc. Am.* **11**, 223 (1925).
- <sup>14</sup>S. S. Wong, J.S. Cho, H.K. Kang, and C.H. Ting, *Mat. Res. Soc. Symp. Proc.* **203**, 347 (1991).
- <sup>15</sup>G.G. Stoney, *Proc. R. Soc. London Ser. A* **82**, 172 (1909).
- <sup>16</sup>M.E. Thomas, M.P. Hartnett, and J.E. Mckay, *J. Vac. Sci. Technol.* **A6**, 2570 (1988).
- <sup>17</sup>J.A. Ruud, D. Josell, F. Spaepen, and A.L. Greer, *J. Mater. Res.* **8**, 112 (1993).
- <sup>18</sup>M. Janda, *Thin Solid Films* **142**, 37 (1986).
- <sup>19</sup>R.M. Cannon, R.M. Fisher, and A.G. Evans, *Mat. Res. Soc. Symp. Proc.* **54**, 799 (1986).
- <sup>20</sup>J.G. Li, *J. Mater. Sci. Lett.* **11**, 903 (1992).

## APPENDIX

### THE STRAIN ENERGY RELEASE RATE

Interfacial decohesion, motivated by residual stresses in deposited thin film layers, occurs subject to a the steady state strain energy release rate,  $G_{ss}$ , when the interfacial flaw size,  $a_0$ , exceeds the film thickness.<sup>3</sup> For thin film systems a strain energy balance may be used to calculate  $G_{ss}$ , wherein two elements, having width  $\Delta a$ , are chosen far ahead and far behind the growing interfacial crack (Fig. A1). If  $U_a$  and  $U_b$  denote the strain energies in these volume elements, then

$$G_{ss}\Delta a = U_a - U_b \quad (A1)$$

This result applies provided that the substrate thickness is much larger than the film thickness. The element far ahead of the crack tip is in biaxial plane stress,

$$\begin{aligned} \sigma_x^i &= \sigma_y^i = \sigma_i; \\ \sigma_i &= \epsilon_i E_i / (1 - \nu_i) = \epsilon_i E_i^*; \\ \sigma_z^i &= \tau_{xy}^i = \tau_{yz}^i = \tau_{zx}^i = 0 \quad (i = 1, 2) \end{aligned} \quad (A2)$$

where  $\sigma_1, \sigma_2$  are the residual stresses in the two layers and  $\epsilon_1, \epsilon_2$  the corresponding residual strains. The elastic strain energy density associated with each layer ( $i = 1, 2$ ), per unit width, is

$$\Delta U_a^i / h_i \Delta a = \frac{\sigma_i^2}{E_i} \quad (A3)$$

where  $E_i^*$  are the biaxial moduli of the film layers. Consequently, for a bilayer



$$\begin{aligned}
U_s &\equiv \sum \Delta U_s^i \\
&= \left[ \frac{\sigma_1^2 h_1}{E_1} + \frac{\sigma_2^2 h_2}{E_2} \right] \Delta a
\end{aligned} \tag{A4}$$

When both layers are in residual tension (as in the present experiment) and when  $\epsilon_1 > \epsilon_2$ , the film bends upwards after decohesion in an attempt to relax the strains (Fig. 4). The resultant stresses in each layer can be related to the forces,  $P_i$ , moments,  $M_i$ , and curvature,  $\kappa$ , defined in Fig. 5, by <sup>13</sup>

$$\begin{aligned}
\sigma_i(z) &= P_i / h_i + z E_i \kappa; \\
E_i \kappa &= M_i / I_i; \\
I_i &= h_i^3 / 12
\end{aligned} \tag{A5}$$

where  $z$  now denotes the vertical distance from the neutral axis in each separate layer, whereas  $I_i$  are the sectional moduli. The strain energy is then <sup>3</sup>

$$U_b = \sum_i \frac{1}{E_i} \left[ \frac{P_i^2}{h_i} + \frac{M_i^2}{I_i} \right] \Delta a \tag{A6}$$

It is now required to provide expressions that relate  $P_i$ ,  $M_i$  and  $\kappa$  to the stresses and the film thicknesses, by using beam theory. For a bilayer, this procedure provides five linear equations involving the five unknowns, namely  $P_1$ ,  $P_2$ ,  $M_1$ ,  $M_2$  and  $\kappa$ . Equilibrium dictates that, for a bilayer

$$\begin{aligned}
\sum P_i &= 0; \Rightarrow P_1 = P_2 = P \\
\sum M_i &= 0; \Rightarrow M_1 + M_2 = P \left( \frac{h_1 + h_2}{2} \right)
\end{aligned} \tag{A7}$$

Geometry requires that,

$$\begin{aligned} M_1 &= E_1 I_1 \kappa \\ M_2 &= E_2 I_2 \kappa \end{aligned} \quad (A8)$$

Strain compatibility at the interface gives

$$-\epsilon_1 + \frac{P_1}{E_1 h_1} + \frac{h_1 \kappa}{2} = -\epsilon_2 - \frac{P_2}{E_2 h_2} - \frac{h_2 \kappa}{2} \quad (A9)$$

In this case, analytical solutions for  $P$ ,  $M_i$  and  $\kappa$  are obtained as<sup>13</sup>

$$M_i = E_i I_i \kappa$$

$$P = \left[ \frac{E_1 h_1^3 + E_2 h_2^3}{6(h_1 + h_2)} \right] \kappa$$

and

$$\kappa = \frac{6(h_1 + h_2)(\epsilon_1 - \epsilon_2)}{\left[ h_1^2 + E_2 h_2^3 / E_1 h_1 + E_1 h_1^3 / E_2 h_2 + h_2^2 + 3(h_1 + h_2)^2 \right]} \quad (A10)$$

The strain energy release rate is then ( $i = 1, 2$ )

$$G_m = \sum_i \frac{\sigma_i^2 h_i}{E_i} - \sum_i \frac{1}{E_i} \left[ \frac{P}{h_i} + \frac{12M_i}{h_i^3} \right] \quad (A11)$$

The above result can be generalized for a multilayer film ( $i = 1, 2, 3, \dots, n$ ). The number of unknowns is  $2n+1$ , because each layer has two (a force,  $P_i$ , and a moment,  $M_i$ ) in addition to the curvature,  $\kappa$ , of the film after decohesion. The solution requires  $2n+1$  linear equations. The first two stem from equilibrium considerations

$$\Sigma \text{ FORCE} = 0; \Rightarrow P_1 + P_2 + \dots + P_n = 0 \quad (\text{A12})$$

$$\Sigma \text{ MOMENT} = 0; \Rightarrow \sum_{i=1}^n M_i = \sum_{i=1}^{n-1} P_i \left( \frac{h_i + h_{i+1}}{2} + \sum_{k=i+1}^{n-1} h_k \right) \quad (\text{A13})$$

The next  $n$  equations relate the moments to the curvature ( $i = 1, 2, \dots, n$ )

$$M_i = E_i I_i \kappa_i \quad (\text{A14})$$

Finally, the remaining  $n-1$  equations involve strain compatibility at the  $n-1$  interfaces. For the  $r$ -th interface, this can be expressed as ( $r = 1, 2, \dots, n-1$ )

$$\epsilon_r + \frac{P_r}{E_r h_r} + \frac{h_r \kappa_r}{2} = \epsilon_{r+1} + \frac{P_{r+1}}{E_{r+1} h_{r+1}} - \frac{h_{r+1} \kappa_{r+1}}{2}; \quad (\text{A15})$$

A program needed to solve these equations has been developed using MATLAB.

## FIGURE CAPTIONS

- Fig. 1. A schematic indicating the effect of loading mixity on the interface fracture energy,  $\Gamma_i$ . The values used are typical for metal/oxide interfaces. Also shown is a schematic of crack growth with plastic dissipation.
- Fig. 2. Some test methods used to measure the interface fracture energy.
- Fig. 3. Effect of metal yield strength on the interface fracture energy:  $\sigma_0$  is the yield strength,  $\hat{\sigma}$  the bond strength and  $\Delta a$  the crack extension (Tvergaard and Hutchinson).
- Fig. 4. A schematic showing the behavior of a bilayer film subject to residual tension as it decoheres from the substrate. The stresses  $\sigma_1, \sigma_2$  are the misfit stresses, which provide the forces  $P_i$  and the moments  $M_i$  in the metal bilayer above the decohesion crack. The curvature of the decohered bilayer film is  $\kappa$ .
- Fig. 5. The procedure used to measure the debond energy of the interface.
- Fig. 6. A flow chart indicating the sequence used to measure the debond energy.
- Fig. 7. An optical micrograph of the processed test specimen.
- Fig. 8. A plot of the total film stress with the normalized Cr layer thickness.
- Fig. 9. A plot of the calculated energy release rates with the normalized Cr layer thickness. Also shown are the lines separating the film that decohered from that which remained attached and associated bounds in the interface fracture energy.
- Fig. 10. Specimens providing the lower and upper bounds in the fracture energy, with the Cr superlayer thickness (A)  $h_1 = 450\text{\AA}$ , *below* the critical thickness and (B)  $h_1 = 900\text{\AA}$ , *above* the critical thickness.
- Fig. A1. A schematic describing the energy balance approach to find the strain energy release rate for a bilayer thin film.

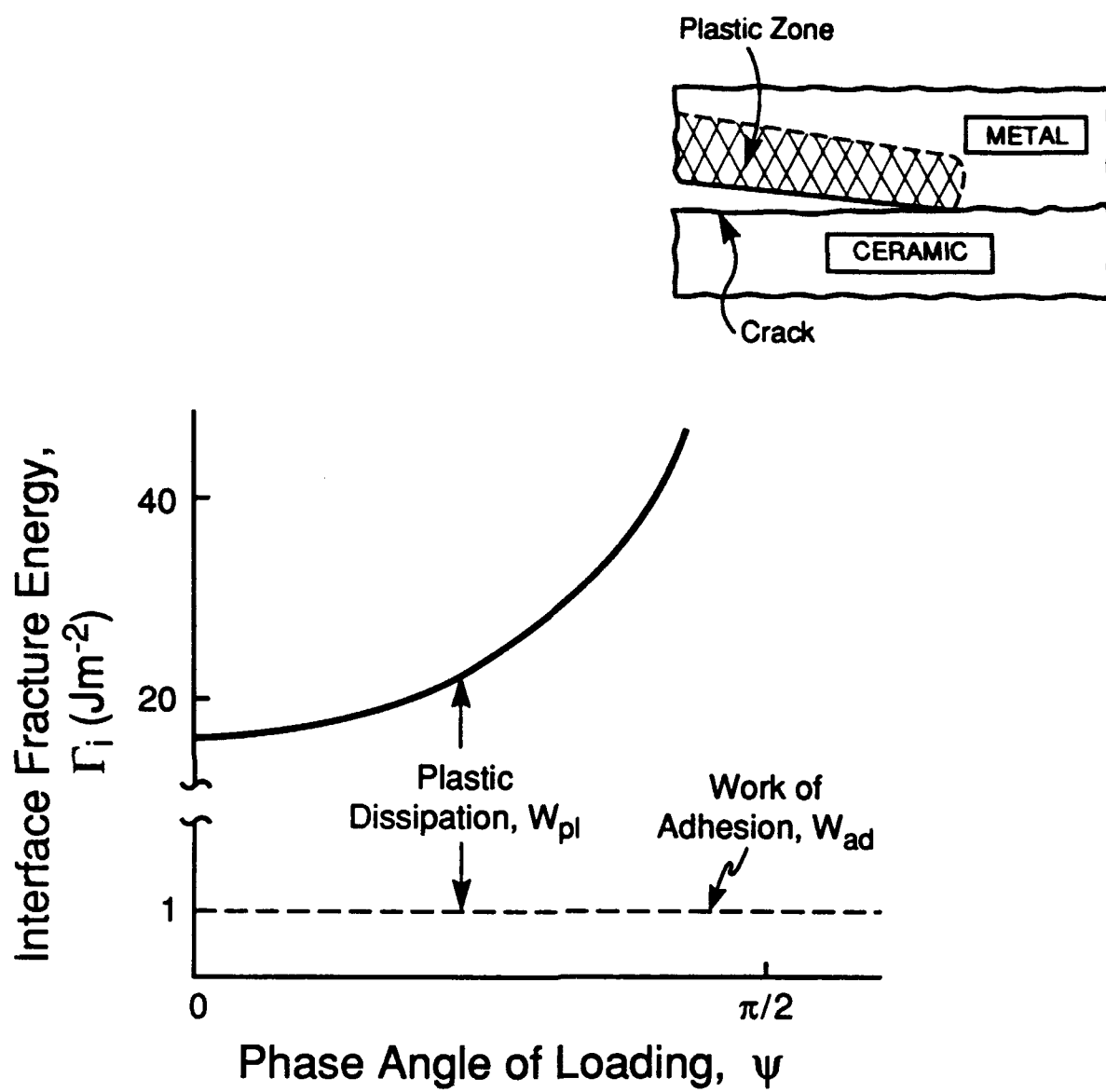
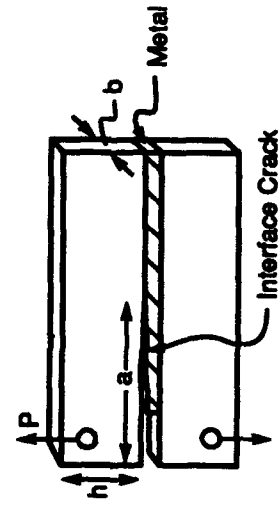


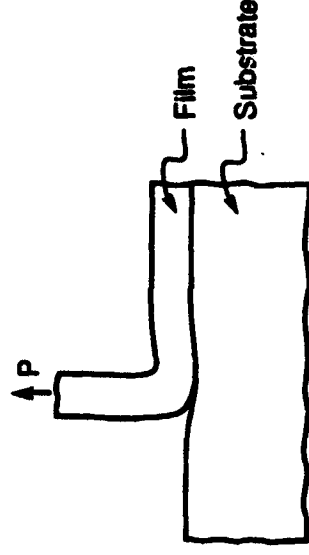
Figure 1

# AVAILABLE TESTS TO MEASURE $\Gamma_i$



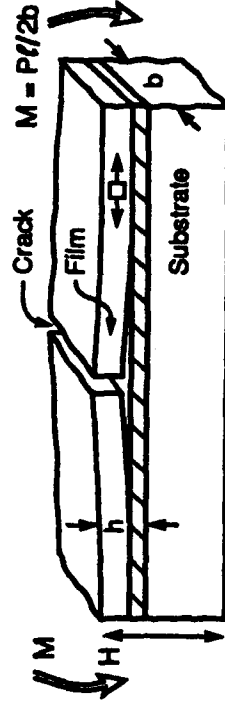
$$0 \leq \psi \leq 50^\circ$$

a) Clever Beam



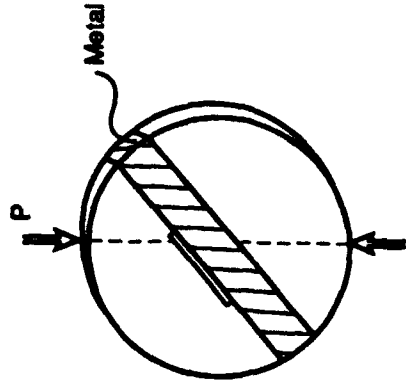
$$\psi < 0^\circ$$

b) Peel Test



$$\psi \approx 50^\circ$$

c) Mixed Mode Flexure



$$0 \leq \psi \leq 90^\circ$$

c) Brasli Specimen

Figure 2

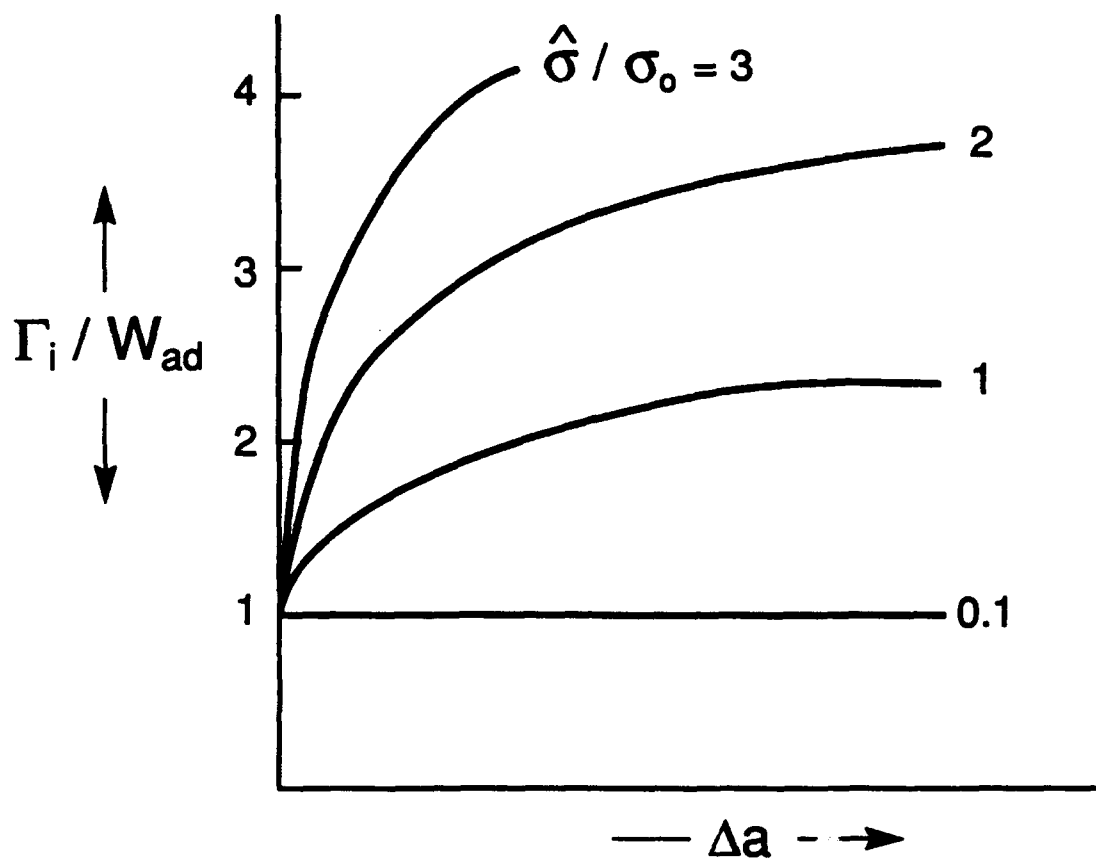


Figure 3

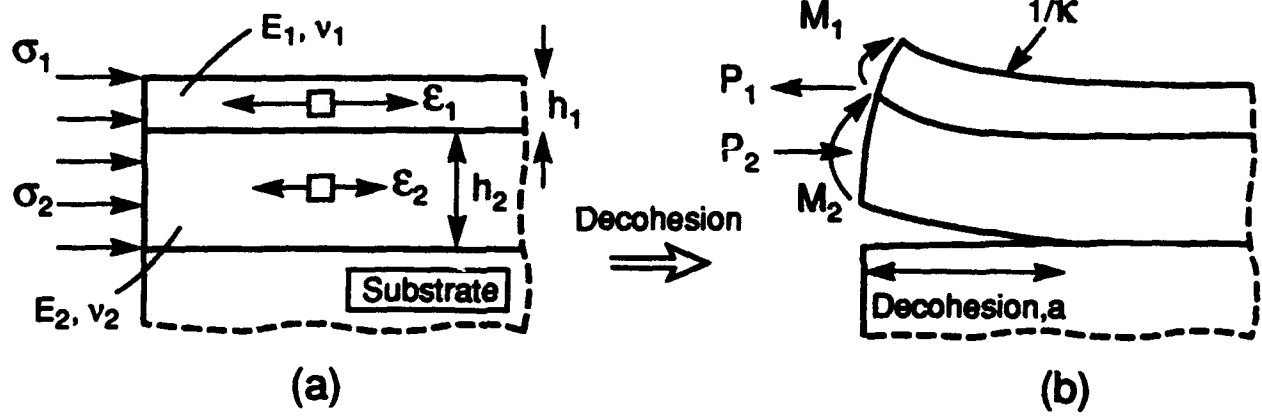
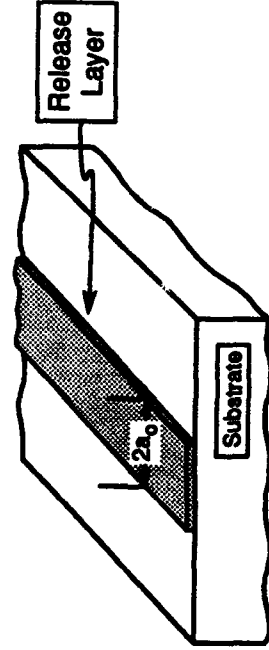


Figure 4



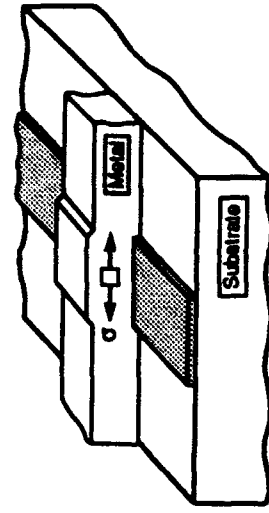
**STEP I**

Release Layer Deposition



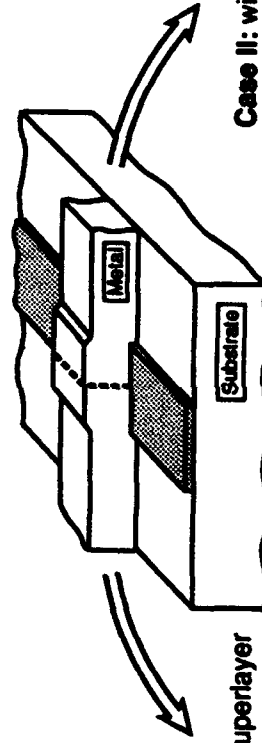
**STEP II**

Metal Layer & Superlayer Deposition

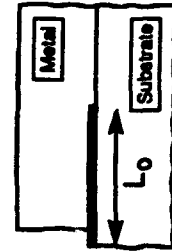


**STEP III**

Bilayer Cut

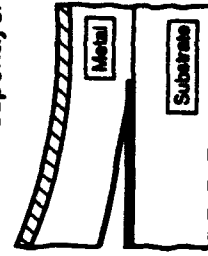


Case I: without superlayer



$$G_{ss} < \Gamma_i$$

Case II: with superlayer



$$G_{ss} > \Gamma_i$$

Figure 5

## FLOW CHART

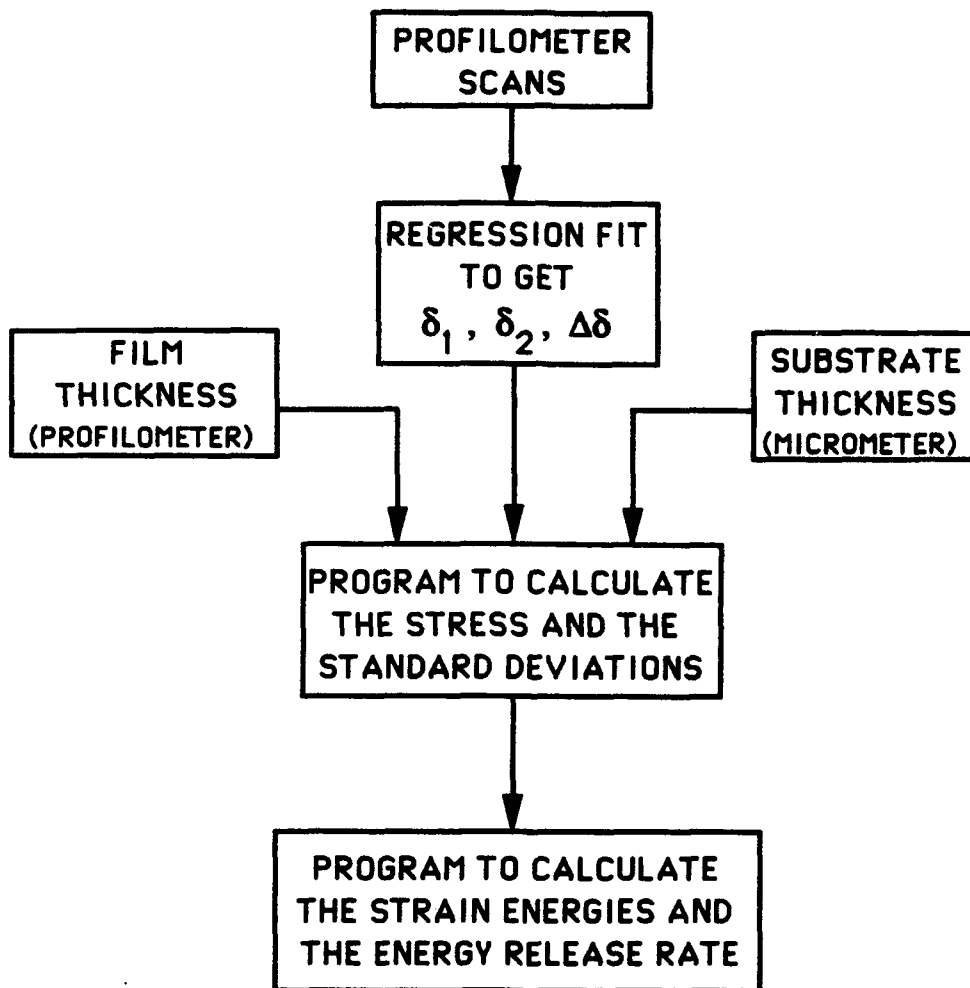


Figure 6

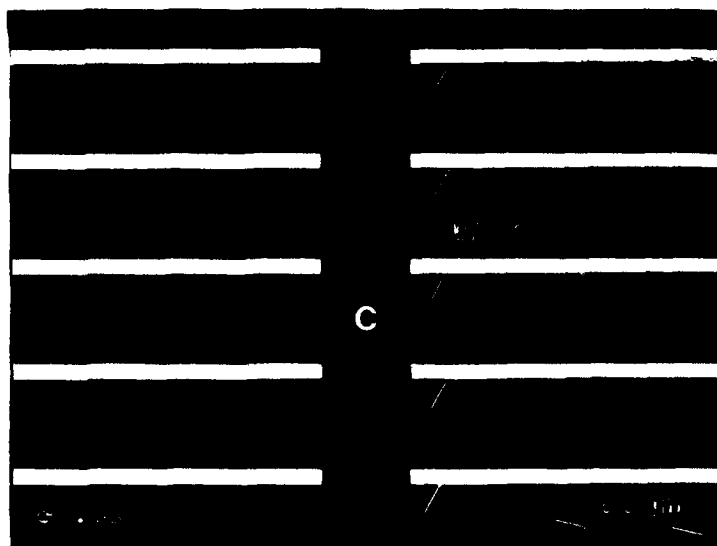


Figure 7

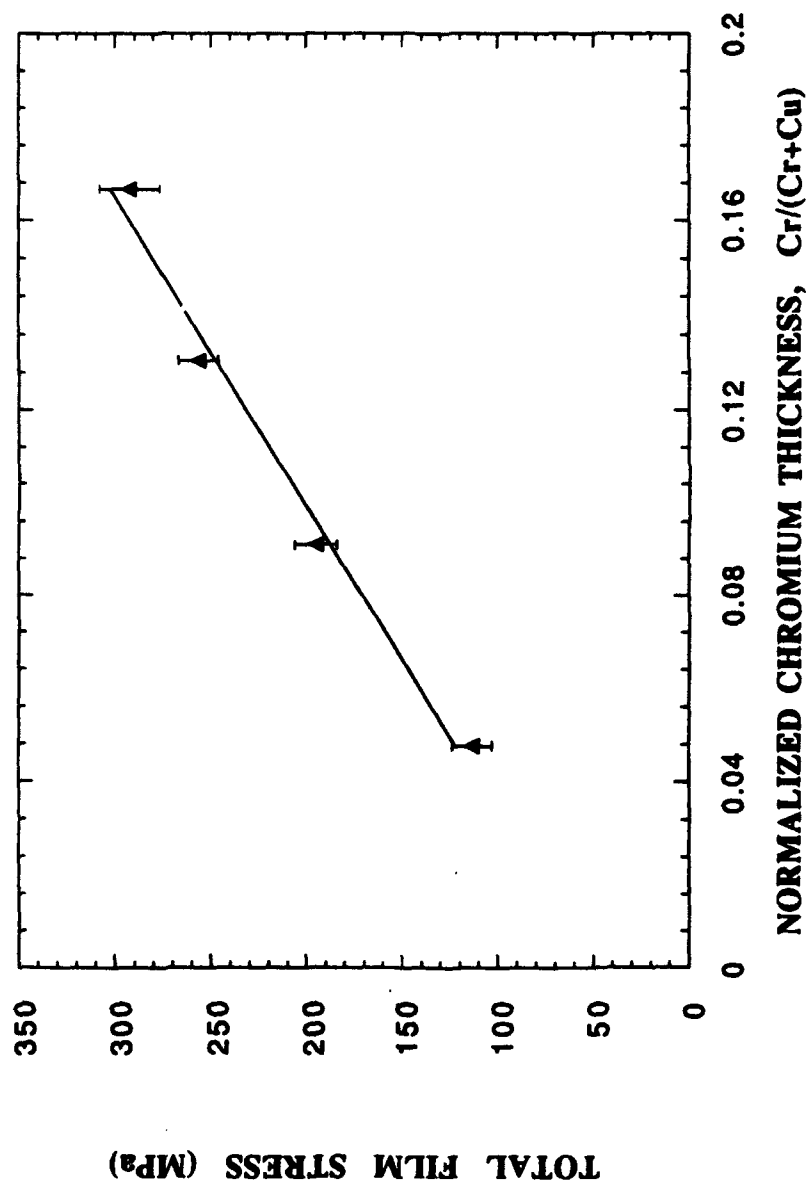


Figure 8

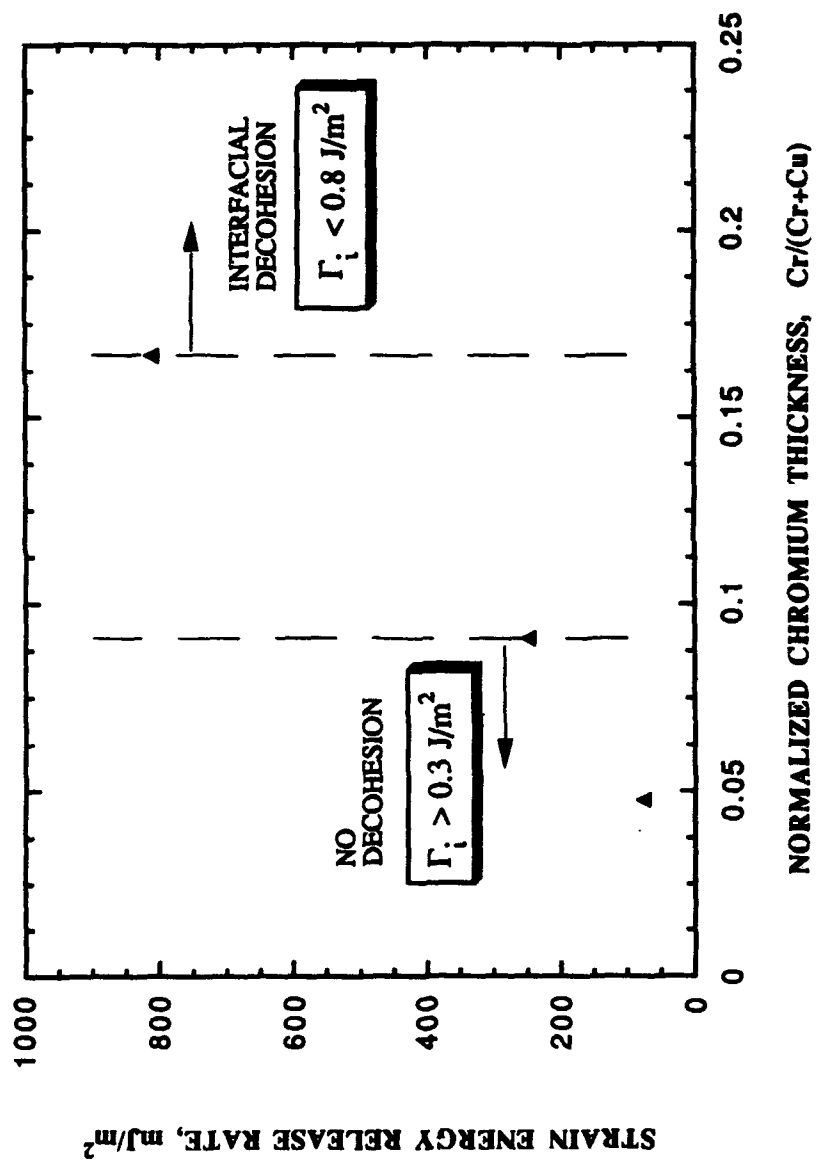


Figure 9

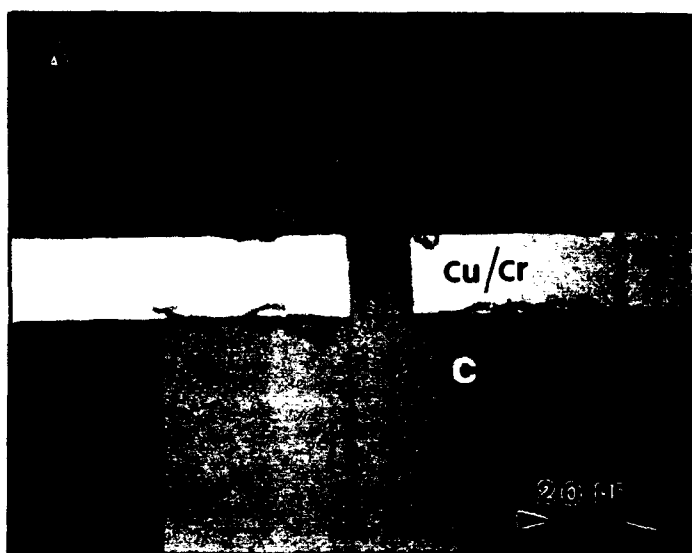


Figure 10

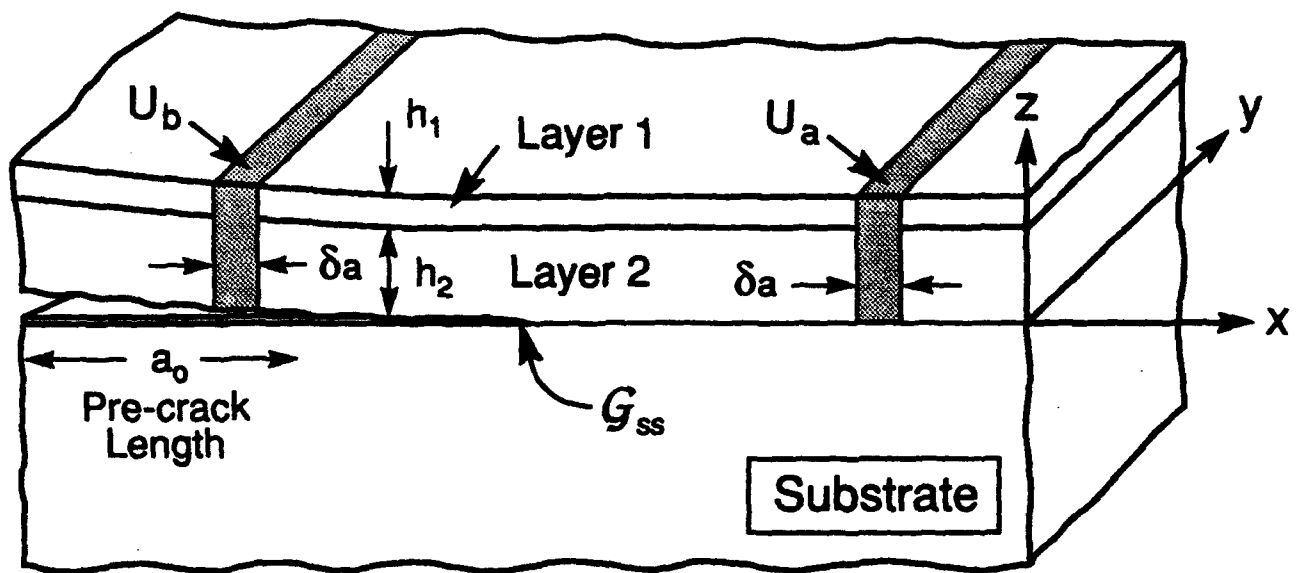
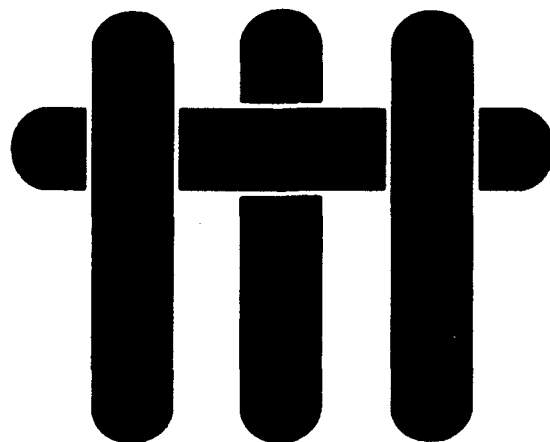


Figure A1

# **M A T E R I A L S**



## **THE STRUCTURE AND THERMOMECHANICAL PROPERTIES OF $\text{Mo}/\text{Al}_2\text{O}_3$ INTERFACES**

by

**M.R. Turner, J.P.A. Löfvander, J.B. Davis and A.G. Evans**  
Materials Department  
College of Engineering  
University of California, Santa Barbara  
Santa Barbara, California 93106-5050



## ABSTRACT

The debonding and sliding resistances of interfaces formed between Mo and  $\text{Al}_2\text{O}_3$  have been measured. The Mo/ $\text{Al}_2\text{O}_3$  interface exhibits a relatively low *interfacial fracture energy*,  $\Gamma_i$ , comparable in magnitude to the work of adhesion,  $W_{ad}$ . Debonding appears to occur with minimal plastic dissipation in the metal. Fine-scale plasticity phenomena occurring near the debond, within the Mo, are considered responsible for this behavior. The *sliding resistance* of the interface, subsequent to debonding, was found to depend on the shear yield strength of the Mo, consistent with observations of plastic grooving during fiber pull-out in composites containing Mo-coated sapphire fibers.

## 1. INTRODUCTION

The failure of interfaces between metals and oxides occurs by a variety of mechanisms.<sup>1-3</sup> In the absence of reaction products, some interfaces exhibit ductile fracture.<sup>1,4</sup> Others fail by brittle debonding, but with plastic dissipation occurring in the metal.<sup>5,6</sup> When reaction products form or interlayers exist, the behavior is usually brittle. The fracture occurs either *within* the reaction product or at one of the interfaces<sup>7,8</sup> (usually, the metal/interphase interface).

Most bimaterial interfaces produced at high homologous temperatures exhibit a fracture energy,  $\Gamma_i$ , substantially larger than the work of adhesion,  $W_{ad}$ .<sup>1,9</sup> Notable exceptions include the interfaces between  $Al_2O_3$  and certain refractory metals, particularly Mo.<sup>1,10</sup> These have fracture energies,  $\Gamma_i \approx W_{ad}$ . This phenomenon has not been explained. One motivation for the present study is to address the origin of the low fracture energy found for the Mo/ $Al_2O_3$  interface.

There are two basic approaches for creating a metal/oxide interface with a small debond energy. These approaches are evident from the basic correlation between the work of adhesion and the plastic dissipation<sup>10-12</sup>

$$\Gamma_i \approx W_{ad} \mathcal{P}(\hat{\sigma}/\sigma_o) \quad (1)$$

where the plastic dissipation parameter  $\mathcal{P}$  is a function of the ratio between the peak stress,  $\hat{\sigma}$ , needed to rupture the interface bonds and  $\sigma_o$ , the uniaxial yield strength of the matrix. Calculations conducted using continuum concepts predict variations in  $\mathcal{P}$  upon interface crack extension,  $\Delta a$  (Fig. 1).<sup>11</sup> Clearly,  $\Gamma_i \rightarrow W_{ad}$ , when  $\hat{\sigma}/\sigma_o$  is small. Moreover,  $W_{ad}$  is related to the bond rupture stress by,<sup>10,12</sup>

$$W_{ad} \approx \hat{\sigma} a_o / 2 \quad (2)$$

where  $a_0$  is the separation distance of atoms across the interface. From Eqns. (1) and (2), it is evident that debonding can be encouraged either by having a small work of adhesion, or by using a high yield strength metal. These properties can be affected by segregation and alloying. Segregation changes  $\hat{\sigma}$ ,<sup>10</sup> whereas alloying influences  $\sigma_0$ . Such effects are addressed for  $\text{Al}_2\text{O}_3/\text{Mo}$  interfaces by measuring  $W_{\text{ad}}$  and  $\sigma_0$ , and then relating these to measurements of  $\Gamma_i$ . In Mo, the strong influence of oxygen on flow strength and ductility,<sup>13</sup> has special relevance.

The Mo/ $\text{Al}_2\text{O}_3$  interface also has thermomechanical characteristics consistent with those needed for  $\text{Al}_2\text{O}_3$  fiber reinforcements, which impart high composite strength, as well as good fracture and fatigue resistance.<sup>13-16</sup> In this application, not only are *small* values of  $\Gamma_i$  preferred, but also the sliding along debonded interfaces must occur with a controlled shear resistance,  $\tau$ . This study addresses measurement of  $\tau$ <sup>17</sup> and relationships with the interface structure.

## 2. MATERIALS AND PROCESSING

Interfaces between Mo and either sapphire or polycrystalline  $\text{Al}_2\text{O}_3$  have been investigated. The sapphire used to create these interfaces had two basic geometries, either discs with basal plane orientation, or fibers with c-axis orientation.† In some cases, polycrystalline  $\text{Al}_2\text{O}_3$  plates, with two different compositions, have been used instead of sapphire.‡ Bodies comprising Mo-coated sapphire fibers in polycrystalline  $\text{Al}_2\text{O}_3$  matrices produced from a high purity powder,‡‡ have also been studied.

Precautions have been taken to minimize the oxygen present in the Mo, by using high purity material and by conducting all steps of the bonding in environments with

---

† Supplied by Sapphikon

‡ Coors AD-995 and Coors AD-96

‡‡ Sumitomo Chemical Company, Inc.

low oxygen partial pressure. The Mo was deposited onto the sapphire either by evaporation or sputtering from high purity ( $> 99.9\%$ ) targets. *Sputtered material* was deposited in an R.F. diode unit, in an atmosphere that comprised research grade argon at 6 millitorr working gas pressure. The top and bottom target voltages were maintained at 3kV and 0.5kV, respectively. Typical sputtered coating thicknesses were  $\sim 5 \mu\text{m}$  for planar substrates and  $0.7\text{--}1.4 \mu\text{m}$  for fibers.\*\* Coatings deposited by *electron beam evaporation* were produced at relatively high vacuum ( $< 10^{-6}$  torr). Evaporated coating thicknesses were  $\sim 0.5 \mu\text{m}$ . A glow discharge cleaning procedure was used prior to deposition.

The coated discs were diffusion bonded at relatively high vacuum ( $< 10^{-6}$  torr). In some cases, a high purity ( $> 99.95\%$ ) Mo foil\* ( $127 \mu\text{m}$ ) was inserted between the Mo coated surfaces prior to bonding. The diffusion bonding was conducted at  $1450^\circ\text{C}$  for 12 h, using an applied pressure of 3–5 MPa. The fiber-containing composites were produced by hot pressing. For this purpose, the coated sapphire fibers were incorporated into an  $\text{Al}_2\text{O}_3$  matrix and consolidated at  $1500^\circ\text{C}$  for 120 min., using an applied pressure of  $\sim 2$  MPa.

### 3. ANALYTICAL TECHNIQUES

All interfaces were examined using transmission electron microscopy (TEM) techniques. For this purpose, electron transparent foils were prepared by cutting thin slices with a low speed diamond saw perpendicular either to the bonded surface or the fiber axis. These slices were ground to roughly  $100 \mu\text{m}$  using diamond paste and 3 mm diameter discs were ultrasonically drilled. One side was polished with  $3 \mu\text{m}$  diamond paste. The other side was dimple ground using 3 and  $1 \mu\text{m}$  pastes, followed by a  $1/4$

---

\*\* The fibers were rotated during coating at  $\sim 1$  rpm.

\* Johnson Mattheys

μm final polish. Subsequent thinning was accomplished by ion milling with Ar at 5kV, 1mA and 14° incidence angle. In many cases, thin foil cross-sections could not be produced because of the tendency to debond at the interfaces. In such cases, the coating was first removed from the substrate and mounted on a copper grid. All samples were examined\* in a microscope equipped with a high take-off angle energy dispersive spectroscopy system. Crystallographic computations, simulations and indexing of diffraction patterns were carried out with the Diffract software. As-sputtered coatings were also examined using PEELS.

Scanning Auger microscopy (SAM) was used to characterize the interface chemistry, with spectra collected from debonded interfaces.† Depth profiles were performed by Ar ion sputtering of the Mo fracture surface. Debonded surfaces were also examined by scanning electron microscopy (SEM).\*\* For this purpose, a thin carbon or gold layer was evaporated onto the surfaces. Chemical analyses were performed on surface features by using energy dispersive X-ray (EDS) methods.\* The same surfaces were analyzed by X-ray diffraction methods.º

The morphology of the debond surfaces was established using atomic force microscopy (AFM).†

#### 4. MECHANICAL MEASUREMENTS

The fracture energies of the Al<sub>2</sub>O<sub>3</sub>/ Mo interfaces were measured by using either four point flexure<sup>6,18</sup> or Hertzian indentation.<sup>19</sup> In both cases, interface debonding was monitored *in situ*, with an optical microscope focused through the sapphire layer. The

---

\* JOEL 2000FX TEM at 200 kV

† Perkin Elmer PHI 660 Auger microscope

\*\* Jeol SM840 SEM

\* Tracor Northern TN5500 system

º Scintag XDS2000 diffractometer

† Nanoscope II from Digital Instruments

fracture energy,  $\Gamma_i$  was ascertained from the loads at which the cracks extended, as well as the specimen dimensions.<sup>18,19</sup> For flexure tests, a pre-crack was introduced along the interface by propagating a controlled crack from a row of indentations emplaced on one of the sapphire surfaces.<sup>6</sup> A typical debond region is depicted in Fig. 2. In systems produced with either the higher purity polycrystalline  $\text{Al}_2\text{O}_3$  or sapphire, the loads at which these precracks extended gave debond energies in the range,  $\Gamma_i \approx 1\text{--}4 \text{ Jm}^{-2}$ . These results were insensitive to the Mo deposition method (sputtering or evaporation) and to the Mo thickness. Conversely, when the lower purity  $\text{Al}_2\text{O}_3$  was used,  $\Gamma_i$  was substantially larger. It was typically in the range,  $\Gamma_i = 10\text{--}20 \text{ Jm}^{-2}$ .

The sliding behavior was measured on hot pressed fiber specimens by using a fiber push-through test method.<sup>10,17</sup> Typical load-displacement curves involve a load drop, indicative of interface debonding, followed by fiber push-out (Fig. 3). The loads at which push-through displacements initiated (Fig. 3) gave the sliding resistance  $\tau$ . It was found to be in the range,  $\tau \approx 130\text{--}225 \text{ MPa}$ . Grooves in the Mo were evident along the push-out zone (Fig. 4), indicative of plastic deformation occurring within the Mo.

The yield strength of the Mo subsequent to diffusion bonding was determined by microhardness measurements. The measurements were made at low loads, such that the indentation depth was less than 1/3 the Mo layer thickness. The results gave a hardness in the range,  $H \approx 900 \text{ MPa}$  for the Mo foil after bonding. The corresponding uniaxial yield strength is,<sup>21</sup>  $\sigma_0 \approx H/3 \approx 300 \text{ MPa}$ . The sputtered coatings, deposited on the sapphire fibers, gave larger values of hardness, corresponding to  $\sigma_0 \approx 600 \text{ MPa}$ .

## 5. INTERFACE STRUCTURE

The cross-section of an *as-deposited*, sputtered, Mo layer revealed a columnar growth structure with faceted grains,  $\sim 100 \text{ nm}$  in diameter (Fig. 5). Diffraction patterns (Fig. 6) were consistent with the pattern simulated for randomly oriented grains with a

common  $\langle 111 \rangle$  direction. Furthermore, PEELS results indicated the presence of thin oxide layers located both at the free surface and at the film/substrate interface.

All of the materials, regardless of the methods used to prepare the Mo, exhibited some metal oxide formation along the interfaces. Usually this oxide was *intermittent*. After debonding, the oxide was invariably attached to the sapphire, as evident from views of the sapphire side of a fracture surface (Fig. 7). Image analysis on sapphire fracture surfaces revealed an area of fraction of oxide grains of  $\sim 0.2$ . X-ray diffraction patterns obtained from these surfaces indicated that the oxide was  $\text{MoO}_2$ . The presence of an oxide was further verified by SAM studies of the same surfaces.

In the system produced using the lower purity alumina (Fig. 8), the metal oxide layer was continuous,  $\sim 300$  nm thick and could be analyzed by cross section TEM. This oxide phase was identified by tilting experiments, performed on single grains, to obtain diffraction patterns for the  $[101]$ ,  $[102]$ , and the  $[213]$  zone axes (Fig. 9a, b, c), which could be compared with patterns simulated for monoclinic  $\text{MoO}_2$  (Fig. 9d, e, f). The simulations were achieved by using the space group, lattice parameters and fractional atom positions listed in Table I. The oxide consistently exhibited an orientation relationship with the sapphire substrates, exemplified by the diffraction pattern in Figs. 10a and b, which show the  $[1\bar{1}00]$  sapphire //  $[\bar{1}\bar{2}0]$   $\text{MoO}_2$  and  $[2\bar{1}\bar{1}0]$  sapphire //  $[\bar{3}\bar{2}0]$   $\text{MoO}_2$ , respectively. The orientation relationship may be described by

$$(0001)_{\text{Sapphire}} // (00\bar{1})_{\text{MoO}_2}$$

$$[\bar{1}\bar{2}10]_{\text{Sapphire}} // [010]_{\text{MoO}_2}$$

A structure diagram of the sapphire basal plane and the  $(00\bar{1})$  plane in  $\text{MoO}_2$ , oriented with the above crystallographic relationships indicate the resemblance of the oxygen sub-lattices (Fig. 11). The distance between two oxygen atoms along the  $[\bar{1}\bar{2}10]$  direction

in sapphire is 4.76 Å. The distance between two oxygen atoms in the MoO<sub>2</sub> along the [010] direction is 4.86 Å. This misfit is less than 2% and supports the observed preference for this orientation relationship.

Also observed in this system was a continuous amorphous phase separating the MoO<sub>2</sub> layer from the Mo. These regions had chemical composition, 61 Si, 28 Al, 6 Ca, 3.5 Mg, 1.5 K (in atomic percent for metallic constituents only), as determined by EDS. The silicate was also observed throughout the Mo pore channels. In addition, MgAl<sub>2</sub>O<sub>4</sub> spinel, with two distinct morphologies, was identified at the interface between the polycrystalline Al<sub>2</sub>O<sub>3</sub> and the Mo (Fig. 12). These consisted of either block precipitates or a semicontinuous layer.

For bonds made with high purity Al<sub>2</sub>O<sub>3</sub>, a non-planar interface formed between the sapphire and the Mo (Fig. 13) with no apparent orientation relationship. A number of small (300–400 nm) MoO<sub>2</sub> grains were usually present throughout the sputtered Mo. The average grain diameter was 2–5 µm, indicating that there had been substantial grain growth during processing. Matching topographic features were evident in regions of direct contact between the sapphire and the Mo. These features formed by interface and surface diffusion, both in the Al<sub>2</sub>O<sub>3</sub> and the Mo, during diffusion bonding.

Measurements of the profiles around the grain boundaries in the Mo, obtained both by TEM (Fig. 14) and AFM (Fig. 15) provided estimates of the dihedral angle. These are in the range, 130 ± 14°. Non-matching features also exist, which relate to residual porosity at the interface. The area fraction of such porosity was ~ 0.45 for the sputtered Mo.

The oxygen content measured by SAM ranged between 4 and 6 atom % throughout the layer, despite precautions taken to minimize access of oxygen. The solubility limit of oxygen in Mo is ~ 0.2 atom %. The presence of MoC<sub>2</sub> oxide grains in the Mo is consistent with these measurements.



## 6. DISCUSSION

### 6.1 Debonding

The measured debond energy appears to be relatively invariant and thus, insensitive to the amounts of either interface porosity or  $\text{MoO}_2$  detected on the sapphire side of the debond surface. Such observations suggest that both the  $\text{Mo}/\text{Al}_2\text{O}_3$  and the  $\text{Mo}/\text{MoO}_2$  interfaces have low fracture energies. Conversely, failure *never* occurs at the  $\text{Al}_2\text{O}_3/\text{MoO}_2$  interface. Its resistance to failure must be relatively high. This is consistent with the results of other investigations for oxide/oxide interfaces.<sup>10</sup> Subsequent emphasis is given to the metal/oxide interfaces.

An attempt is made to understand the small value of  $\Gamma_i$  based on separate assessments of  $W_{ad}$  and  $\sigma_o$ , in accordance with the concepts expressed in Eqns. (1) and (2). The dihedral angle,  $\phi$ , measurements provide one estimate of  $W_{ad}$ . These angles, established at high temperatures, relate the equilibrium interface energy,  $\gamma_i$ , to the Mo grain boundary energy,  $\gamma_b$ , through the relationship

$$\gamma_b = 2\gamma_i \cos\phi \quad (3)$$

Atomistic calculations<sup>22</sup> suggest that  $\gamma_b$  for Mo is in the range,  $\gamma_b = 1.2 \pm 0.6 \text{ Jm}^{-2}$ . The interface energy is thus,  $\gamma_i = 1.5 \pm 1.2 \text{ Jm}^{-2}$ . The interface energy is, in turn, related to the work of adhesion by<sup>10</sup>

$$W_{ad} = \gamma_{oxide} + \gamma_{mo} - \gamma_i \quad (4)$$

where  $\gamma_{oxide}$  is the surface energy for either  $\text{Al}_2\text{O}_3$  or  $\text{MoO}_2$  and  $\gamma_{mo}$  is the Mo surface energy. Again, atomistic calculations provide the equilibrium energies:<sup>22,23</sup>

$\gamma_{\text{mo}} \approx 2.0 \pm 0.2 \text{ Jm}^{-2}$  and  $\gamma_{\text{Al}_2\text{O}_3} \approx 1 \pm 0.1 \text{ Jm}^{-2}$  for the basal plane. With these values, the work of adhesion is determined to be in the range,  $W_{\text{ad}} = 1.7 \pm 1.1 \text{ Jm}^{-2}$ .

This work of adhesion is typical of that found for many other metal/oxide interfaces.<sup>9</sup> It is also similar in magnitude to the measured debond energies,  $\Gamma_i$ . Consequently, there is a minimal contribution to  $\Gamma_i$  from plastic dissipation. Yet,  $\sigma_0$  is only somewhat larger than the range found for other metal/oxide interfaces, which exhibit much larger debond energies, ( $\Gamma_i \gg W_{\text{ad}}$ ). There is no obvious rationale, at this level of analysis, for the low  $\Gamma_i$  found for the Mo/Al<sub>2</sub>O<sub>3</sub> interface. Further understanding must be based on more quantitative measurements and calculations.

The continuum plasticity analysis of crack growth (Fig. 1) requires that  $\hat{\sigma}/\sigma_0 \lesssim 3$ , for the measured  $\Gamma_i/W_{\text{ad}}$  (1.5  $\rightarrow$  6.0). Consistency with Eqn. (2) thus requires that

$$\sigma_0 a_0 / W_{\text{ad}} \gtrsim 0.7 \quad (5)$$

For the Mo/Al<sub>2</sub>O<sub>3</sub> interface,  $a_0$  is not known. However, for similar interfaces, such as Nb/Al<sub>2</sub>O<sub>3</sub>, atomistic calculations give,  $a_0 \approx 0.3 \text{ nm}$ .<sup>25</sup> If this  $a_0$  is appropriate, since  $W_{\text{ad}} \approx 1/2 - 2 \text{ Jm}^{-2}$  and  $\sigma_0 \approx 300\text{--}600 \text{ MPa}$ , then  $\sigma_0 a_0 / W_{\text{ad}}$  is in the range  $0.05 \rightarrow 0.4$ . This does not satisfy Eqn. (5).<sup>†</sup> A full understanding of the debond energy must involve fine-scale plasticity phenomena occurring near the interface crack front.<sup>1,24</sup> The influence of this zone, width  $D$ , on the steady-state interface fracture energy (Fig. 16) provides perspective through the non-dimensional parameter,  $D \sigma_0^2 / EW_{\text{ad}}$ . Upon inserting measured values of  $\Gamma_i$ ,  $W_{\text{ad}}$  and  $\sigma_0$  for the Mo/Al<sub>2</sub>O<sub>3</sub> interface, Fig. 16 gives  $D \approx 25 \text{ nm}$ . Much larger values obtain for other metal/oxide interfaces ( $D \approx 0.2 \mu\text{m}$ <sup>24</sup>) because of the strong sensitivity of  $D$  to yield strength ( $D \sim \sigma_0^{-2}$ , Fig. 16). This analysis

<sup>†</sup> Moreover, in other metal/oxide interfaces, there is a more considerable discrepancy with Eqn (5).<sup>1</sup>

reinforces the need to understand fine-scale plasticity and its association with  $D$  for different metal/oxide interfaces.

The interface between Mo and low purity polycrystalline  $\text{Al}_2\text{O}_3$  has a considerably greater debond resistance than that between Mo and pure  $\text{Al}_2\text{O}_3$ . The development of silicate phases in the bond zone (by viscous flow out of the alumina) appears to be responsible. In this case, the fracture energy is similar to that for the silicate phase itself ( $\Gamma_i \approx 10 \text{ Jm}^{-2}$ ), which fractures as the bond separates. Similar results have been obtained for Pt/ $\text{Al}_2\text{O}_3$  interfaces.<sup>8</sup> This behavior is probably responsible for the 'high strength' that occurs when low purity  $\text{Al}_2\text{O}_3$  is bonded with Mo, for metal/ceramic seal technology.

## 6.2 Sliding

The observation of plastic grooving (Fig. 4), suggests that slip is controlled by shear yielding of the Mo. This should occur at a stress,  $\tau \approx \sigma_0/\sqrt{3}$ . Based on the hardness measurements for the sputtered Mo coatings ( $\sigma_0 \approx 600 \text{ MPa}$ ), sliding by shear yielding should occur at  $\tau \approx 340 \text{ MPa}$ . This is about twice the measured sliding resistance,  $\tau \approx 130\text{--}225 \text{ MPa}$  (Fig. 3). However, sliding only occurs at contact points along the interface (Fig. 4). By normalizing the sliding resistance with the ratio of the *contact area to fiber surface area*, the lower measured values are compatible with a plastic grooving mechanism.

## 7. CONCLUSIONS

The mechanical properties of molybdenum/alumina interfaces have been investigated. The fracture energy  $\Gamma_i$  was compared to the work of adhesion,  $W_{ad}$  estimated using AFM and TEM techniques. The range of values obtained for  $W_{ad}$  are similar to measurements for other metal/ceramic systems. However, unlike other

systems, the measured fracture energy is similar to the work of adhesion, indicating that plastic dissipation in the molybdenum is minimal. Furthermore, fractographic examinations of failed interfaces show no discernible deformation. Yet, quantitative distinctions between Mo/Al<sub>2</sub>O<sub>3</sub> and other metal/oxide interfaces, based on  $W_{ad}$  and the yield strength,  $\sigma_0$ , have not been identified. However, the inference that the zone of fine-scale plasticity occurring near the interface is smaller for Mo/Al<sub>2</sub>O<sub>3</sub>, than other interfaces is considered relevant. A full understanding awaits further analysis of fine-scale plasticity.

The interfacial fracture energies were found to be sensitive to the alumina purity but only weakly dependent on the method used to prepare the Mo. The apparent insensitivity to the Mo processing conditions may result from the presence of oxygen (in solution and as oxides), which was invariably present throughout the metal layer and at the interfaces. The role of oxygen in the fracture process remains unclear, in part because it is difficult to eliminate. The effect of alumina impurities appears to be relatively straightforward. The fracture energy is increased when the silicate phase migrates from the polycrystalline alumina to the Mo/sapphire interface. For this case the interface exhibits the fracture resistance of the amorphous *interphase*.

The sliding resistance,  $\tau$ , of the Mo/sapphire interface was found to be about half the shear yield strength of the metal. The basic scaling between  $\tau$  and  $\sigma_0$  has important ramifications for ductile coating concepts for ceramic matrix composites. Clearly, the coating yield strength emerges as a key parameter for controlling the interfacial sliding resistance.

**TABLE I**

**Structure Type, Space Group, Lattice Parameters, Wyckoff Position and Fractional Atom Coordinates for the Structures Identified in This Study**

Structure	Space Group	Unit cell (Å)	Atom	Fractional Coordinates		
Mo	$Im\bar{3}m$	$a = 3.1470$	Mo (2a)	0000	0000	0000
MoO <sub>2</sub>	$P2_1/c$	$a = 5.6109$ $b = 4.8562$ $c = 5.6285$ $\beta = 120.95$	Mo (4e) O <sub>1</sub> (4e) O <sub>2</sub> (4e)	2316 1123 3908	9916 2171 6969	0164 2335 2987
Al <sub>2</sub> O <sub>3</sub>	$R\bar{3}c$	$a = 4.754$ $c = 12.99$	Al (12c) O (18e)	0000 3064	0000 0000	3523 2500
Al <sub>2</sub> MgO <sub>4</sub>	$Fd\bar{3}m$	$a = 8.075$	Al (16d) Mg (8a) O (32e)	5000 1250 2510	5000 1250 2510	5000 1250 2510

## REFERENCES

- [1] A.G. Evans and B.J. Dalgleish, *Acta Metall. Mater.*, **40** (1992) S295.
- [2] N.P. O'Dowd, M.G. Stout and C.F. Shih, *Phil. Mag. A*, **V66**[6] (1992) 1037-64.
- [3] B. Gibbeschg and G. Elsner, *Acta Metall. Mater.*, **40** (1992) 59.
- [4] B.J. Dalgleish, K.P. Trumble and A.G. Evans, *Acta Metall. Mater.*, **37** (1989) 1923.
- [5] G. Beltz and J.R. Rice, *Acta Metall. Mater.*, **40** (1992) S321-S331.
- [6] I.E. Reimanis, B.J. Dalgleish and A.G. Evans, *Acta Metall. Mater.*, **39** (1991) 3133.
- [7] A. Bartlett and A.G. Evans, *Acta Metall. Mater.*, **41** (1993) 497-504.
- [8] M. De Graef, M.R. Turner, B.J. Dalgleish and A.G. Evans, *Acta Metall. Mater.*, **40** (1991) S333.
- [9] A.G. Evans, M. Rühle, B.J. Dalgleish and P.G. Charalambides, *Mat. Sci. Eng.*, **A126** (1990) Se.
- [10] J.B. Davis, J.P.A. Löfvander, E. Bischoff, A.G. Evans and M.L. Emiliani, *J. Am. Ceram. Soc.*, **76**[5] (1993) 1249-57.
- [11] J.R. Rice and J.S. Wang, *Mat. Sci. Eng.*, **A107** (1989) 23-40.
- [12] V. Tvergaard and J.W. Hutchinson, *J. Mech. Phys. Solids*, **40**[6] (1992) 1377-97.
- [13] J.R. Smith, H. Schlosser, J. Ferrante, *Phys. Rev. B*, **44**[17] (1991) 9696-9699.
- [14] M.Y. He, A.G. Evans and W.A. Curtin, *Acta Metall. Mater.*, **41** (1993) 871.
- [15] D. Walls, G. Bao and F.W. Zok, *Scripta Metall. Mater.*, **25** (1991) 911.
- [16] O. Sbaizero, C. Horn, F.W. Zok and A.G. Evans, *J. Am. Ceram. Soc.*, **74**[1] (1991) 187-93.
- [17] P. Warren, T.J. Mackin and A.G. Evans, *Acta Metall. Mater.*, **40**[6] (1992) 1243-49.
- [18] P.G. Charalambides, J. Lund, R.M. McMeeking and A.G. Evans, *J. Appl. Mech.*, **111** (1989) 77.
- [19] J.B. Davis, G. Bao, H.C. Cao and A.G. Evans, *Acta Metall. Mater.*, **39**[5] (1991) 1019-24.
- [20] C. Liang and J.W. Hutchinson, *Mech. of Mtls.*, **14**[3] (1993) 207-21.
- [21] J.F.W. Bishop and R.J. Hill, *Phil. Mag.*, **42** (1951) 414.

- [22] D. Wolf, *Jnl. Appl. Phys.*, **69**[1] (1991) 185.
- [23] M. Finnis, to be published.
- [24] Z. Suo and C.F. Shih, *Acta Metall. Mater.*, **41** [5] (1993) 1551.

## FIGURE CAPTIONS

- Fig. 1. Effects of the ratio of yield strength,  $\sigma_0$ , to the bond strength,  $\hat{\alpha}$  on the relative debond resistance of metal/ceramic interfaces (Tvergaard and Hutchinson):<sup>12</sup> calculations performed assuming continuum plasticity.
- Fig. 2. Optical observation of debonded region at Mo/sapphire interface.
- Fig. 3. Typical push-out curve for Mo-coated sapphire fibers in an  $\text{Al}_2\text{O}_3$  matrix.  $\tau$  is the sliding stress.
- Fig. 4. SEM image of push-out zone showing grooves on Mo.
- Fig. 5. TEM view of faceted Mo grains  $\sim 100$  nm in diameter in as-deposited Mo film.
- Fig. 6. Diffraction patterns of sputtered Mo film, which indicate a common  $\langle 111 \rangle$  zone; a) measured pattern, b) simulated pattern.
- Fig. 7. SEM image of sapphire fracture surface showing metal oxide attached to sapphire. The light grey grains are  $\text{MoO}_2$ .
- Fig. 8. TEM image of continuous oxide layer formed with lower purity  $\text{Al}_2\text{O}_3$ .
- Fig. 9. a-c) Diffraction patterns for the  $[101]$ ,  $[102]$  and  $[213]$  zone axes. d-f) Corresponding simulated patterns.
- Fig. 10. Diffraction patterns for Mo oxide indicating orientation relationships.
- Fig. 11. Oxygen sublattice of  $(0001)$  sapphire resembles that of  $(001)$   $\text{MoO}_2$ .
- Fig. 12. TEM imaged  $\text{MgAl}_2\text{O}_4$  spinel at the interface between  $\text{Al}_2\text{O}_3$  and Mo.
- Fig. 13. TEM image of a non-planar interface between sapphire and Mo with no orientation relationship.
- Fig. 14. TEM image of dihedral angles (arrowed) formed between a sapphire fiber and Mo grain boundaries.



Fig. 15. a) AFM trace across Mo grain boundaries at the interface. b) Corresponding image. The grain boundary at 0 is highlighted by the arrows on the trace in (a).

Fig. 16. Effects of fine-scale plasticity in a zone, width  $D$ , on the steady-state debond energy,  $\Gamma_s$ .

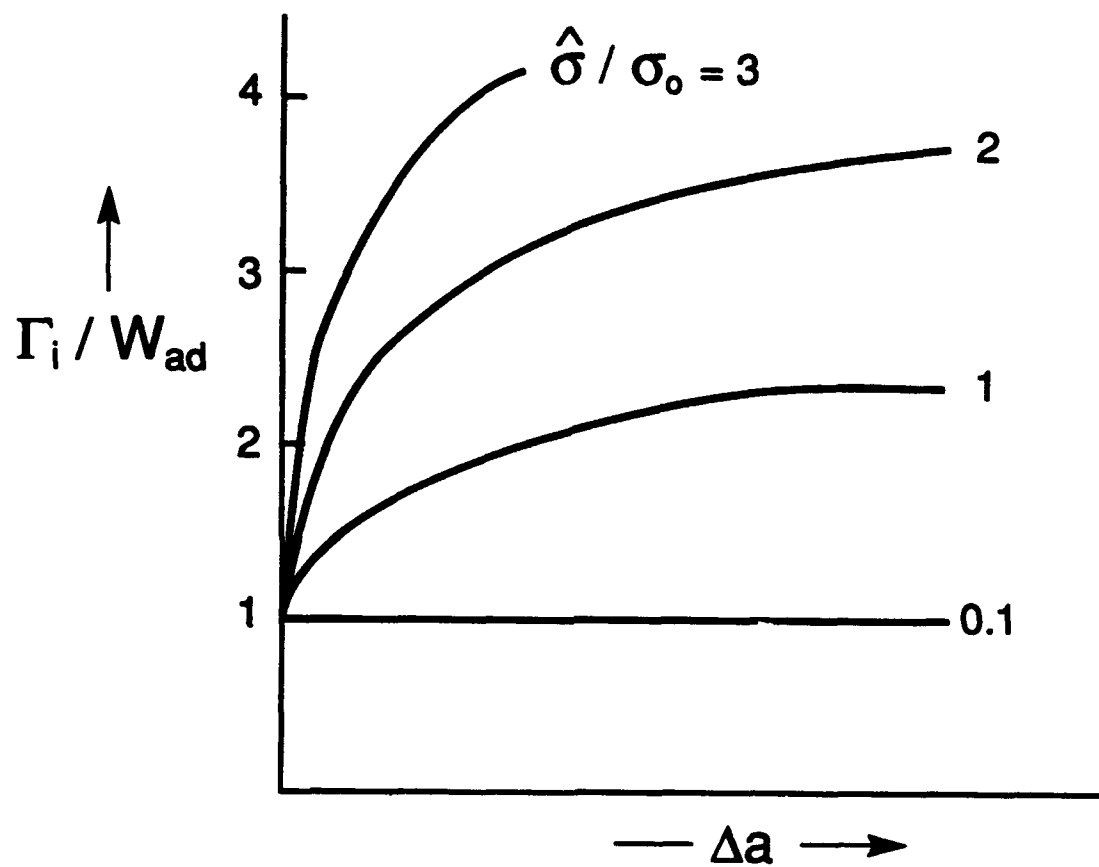


Figure 1

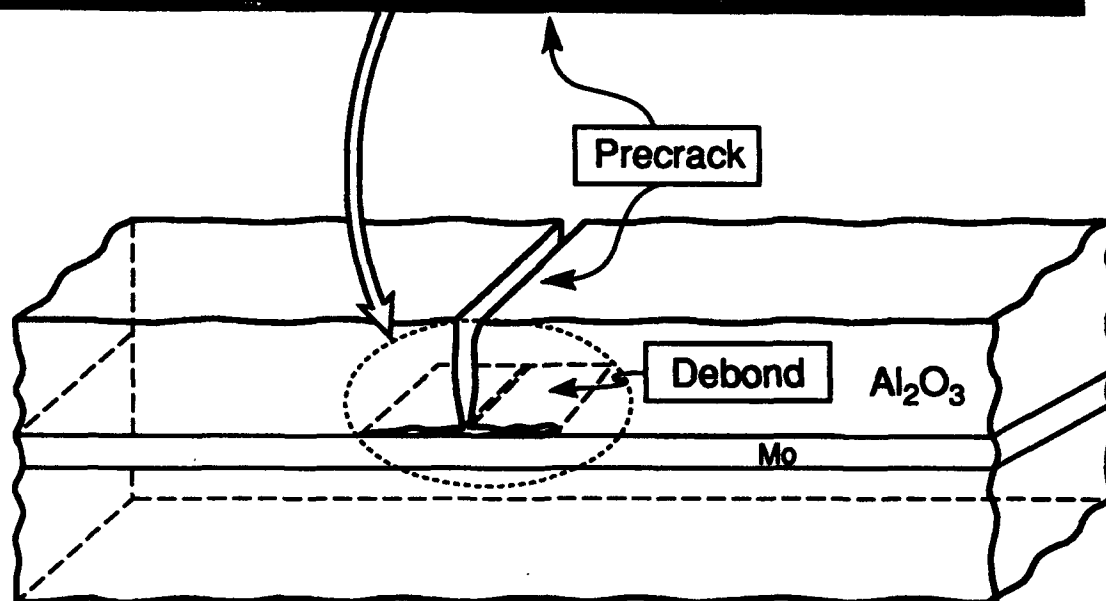
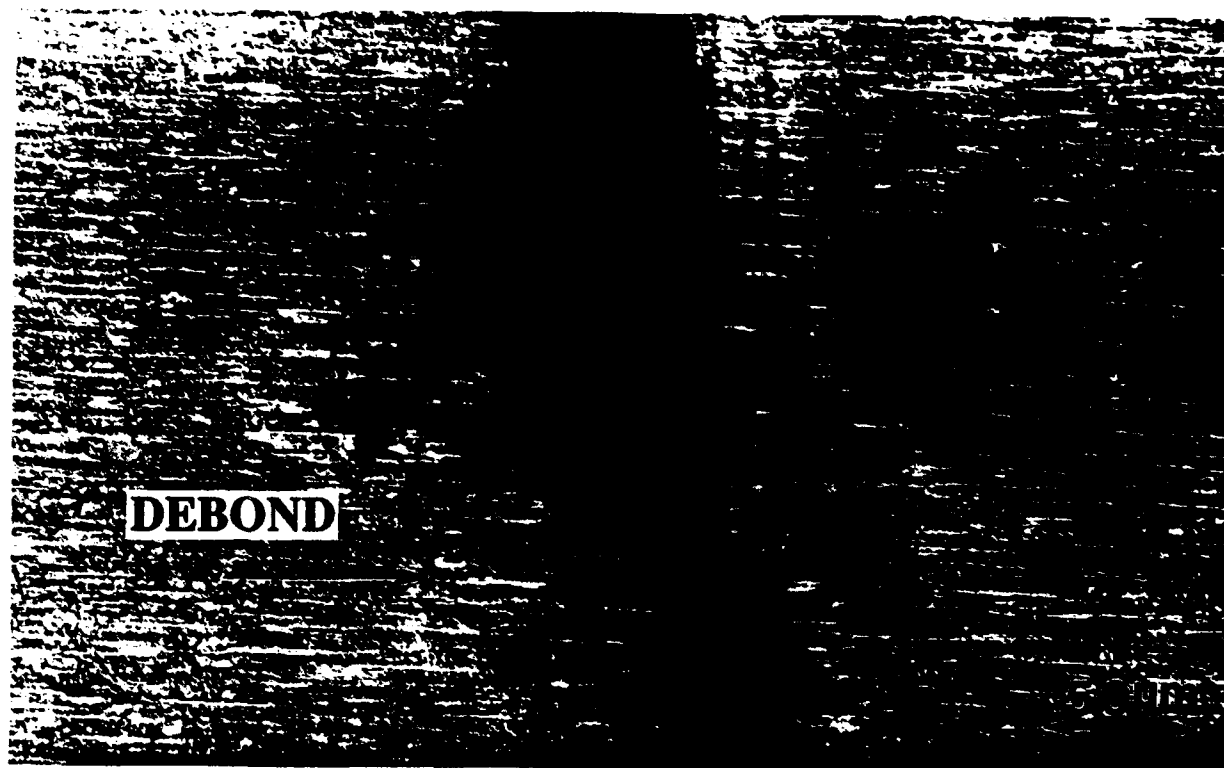


Figure 2

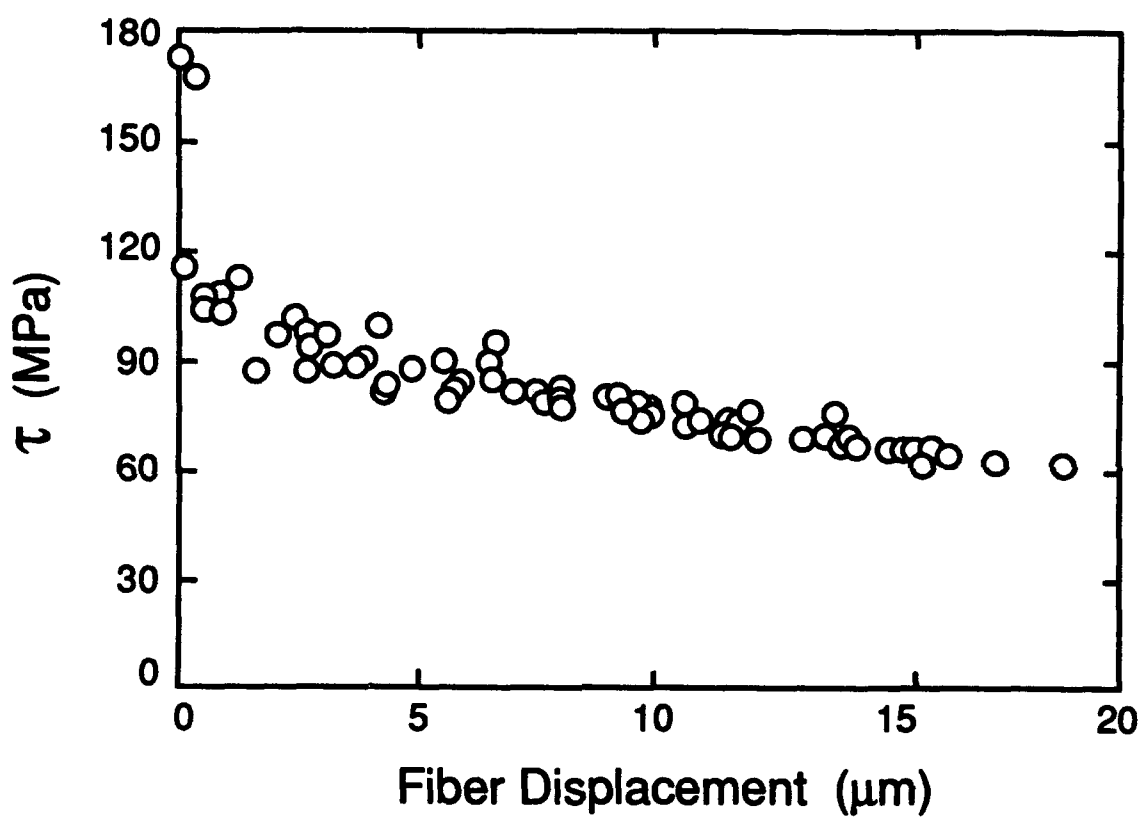


Figure 3



Figure 4

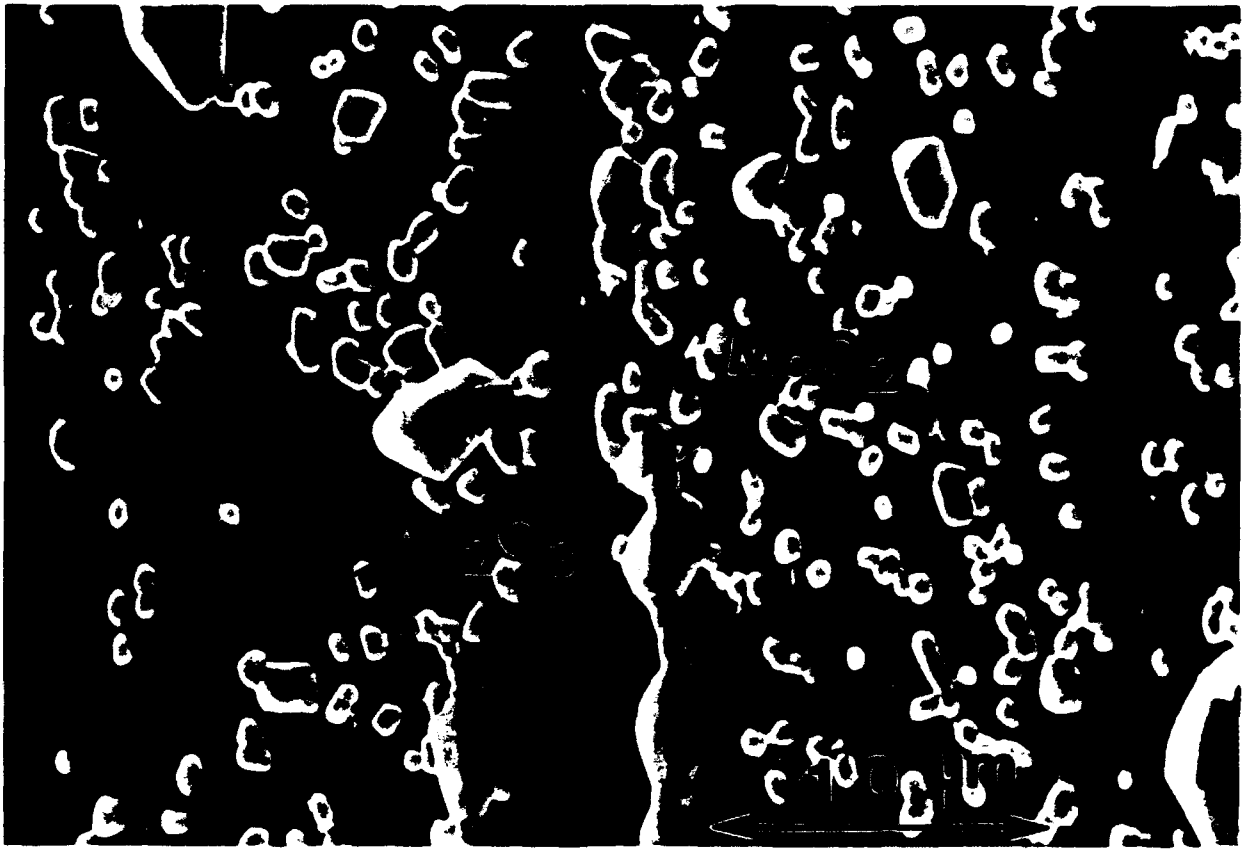


Figure 7



Figure 8

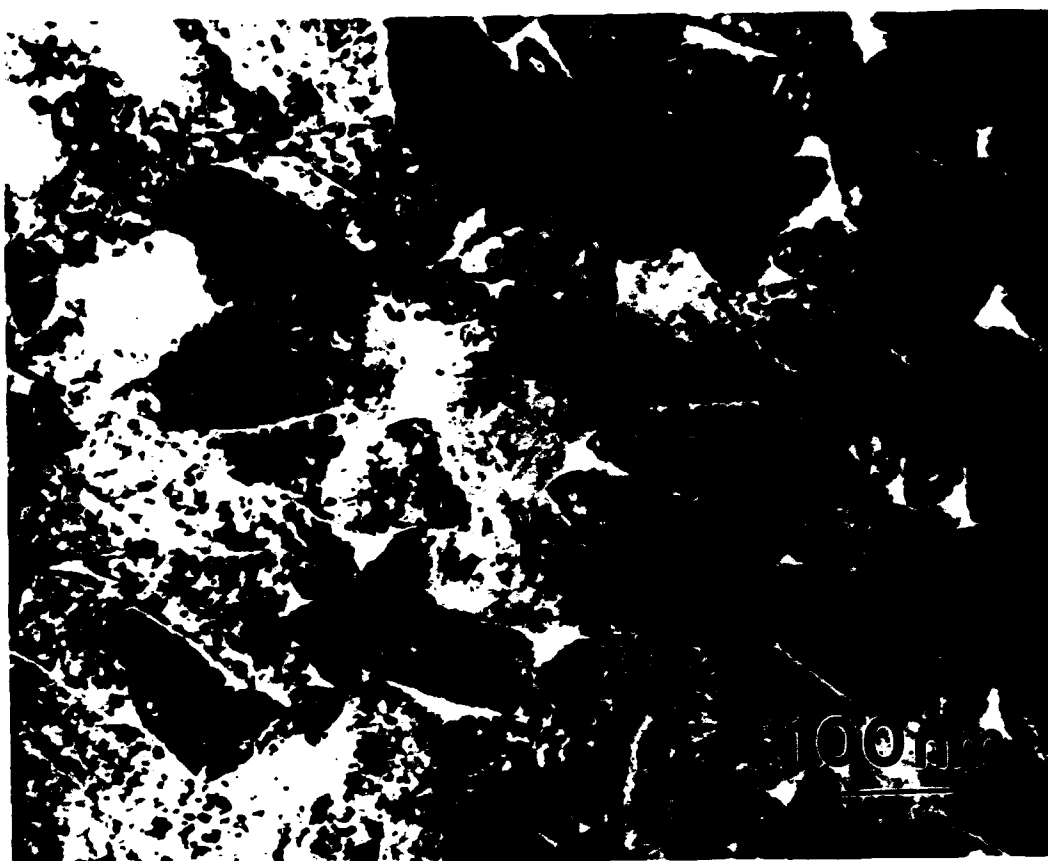


Figure 5



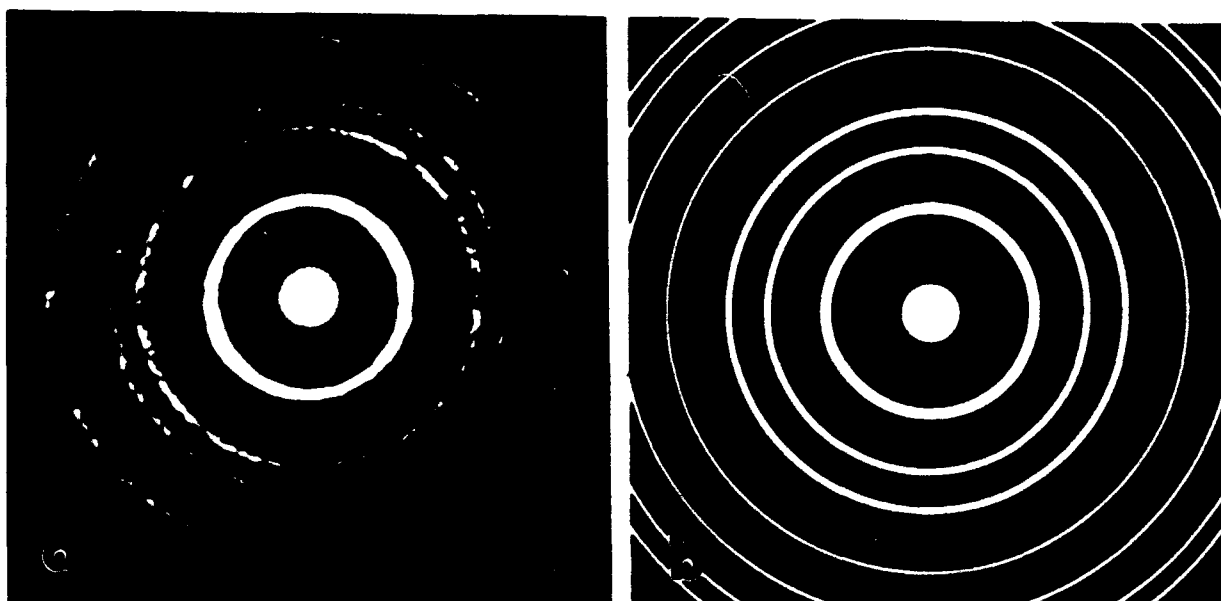


Figure 6

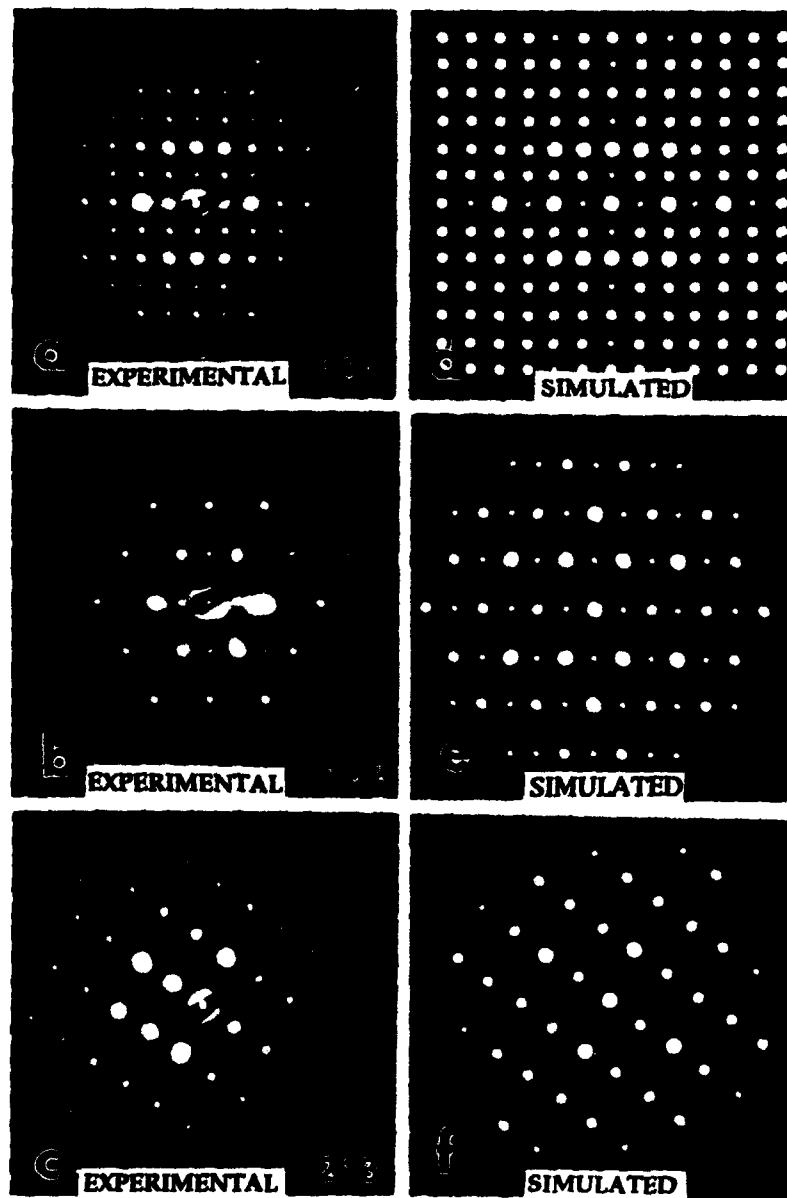


Figure 9

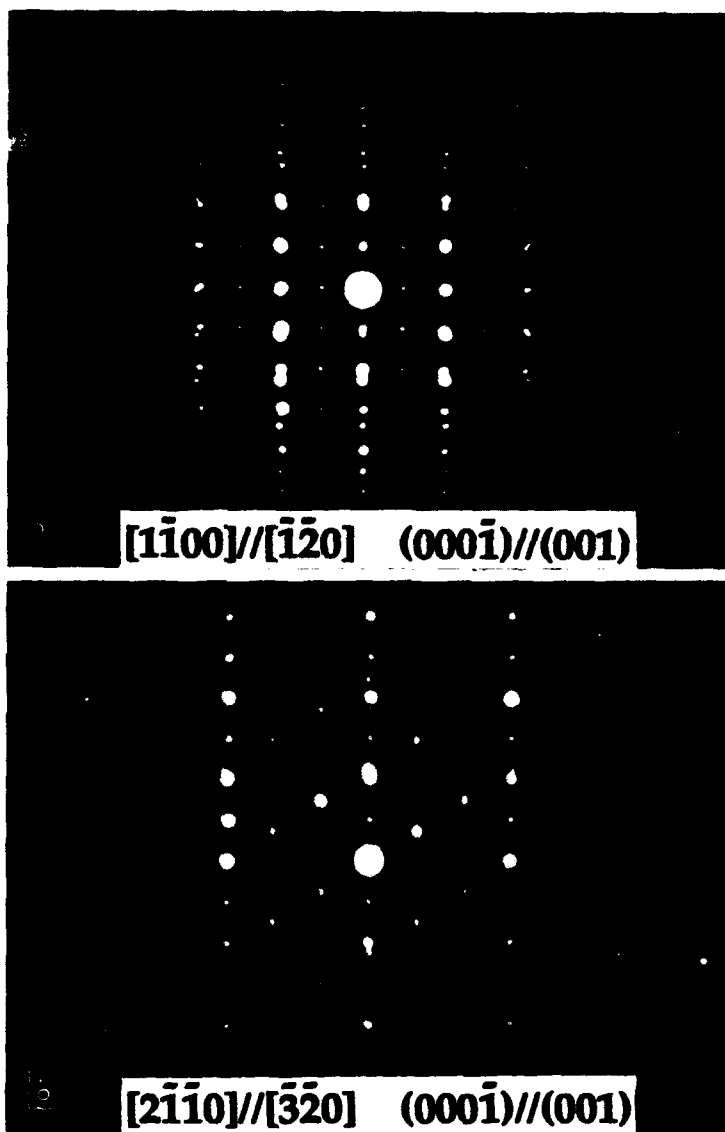
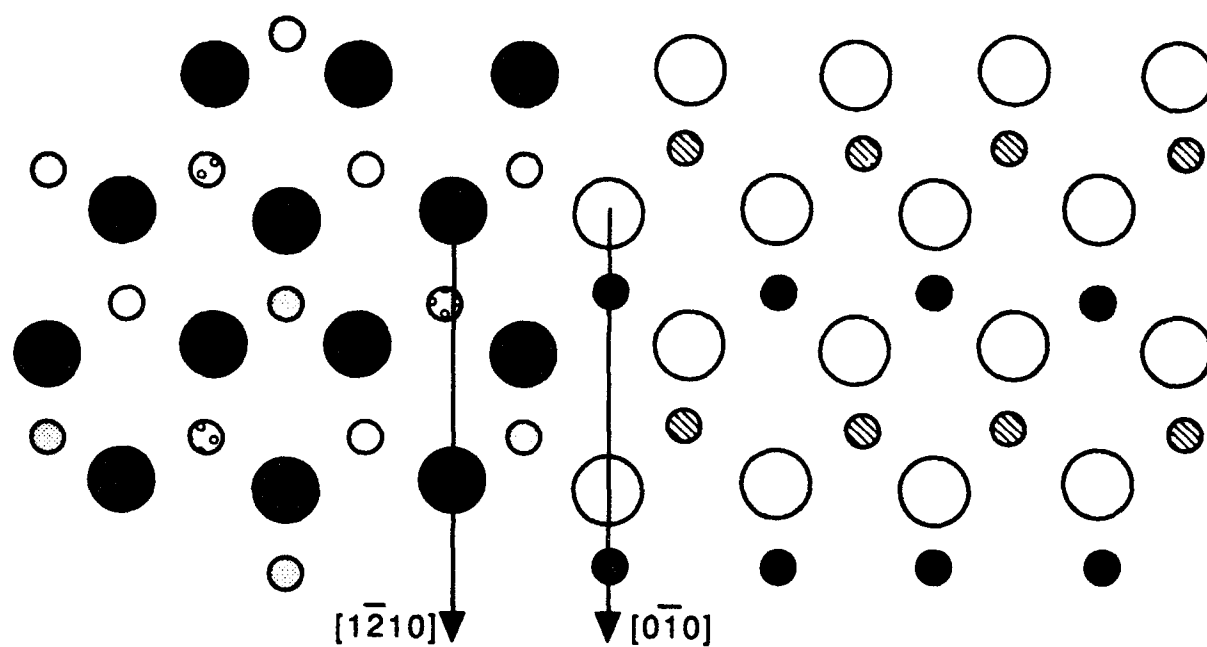


Figure 10



● O atom in sapphire in the plane

○ O atom in MoO<sub>2</sub> (+/- 0.32Å)

⊙ Al 0.85Å above plane

○ Al 0.83Å below plane

○ Al 1.32Å below plane

⊙ Mo 1.05-1.20Å above plane

● Mo 1.13-1.21Å below plane

Figure 11



Figure 12

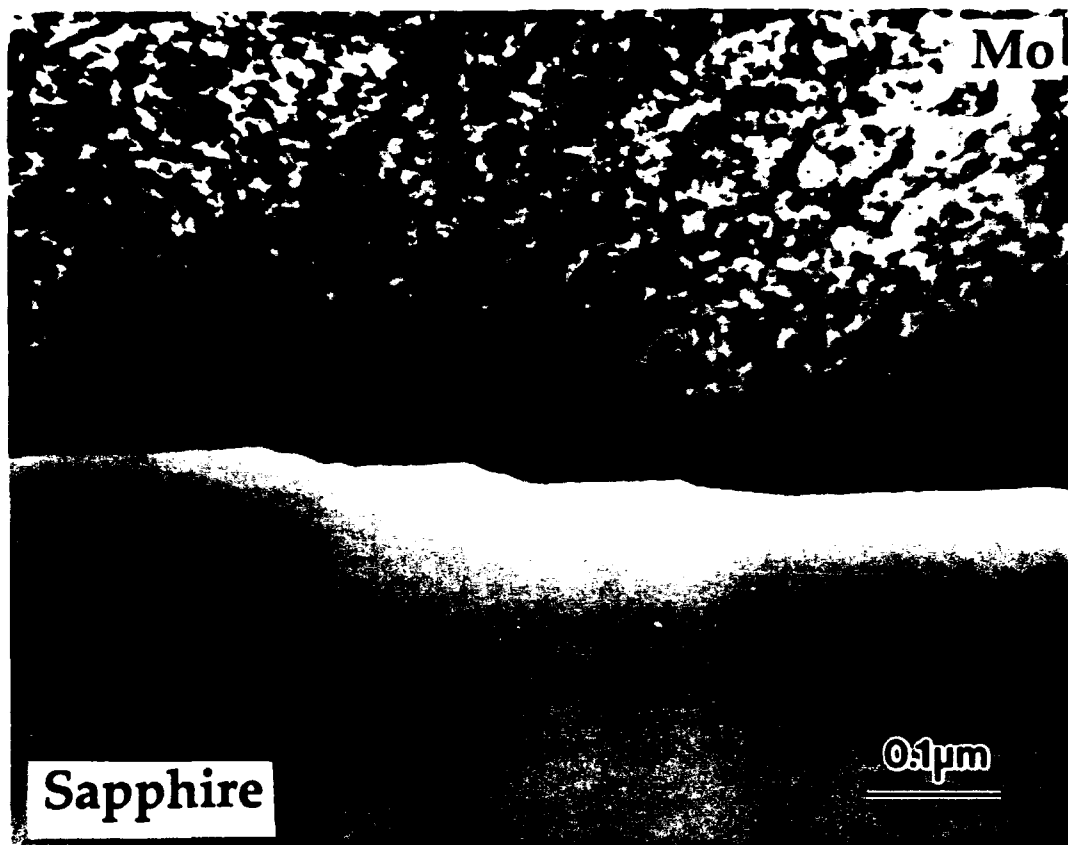


Figure 13

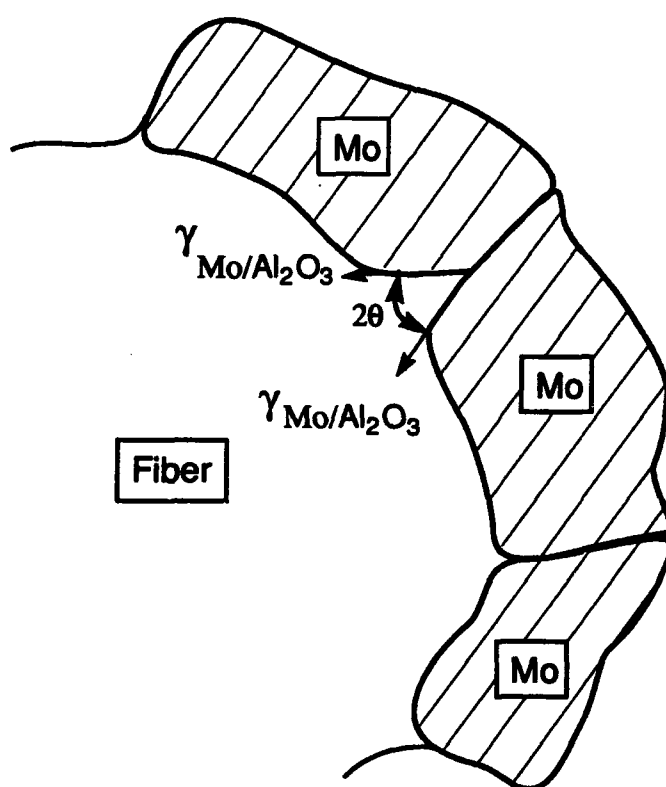


Figure 14

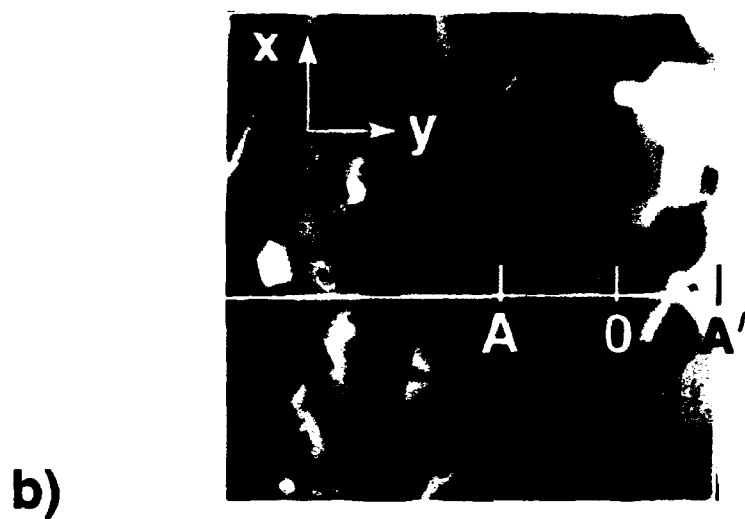
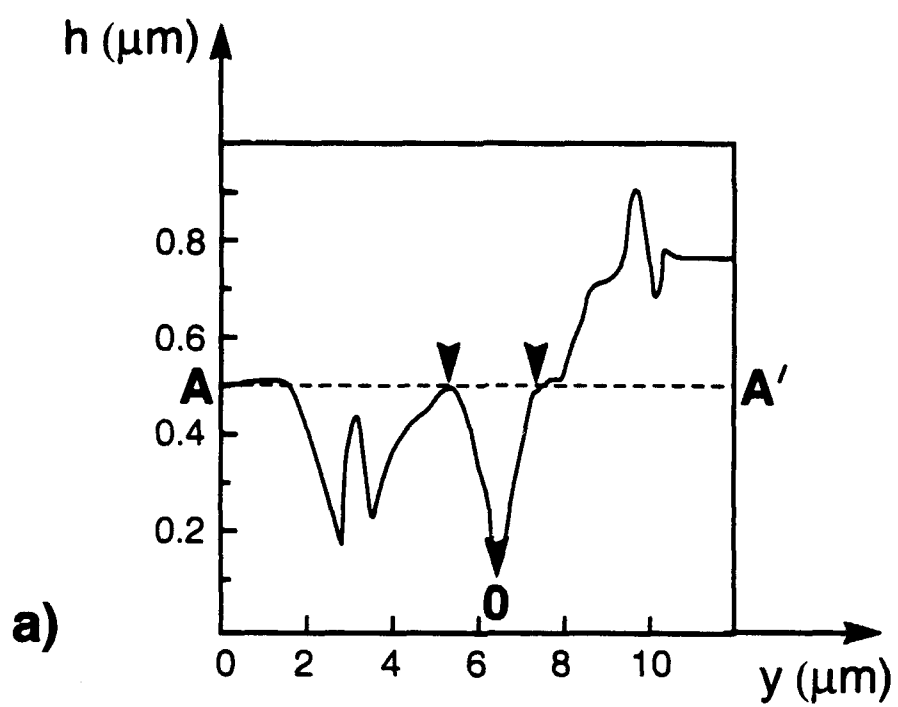


Figure 15



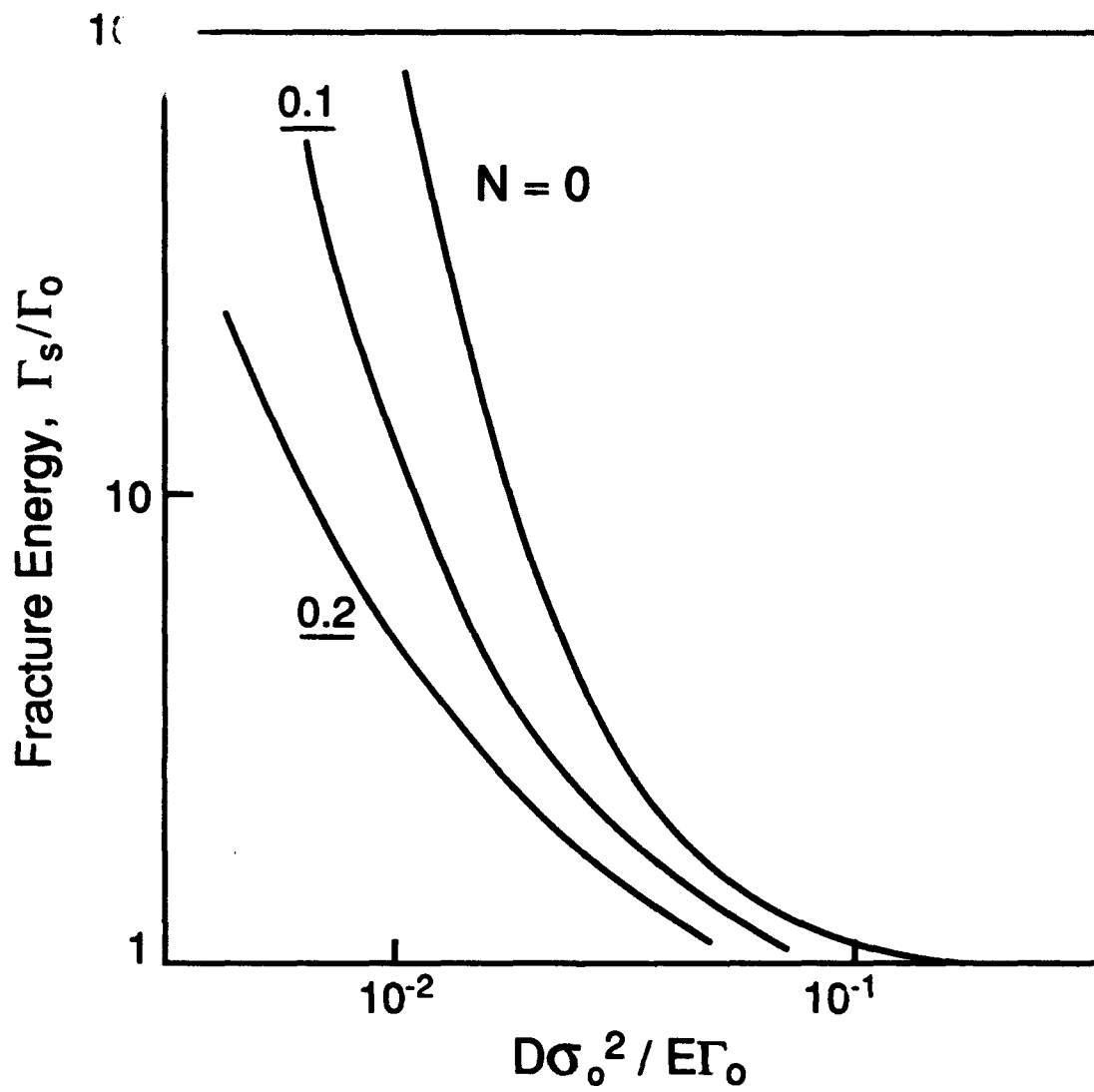
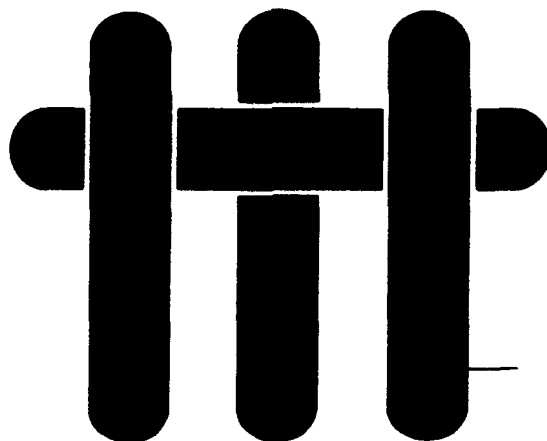


Figure 16

# M A T E R I A L S



## FATIGUE CRACK GROWTH AND STRESS REDISTRIBUTION AT INTERFACES

by

M.C. Shaw,<sup>†‡</sup> D.B. Marshall,<sup>‡</sup> B.J. Dalgleish,<sup>\*</sup> M.S. Dadkhah,<sup>‡</sup> M.Y. He,<sup>†</sup> and A.G. Evans<sup>†</sup>

<sup>†</sup>Materials Department  
College of Engineering  
University of California, Santa Barbara  
Santa Barbara, California 93106-5050

<sup>‡</sup>Rockwell Science Center  
Camino Dos Rios  
Thousand Oaks, California 91360

<sup>\*</sup>Department of Materials Science  
University of California, Berkeley  
Berkeley, California 94720

## ABSTRACT

The role of the interface in redistributing stress around cracks in multilayered ceramic/metal composites is investigated. The emphasis is on the different effects of interfacial debonding or of plastic slip in the metal phase adjacent to strongly bonded interfaces. The experiments are conducted on alumina/aluminum multilayered composites. Monotonic loading precracked test pieces causes plastic shear deformation within the aluminum layer at the tip of the notch without debonding. However, interfacial debonding can be induced by cyclic loading, in accordance with a classical fatigue mechanism. Measurements of the stress around the crack demonstrate that debonding is much more effective than slip at reducing the stress ahead of the crack.

## 1. INTRODUCTION

In layered materials with alternating ductile and brittle constituents, various modes of crack growth are possible.<sup>1-6</sup> Under in-plane loading, cracks form in the brittle layers. A crack in one layer may induce cracks in an adjacent layer. Whether or not this occurs depends upon the nature of the stress concentration transmitted across the intervening ductile material. If this stress concentration is large, a series of near-coplanar cracks form, which can be viewed as a single, *dominant crack*. Conversely, a weakened stress concentration allows *distributed damage*. The stress concentration may be reduced either by debonding at the interface between the brittle and ductile layers or plastic slip within the ductile layers. An asymptotic calculation<sup>6</sup> (Fig. 1) predicts that debonding is more effective than slip at reducing the peak stress in the intact brittle layers and hence, should suppress crack renucleation. This prediction has yet to be verified by experiment.

The incidence of debonding, as opposed to slip adjacent to interfaces is influenced by the loading history. Interfaces that remain bonded upon monotonic loading may debond upon cyclic loading.<sup>7</sup> Moreover, the ratio of mode II (shear) to mode I (tensile) loading acting upon an interface crack may affect the relative tendencies for debonding and slip.<sup>8</sup>

The three objectives of this study are as follows. (i) Contrast the debonding and sliding characteristics of interfaces subject to monotonic and cyclic loads. (ii) Examine the validity of models for the role of debonding and sliding on stress redistribution. This is achieved by comparing predicted stresses with measured stresses. For this purpose, the fluorescence spectroscopy method is used with aluminum oxide/Al multilayers. (iii) Establish the basic mechanism of cyclic debonding (fatigue) at metal/ceramic interfaces.

## 2. EXPERIMENTAL METHODS

### 2.1 Materials

Multilayered composites of Al and  $\text{Al}_2\text{O}_3$  were prepared by diffusion bonding.<sup>1,4</sup> For this purpose, thin discs of sapphire and polycrystalline  $\text{Al}_2\text{O}_3$  were mechanically polished with diamond, to produce planar, parallel surfaces, which were then heat treated in air at  $1000^\circ\text{C}$  for 1 h to remove carbon based impurities. Thin sheets of Al (40, 100 or  $250\text{ }\mu\text{m}$  thick) were prepared from 99.99% pure foils by cold rolling. These were interspersed between the sapphire and  $\text{Al}_2\text{O}_3$  plates, with a sapphire layer on one outside surface and  $\text{Al}_2\text{O}_3$  layers elsewhere. The layers were then vacuum hot pressed at temperatures of  $640^\circ\text{C}$  at a compressive stress of  $\sim 5\text{ MPa}$  for 48 h, resulting in a diffusion bond with essentially no residual porosity.

The diffusion-bonded discs were cut into beams suitable for flexural testing (dimensions  $\sim 3 \times 3.5 \times 50\text{ mm}$ ) by using a diamond saw. Both side surfaces were polished to an optical finish to facilitate observations of interfacial debonding and crack growth, as well as for stress measurements.

### 2.2 Mechanical Tests

The location of the dominant crack in each specimen was pre-determined by placing a row of 50 N Knoop indentations,  $500\text{ }\mu\text{m}$  apart, into the sapphire surface (Fig. 2). Direct observation of the specimen, using a long focal length optical microscope, revealed that these indentations produced precracks approximately  $50\text{--}100\text{ }\mu\text{m}$  in length. The specimen was then loaded in four-point flexure with the indented surface in tension, within a fixture that permitted *in situ* monitoring of the side surfaces of the beams by using an optical microscope (Fig. 2). At a critical load, the flaws coalesced into a crack that propagated unstably, but arrested at the metal/sapphire interface.

These precracked specimens were loaded either monotonically or cyclically in four-point flexure. During each cyclic loading experiment, the range of load,  $\Delta P$ , and the peak load,  $P_{\max}$ , were kept constant. The tests were interrupted after 1000, 5000 and 20,000–50,000 cycles to allow observation of the interface between the sapphire and the first aluminum layer. Interfacial debond cracks (Fig. 3a, b) were characterized by viewing through the transparent sapphire using an optical microscope. The growth rates of interfacial cracks were also determined in this manner. Following the cyclic experiments, the interfacial cracks were characterized further by scanning electron microscopy, after removal of the sapphire layer by fracture of the specimen.

### 2.3 Stress Measurement

After cycling, some specimens were reloaded in flexure, using a fixture located on the stage of a Raman microprobe.<sup>†</sup> This apparatus allows stress measurement by fluorescence spectroscopy within the  $\text{Al}_2\text{O}_3$ .<sup>9</sup> The loads were monitored using a miniature load cell. Chromium fluorescence spectra were collected at sites within the intact  $\text{Al}_2\text{O}_3$  layer ahead of the precrack, as indicated in Fig. 2, with the specimen in both the loaded and unloaded states. Analysis of these spectra gave fluorescence peak locations that provided a measure of the stress in the  $\text{Al}_2\text{O}_3$  layer: the relation between peak shift and stress was obtained from a separate series of calibration experiments (Section 4.1). In polycrystalline alumina, the method has ~ 20 MPa stress resolution and 100–200  $\mu\text{m}$  spatial resolution.<sup>9-11</sup>

In some cases, the precrack was extended into the underlying  $\text{Al}_2\text{O}_3$  layers by monotonic loading. Again, cyclic loading experiments were conducted and the responses of the intervening Al layers were characterized by using both optical and scanning electron microscopy (SEM).

---

<sup>†</sup> Instruments SA, Model U1000.

### 3. INTERFACE RESPONSE

Monotonic loading of precracked specimens caused plastic slip within the metal layer at the tip of the precrack, prior to crack renucleation in the next  $\text{Al}_2\text{O}_3$  layer. The characteristics of such plasticity have been measured using high-resolution strain mapping techniques.<sup>4</sup> Cracks formed sequentially in adjacent polycrystalline  $\text{Al}_2\text{O}_3$  layers, with increasing load. Each crack was nearly coplanar with the precrack. By considering this assembly as a dominant, mode I crack and by measuring its length, a nominal crack growth resistance,  $K_R$ , was determined from the applied loads (Fig. 4).

Cyclic loading of similar precracked specimens gave a different response. When the peak load was below that at which a crack renucleated in the next  $\text{Al}_2\text{O}_3$  layer, *stable debonding* occurred along the sapphire/Al interface (Fig. 3). The crack growth rate,  $da/dN$ , was found to decrease slightly with increase in crack length,  $L_a$ , for a given load range,  $\Delta P$  (typically by a factor of 2–4 after 20,000–50,000 cycles). After fracturing the specimen to remove the sapphire from the region above the interface fatigue crack, classical fatigue striations were observed by scanning electron microscopy on the Al crack surface (Fig. 5). In the case shown in Fig. 5, the striation spacing is about equal to the crack extension per cycle ( $\sim 1 \mu\text{m}/\text{cycle}$ ). Moreover, the striations are strongly affected by crystallography, having different orientations in different grains (Fig. 5b). The basic crack growth mechanism thus appears to be similar to that occurring in monolithic alloys.<sup>12-15</sup>

The range of energy release rates,  $\Delta G$ , applicable to each cyclic loading experiment was estimated from the load range,  $\Delta P$ , by using a previous analysis of the flexural geometry (Fig. 2).<sup>16,17</sup> The analysis provides solutions for steady-state cracks ( $L_s/a_0 > 0.4$ ) in homogeneous elastic beams with no residual stress.<sup>17</sup> The estimates were obtained by neglecting the effect of residual stress and plasticity in the metal on  $G$

and by using the steady-state formulae. The present results were obtained for  $0.2 < L_s/a_0 < 4.0$ , except for the lower left point in Fig. 6, where  $L_s/a_0 \sim 0.04$ . Note that these results refer to mixed-mode cyclic debonding<sup>16</sup> with a mode mixity,  $\psi \approx 50^\circ$ . These values of  $\Delta G$ , in conjunction with the crack growth rates per cycle,  $da/dN$ , allow comparison with fatigue data for monolithic aluminum alloys obtained from the literature (Fig. 6 and Table I).<sup>18-20</sup> It is evident that the rates of cyclic interfacial debonding exceed the mode I fatigue crack growth rates for monolithic alloys, at all  $\Delta G$  used during the present investigation. Therefore, *mixed-mode* fatigue crack growth can occur along strongly bonded metal/ceramic interfaces in preference to mode I crack growth through the alloy. These interface measurements complement data obtained previously in mode I.<sup>7</sup>

Conversely, in specimens that had been loaded monotonically to grow a crack through *several*, successive  $Al_2O_3$  layers, subsequent cyclic loading caused rapid fatigue failure of the intervening, intact Al layers. This occurred by mode I cyclic growth emanating from cracks in the adjacent alumina layers (Fig. 7). Similar results have been reported for multilayered intermetallic/metal composites.<sup>21</sup>

## 4. STRESS MEASUREMENTS AND COMPARISON WITH THEORY

### 4.1 Piezospectroscopic Calibration

The relationship between the applied stress,  $\sigma_{ij}$ , and the fluorescence peak shift,  $\Delta v$ , is a tensorial relation,<sup>10</sup>

$$\Delta v = \Pi_{ij} \sigma_{ij} \quad (1)$$

where  $\Pi_{ij}$  are the piezospectroscopic coefficients. It has been shown that the off-diagonal components of  $\Pi_{ij}$  are negligibly small for the fluorescence peaks of chromium



in aluminum oxide.<sup>10</sup> This expression may be further simplified for a polycrystalline material to<sup>10</sup>

$$\Delta v = Q \sigma_{kk} \quad (2)$$

where  $Q = 1/3 (\Pi_{11} + \Pi_{22} + \Pi_{33})$  and  $\sigma_{kk}$  is the sum of the principal stresses,  $\sigma_{kk} = \sigma_{11} + \sigma_{22} + \sigma_{33}$ .

The coefficient,  $Q$ , for the stress dependence of the  $R_2$  chromium fluorescence peak in the alumina used in the present case was calibrated by collecting spectra from the side surface of a polished alumina beam subjected to various levels of four-point flexural loading. These spectra were analyzed to yield the relative peak position as a function of applied stress (Fig. 8). From these results,  $Q = 2.48 \pm 0.05 \text{ cm}^{-1}/\text{GPa}$ : consistent with values previously reported for alumina ( $2.46\text{--}2.52 \text{ cm}^{-1}/\text{GPa}$ ).<sup>10</sup>

## 4.2 Stresses

The distributions of stress before and after monotonic and cyclic loading were measured by optical fluorescence. In each specimen, the measurements were obtained from the first intact  $\text{Al}_2\text{O}_3$  layer along a line  $20 \mu\text{m}$  from the interface with the metal layer. Typical results are shown in Fig. 9. The stress distribution during monotonic loading (at  $K = 7 \text{ MPa}\sqrt{\text{m}}$ ) exhibited a broad maximum ahead of the crack front. After unloading, the stress along the same line exhibited a minimum ahead of the crack front (Fig. 9). The measured peak stress at the maximum load is similar to that given by the solution for a homogeneous elastic body (Appendix A), consistent with previous measurements in other ceramic/metal multilayered composites.<sup>4,11</sup> These have shown that slip in the metal layer does not diminish the  $\sigma_{yy}$  stress in the ceramic layer ahead of the crack tip (Fig. 1) significantly, unless the relative slip length,  $L_p/h$ , is large ( $> 10$ ).<sup>6</sup>

After cyclic loading to attain a debond length,  $L_s > 2 \text{ mm}$ ,<sup>‡</sup> the stress concentration ahead of the crack was found to be eliminated, within the sensitivity of the fluorescence measurements (Fig. 9). Comparison of this result with analysis is complicated by finite geometry effects: because of the large values of the ratio: debond length/precrack length,  $L_s/h \approx 5$ , the asymptotic solution (Fig. 1) is not relevant. A finite element solution has thus been obtained for the specific flexural geometry used in these tests. The solution (Fig. 10) establishes that, for  $L_s/a_0 \approx 5$ , the stress concentration ahead of the precrack is, indeed, eliminated. These measurements and calculations directly confirm that debonding is more effective than plastic slip at reducing the stress ahead of a crack in ceramic/metal multilayers.

## 5. FATIGUE CRACK TRAJECTORIES

Two trajectories are possible for a fatigue crack arrested at the interface (Fig. 11). The crack may propagate into the metal under essentially mode I conditions (Fig. 7). Alternatively, it may deflect and propagate along the interface (Fig. 3). The parameters controlling the choice between these two trajectories are the relative strain energy release rate ranges,  $\Delta G$ , the crack growth rates,  $da/dN$  and the mode mixity,  $\Psi$ . For a surface crack,  $\Delta G$  for mixed mode growth along the interface is *less* than  $\Delta G$  for mode I growth through the Al alloy (Appendix B). Nevertheless, in flexural loading, for which  $\Psi \approx 50^\circ$ <sup>8</sup> (Section 3), growth along the interface is preferred for both the Al/sapphire and the Al/polycrystalline alumina interfaces. This behavior arises because at given  $\Delta G$ , the mixed-mode interfacial crack growth rate,  $da/dN$  is *larger* than the mode I growth rate through the alloy (Fig. 12), as elaborated in Appendix B.

---

<sup>‡</sup> ( $\Delta K = 5 \text{ MPa}\sqrt{\text{m}}$  and  $K_{\text{max}} = 7 \text{ MPa}\sqrt{\text{m}}$ )

The preference for fatigue crack growth through the metal rather than along the interface when the metal layer is one of the intact ligaments remaining after monotonic cracking of several ceramic layers, as in Fig. 7, now remains to be explained. The relative values of  $\Delta G$  for interfacial debonding and growth through the Al alloy are essentially the same as for the surface crack (Appendix B). One significant difference, however, is the mode mixity. For interfacial debonding at metal ligaments, the loading is mode II<sup>8</sup> ( $\Psi = 90^\circ$ ). It is likely that mode II cyclic debond rates are considerably lower than those measured in mixed mode, because of crack face contact.<sup>22,23</sup> It is plausible that the debond rate is reduced to such a level that mode I ligament failure is preferred. If these arguments are correct, the effect of mode mixity on the cyclic debonding of the interface has major implications for the fatigue performance of multilayers.

The basic mechanisms that determine the different cyclic crack growth rates are governed by the cyclic stresses and strains that occur near the crack tip. For a crack near a bimaterial interface, the cyclic shear stresses can exceed those expected in a monolithic alloy.<sup>24</sup> These large stress amplitudes should coincide with a larger cyclic growth rate near the interface, at the equivalent loading mode. However, a comprehensive analysis that relates these stress amplitudes to crack growth for a range of mode mixities is needed to rationalize the behaviors found in this study.

## 6. CONCLUDING REMARKS

Two competing mechanisms of fatigue cracking have been observed in  $\text{Al}_2\text{O}_3/\text{Al}$  multilayers. Mixed-mode cracks extend along the metal/ceramic interfaces, normal to the tip of a main crack, in accordance with a classical fatigue mechanism. Conversely, intact metal ligaments rupture rapidly by mode I fatigue crack growth. The interfacial cracking at the crack tip has the *beneficial* effect of reducing the stresses ahead of the

main crack and thereby suppressing further growth of that crack. The rupture of ligaments in the crack wake is detrimental, because it reduces the crack tip shielding imparted by the bridging ligaments. This duality in fatigue behavior might be exploited in order to optimize the fatigue resistance of metal/ceramic multilayers.

The mixed mode fatigue crack growth rate along the Al/Al<sub>2</sub>O<sub>3</sub> interface exceeds the mode I rate in monolithic Al alloys. The large growth rate arises because of the enhanced shear stress amplitude at the tip when the crack is at a bimaterial interface.<sup>25</sup> Further analysis of the relationship between the growth rates in the interface and the alloy is in progress.

The experimental measurements of the relative effects of slip and debonding on stress redistribution ahead of a mode I crack are consistent with calculations.<sup>6</sup> Debonding was found to be substantially more effective than slip at reducing the stress. The development of interfaces that experience controlled debonding upon either cyclic loading or monotonic loading thus represents an opportunity for achieving fracture and fatigue-resistant layered materials.

## APPENDIX A

### Fluorescence Measurements And Probe Size Effects

The signal intensity at a given frequency within a fluorescence spectrum of a stress-sensitive material is influenced by the state of stress of the material throughout the volume sampled by the probe. If stress gradients are significant within this volume, calculation of the fluorescence peak position requires a somewhat complicated calculation of the entire spectrum. To obtain an estimate of probe size effects in the present experiments, a simpler calculation, which assumes that the measured peak position is a weighted average of the peak positions from each element within the sampling volume, was used:

$$\sigma'_{kk}(x_0, y_0) = \frac{\int_{-y^*}^{y^*} \int_{-x^*}^{x^*} \sigma_{kk}(x, y) R(x_0 - x, y_0 - y) dx dy}{\int_{-y^*}^{y^*} \int_{-x^*}^{x^*} R(x, y) dx dy} \quad (A1)$$

where  $R(x-x_0, y-y_0)$  is the probe response function,  $\sigma_{kk}(x, y)$  is the local stress field and  $x^*$  and  $y^*$  represent the boundaries of the region from which the probe collects information.

Previous studies have established that the stresses of interest for layered materials with strongly bonded interfaces are given to a good approximation by the asymptotic elastic field around a crack in a homogenous body.<sup>24</sup> For mode I loading, the stress,  $\sigma_{kk}(x, y)$  is, therefore,<sup>25</sup>

$$\sigma_{kk}(x, y) = \left[ K \sqrt{\frac{2}{\pi(x^2 + y^2)^{3/2}}} \right] \cos(\tan^{-1}(y/x)/2) \quad (A2)$$

where  $x$  and  $y$  are the Cartesian coordinates measured from the crack tip. In the present analysis, the measured stress is compared with this solution at the location directly opposite the precrack ( $x = h_m, y = 0$ ), where Eqn. (A2) becomes

$$\sigma_{kk} = \frac{2K_I}{\sqrt{2\pi h_m}}. \quad (A3)$$

The response function was characterized experimentally by placing the probe on a horizontal surface of a thick beam of alumina, at a location immediately adjacent to a vertical free surface. The intensity of the signal was measured as the probe was translated away from the vertical surface, until the signal reached a level that did not change appreciably with further movement of the probe. The results were consistent with a response function of the form

$$R(x, y) = \exp[-(x^2 + y^2)/b^2] \quad (A4)$$

where  $b$  is a measure of the size of the volume of material sampled by the probe. The value of  $b$  ( $\approx 200 \mu\text{m}$ ) is much larger than the area illuminated on the specimen surface (spot size  $\sim 2 \mu\text{m}$ ); indirect illumination from internal scattering determined the volume from which the fluorescence signal was collected.

With the parameters pertinent to the data of Fig. 9 ( $K_I = 7.0 \text{ MPa}\sqrt{\text{m}}$ ,  $h_m = 250 \mu\text{m}$ ), the stress directly opposite the crack tip is, from Eqn. (A3),  $\sigma_{kk}(h_m, 0) = 350 \text{ MPa}$ . The stress given by Eqn. (A1), with the center of the probe at  $(x_0, y_0) = (h_m, 0)$  is significantly lower:  $325 \text{ MPa}$ . However, both values are reasonably close to the value in Fig. 9 deduced from the measured peak shift ( $360 \pm 20 \text{ MPa}$ ), consistent with the findings of previous studies.<sup>4,11</sup>

## APPENDIX B

### Fatigue Crack Trajectory

The preferred path taken by a fatigue crack depends on the ratio of energy release rate ranges,  $\Delta G$ , compared with the ratio of crack growth rates at the relevant phase angle,  $\Psi$ , for the different possible trajectories. For a surface crack, an interface debond is mixed mode ( $\Psi \approx 50^\circ$ ).<sup>16</sup> The comparison is thus made for mixed mode crack growth along the interface and mode I growth through the alloy (Fig. 6). The energy release rate range for mode I growth through the alloy is<sup>26</sup>

$$\Delta G \approx 1.26 \pi a (\sigma_{\max}^2 - \sigma_{\min}^2) / E \quad (B1)$$

where  $a$  is one-half the ceramic layer thickness,  $\sigma_{\max}$  and  $\sigma_{\min}$  are the maximum and minimum stresses applied during load cycling and  $E$  is the modulus of the ceramic. For mixed-mode growth along the interface, upon initial cyclic debonding<sup>27</sup>

$$\Delta G_{I/II} \approx 0.3 \pi a (\sigma_{\max}^2 - \sigma_{\min}^2) / E. \quad (B2)$$

Then, upon further growth, when steady state is reached ( $\Delta G = \Delta G_{ss}$ ),<sup>16</sup>

$$\Delta G_{I/II}^{ss} \approx 0.5 a (\sigma_{\max}^2 - \sigma_{\min}^2) / E. \quad (B3)$$

The ratio of energy release rates for mode I growth into the alloy and for mixed mode I/II growth along the interface, is thus in the range  $4.2-2.5 \pi$ . Imposing this ratio onto the crack growth curves dictates whether interface debonding is preferred or vice versa

(Fig. 12). The present data for  $\text{Al}_2\text{O}_3/\text{Al}$  (Fig. 6) indicate that interface crack growth is preferred, at least for  $\Delta G$  in the range,  $10 \rightarrow 10,000 \text{ Jm}^{-2}$ .

For intact metal ligaments, the  $\Delta G$  ratio is similar, with a somewhat larger value for mode I,<sup>26</sup>

$$\Delta G_I \approx 2b(\sigma_{\max}^2 - \sigma_{\min}^2) [\tan(\pi a/2b)] / E. \quad (\text{B4})$$

where  $2(b - a)$  is the ligament thickness. More importantly, the loading for an interface debond crack is now mode II. It is expected that the mode II debond growth rate,  $da/dN$ , is appreciably lower than that in mixed mode. Such reductions arise because of frictional contacts along the debond faces, as found in monolithic alloys in fatigue,<sup>22</sup> and for monotonic interface debonding.<sup>23</sup> In this case, mode I growth through the alloy is preferred over interface debonding.



**TABLE I**

**Interface Fatigue Crack Growth for Al/Al<sub>2</sub>O<sub>3</sub>**

<b>Metal Layer Thickness (<math>\mu\text{m}</math>)</b>	<b>Energy Release Rate Range, <math>\Delta G</math> (<math>\text{Jm}^{-2}</math>)</b>	<b>Average Crack Growth Range, <math>d\bar{a}/dN</math> (m/cycle)</b>
40	13	$2.9 \times 10^{-8}$
	144	$1.0 \times 10^{-8}$
	180	$1.5 \times 10^{-6}$
100	13	$1.4 \times 10^{-9}$
	139	$2.2 \times 10^{-8}$
250	4	$2.8 \times 10^{-9}$
	130	$3.4 \times 10^{-8}$

## REFERENCES

- [1] B.J. Dalgleish, K.P. Trumble and A.G. Evans, "The Strength and Fracture of Alumina Bonded with Aluminum Alloys," *Acta Metall.*, 37[7] (1989) 1923-31.
- [2] H.C. Cao and A.G. Evans, "On Crack Extension in Ductile/Brittle Laminates," *Acta Metall. Mater.*, 39[12] (1991) 2997-3005.
- [3] M.Y. He, F.E. Heredia, M.C. Shaw, D.J. Wissuchek and A.G. Evans, *Acta Metall. Mater.*, 41 (1992) 369.
- [4] M.C. Shaw, D.B. Marshall, M.S. Dadkhah and A.G. Evans, *Acta Metall. Mater.*, 41[11] (1993) 3311-22.
- [5] A.G. Evans and B.J. Dalgleish, *Acta Metall. Mater.*, 40 (1992) S295.
- [6] K.S. Chan, M.Y. He and J.W. Hutchinson, *Mat. Sci. Eng.*, in press.
- [7] R.M. Cannon, B.J. Dalgleish, R.H. Dauskart, T.S. Oh and R.O. Ritchie, *Acta Metall. Mater.*, 39, (1991) 2145.
- [8] J.W. Hutchinson and Z. Suo, *Appl. Mech. Rev.*, 28 (1991).
- [9] S.E. Molis and D.R. Clarke, *J. Am. Ceram. Soc.*, 73 (1990) 3189.
- [10] Q. Ma and D.R. Clarke, *J. Am. Ceram. Soc.*, 76 (1993) 1433.
- [11] M.C. Shaw, A.G. Evans, D.B. Marshall, D.R. Clarke and Q. Ma, to be published.
- [12] R.M. Pelloux, *Trans. Quart.*, ASM, 62[1] (1969) 281.
- [13] R.W. Hertzberg and P.C. Paris, *Proceedings, International Fracture Conference, Sendai, Japan*, 1 (1965) 459.
- [14] R.C. Bates and W.G. Clark, Jr., *Trans. Quart.*, ASM 62[2] (1969) 380.
- [15] P.C. Paris, *Fatigue—An Interdisciplinary Approach*, Proceedings 10<sup>th</sup> Sagamore Conference, Syracuse University Press, Syracuse, NY (1964) p. 107.
- [16] P.G. Charalambides, J. Lund, R.M. McMeeking and A.G. Evans, *J. Appl. Mech.*, 56 (1989) 77-82.
- [17] P.G. Charalambides, H.C. Cao, J. Lund and A.G. Evans, *Mech. of Mtls.*, 8[4] (1990) 269-83.
- [18] S.R. Swanson, F. Cicci and W. Hoppe, *ASTM STP 415* (1967) 312.
- [19] P.C. Paris and F. Erdogan, *J. Basic Eng. Trans.*, ASME, Series D, 85[4] (1963) 528.

- [20] Society of Materials Science, Japan, "Data Book on Fatigue Crack Growth Rates of Metallic Materials," [1] (1983).
- [21] K.T. Rao, R.O. Ritchie and G.R. Odette, *Acta Metall. Mater.*, **40** (1992) 353.
- [22] R.O. Ritchie, F.A. McClintock, H. Nayeb-Hashemi and M.A. Ritter, "Mode III Fatigue Crack Propagation in Low Alloy Steel," *Met. Trans. A*, Vol. **13A**, 1, 1982, pp. 101-110.
- [23] A.G. Evans and J.W. Hutchinson, *Acta Metall.*, **37** (1989) 909.
- [24] C. Woeltjen, C.F. Shih and S. Suresh, *Acta Metal. et Mater.*, **41** (1993) 2317.
- [25] B.R. Lawn and T. Wilshaw, *Fracture of Brittle Solids*, Cambridge Univ. Press (1975).
- [26] H. Tada, P.C. Paris and G.R. Irwin, *The Stress Analysis of Cracks Handbook*, Paris Productions (1985).
- [27] M.Y. He and J.W. Hutchinson, *Intl. Jnl. Solids Structures*, **25**[9] (1989) 1053-67.

## FIGURE CAPTIONS

- Fig. 1. Effects of slip and debonding on the stress ahead of a semi-infinite crack.<sup>6</sup>
- Fig. 2. The specimen configuration and the locations used for stress measurement.
- Fig. 3. a) Optical micrographs of two Al/Al<sub>2</sub>O<sub>3</sub> beams, the top beam subjected to a single load cycle, the lower beam subjected to 50,000 cycles of flexural fatigue.  
b) Optical micrograph of an interface debond created from the precrack by cyclic loading, as viewed through the transparent outer sapphire layer.
- Fig. 4. Crack growth resistances measured for the multilayers used in the present study.
- Fig. 5. Scanning electron micrographs of fatigue striations observed in the aluminum layer after debonding and removal of the upper sapphire layer: a) within one grain, b) different orientations in different grains.
- Fig. 6. Plot of the average crack growth rate,  $d\bar{a}/dN$  vs.  $\Delta G$  for multilayers with different metal layer thicknesses. Also shown are data for Type 7075-T6 and 1100-T0 aluminum alloys, taken from References 7 and 18-20.
- Fig. 7. Scanning electron micrograph of an aluminum ligament that failed in fatigue.
- Fig. 8. Piezospectroscopic calibration curve for the alumina used in the present investigation.
- Fig. 9. Stress ahead of precrack with load applied (nominal  $K = 7 \text{ MPa}\sqrt{\text{m}}$ ) and unloaded. Comparison with and without debonding.
- Fig. 10. Effect of debonding in a flexural configuration on stresses ahead of the surface precrack.
- Fig. 11. Schematic illustrating possible fatigue crack trajectories: a) Mode I extension of cracks from cracked ceramic layers into the intervening metal layer and b), c) Extension of mode II cracks along the interface.

Fig. 12. Schematic of the effect of mode mixity on the relative crack growth rates for different crack trajectories. Also shown is the ratio of  $\Delta G$ 's. For this case, interface debonding is preferred over mode I growth into the alloy.

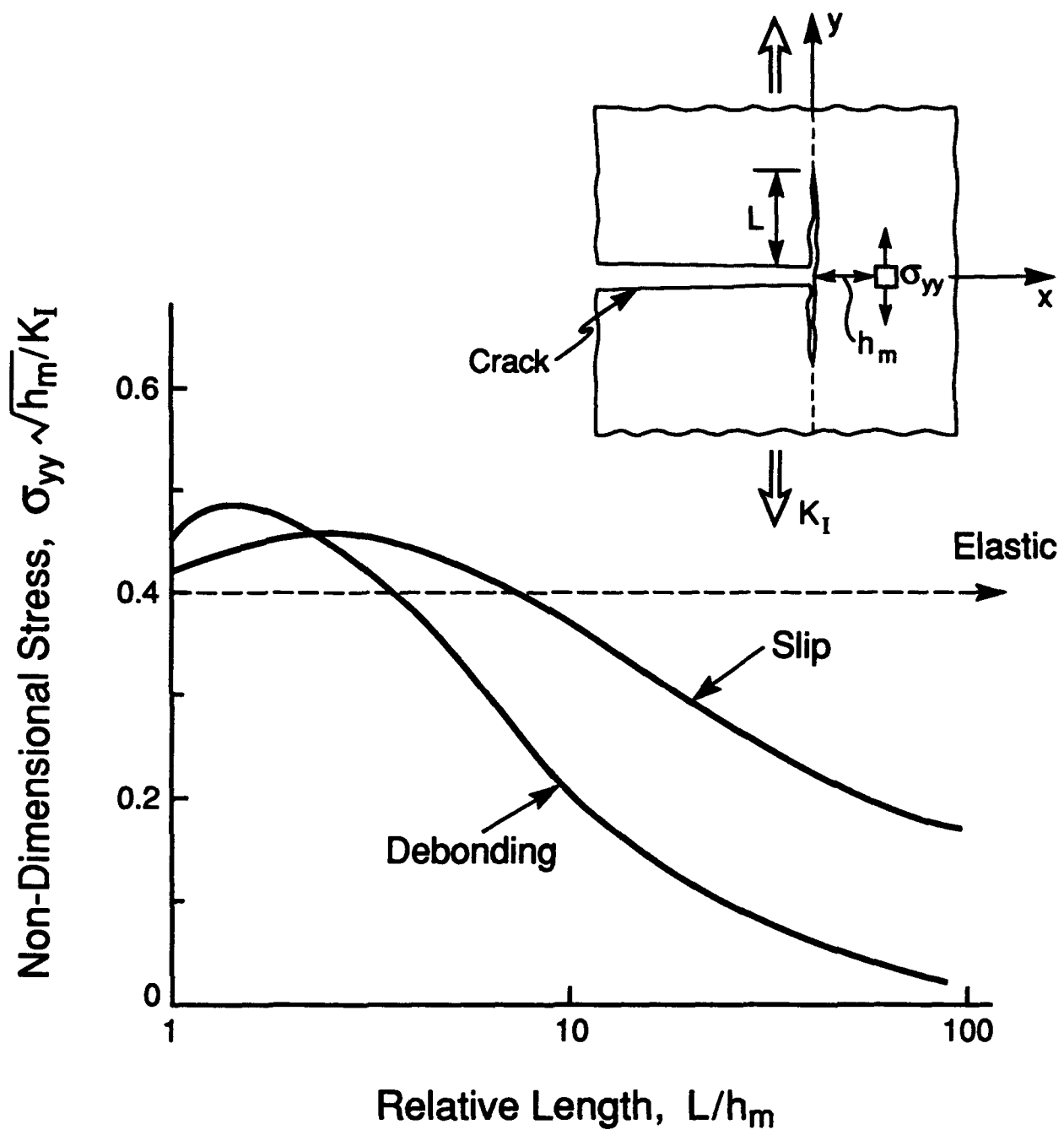


Figure 1

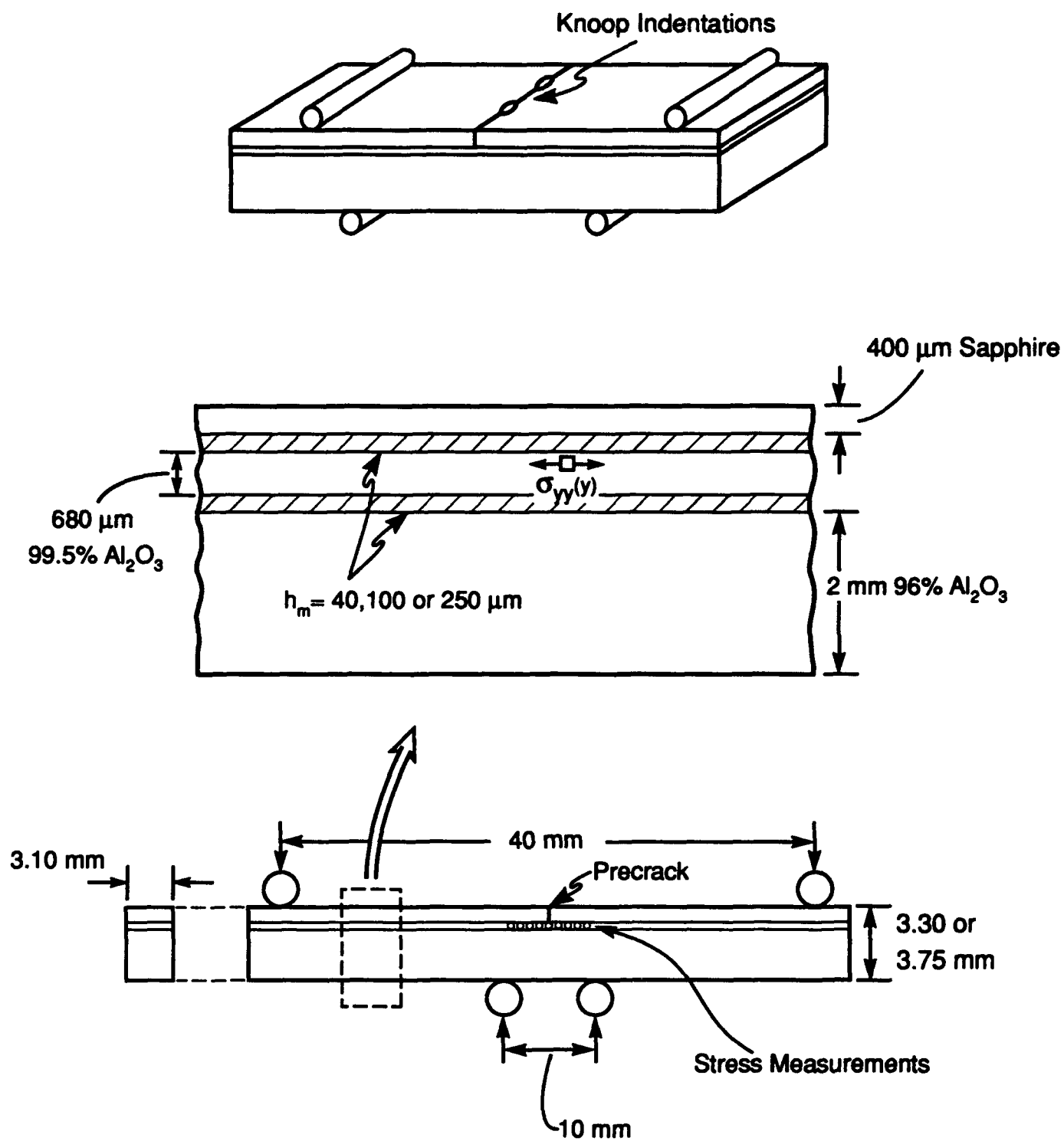
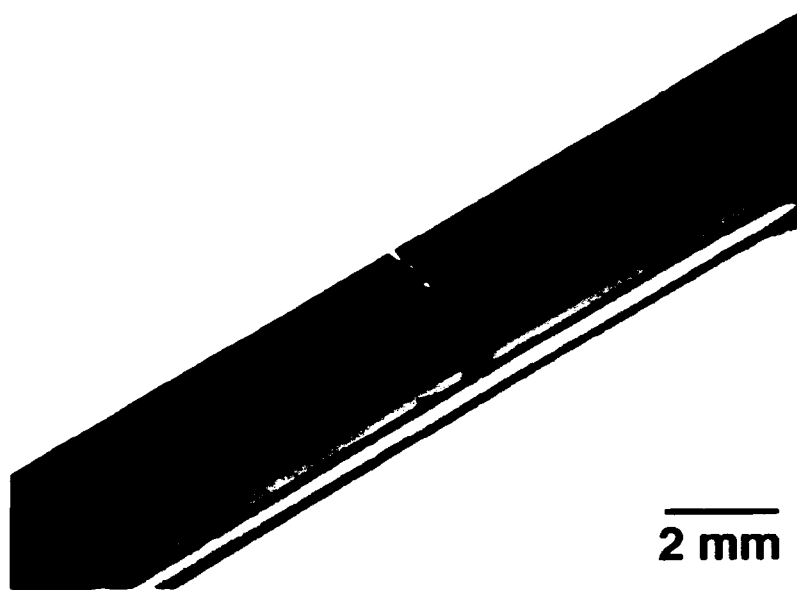
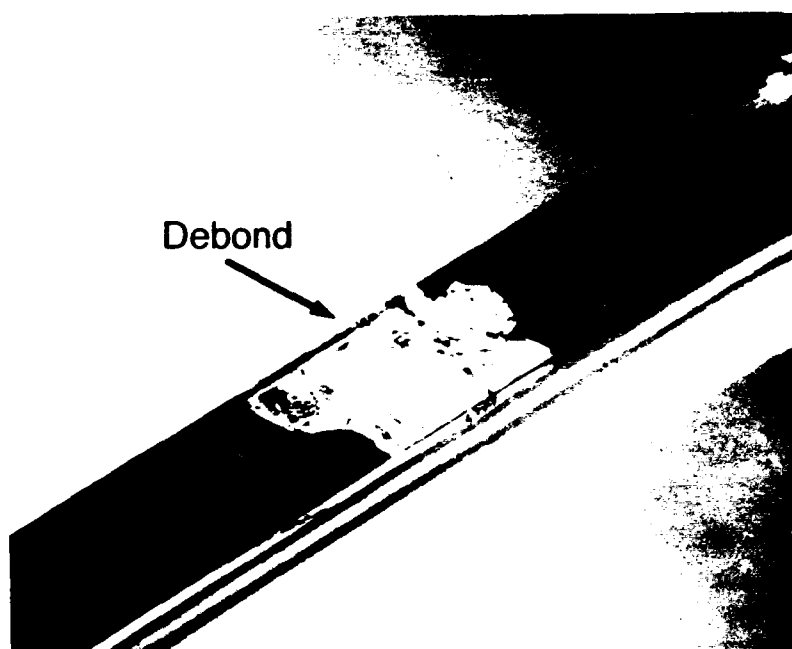


Figure 2



**1 Load Cycle**



**50,000 Load Cycles**

Figure 3(a)



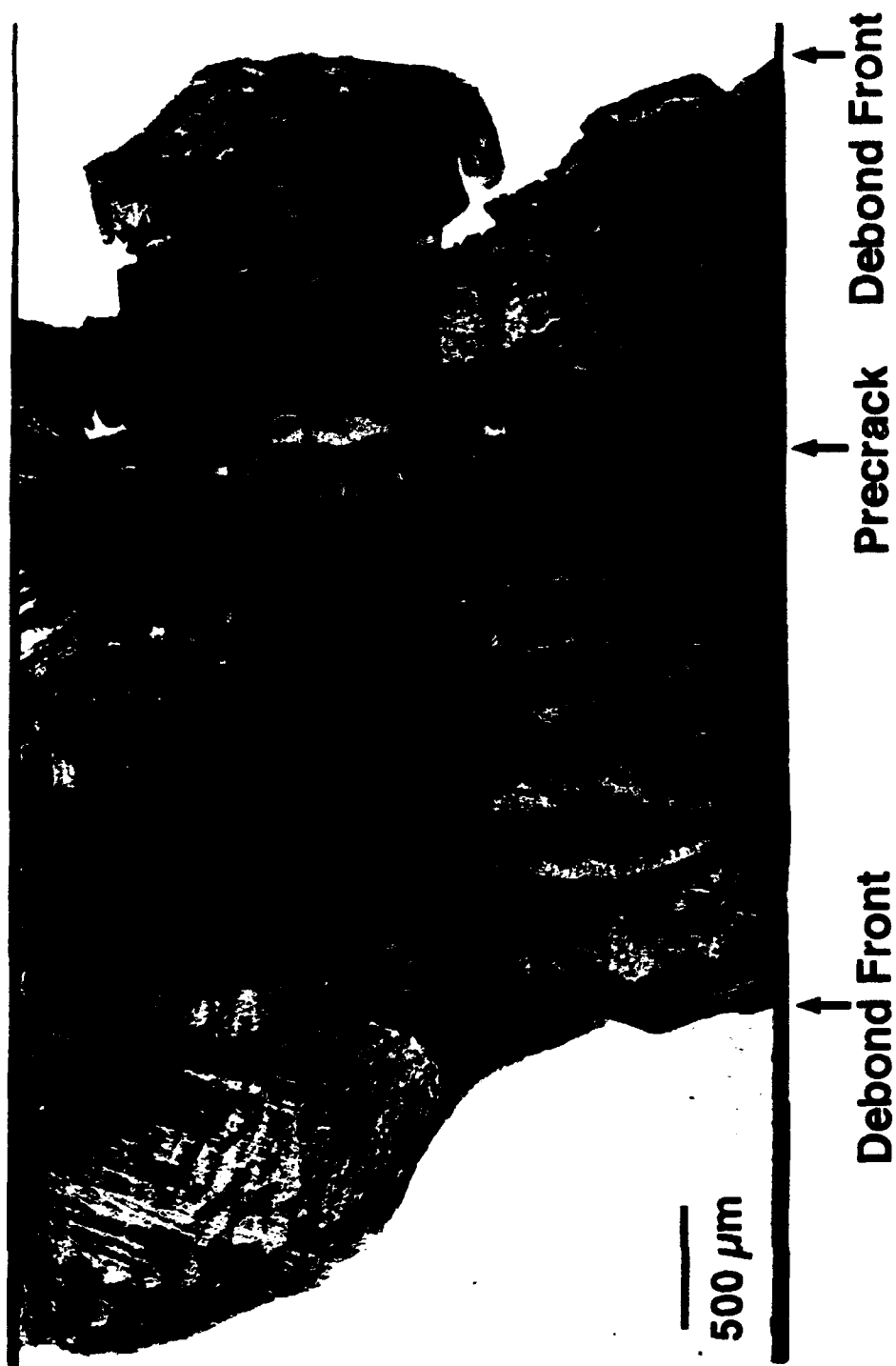


Figure 3(b)

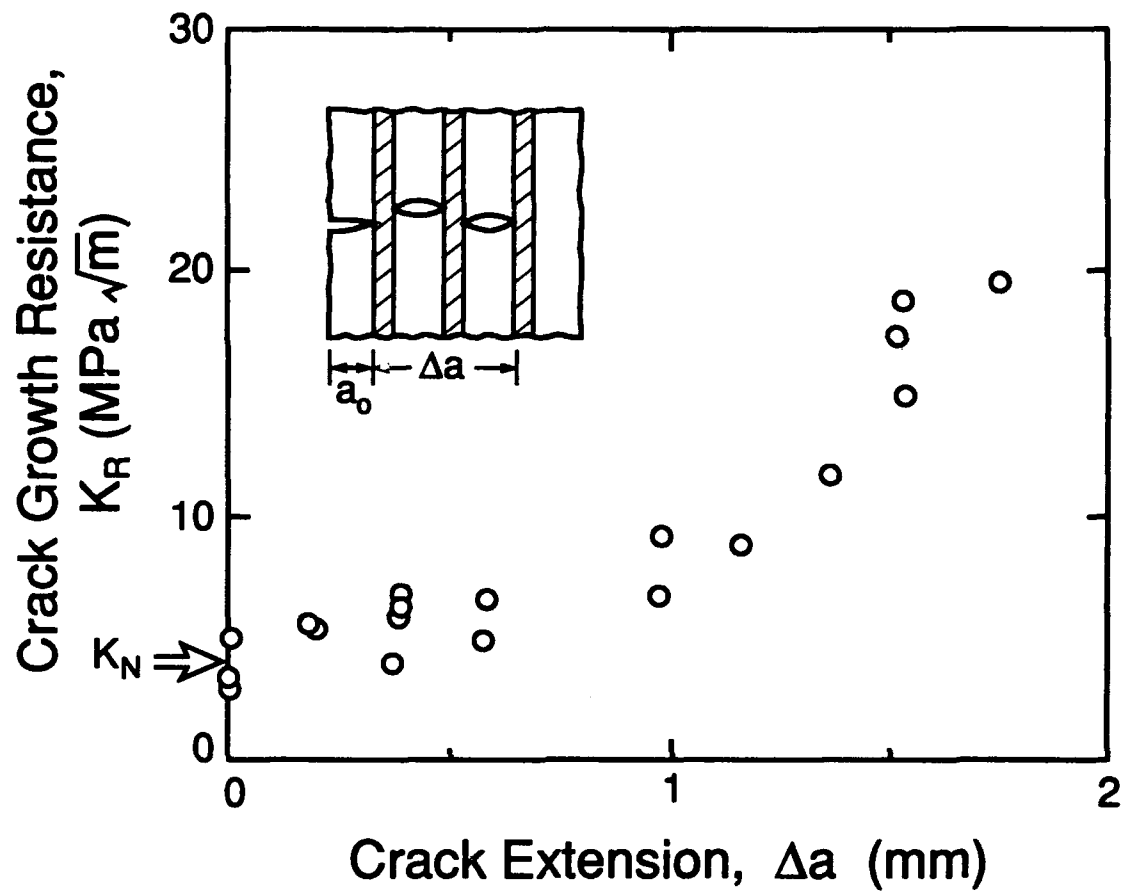
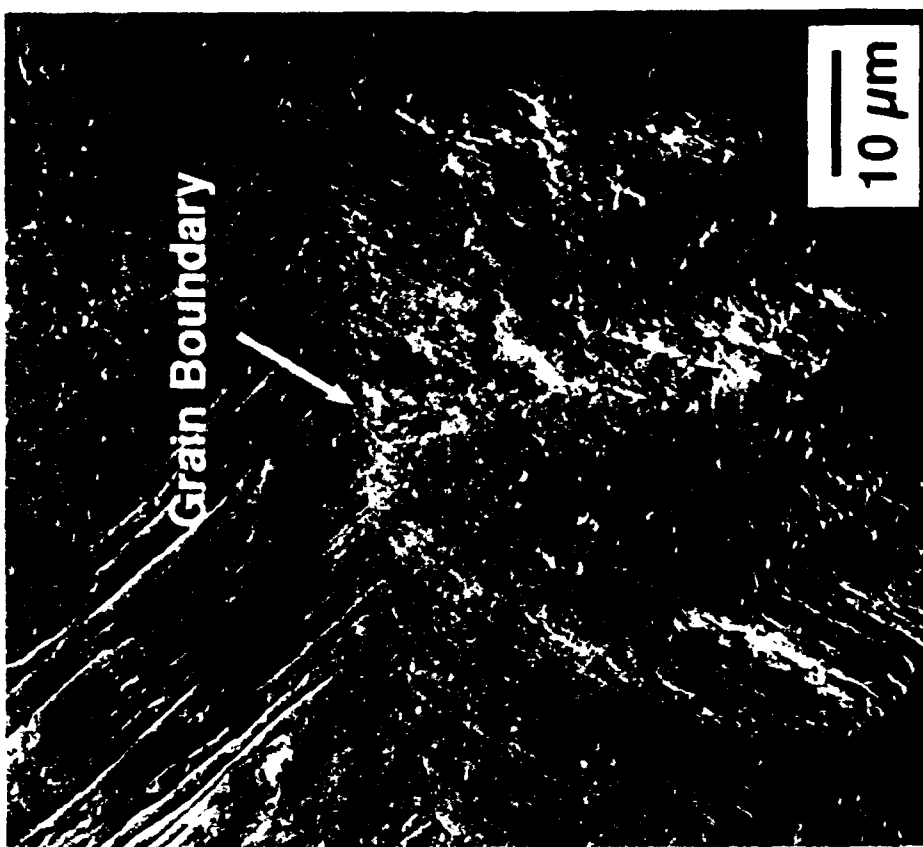


Figure 4



(a)



(b)

Figure 5

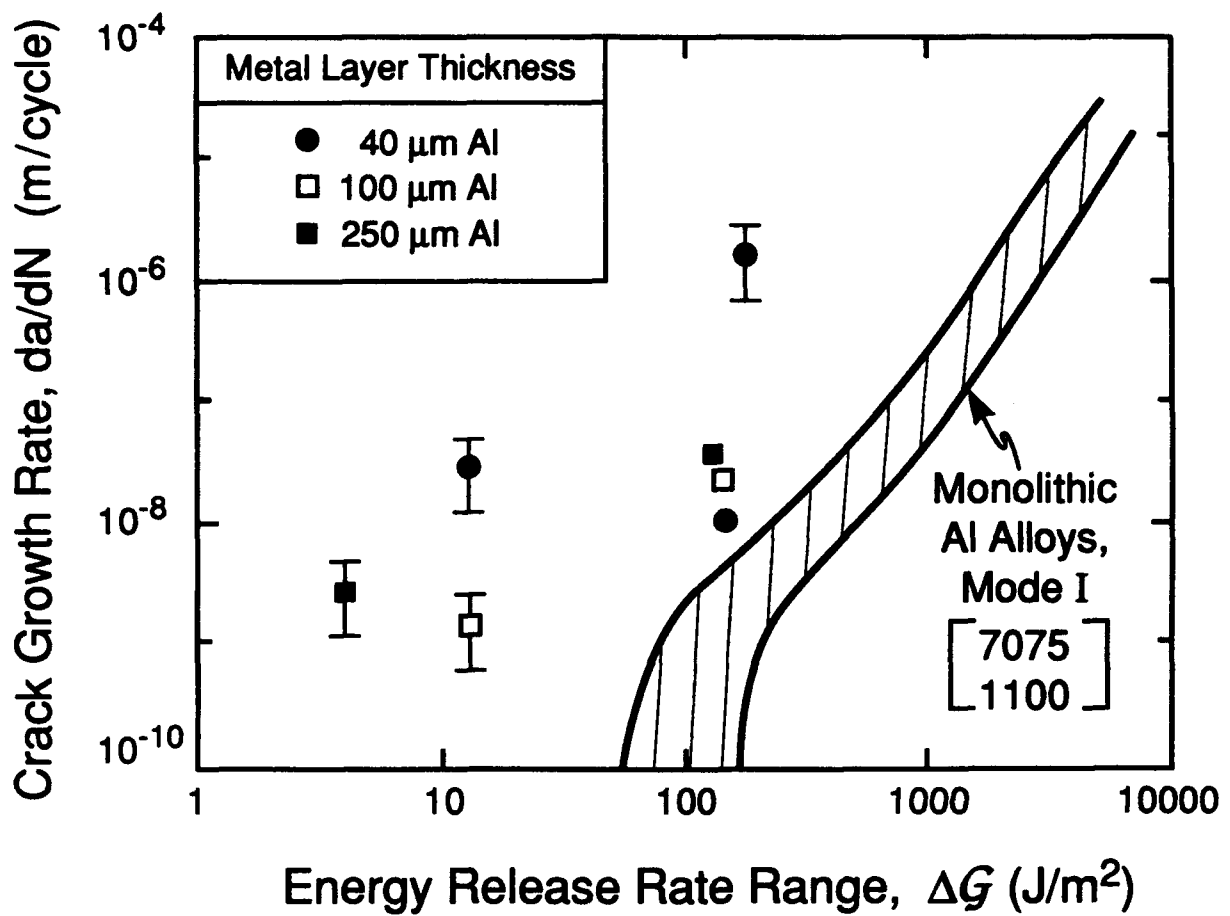


Figure 6



Figure 7

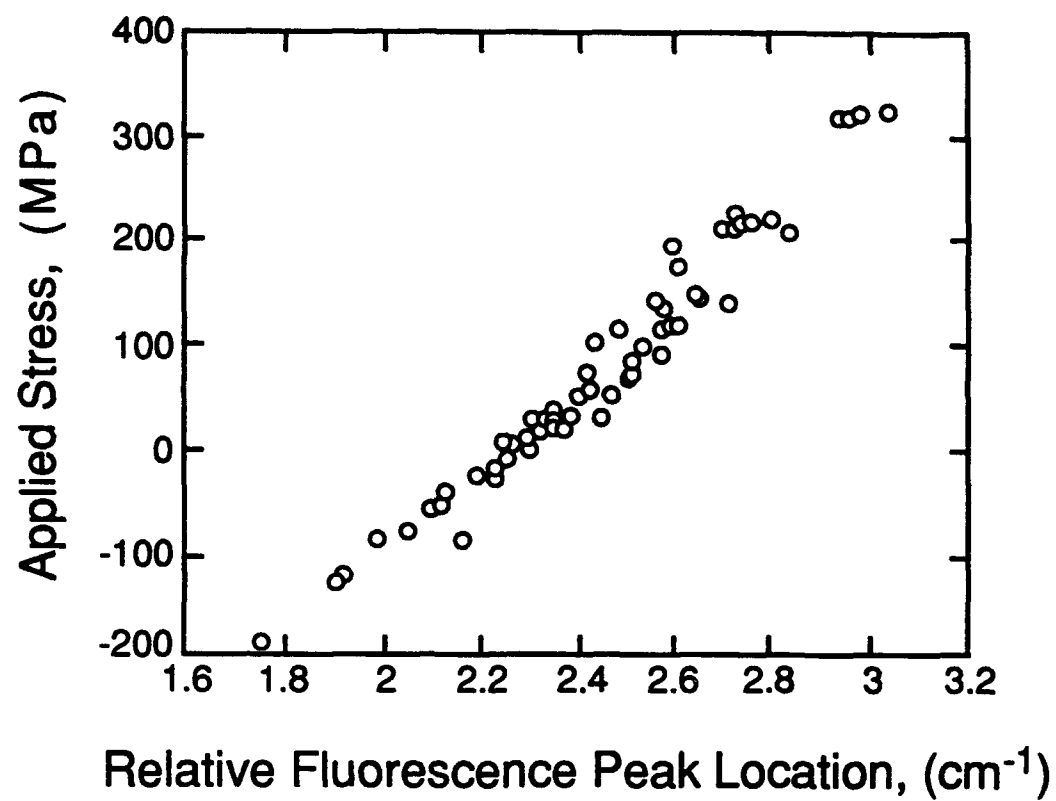


Figure 8

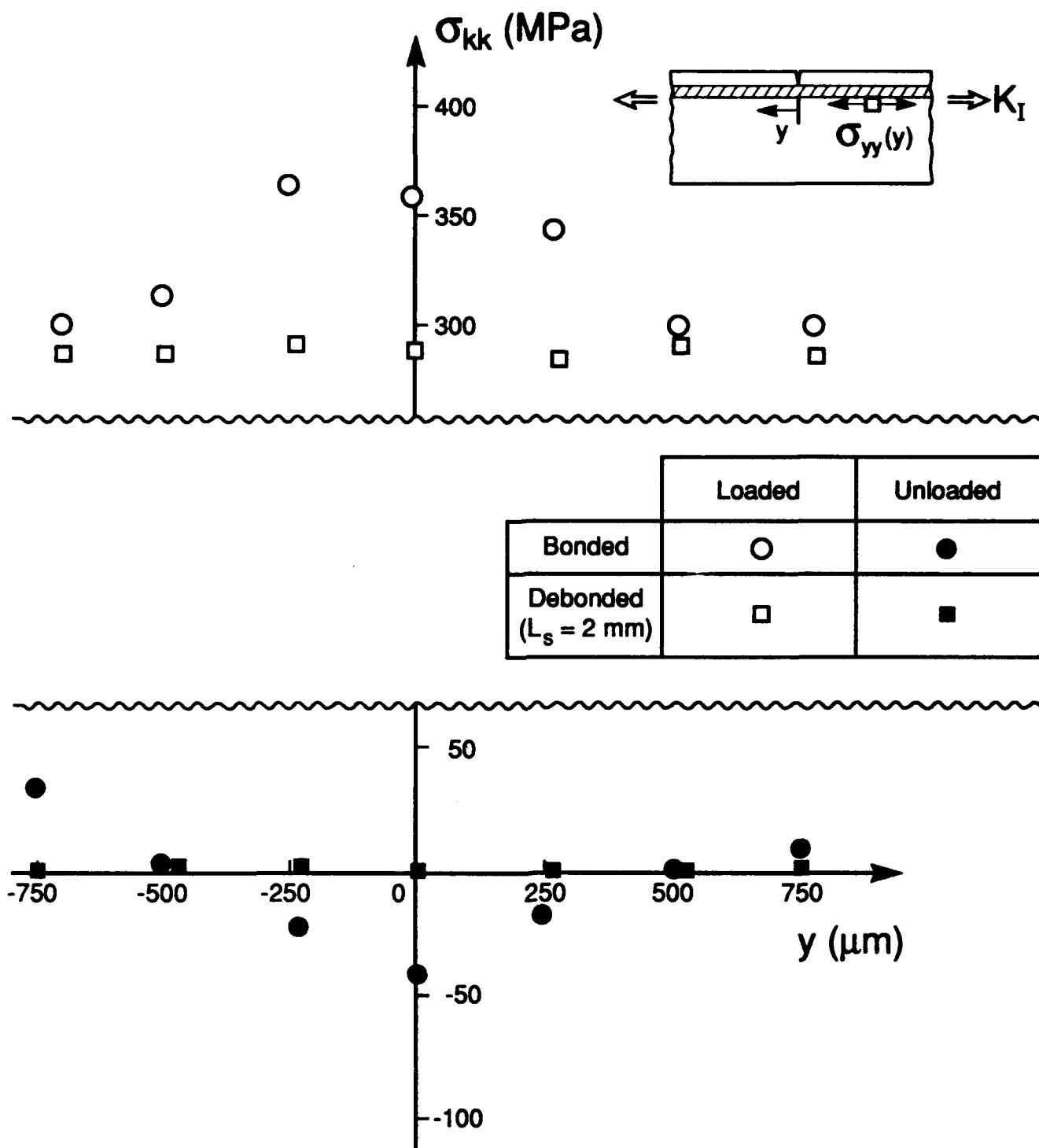


Figure 9

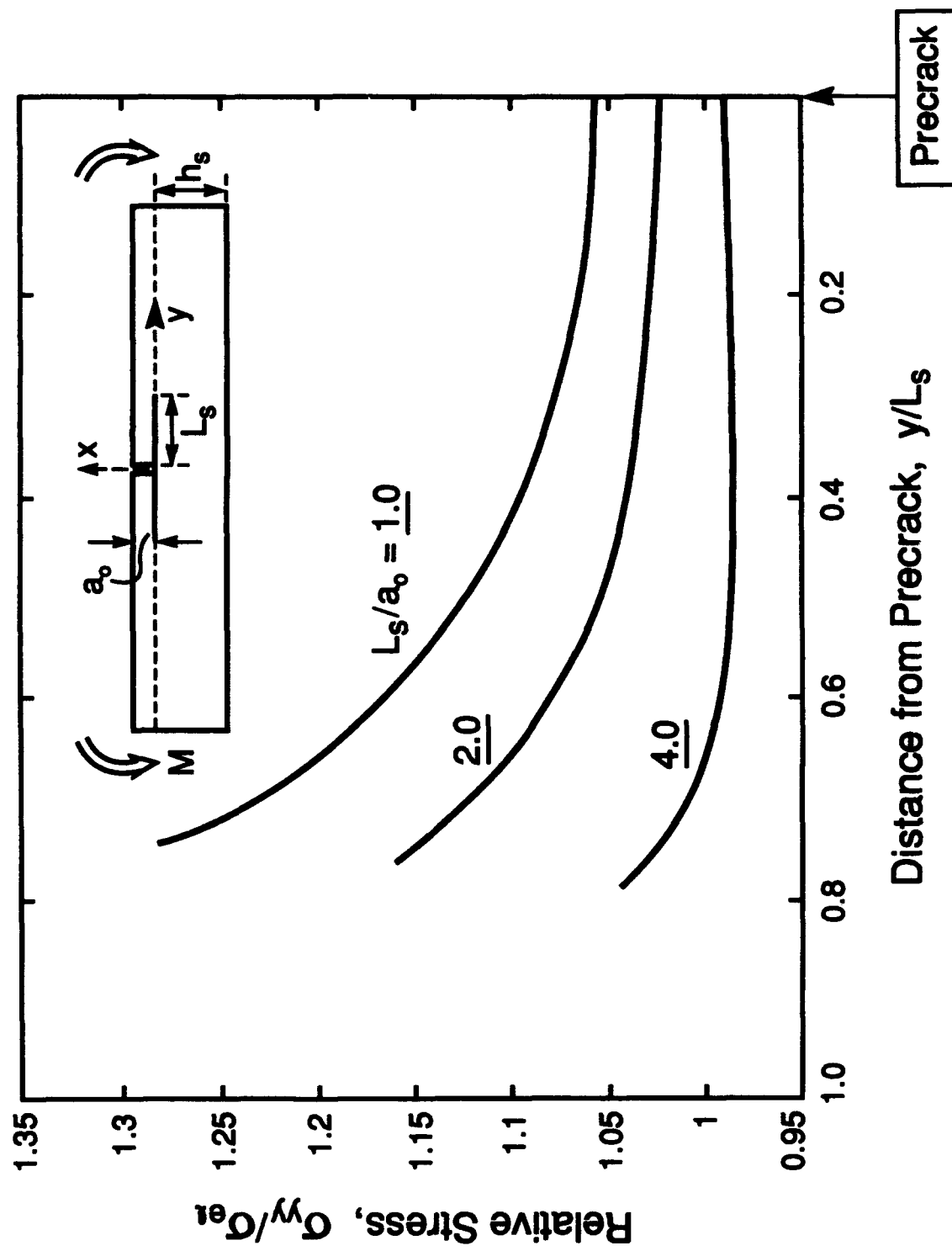


Figure 10



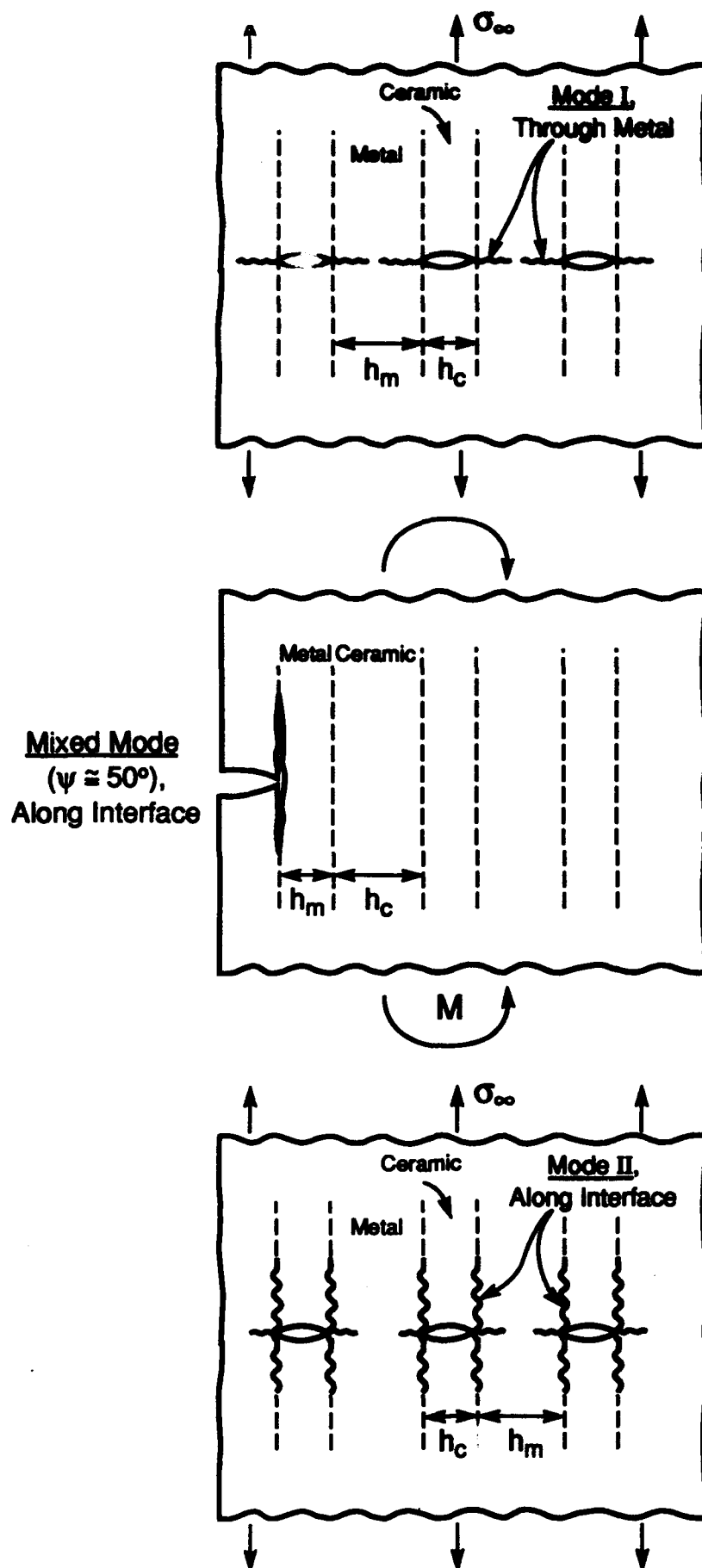


Figure 11

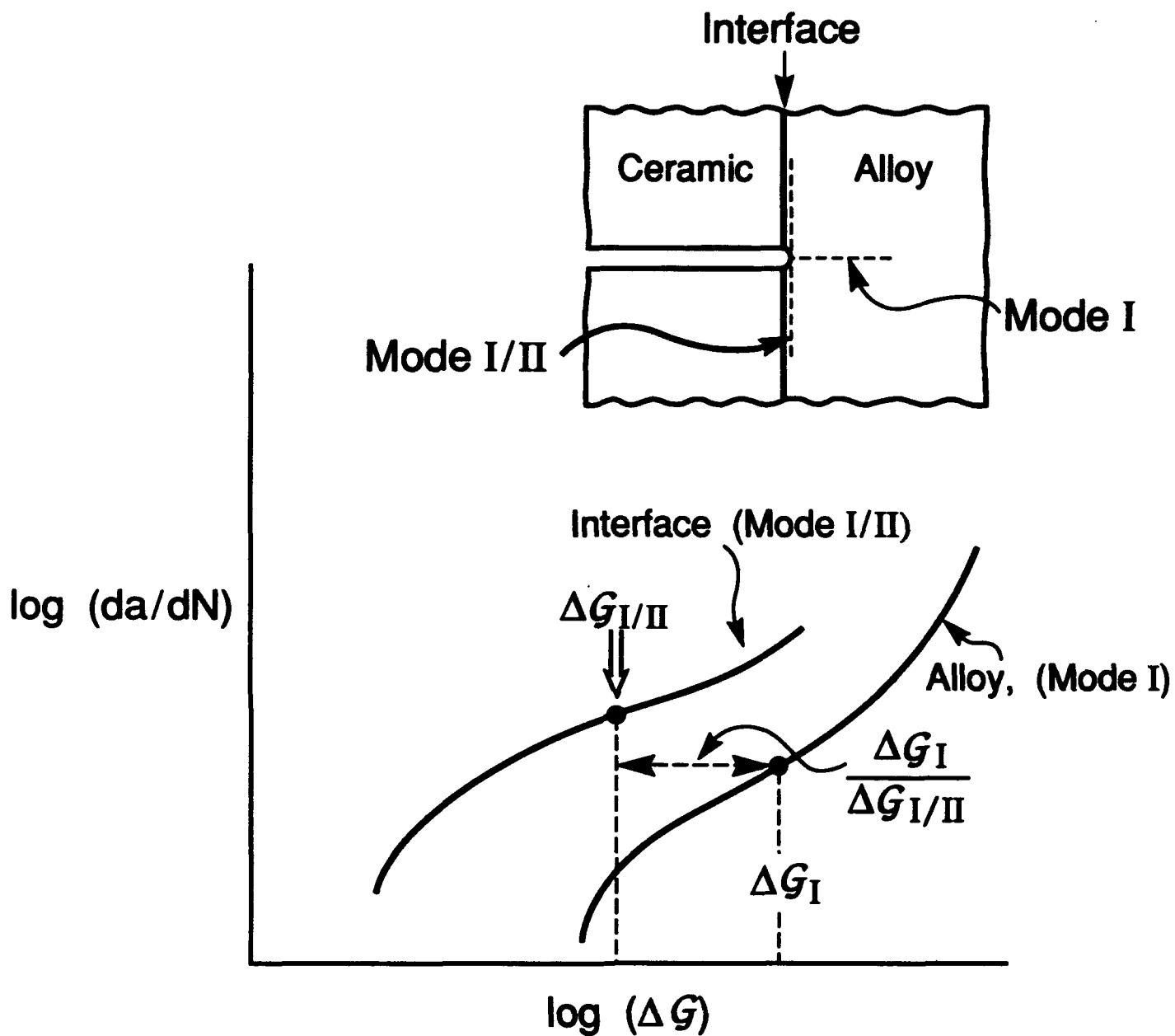
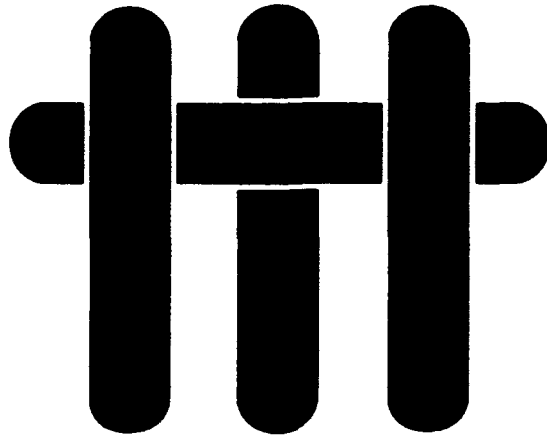


Figure 12

# M A T E R I A L S



## **EFFECTS OF COMPOSITE PROCESSING ON THE STRENGTH OF SAPPHIRE FIBER-REINFORCED COMPOSITES**

by

J.B. Davis, J. Yang and A.G. Evans  
Materials Department  
College of Engineering  
University of California, Santa Barbara  
Santa Barbara, California 93106-5050

## **ABSTRACT**

The current interest in tough, high-temperature materials has motivated fiber coatings development for sapphire fiber-reinforced alumina composites. For this system, it has been demonstrated that the interfacial properties can be controlled with coatings which can be eliminated from the interface subsequent to composite consolidation. However, these fugitive coatings can contribute to the high temperature strength degradation of sapphire fibers. Such degradation, which compromises the composite strength and toughness, is the focus of the current investigation. It has been observed that in some cases selecting appropriate composite processing conditions can minimize such effects but overcoming fiber strength loss remains an important issue for the use of these composites.

## 1. INTRODUCTION

The current limitations to the advancement of ceramic matrix composites are associated with the development of high strength, oxidation and creep resistant fiber-reinforcements and the control of the interfacial debonding and sliding behaviors. One approach to reinforcements has been to develop single crystal oxide fibers. The most thoroughly studied of these is sapphire. One promising class of coating is fugitive,<sup>1-2</sup> whereby the coating is removed from the interface subsequent to composite consolidation in order to leave a gap between the fiber and matrix. Carbon and molybdenum are examples of such coatings. The coating thickness and resulting gap size are used to manipulate the interfacial sliding resistance. However, the coating chemistry and thickness can affect the surface morphology of the fibers during either composite processing or subsequent exposures to high temperatures. This can lead to pronounced changes in fiber strengths. Such effects are the focus of this investigation.

This study has five essential elements. (i) Uncoated fibers were heat treated and their strengths measured in order to classify inherent strength degradation mechanisms. (ii) Coated fibers were given similar heat treatments and tested to establish additional degradation phenomena that may arise. (iii) Fibers with thick fugitive coatings of C and Mo were introduced into an alumina matrix by hot pressing. The fibers were removed by using the fugitive character of the coating. The withdrawn fibers were tested. These tests identified new degradation mechanisms that may operate with this coating. (iv) Unidirectional composites were fabricated with several coating thicknesses. The tensile properties of the composite were measured and fiber push-out tests performed. These tests indicated whether there are other strength loss phenomena associated with composite consolidation. They also allowed correlation to be made between composite behavior and the fiber strength and the interface debonding and sliding resistance.

(v) The fiber morphological changes have been examined in order to provide an understanding of the mechanisms involved.

## **2. EXPERIMENTAL PROCEDURES**

### **2.1 Fiber Strength Tests**

The fibers were obtained from a single spool of Saphikon sapphire fiber (diameter  $\sim 130 \mu\text{m}$ ). Their tensile strengths were measured for several fiber conditions by using a commercially available fiber testing machine\* and a one-inch gauge length. The first set was tested in the as-received state. The second was washed in cold water followed by acetone and ethanol, and then subjected to the series of heat-treatments summarized in Table I. The remaining two sets were first washed and then coated with either Mo or C to a thickness of  $\sim 10\text{--}15 \mu\text{m}$ . These were hot pressed into a high purity alumina matrix using the conditions specified in Table I. After hot pressing, the composites were heat treated at  $1100^\circ\text{C}$  in air for  $\sim 2 \text{ h}$  to remove the coatings from the interfaces. The fibers were extracted from the matrix and their strengths were measured directly.

Fiber strength data sets were comprised of  $\sim 20$  measurements. While this set size is too small to give an accurate determination of the fiber strength distribution parameters, it is sufficient to establish definitive trends in the median fiber strength.<sup>3,4</sup>

### **2.2 Composite Specimen Fabrication**

Unidirectional alumina matrix composites containing Mo coated sapphire fibers were produced for correlating composite behavior with the properties of the fibers and interfaces. Coatings with three thicknesses ( $0.2$ ,  $0.7$  and  $1.4 \mu\text{m}$ ) were used. Composites were produced by hot isostatic pressing (HIPing). These have been made by first

---

\* Micropull Sciences, Thousand Oaks, California

fabricating a preform comprising coated fibers within a slurry of the matrix material. These composites were sealed in an evacuated niobium can. Consolidation was achieved at a pressure of 30 MPa at 1350°C for 30 min (Fig. 1). Dog-bone shaped tensile specimens were diamond machined from the consolidated composite and the coatings were removed from the interface by heat-treating in air at 1150°C for 50 h.

### 2.3 Microstructural Characterization

Scanning electron microscopy (SEM) techniques with energy dispersive X-ray analysis were used to identify the strength limiting flaws for each data set. In addition, the morphologies of heat-treated fibers were examined in a field emission scanning electron microscope (JEOL 6300F) in order to classify and compare various surface and fracture features.

The interfaces in the composites were examined by transmission electron microscopy (TEM). For this purpose, electron transparent foils were prepared as described elsewhere. After tensile testing, the fiber pull-out length distributions were measured from scanning electron micrographs and the surface features of the fibers characterized. In addition, interactions between the fibers and the matrix were also classified.

### 2.4 Composite Testing

Tension tests were performed on the composite in a fixture located within a scanning electron microscope (Fig. 2). The forces were measured from a load cell. The behavior at small strains was monitored from strain gauges affixed to the specimen. At larger strains, the specimen displacement was measured with an LVDT. These strain data were compared with photomicrographic measurements.

The interfacial sliding resistances were measured by using the fiber push-through technique.

### 3. FIBER STRENGTHS

The fibers in the as-received condition were found to have a median strength,  $\bar{S} \approx 2.7$  GPa, and a Weibull modulus,  $m \approx 6.5$  (Fig. 3a), consistent with values reported in the literature.<sup>5</sup> After heating the washed, uncoated fibers to successively higher temperatures (1250°C, 1350°C and 1450°C), there were small, though significant, reductions in either the mean strength,  $\bar{S}$ , or the Weibull modulus,  $m$ , (Fig. 3b, Table I). Conversely, extracted fibers originally coated with Mo showed considerable strength loss, at all heat-treatment temperatures (Fig. 3b). The fibers originally coated with carbon exhibited a smaller reduction in median strength but had the most substantial strength *variability*, reflected in the highest coefficient of variation and the low Weibull modulus ( $m \approx 2.6$ ).



**Table I**  
**Fiber Strength Data**

Heat Treatment*		Median Strength (GPa)	Coefficient of Variation	Weibull Modulus
Uncoated	1250°C	2.6	0.10	9.8
	1350°C	2.0	0.15	6.8
	1450°C	2.1	0.18	5.8
Mo	1250°C	1.9	0.16	6.2
Coated:	1350°C	1.4	0.32	2.2
Extracted	1450°C	1.0	0.33	3.2
C Coated: Extracted	1450°C	1.6	0.38	2.6
	As-Received	2.9	0.13	6.5

\* With the exception of the As-Received set, all fibers were heated in an air furnace at 1150°C for 2 hours subsequent to the heat treatments shown above.

## 4. FIBER MORPHOLOGY

Upon heat treatment, the fiber morphology is found to be strongly influenced by both diffusional effects and chemical reactions, especially in the presence of either fiber coatings or a composite matrix. There are four basic phenomena (Fig. 4), each exemplified by the observations presented below. (i) Surface diffusion causes fiber faceting, even in isolated fibers. (ii) Thin polycrystalline coatings, when chemically inert (no reaction products), are morphologically unstable and develop holes. Equilibrium at the hole edges then motivates surface diffusion and induces the formation of ridges on the fibers. (iii) Chemical reactions occur between the coating and the fiber resulting in fiber surface damage. This may produce either solid or gaseous reaction products. (iv) After a coating has either become discontinuous during composite consolidation or has been removed by oxidation, the matrix may sinter to the fiber. This results in localized bonding, causing matrix grains to remain attached to the fiber during pull-out, upon composite testing.

### 4.1 Uncoated Fibers

The fibers display sinusoidal diameter modulations along their length with characteristic wavelengths and amplitudes, described elsewhere.<sup>6</sup> Flaws observed in the as-received fibers were primarily associated with porosity. Pores develop during fiber growth and have been observed within the fibers and at the fiber surfaces (Fig. 5). The strength range is consistent with calculations for cylindrical rods containing cracks having the same dimensions as the pores<sup>7</sup> (Fig. 6).

The surface features were altered by high temperature heat-treatments. The fibers facet (Fig. 7), illustrating the inherent morphological instability of single crystal fibers. Frequently, local surface damage was evident resulting from chemical reactions (Fig. 8a). These sites usually correlate with failure origins and account for the strength

loss. Energy dispersive X-ray spectroscopy measurements identified Si and Mg at these sites (Fig. 8b). Two likely sources of contamination include the incomplete removal of the fiber sizing and reactions with inorganic contaminants that condense onto the fiber surfaces during heat treatment in the air furnace. Such contaminant reactions are avoidable upon encapsulation of the fibers and are of moderate practical concern.

#### 4.2 Carbon Coated Fibers

The heat treated carbon coated fibers displayed surface regions indicative of a chemical reaction between the coating and the fiber, localized near fiber ends and at locations where the coatings were discontinuous. The reaction product, identified by X-ray analysis as  $Al_4C_3$ , severely degraded the fiber surface (Fig. 9). The extent of reaction increased with temperature (Fig. 10). In addition, accentuated fiber faceting occurred near the reaction sites.

Thermodynamic calculations (Appendix 1) indicate that alumina and C can react to form volatile aluminum suboxides at temperatures as low as 1100°C, at least when heat treatments are conducted in an open system.<sup>8-11</sup> The progress of these reactions requires a means of removing CO from the reaction site, consistent with the reactions being preferentially located at the fiber ends and at coating discontinuities. This tendency for localized attack is presumably responsible for the strength *variability* of the fibers. Some fibers were relatively undamaged in the gauge section and exhibit strengths similar to the uncoated fibers heat treated to the same temperature. Others were damaged in the gauge length associated with areas where the coating was discontinuous.

#### 4.3 Mo Coated Fibers

Observations of the extracted Mo coated fibers reveal substantial changes in surface morphology. At least two phenomena contribute. The first involves the breakup

of the polycrystalline Mo coating.<sup>12,13</sup> The Mo/Al<sub>2</sub>O<sub>3</sub> interface then forms ridges on the surface of the sapphire, at the Mo grain edges. This process proceeds by *surface and interface diffusion*. The ridges are visible when the coating is chemically etched from the fibers (Fig. 11). They heighten as the heat treatment temperature increases. Upon removing the coating, further heat treatment causes the ridges to become unstable. The morphology then resembles fiber facetting, but with an additional surface roughness that originates with the ridges.

A second potential phenomenon involves the dissolution of alumina in Mo. If it occurs, the same morphological changes discussed above would proceed, but the kinetics could be more rapid than those for interface diffusion. Such dissolution has been well documented for Nb/Al<sub>2</sub>O<sub>3</sub> interfaces<sup>14</sup> and has been reported to occur for Mo/Al<sub>2</sub>O<sub>3</sub> composites as well at temperatures similar to those used in this study (subject to the oxygen partial pressure).<sup>15</sup> However, it has not been verified for Mo, because high resolution TEM specimens are difficult to produce without interface debonding.

The large strength reduction found for the Mo coated fibers is presumed to relate to the ridges and troughs formed by diffusion or dissolution. It has not been possible to quantify the measured strengths, because an appropriate surface flaw model has not been developed. However, the general trend toward a lower strength with increased ridge height, as the temperature increases, suggests that a model based on the stress intensification caused by ridges and troughs is consistent with the measurements.

#### **4.4 Fibers Within A Composite**

Thin (0.2 and 0.7  $\mu\text{m}$ ) Mo fiber coatings do not remain continuous after composite consolidation (Fig. 12). Consequently, submicron thick Mo fiber coatings permit the fibers to sinter to the matrix, during HIPing, in those areas where the coating has become discontinuous (Fig. 13). The thicker (1.4  $\mu\text{m}$ ) Mo coatings are continuous

(Fig. 12), but the thickness is non-uniform. For these coatings, local sintering of the fiber to the matrix does not occur upon HIPing, but can still occur *after the coating has been removed*. In such cases, upon debonding, some matrix grains remain attached to the fiber, with associated ridge formation and fiber damage (Fig. 14). Chipping of the fibers can also occur (Fig. 15). Such visual evidence of fiber, matrix sintering allows measurement of the sintered regions to give the area fraction of fiber bonded to the matrix,  $f_A$  (Table II). In some locations, additional features are evident, manifest as large ridges and troughs between neighboring sintered sites (Fig. 16).

Sintered areas resist debonding and increase the interfacial fracture energy in proportion to the area fraction of bonding. Moreover, when the matrix sinters to the fibers, the resulting damage (Fig. 14, 15) reduces the fiber strength. The relatively large depth of these damaged regions compared with the size of the ridges and troughs found for the extracted Mo coated fibers (Fig. 3) suggests that the strengths may be substantially lower in the HIPed composites. The magnitude of the additional strength reduction is implied from analyses conducted below.

Localized sintering would also induce residual stress upon cooling, because of the thermal expansion mismatch between c-axis sapphire and polycrystalline  $Al_2O_3$ . Such stresses should be of order 100 MPa and may influence trough formation (Appendix II).

## 5. COMPOSITE PROPERTIES

Composites with Mo coated fibers were tested after removing the Mo. All failed from a single dominant crack because of the low fiber volume fractions ( $f < 0.20$ ). However, the fracture resistance and the extent of fiber pull-out were very different for the three coating thicknesses (Table II). The specimens with thin (0.2  $\mu m$ ) gaps had low toughness and exhibited co-planar fracture (Fig. 17), with no pull-out. Conversely, appreciable pull-out was evident for the two larger interfacial gaps (Fig. 18). Moreover,

the material with the 1.4  $\mu\text{m}$  interface gaps exhibited substantially more pull-out (average pull-out length,  $\bar{h} \sim 640 \mu\text{m}$ ) than the material with the 0.7  $\mu\text{m}$  gaps ( $\bar{h} \sim 90 \mu\text{m}$ ). A typical load-displacement curve for these materials illustrates the fiber pull-out contribution to the composite fracture resistance (Fig. 19). The magnitude of the fracture dissipation is 40  $\text{kJ m}^{-2}$ . The associated ultimate tensile strengths (UTS), summarized in Table I indicate a similar trend, with the larger gap giving a considerably higher UTS.

The corresponding push-out behaviors are summarized in Fig. 20. The composite with the thinnest coating did not exhibit push-out. The inability of this interface to slide and pull-out results from sintering. Conversely, sliding was induced in the other two composites. Both materials exhibited essentially the same sliding resistance, probably because local variations in the coating thickness, rather than the average gap width, dominate sliding.

## 6. ANALYSIS

### 6.1 Method and Assumptions

An attempt is made to interpret the above composite behavior in terms of the fiber strength degradation phenomena, discussed above, in conjunction with related trends in interface properties. For this purpose, three basic assumptions are made and used together with models of interface debonding and sliding, as well as fiber pull-out. It is assumed that, when the fiber sinters to the matrix, debonding occurs when the energy release rate reaches the mode I fracture energy of the fine-grained alumina polycrystals ( $\Gamma_c \approx 25 \text{ J m}^{-2}$ ). The debonding energy is then,

$$\Gamma_i \approx f_A \Gamma_c \quad (1)$$

with  $f_A$  given in Table II. It is also assumed that a sliding zone exists behind the debond, subject to a constant sliding resistance,  $\tau$ . In this case, the debond length,  $\ell$ , at stress,  $\sigma$ , is<sup>16</sup>

$$\ell = \frac{R(1-f)}{2\tau f}(\sigma - \sigma_i) \quad (2)$$

where  $R$  is the fiber radius,  $f$  is the fiber volume fraction and  $\sigma_i$  is the debond stress given by,

$$\sigma_i = \frac{1}{C_1} \sqrt{E\Gamma_i/R} - \sigma^T \left( \frac{C_2}{C_1} \right) \quad (3)$$

where  $\sigma^T$  is the axial misfit stress caused by thermal expansion mismatch and  $C_1$  and  $C_2$  are constants defined by Hutchinson and Jensen.<sup>16</sup>

Finally, it is assumed that fiber failure occurs *within the debond zone*, in accordance with weakest link statistics. The fiber pull-out length  $\bar{h}$  should then be related to  $\ell$ . The relationship between  $\ell$  and  $\bar{h}$  is considered to be similar to that devised by Curtin,<sup>17</sup>

$$\bar{h} = \ell \lambda'(m) \quad (4)$$

where  $\lambda'$  is a function of the Weibull modulus of the fibers. Equation (4) must be a lower bound for the pull-out length.

## 6.2 Interpretation

The preceding formulae allow an understanding and rationalization of the observation that composites with the 0.7  $\mu\text{m}$  gap have smaller pull-out lengths than

materials with a 1.4  $\mu\text{m}$  gap, but yet have similar sliding resistance. There are two factors involved. (i) A smaller debond length is expected with the narrower gap, because of the larger debond resistance that has been induced by the more extensive fiber/matrix sintering. Slip is limited by the debond length.<sup>‡</sup> (ii) Fiber weakening occurs when matrix grains sinter to the fibers and create damage sites (Fig. 14, 15).

The measured UTS,  $\sigma_u$ , may be inserted into Eqn. (2) and, upon using Eqns. (1) and (3), the debond lengths at failure may be estimated. The results (Table II) verify that a considerably larger debond length develops for the composite with the wider interface gap. Moreover, the proportionality constant,  $\lambda'$ , between the pull-out length,  $\bar{h}$ , and the debond length  $l$  (Eqn. 4) is similar for both materials.

The strengths of the fibers in the composite  $S_c$  is out of order (Table II),

$$S_c = \sigma_u / f \quad (5)$$

These strengths are considerably lower than those measured for the extracted fibers with the thick coatings. It is implied that the strengths have been markedly degraded by sintering of the matrix to the fibers. Furthermore, because  $S_c$  represents the strength measured at a gauge length of order the debond length, even smaller values would obtain at a 1" gauge length.

---

<sup>‡</sup> In addition, local residual stresses at the bonded sites along the interface may influence the interface crack trajectory.<sup>18</sup>



**Table II**  
**Composite Properties**

Coating Thickness ( $\mu\text{m}$ )	$\tau$ (MPa)	$\bar{h}$ ( $\mu\text{m}$ )	Fracture of Fiber/Matrix Bonded	Measured UTS (MPa)	$S_c$ (GPa)	$l$ ( $\mu\text{m}$ )	$\lambda'$ (m)
0.7	17	90	~ 0.05	22	0.1	250	0.3
1.4	15	640	~ 0.01	79	0.4	1000	0.7

## 7. SUMMARY

Single crystal sapphire fibers have been suggested as a high strength reinforcement for ceramic matrix composites. Interfaces have been developed based on a fugitive coating concept which satisfies the fiber debonding and sliding conditions for toughness enhancement in these materials. However, the strengths of the fibers are reduced by the presence of the coatings and are further reduced upon forming a composite. The mechanisms for the strength loss of coated fibers include: i) gas phase reactions with the coating which produce aluminum sub-oxides and etch the fibers ii) chemical reactions which form solid state reaction products and iii) facetting or ridging by surface diffusion. Carbon coated fibers are susceptible to the first two modes of degradation. However, it should be possible to minimize these effects by selecting composite processing conditions that provide a controlled CO/CO<sub>2</sub> atmosphere. For the Mo coatings, the degradation mechanisms are primarily of the third type and more difficult to eliminate.

Additional fiber strength reduction results after composite processing with thin coatings, due to localized sintering of the matrix to the fiber. Such bonding affects the surface of the fibers. It also imposes a residual stress, which may further alter the surface morphology. It is believed that this strength loss could be minimized by manipulating the matrix microstructure and chemistry (by incorporating segregants) to reduce the sintering potential.

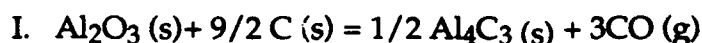
## REFERENCES

- [1] T. Mah, K. Keller, T.A. Parthasarathy and J. Guth, *Ceram. Eng. Sci. Proc.*, **12** [9-10] p. 1802-15 (1991).
- [2] J.B. Davis, J.P.A. Löfvander, E. Bischoff, A.G. Evans and M.L. Emiliani, *J. Am. Ceram. Soc.*, **76** [5] 1249-57 (1993).
- [3] K. Trustrum, and A. De S. Jayatilaka, *J. Mat. Sci.*, **14** 1080-1084 (1979).
- [4] J.R. Porter, *MRS Symp. Proc.*, **273** 315-324 (1992).
- [5] E. Trembauer and R. Tressler, *HITEMP Conference Proceedings* (1992).
- [6] T.J. Mackin, J. Yang and P.D. Warren, *J. Am. Ceram. Soc.*, **75** [12] 3358-62 (1992).
- [7] H. Tada, P.C. Paris and C.R. Irwin, *The Stress Analysis of Cracks Handbook*, Del Research Corp., Pennsylvania (1973).
- [8] L.M. Foster, G. Long and M.S. Hunter, *J. Am. Ceram. Soc.*, **39** [1] 1-11 (1956).
- [9] D.R. Stull and H. Prophet, *JANAF Thermochemical Tables*, 2nd ed., NSRDS-NBS 37, U.S. Department of Commerce, Washington, D.C., 1971.
- [10] I. Barin and O. Knacke, *Thermochemical Properties of Inorganic Substances*, Springer-Verlag, New York, 1973.
- [11] I. Barin, O. Knacke, and O. Kubaschewski, *Thermochemical Properties of Inorganic Substances, Supplement*, Springer-Verlag, New York, 1977.
- [12] W.W. Mullins, *Journal of Applied Physics*, **28** [3] 333-339 (1957).
- [13] K.T. Miller, F.F. Lange and D.B. Marshall, *Mat. Res. Soc. Proc. Sym. on Ultrastr. Proc.*, **121** [3] 823-30 (1988) and *J. Mater. Res.*, **1** [5] 151-60 (1990).
- [14] M. Rühle and A.G. Evans, *Materials Science and Engineering*, **A107** 187-197 (1989).
- [15] G.H.M. Gubbels, *Materials Science and Engineering*, **A135** (1991) 135-139.
- [16] J. W. Hutchinson and H. M. Jensen, *Mech. Mtls.*, **9** 139 (1990).
- [17] W.A. Curtin, *J. Am. Ceram. Soc.*, **74** [11] 2837-45 (1991).
- [18] M.Y. He, A. Bartlett, A.G. Evans and J.W. Hutchinson, *J. Am. Ceram. Soc.*, **74** [4] 767-71 (1991).
- [19] W.H. Yang and D.J. Srolovitz, "Crack-Like Surface Instabilities in Stressed Solids," *Phys. Rev. Lett.*, in press.

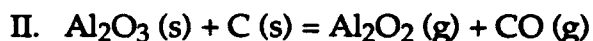
## APPENDIX I

### Thermodynamic Calculations

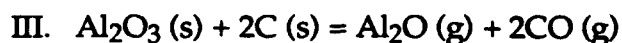
For alumina to be reduced by carbon during diffusion bonding, a maximum pressure for the reaction system can be determined. The chemical reactions of interest and their standard free energies,\*  $\Delta G^\circ$  (J/ mole), per mole of CO, are as follows:



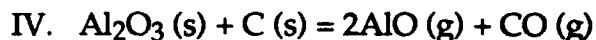
$$\Delta G^\circ = 1260904.5 - 575.5 T$$



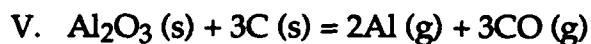
$$\Delta G^\circ = 1141595 - 389.3 T$$



$$\Delta G^\circ = 1262879 - 551.7 T$$



$$\Delta G^\circ = 1600515 - 522.2 T$$



$$\Delta G^\circ = 1929403 - 799.7 T$$



$$\Delta G^\circ = -111700 - 87.65 T$$



$$\Delta G^\circ = -54800 + 173.6 T$$

where T is the temperature. Reaction I was calculated to have the lowest free energy for the temperature range of interest (1250°C-1450°C). Furthermore, since this reaction

---

\* Thermodynamic data are taken from references 8-11.

involves the formation of one gaseous species the equilibrium CO partial pressure can be determined as a function of temperature.\* The equilibrium CO partial pressure is calculated (Table A.1), using

$$P_{\text{CO}} = \exp\left[\frac{\Delta G^\circ}{3RT}\right]$$

For Reaction I to proceed, the partial pressures of CO in the system must not exceed the equilibrium values. The partial pressures of the CO<sub>2</sub>, O<sub>2</sub> and the aluminum suboxides can also be determined using these CO partial pressures (Table A2).

**Table AI**  
**Equilibrium Partial Pressure of CO for Reaction I**

T (°C)	pCO (atm)
1250	4.0*10 <sup>-5</sup>
1350	3.1*10 <sup>-4</sup>
1450	1.9*10 <sup>-3</sup>

For Reaction I to proceed, the CO partial pressures in the system must not exceed the equilibrium values. Such pressures cannot develop in the vacuum system used for the present experiments.

With P<sub>CO</sub> specified at its equilibrium value, the partial pressures of the aluminum suboxides can be determined for Reactions II to V (Table AII).

---

\* It is assumed that the buffer system described by reactions VI. and VII. does not dictate the CO partial pressure in the system.

Fig. 12. Schematic of the effect of mode mixity on the relative crack growth rates for different crack trajectories. Also shown is the ratio of  $\Delta G$ 's. For this case, interface debonding is preferred over mode I growth into the alloy.

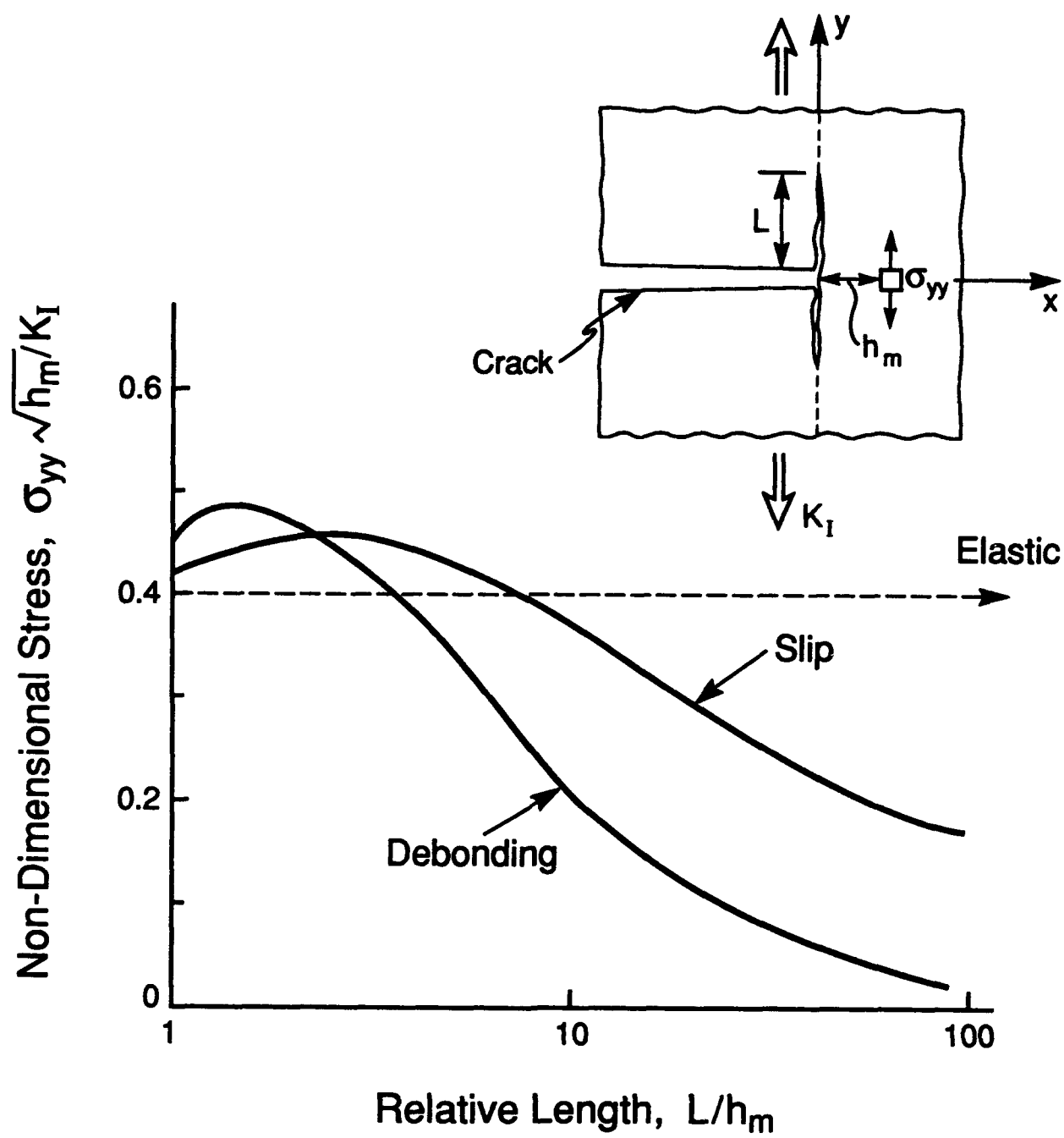


Figure 1

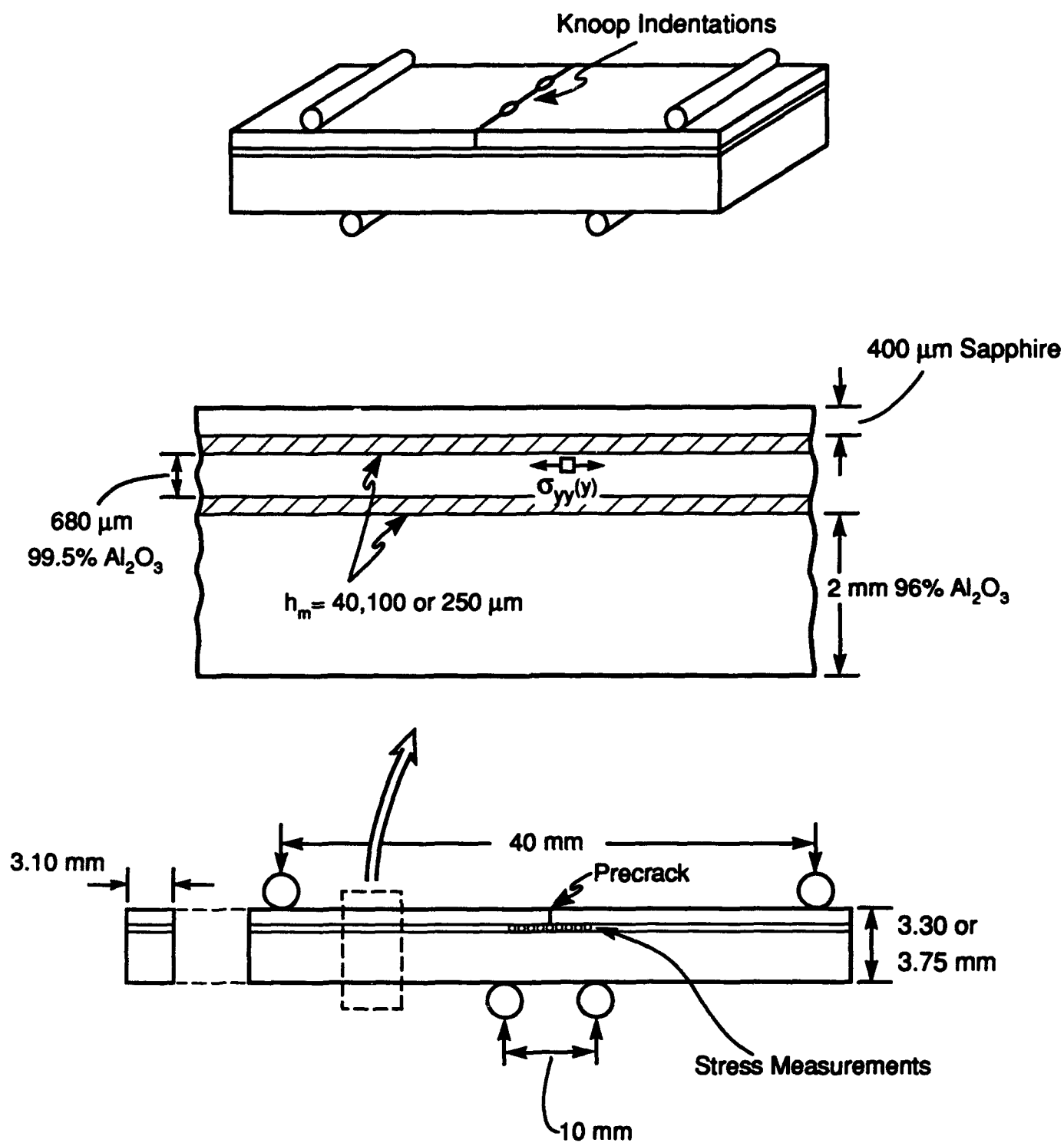
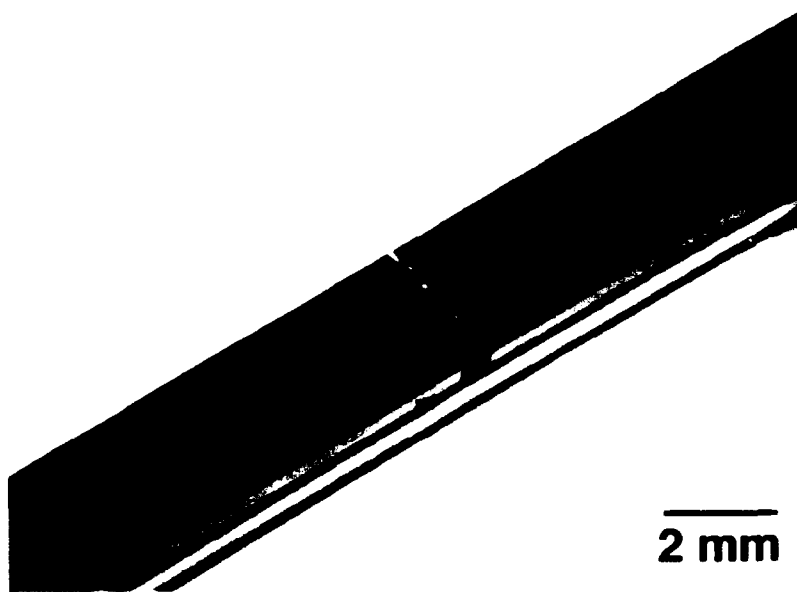
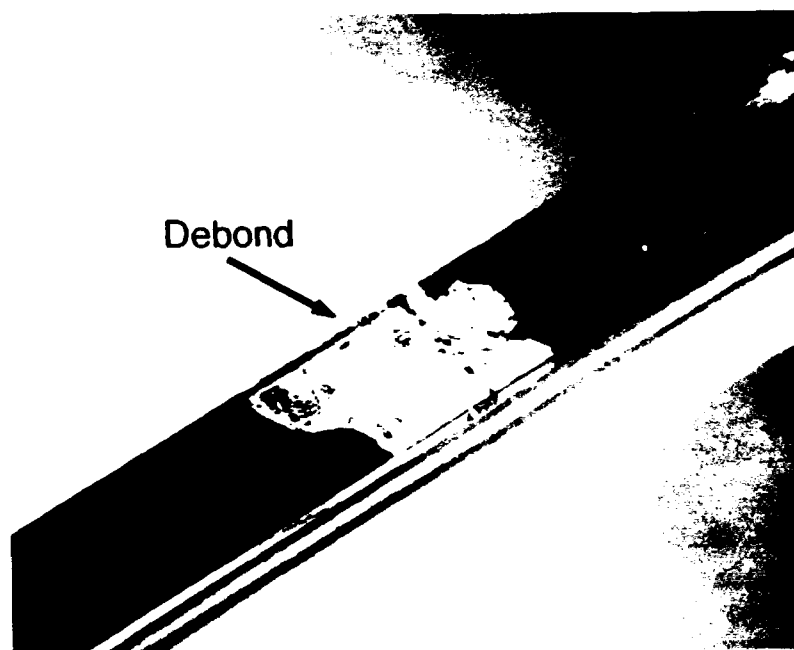


Figure 2





**1 Load Cycle**



**50,000 Load Cycles**

Figure 3(a)

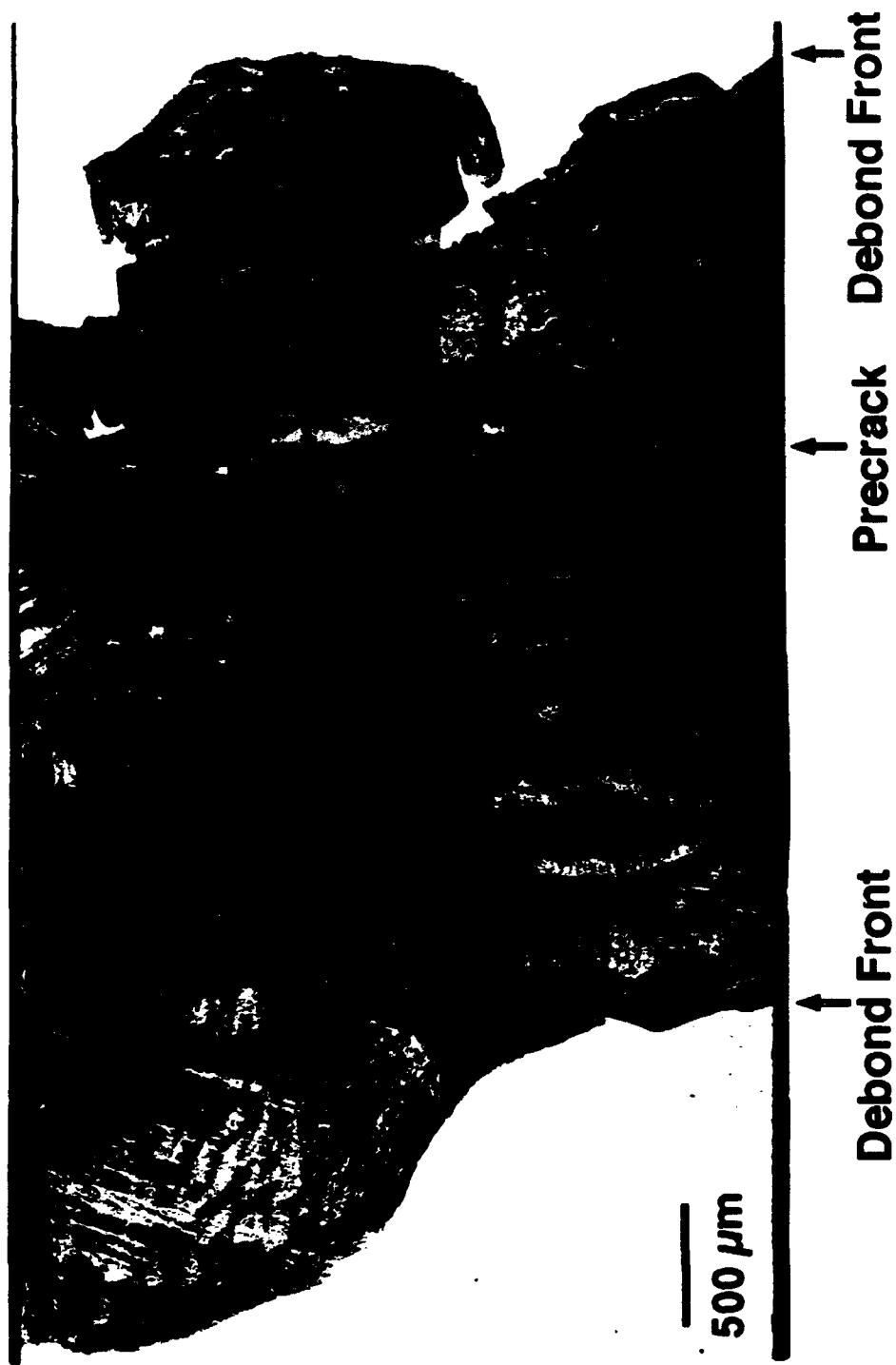


Figure 3(b)

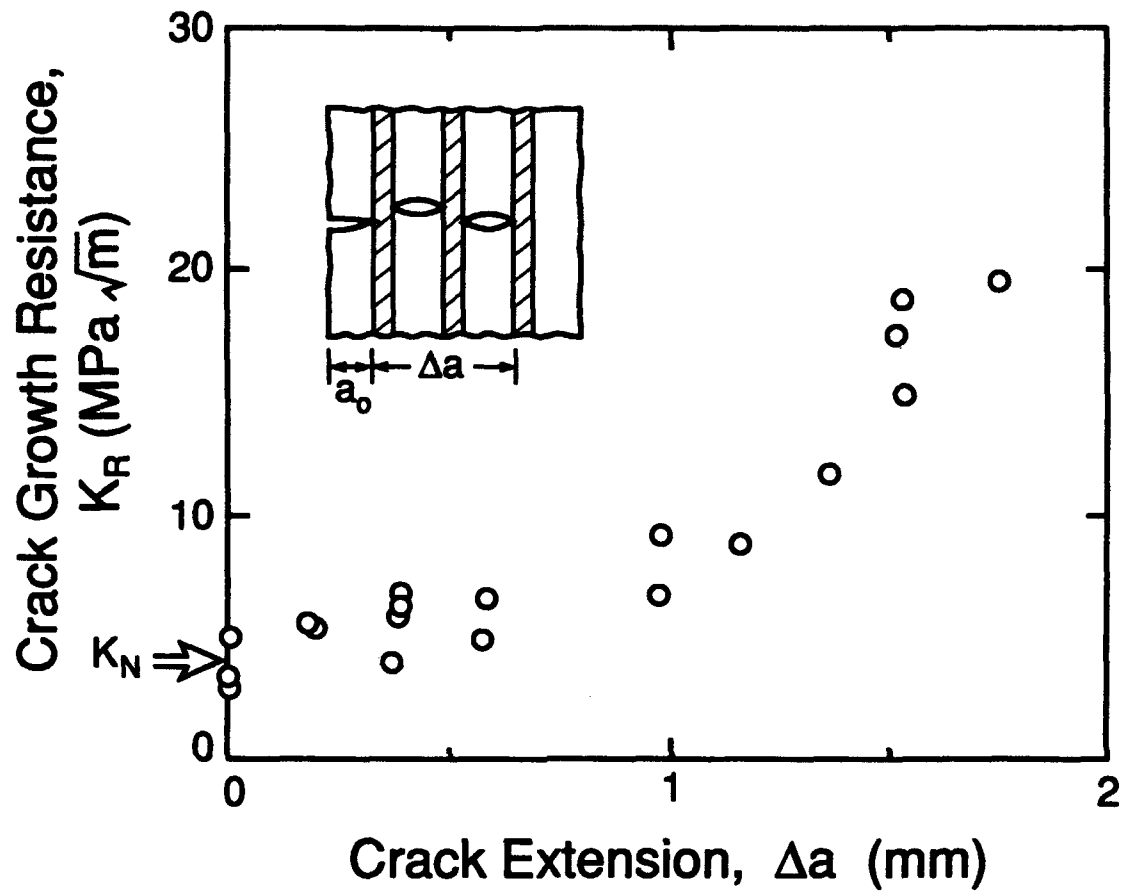
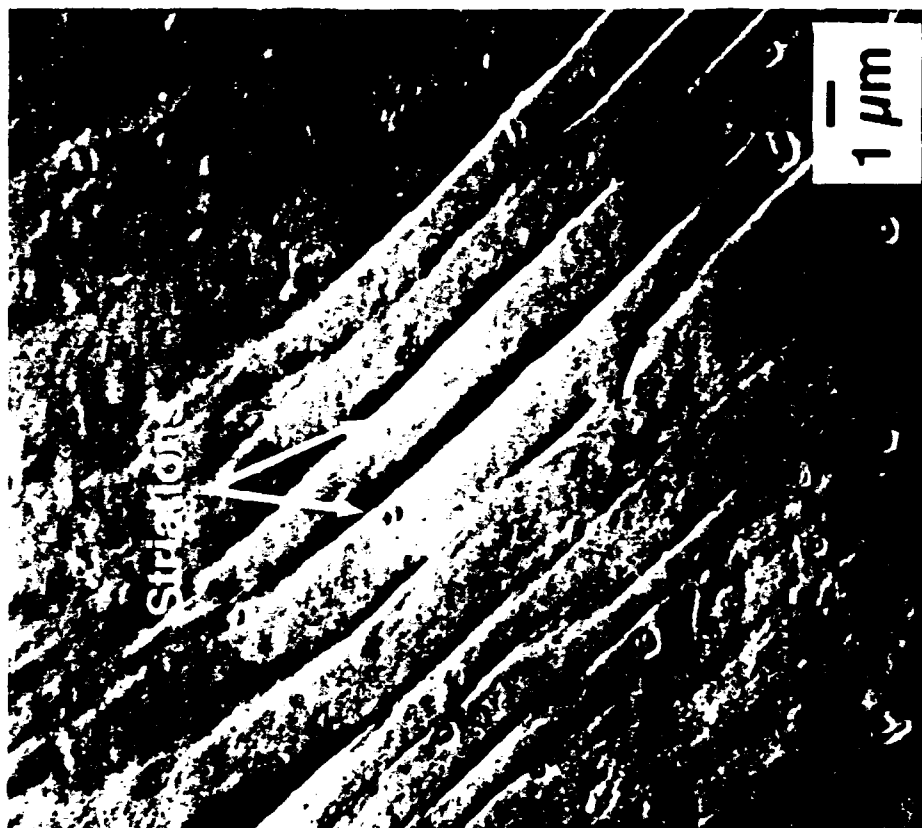
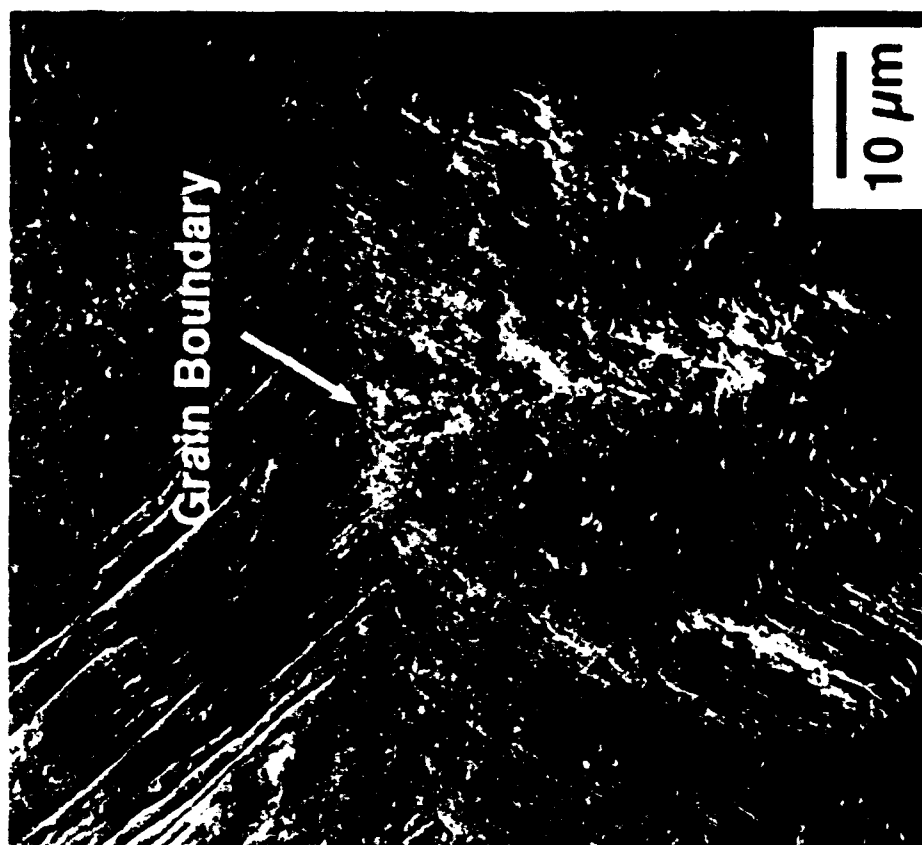


Figure 4



(a)



(b)

Figure 5

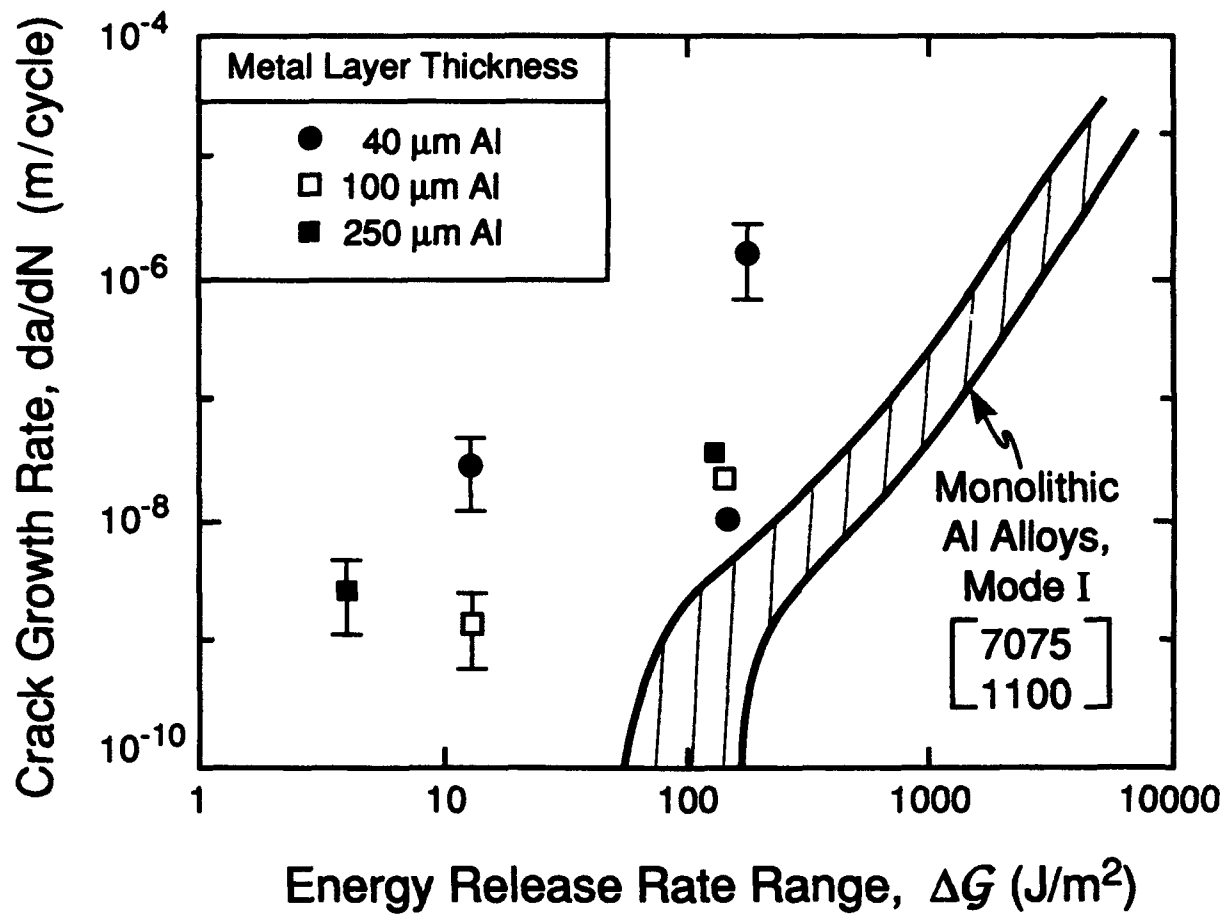


Figure 6



Figure 7

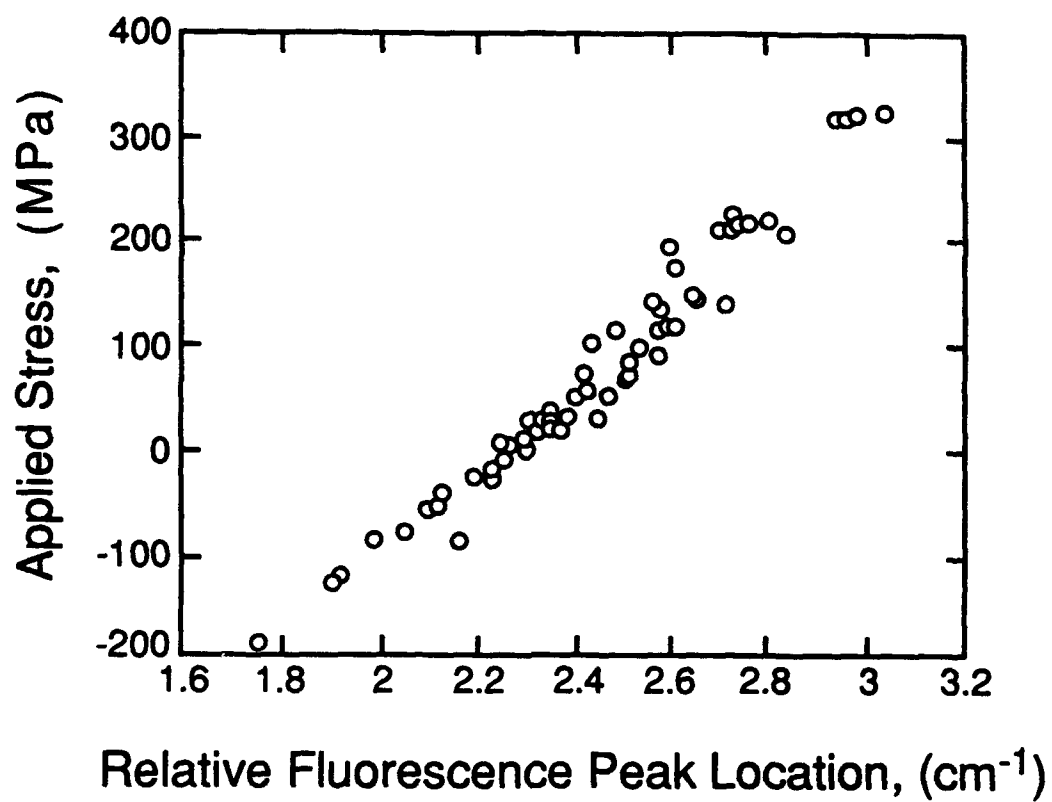


Figure 8

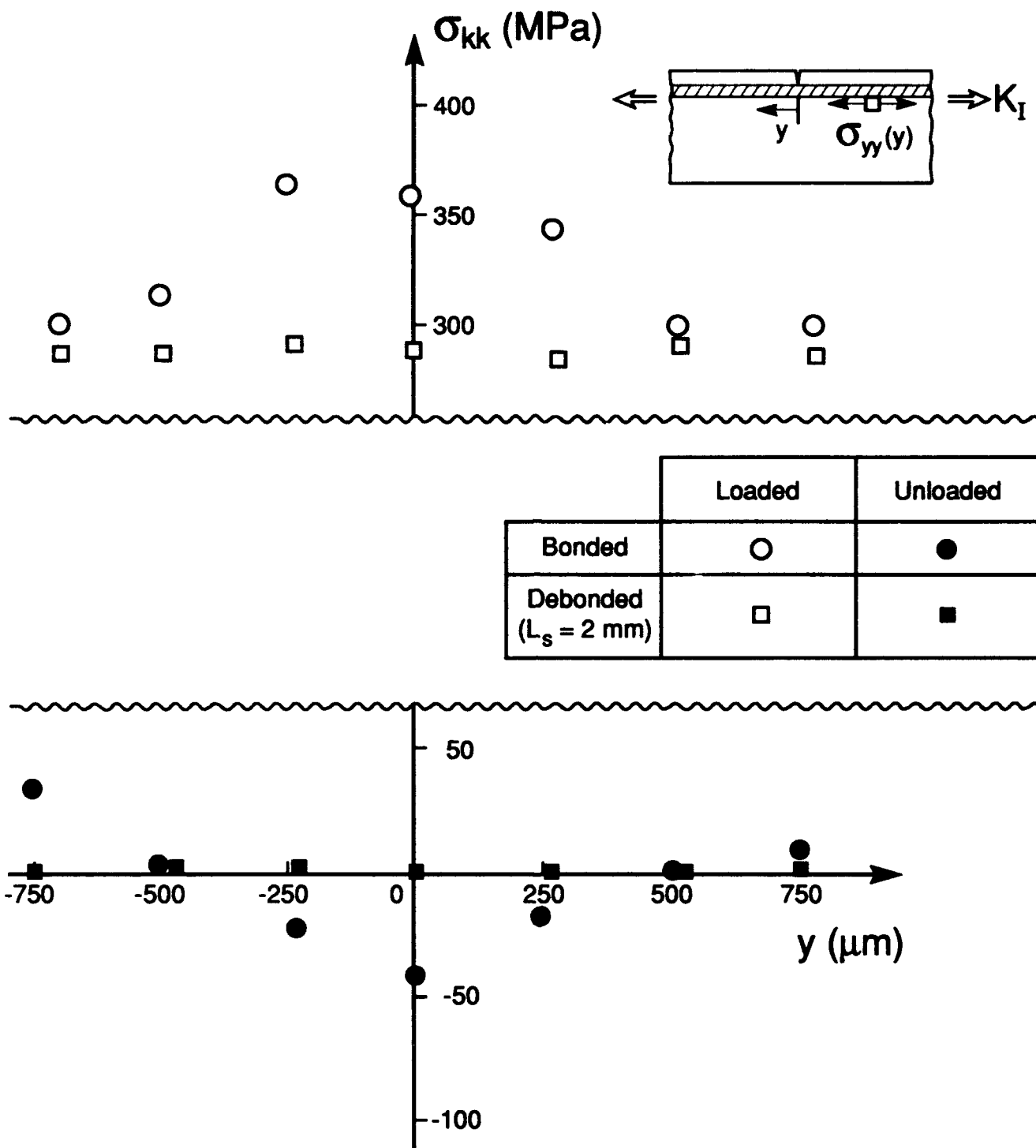


Figure 9



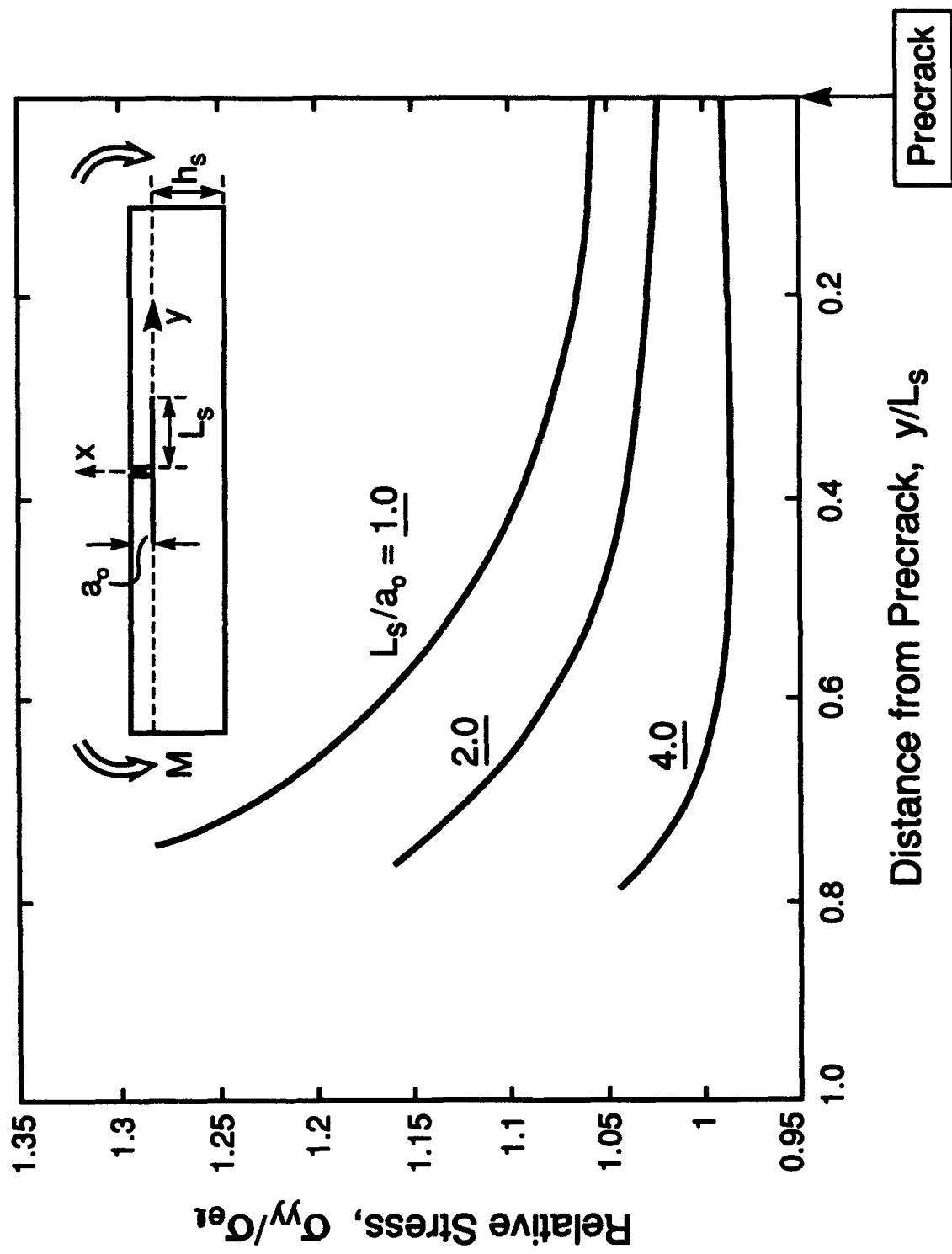


Figure 10

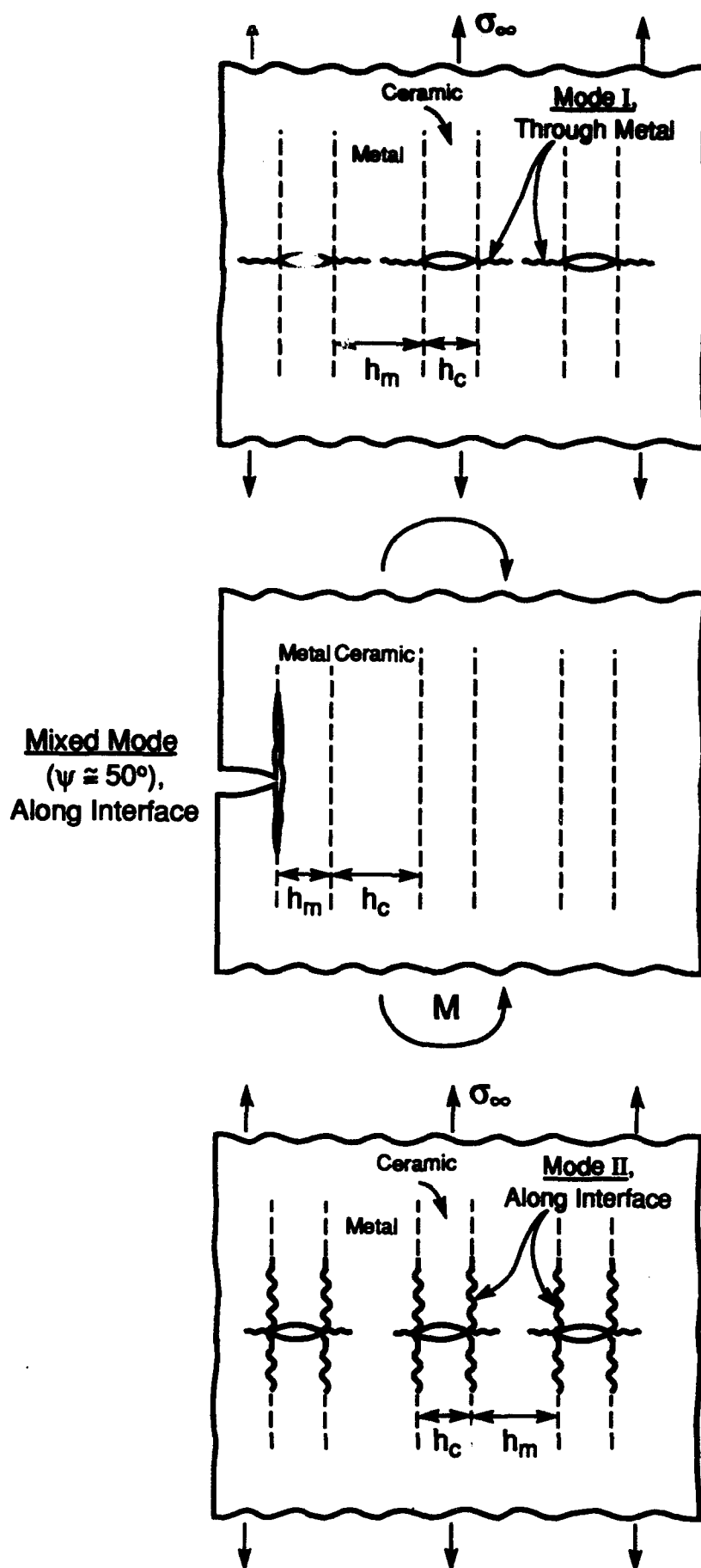


Figure 11

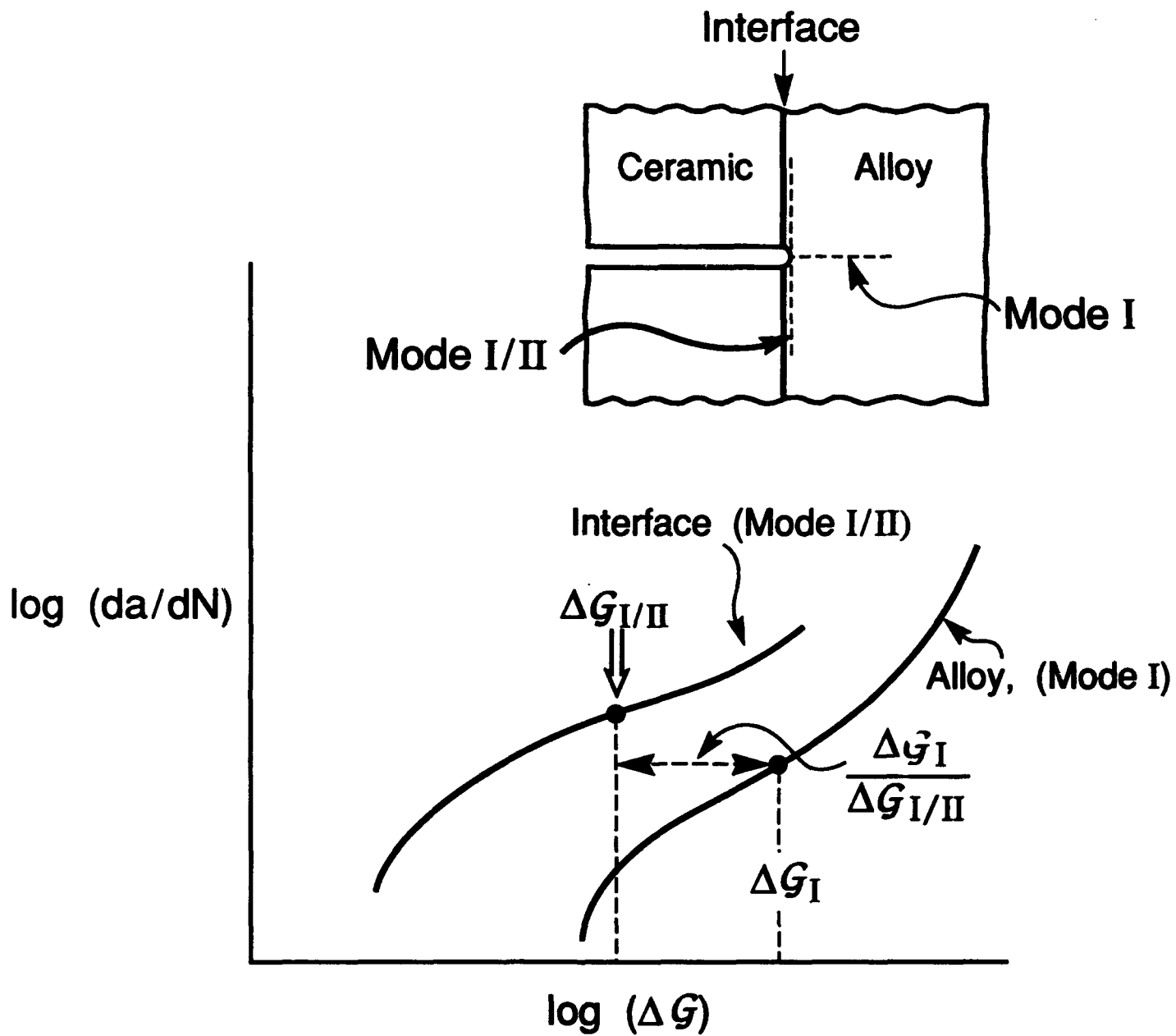
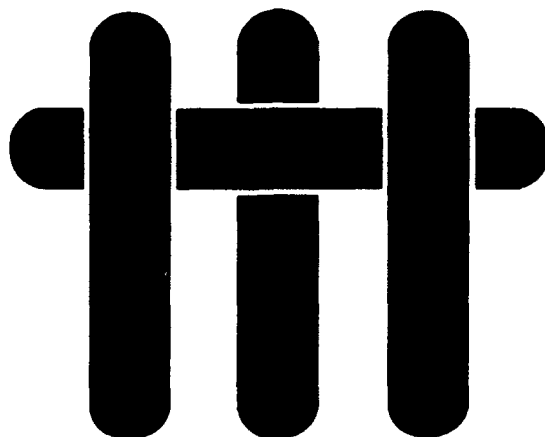


Figure 12

# M A T E R I A L S



## **EFFECTS OF COMPOSITE PROCESSING ON THE STRENGTH OF SAPPHIRE FIBER-REINFORCED COMPOSITES**

by

J.B. Davis, J. Yang and A.G. Evans  
Materials Department  
College of Engineering  
University of California, Santa Barbara  
Santa Barbara, California 93106-5050

## ABSTRACT

The current interest in tough, high-temperature materials has motivated fiber coatings development for sapphire fiber-reinforced alumina composites. For this system, it has been demonstrated that the interfacial properties can be controlled with coatings which can be eliminated from the interface subsequent to composite consolidation. However, these fugitive coatings can contribute to the high temperature strength degradation of sapphire fibers. Such degradation, which compromises the composite strength and toughness, is the focus of the current investigation. It has been observed that in some cases selecting appropriate composite processing conditions can minimize such effects but overcoming fiber strength loss remains an important issue for the use of these composites.

## 1. INTRODUCTION

The current limitations to the advancement of ceramic matrix composites are associated with the development of high strength, oxidation and creep resistant fiber-reinforcements and the control of the interfacial debonding and sliding behaviors. One approach to reinforcements has been to develop single crystal oxide fibers. The most thoroughly studied of these is sapphire. One promising class of coating is fugitive,<sup>1-2</sup> whereby the coating is removed from the interface subsequent to composite consolidation in order to leave a gap between the fiber and matrix. Carbon and molybdenum are examples of such coatings. The coating thickness and resulting gap size are used to manipulate the interfacial sliding resistance. However, the coating chemistry and thickness can affect the surface morphology of the fibers during either composite processing or subsequent exposures to high temperatures. This can lead to pronounced changes in fiber strengths. Such effects are the focus of this investigation.

This study has five essential elements. (i) Uncoated fibers were heat treated and their strengths measured in order to classify inherent strength degradation mechanisms. (ii) Coated fibers were given similar heat treatments and tested to establish additional degradation phenomena that may arise. (iii) Fibers with thick fugitive coatings of C and Mo were introduced into an alumina matrix by hot pressing. The fibers were removed by using the fugitive character of the coating. The withdrawn fibers were tested. These tests identified new degradation mechanisms that may operate with this coating. (iv) Unidirectional composites were fabricated with several coating thicknesses. The tensile properties of the composite were measured and fiber push-out tests performed. These tests indicated whether there are other strength loss phenomena associated with composite consolidation. They also allowed correlation to be made between composite behavior and the fiber strength and the interface debonding and sliding resistance.

(v) The fiber morphological changes have been examined in order to provide an understanding of the mechanisms involved.

## **2. EXPERIMENTAL PROCEDURES**

### **2.1 Fiber Strength Tests**

The fibers were obtained from a single spool of Saphikon sapphire fiber (diameter  $\sim 130\text{ }\mu\text{m}$ ). Their tensile strengths were measured for several fiber conditions by using a commercially available fiber testing machine\* and a one-inch gauge length. The first set was tested in the as-received state. The second was washed in cold water followed by acetone and ethanol, and then subjected to the series of heat-treatments summarized in Table I. The remaining two sets were first washed and then coated with either Mo or C to a thickness of  $\sim 10\text{--}15\text{ }\mu\text{m}$ . These were hot pressed into a high purity alumina matrix using the conditions specified in Table I. After hot pressing, the composites were heat treated at  $1100^\circ\text{C}$  in air for  $\sim 2\text{ h}$  to remove the coatings from the interfaces. The fibers were extracted from the matrix and their strengths were measured directly.

Fiber strength data sets were comprised of  $\sim 20$  measurements. While this set size is too small to give an accurate determination of the fiber strength distribution parameters, it is sufficient to establish definitive trends in the median fiber strength.<sup>3,4</sup>

### **2.2 Composite Specimen Fabrication**

Unidirectional alumina matrix composites containing Mo coated sapphire fibers were produced for correlating composite behavior with the properties of the fibers and interfaces. Coatings with three thicknesses ( $0.2$ ,  $0.7$  and  $1.4\text{ }\mu\text{m}$ ) were used. Composites were produced by hot isostatic pressing (HIPing). These have been made by first

---

\* Micropull Sciences, Thousand Oaks, California

fabricating a preform comprising coated fibers within a slurry of the matrix material. These composites were sealed in an evacuated niobium can. Consolidation was achieved at a pressure of 30 MPa at 1350°C for 30 min (Fig. 1). Dog-bone shaped tensile specimens were diamond machined from the consolidated composite and the coatings were removed from the interface by heat-treating in air at 1150°C for 50 h.

### **2.3 Microstructural Characterization**

Scanning electron microscopy (SEM) techniques with energy dispersive X-ray analysis were used to identify the strength limiting flaws for each data set. In addition, the morphologies of heat-treated fibers were examined in a field emission scanning electron microscope (JEOL 6300F) in order to classify and compare various surface and fracture features.

The interfaces in the composites were examined by transmission electron microscopy (TEM). For this purpose, electron transparent foils were prepared as described elsewhere. After tensile testing, the fiber pull-out length distributions were measured from scanning electron micrographs and the surface features of the fibers characterized. In addition, interactions between the fibers and the matrix were also classified.

### **2.4 Composite Testing**

Tension tests were performed on the composite in a fixture located within a scanning electron microscope (Fig. 2). The forces were measured from a load cell. The behavior at small strains was monitored from strain gauges affixed to the specimen. At larger strains, the specimen displacement was measured with an LVDT. These strain data were compared with photomicrographic measurements.

The interfacial sliding resistances were measured by using the fiber push-through technique.



### 3. FIBER STRENGTHS

The fibers in the as-received condition were found to have a median strength,  $\bar{S} \approx 2.7$  GPa, and a Weibull modulus,  $m \approx 6.5$  (Fig. 3a), consistent with values reported in the literature.<sup>5</sup> After heating the washed, uncoated fibers to successively higher temperatures (1250°C, 1350°C and 1450°C), there were small, though significant, reductions in either the mean strength,  $\bar{S}$ , or the Weibull modulus,  $m$ , (Fig. 3b, Table I). Conversely, extracted fibers originally coated with Mo showed considerable strength loss, at all heat-treatment temperatures (Fig. 3b). The fibers originally coated with carbon exhibited a smaller reduction in median strength but had the most substantial strength *variability*, reflected in the highest coefficient of variation and the low Weibull modulus ( $m \approx 2.6$ ).

**Table I**  
**Fiber Strength Data**

Heat Treatment*		Median Strength (GPa)	Coefficient of Variation	Weibull Modulus
Uncoated	1250°C	2.6	0.10	9.8
	1350°C	2.0	0.15	6.8
	1450°C	2.1	0.18	5.8
Mo	1250°C	1.9	0.16	6.2
Coated:	1350°C	1.4	0.32	2.2
Extracted	1450°C	1.0	0.33	3.2
C Coated: Extracted	1450°C	1.6	0.38	2.6
	As-Received	2.9	0.13	6.5

\* With the exception of the As-Received set, all fibers were heated in an air furnace at 1150°C for 2 hours subsequent to the heat treatments shown above.

#### **4. FIBER MORPHOLOGY**

Upon heat treatment, the fiber morphology is found to be strongly influenced by both diffusional effects and chemical reactions, especially in the presence of either fiber coatings or a composite matrix. There are four basic phenomena (Fig. 4), each exemplified by the observations presented below. (i) Surface diffusion causes fiber facetting, even in isolated fibers. (ii) Thin polycrystalline coatings, when chemically inert (no reaction products), are morphologically unstable and develop holes. Equilibrium at the hole edges then motivates surface diffusion and induces the formation of ridges on the fibers. (iii) Chemical reactions occur between the coating and the fiber resulting in fiber surface damage. This may produce either solid or gaseous reaction products. (iv) After a coating has either become discontinuous during composite consolidation or has been removed by oxidation, the matrix may sinter to the fiber. This results in localized bonding, causing matrix grains to remain attached to the fiber during pull-out, upon composite testing.

##### **4.1 Uncoated Fibers**

The fibers display sinusoidal diameter modulations along their length with characteristic wavelengths and amplitudes, described elsewhere.<sup>6</sup> Flaws observed in the as-received fibers were primarily associated with porosity. Pores develop during fiber growth and have been observed within the fibers and at the fiber surfaces (Fig. 5). The strength range is consistent with calculations for cylindrical rods containing cracks having the same dimensions as the pores<sup>7</sup> (Fig. 6).

The surface features were altered by high temperature heat-treatments. The fibers facet (Fig. 7), illustrating the inherent morphological instability of single crystal fibers. Frequently, local surface damage was evident resulting from chemical reactions (Fig. 8a). These sites usually correlate with failure origins and account for the strength

loss. Energy dispersive X-ray spectroscopy measurements identified Si and Mg at these sites (Fig. 8b). Two likely sources of contamination include the incomplete removal of the fiber sizing and reactions with inorganic contaminants that condense onto the fiber surfaces during heat treatment in the air furnace. Such contaminant reactions are avoidable upon encapsulation of the fibers and are of moderate practical concern.

## 4.2 Carbon Coated Fibers

The heat treated carbon coated fibers displayed surface regions indicative of a chemical reaction between the coating and the fiber, localized near fiber ends and at locations where the coatings were discontinuous. The reaction product, identified by X-ray analysis as  $Al_4C_3$ , severely degraded the fiber surface (Fig. 9). The extent of reaction increased with temperature (Fig. 10). In addition, accentuated fiber facetting occurred near the reaction sites.

Thermodynamic calculations (Appendix 1) indicate that alumina and C can react to form volatile aluminum suboxides at temperatures as low as 1100°C, at least when heat treatments are conducted in an open system.<sup>8-11</sup> The progress of these reactions requires a means of removing CO from the reaction site, consistent with the reactions being preferentially located at the fiber ends and at coating discontinuities. This tendency for localized attack is presumably responsible for the strength *variability* of the fibers. Some fibers were relatively undamaged in the gauge section and exhibit strengths similar to the uncoated fibers heat treated to the same temperature. Others were damaged in the gauge length associated with areas where the coating was discontinuous.

## 4.3 Mo Coated Fibers

Observations of the extracted Mo coated fibers reveal substantial changes in surface morphology. At least two phenomena contribute. The first involves the breakup

of the polycrystalline Mo coating.<sup>12,13</sup> The Mo/Al<sub>2</sub>O<sub>3</sub> interface then forms ridges on the surface of the sapphire, at the Mo grain edges. This process proceeds by *surface and interface diffusion*. The ridges are visible when the coating is chemically etched from the fibers (Fig. 11). They heighten as the heat treatment temperature increases. Upon removing the coating, further heat treatment causes the ridges to become unstable. The morphology then resembles fiber facetting, but with an additional surface roughness that originates with the ridges.

A second potential phenomenon involves the dissolution of alumina in Mo. If it occurs, the same morphological changes discussed above would proceed, but the kinetics could be more rapid than those for interface diffusion. Such dissolution has been well documented for Nb/Al<sub>2</sub>O<sub>3</sub> interfaces<sup>14</sup> and has been reported to occur for Mo/Al<sub>2</sub>O<sub>3</sub> composites as well at temperatures similar to those used in this study (subject to the oxygen partial pressure).<sup>15</sup> However, it has not been verified for Mo, because high resolution TEM specimens are difficult to produce without interface debonding.

The large strength reduction found for the Mo coated fibers is presumed to relate to the ridges and troughs formed by diffusion or dissolution. It has not been possible to quantify the measured strengths, because an appropriate surface flaw model has not been developed. However, the general trend toward a lower strength with increased ridge height, as the temperature increases, suggests that a model based on the stress intensification caused by ridges and troughs is consistent with the measurements.

#### **4.4 Fibers Within A Composite**

Thin (0.2 and 0.7  $\mu\text{m}$ ) Mo fiber coatings do not remain continuous after composite consolidation (Fig. 12). Consequently, submicron thick Mo fiber coatings permit the fibers to sinter to the matrix, during HIPing, in those areas where the coating has become discontinuous (Fig. 13). The thicker (1.4  $\mu\text{m}$ ) Mo coatings are continuous

(Fig. 12), but the thickness is non-uniform. For these coatings, local sintering of the fiber to the matrix does not occur upon HIPing, but can still occur *after the coating has been removed*. In such cases, upon debonding, some matrix grains remain attached to the fiber, with associated ridge formation and fiber damage (Fig. 14). Chipping of the fibers can also occur (Fig. 15). Such visual evidence of fiber, matrix sintering allows measurement of the sintered regions to give the area fraction of fiber bonded to the matrix,  $f_A$  (Table II). In some locations, additional features are evident, manifest as large ridges and troughs between neighboring sintered sites (Fig. 16).

Sintered areas resist debonding and increase the interfacial fracture energy in proportion to the area fraction of bonding. Moreover, when the matrix sinters to the fibers, the resulting damage (Fig. 14, 15) reduces the fiber strength. The relatively large depth of these damaged regions compared with the size of the ridges and troughs found for the extracted Mo coated fibers (Fig. 3) suggests that the strengths may be substantially lower in the HIPed composites. The magnitude of the additional strength reduction is implied from analyses conducted below.

Localized sintering would also induce residual stress upon cooling, because of the thermal expansion mismatch between c-axis sapphire and polycrystalline  $\text{Al}_2\text{O}_3$ . Such stresses should be of order 100 MPa and may influence trough formation (Appendix II).

## 5. COMPOSITE PROPERTIES

Composites with Mo coated fibers were tested after removing the Mo. All failed from a single dominant crack because of the low fiber volume fractions ( $f < 0.20$ ). However, the fracture resistance and the extent of fiber pull-out were very different for the three coating thicknesses (Table II). The specimens with thin ( $0.2 \mu\text{m}$ ) gaps had low toughness and exhibited co-planar fracture (Fig. 17), with no pull-out. Conversely, appreciable pull-out was evident for the two larger interfacial gaps (Fig. 18). Moreover,

the material with the 1.4  $\mu\text{m}$  interface gaps exhibited substantially more pull-out (average pull-out length,  $\bar{h} \sim 640 \mu\text{m}$ ) than the material with the 0.7  $\mu\text{m}$  gaps ( $\bar{h} \sim 90 \mu\text{m}$ ). A typical load-displacement curve for these materials illustrates the fiber pull-out contribution to the composite fracture resistance (Fig. 19). The magnitude of the fracture dissipation is 40 k Jm<sup>-2</sup>. The associated ultimate tensile strengths (UTS), summarized in Table I indicate a similar trend, with the larger gap giving a considerably higher UTS.

The corresponding push-out behaviors are summarized in Fig. 20. The composite with the thinnest coating did not exhibit push-out. The inability of this interface to slide and pull-out results from sintering. Conversely, sliding was induced in the other two composites. Both materials exhibited essentially the same sliding resistance, probably because local variations in the coating thickness, rather than the average gap width, dominate sliding.

## 6. ANALYSIS

### 6.1 Method and Assumptions

An attempt is made to interpret the above composite behavior in terms of the fiber strength degradation phenomena, discussed above, in conjunction with related trends in interface properties. For this purpose, three basic assumptions are made and used together with models of interface debonding and sliding, as well as fiber pull-out. It is assumed that, when the fiber sinters to the matrix, debonding occurs when the energy release rate reaches the mode I fracture energy of the fine-grained alumina polycrystals ( $\Gamma_c \approx 25 \text{ Jm}^{-2}$ ). The debonding energy is then,

$$\Gamma_i \approx f_A \Gamma_c \quad (1)$$

with  $f_A$  given in Table II. It is also assumed that a sliding zone exists behind the debond, subject to a constant sliding resistance,  $\tau$ . In this case, the debond length,  $\ell$ , at stress,  $\sigma$ , is<sup>16</sup>

$$\ell = \frac{R(1-f)}{2\tau f}(\sigma - \sigma_i) \quad (2)$$

where  $R$  is the fiber radius,  $f$  is the fiber volume fraction and  $\sigma_i$  is the debond stress given by,

$$\sigma_i = \frac{1}{C_1} \sqrt{E\Gamma_i/R} - \sigma^T \left( \frac{C_2}{C_1} \right) \quad (3)$$

where  $\sigma^T$  is the axial misfit stress caused by thermal expansion mismatch and  $C_1$  and  $C_2$  are constants defined by Hutchinson and Jensen.<sup>16</sup>

Finally, it is assumed that fiber failure occurs *within the debond zone*, in accordance with weakest link statistics. The fiber pull-out length  $\bar{h}$  should then be related to  $\ell$ . The relationship between  $\ell$  and  $\bar{h}$  is considered to be similar to that devised by Curtin,<sup>17</sup>

$$\bar{h} = \ell \lambda'(m) \quad (4)$$

where  $\lambda'$  is a function of the Weibull modulus of the fibers. Equation (4) must be a lower bound for the pull-out length.

## 6.2 Interpretation

The preceding formulae allow an understanding and rationalization of the observation that composites with the 0.7  $\mu\text{m}$  gap have smaller pull-out lengths than



materials with a 1.4  $\mu\text{m}$  gap, but yet have similar sliding resistance. There are two factors involved. (i) A smaller debond length is expected with the narrower gap, because of the larger debond resistance that has been induced by the more extensive fiber/matrix sintering. Slip is limited by the debond length.<sup>‡</sup> (ii) Fiber weakening occurs when matrix grains sinter to the fibers and create damage sites (Fig. 14, 15).

The measured UTS,  $\sigma_u$ , may be inserted into Eqn. (2) and, upon using Eqns. (1) and (3), the debond lengths at failure may be estimated. The results (Table II) verify that a considerably larger debond length develops for the composite with the wider interface gap. Moreover, the proportionality constant,  $\lambda'$ , between the pull-out length,  $\bar{h}$ , and the debond length  $l$  (Eqn. 4) is similar for both materials.

The strengths of the fibers in the composite  $S_c$  is out of order (Table II),

$$S_c \approx \sigma_u / f \quad (5)$$

These strengths are considerably lower than those measured for the extracted fibers with the thick coatings. It is implied that the strengths have been markedly degraded by sintering of the matrix to the fibers. Furthermore, because  $S_c$  represents the strength measured at a gauge length of order the debond length, even smaller values would obtain at a 1" gauge length.

---

<sup>‡</sup> In addition, local residual stresses at the bonded sites along the interface may influence the interface crack trajectory.<sup>18</sup>

**Table II**  
**Composite Properties**

Coating Thickness ( $\mu\text{m}$ )	$\tau$ (MPa)	$\bar{h}$ ( $\mu\text{m}$ )	Fracture of Fiber/Matrix Bonded	Measured UTS (MPa)	$S_c$ (GPa)	$i$ ( $\mu\text{m}$ )	$\lambda'$ (m)
0.7	17	90	~ 0.05	22	0.1	250	0.3
1.4	15	640	~ 0.01	79	0.4	1000	0.7

## 7. SUMMARY

Single crystal sapphire fibers have been suggested as a high strength reinforcement for ceramic matrix composites. Interfaces have been developed based on a fugitive coating concept which satisfies the fiber debonding and sliding conditions for toughness enhancement in these materials. However, the strengths of the fibers are reduced by the presence of the coatings and are further reduced upon forming a composite. The mechanisms for the strength loss of coated fibers include: i) gas phase reactions with the coating which produce aluminum sub-oxides and etch the fibers ii) chemical reactions which form solid state reaction products and iii) facetting or ridging by surface diffusion. Carbon coated fibers are susceptible to the first two modes of degradation. However, it should be possible to minimize these effects by selecting composite processing conditions that provide a controlled CO/CO<sub>2</sub> atmosphere. For the Mo coatings, the degradation mechanisms are primarily of the third type and more difficult to eliminate.

Additional fiber strength reduction results after composite processing with thin coatings, due to localized sintering of the matrix to the fiber. Such bonding affects the surface of the fibers. It also imposes a residual stress, which may further alter the surface morphology. It is believed that this strength loss could be minimized by manipulating the matrix microstructure and chemistry (by incorporating segregants) to reduce the sintering potential.

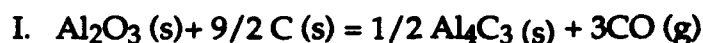
## REFERENCES

- [1] T. Mah, K. Keller, T.A. Parthasarathy and J. Guth, *Ceram. Eng. Sci. Proc.*, **12** [9-10] pp. 1802-15 (1991).
- [2] J.B. Davis, J.P.A. Löfvander, E. Bischoff, A.G. Evans and M.L. Emiliani, *J. Am. Ceram. Soc.*, **76** [5] 1249-57 (1993).
- [3] K. Trustrum, and A. De S. Jayatilaka, *J. Mat. Sci.*, **14** 1080-1084 (1979).
- [4] J.R. Porter, *MRS Symp. Proc.*, **273** 315-324 (1992).
- [5] E. Trembauer and R. Tressler, *HITEMP Conference Proceedings* (1992).
- [6] T.J. Mackin, J. Yang and P.D. Warren, *J. Am. Ceram. Soc.*, **75** [12] 3358-62 (1992).
- [7] H. Tada, P.C. Paris and C.R. Irwin, *The Stress Analysis of Cracks Handbook*, Del Research Corp., Pennsylvania (1973).
- [8] L.M. Foster, G. Long and M.S. Hunter, *J. Am. Ceram. Soc.*, **39** [1] 1-11 (1956).
- [9] D.R. Stull and H. Prophet, *JANAF Thermochemical Tables*, 2nd ed., NSRDS-NBS 37, U.S. Department of Commerce, Washington, D.C., 1971.
- [10] I. Barin and O. Knacke, *Thermochemical Properties of Inorganic Substances*, Springer-Verlag, New York, 1973.
- [11] I. Barin, O. Knacke, and O. Kubaschewski, *Thermochemical Properties of Inorganic Substances, Supplement*, Springer-Verlag, New York, 1977.
- [12] W.W. Mullins, *Journal of Applied Physics*, **28** [3] 333-339 (1957).
- [13] K.T. Miller, F.F. Lange and D.B. Marshall, *Mat. Res. Soc. Proc. Sym. on Ultrastr. Proc.*, **121** [3] 823-30 (1988) and *J. Mater. Res.*, **1** [5] 151-60 (1990).
- [14] M. Rühle and A.G. Evans, *Materials Science and Engineering*, **A107** 187-197 (1989).
- [15] G.H.M. Gubbels, *Materials Science and Engineering*, **A135** (1991) 135-139.
- [16] J. W. Hutchinson and H. M. Jensen, *Mech. Mtls.*, **9** 139 (1990).
- [17] W.A. Curtin, *J. Am. Ceram. Soc.*, **74** [11] 2837-45 (1991).
- [18] M.Y. He, A. Bartlett, A.G. Evans and J.W. Hutchinson, *J. Am. Ceram. Soc.*, **74** [4] 767-71 (1991).
- [19] W.H. Yang and D.J. Srolovitz, "Crack-Like Surface Instabilities in Stressed Solids," *Phys. Rev. Lett.*, in press.

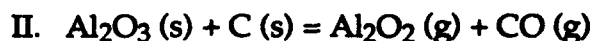
## APPENDIX I

### Thermodynamic Calculations

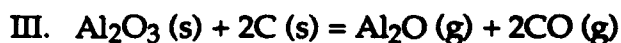
For alumina to be reduced by carbon during diffusion bonding, a maximum pressure for the reaction system can be determined. The chemical reactions of interest and their standard free energies,\*  $\Delta G^\circ$  (J/ mole), per mole of CO, are as follows:



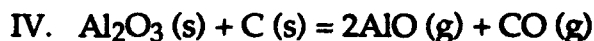
$$\Delta G^\circ = 1260904.5 - 575.5 T$$



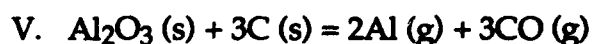
$$\Delta G^\circ = 1141595 - 389.3 T$$



$$\Delta G^\circ = 1262879 - 551.7 T$$



$$\Delta G^\circ = 1600515 - 522.2 T$$



$$\Delta G^\circ = 1929403 - 799.7 T$$



$$\Delta G^\circ = -111700 - 87.65 T$$



$$\Delta G^\circ = -564800 + 173.6 T$$

where T is the temperature. Reaction I was calculated to have the lowest free energy for the temperature range of interest (1250°C-1450°C). Furthermore, since this reaction

---

\* Thermodynamic data are taken from references 8-11.

involves the formation of one gaseous species the equilibrium CO partial pressure can be determined as a function of temperature.\* The equilibrium CO partial pressure is calculated (Table A.1), using

$$P_{\text{CO}} = \exp\left[\frac{\Delta G^\circ}{3RT}\right]$$

For Reaction I to proceed, the partial pressures of CO in the system must not exceed the equilibrium values. The partial pressures of the CO<sub>2</sub>, O<sub>2</sub> and the aluminum suboxides can also be determined using these CO partial pressures (Table A2).

**Table AI**  
**Equilibrium Partial Pressure of CO for Reaction I**

T (°C)	pCO (atm)
1250	4.0*10 <sup>-5</sup>
1350	3.1*10 <sup>-4</sup>
1450	1.9*10 <sup>-3</sup>

For Reaction I to proceed, the CO partial pressures in the system must not exceed the equilibrium values. Such pressures cannot develop in the vacuum system used for the present experiments.

With P<sub>CO</sub> specified at its equilibrium value, the partial pressures of the aluminum suboxides can be determined for Reactions II to V (Table AII).

---

\* It is assumed that the buffer system described by reactions VI. and VII. does not dictate the CO partial pressure in the system.

From these results, it is apparent that both  $\text{Al}_2\text{O}$  and Al have significant partial pressures under conditions that also permit the formation of  $\text{Al}_4\text{C}_3$ . The formation of these volatile phases could occur by reaction with CO in regions adjacent to the C coating, consistent with the observation of rapid facetting near discontinuities in the coating.

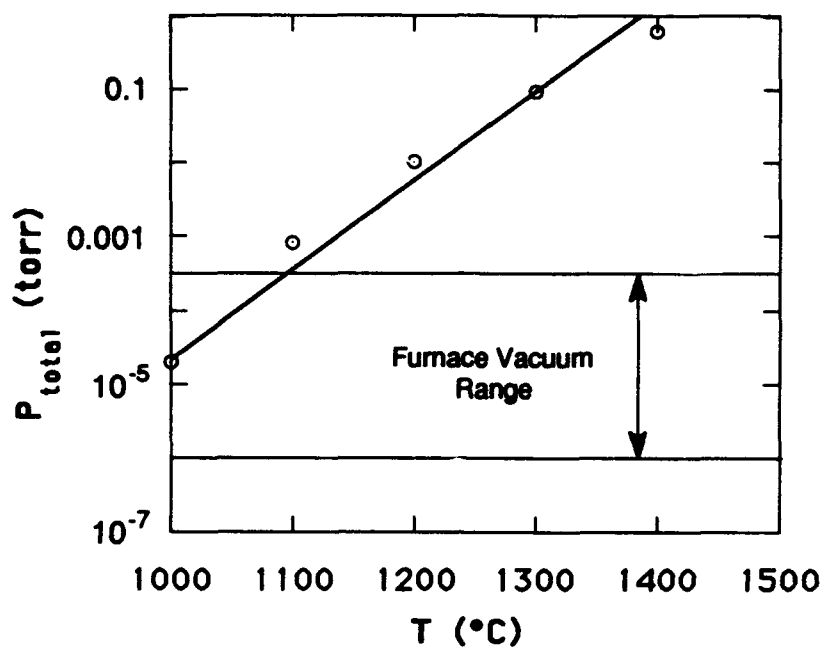
**TABLE AII****Partial Pressures of Gas Phases for the Aluminum Oxide/Carbon System\***

T (°C)	pCO (atm)	pAl <sub>2</sub> O <sub>2</sub> (atm)	pAl (atm)	pAl <sub>2</sub> O (atm)	pAlO (atm)	p <sub>total</sub> (atm)
1250	4.0*10 <sup>-5</sup>	3.0*10 <sup>-15</sup>	2.0*10 <sup>-6</sup>	1.6*10 <sup>-6</sup>	2.3*10 <sup>-12</sup>	2.9*10 <sup>-5</sup>
1350	3.1*10 <sup>-4</sup>	1.3*10 <sup>-13</sup>	1.2*10 <sup>-5</sup>	1.4*10 <sup>-5</sup>	4.0*10 <sup>-11</sup>	3.4*10 <sup>-4</sup>
1450	1.9*10 <sup>-3</sup>	2.8*10 <sup>-12</sup>	5.0*10 <sup>-4</sup>	1.3*10 <sup>-4</sup>	5.0*10 <sup>-10</sup>	2.1*10 <sup>-3</sup>

\* These results are in reasonable agreement with literature values. (Ref.: Sprague in Ref. of High Temp. Sys. vol. 1., ed. G.S. Bahn, Gordon & Breach (1964).



*Reaction I. can proceed if  $p_{total} > p_{furnace}$*



From the graph above it can be seen that Reaction I can proceed in the vacuum furnace at temperatures exceeding 1100°C even for the lower vacuum range ( $5 \cdot 10^{-4}$  torr).

## APPENDIX II

### Crack-Like Surface Instabilities

Recent analyses have shown that surface perturbations can grow into crack-like flaws, by surface diffusion, in bodies subject to stress.<sup>19</sup> The flux is provided by the strain energy contribution to the chemical potential, which can exceed the surface curvature term, at sufficiently high stress. The consequence is that there is a critical stress,  $\sigma_c$ , above which such flaws can develop. The surface troughs observed in some of the fibers may be caused by this phenomenon. In order to explore this possibility, analysis of the critical stress is performed.

The basic requirement for the development of crack-like flaws is that the change in strain energy,  $dU$ , upon crack extension,  $da$ , exceed the increase in surface energy,  $dU_s$ , as in the original Griffith analysis. This condition defines the critical stress. For an array of surface flaws of depth,  $a$ , and separation,  $b$ , the energy release rate at stress,  $\sigma$ , is

$$\frac{dU}{da} = \left( \frac{\sigma^2 \pi b}{E} \right) F(a/b) \quad (A1)$$

where the function  $F(a/b)$  is plotted on Fig. A1. The corresponding change in surface energy is

$$\frac{dU}{da} = 2\gamma_s \quad (A2)$$

where  $\gamma_s$  is the surface energy per unit area. Hence, for flaw growth to be possible,

$$dU/da \geq dU_s/da \quad (A3)$$

resulting in a critical stress,

$$\sigma_c = \sqrt{\frac{2E\gamma_s}{\pi b} F(a/b)} \quad (A4)$$

For flaws with depths in the micron range to extend in sapphire, Eqn. (A4) indicates that stresses of order 500 MPa are required (Fig. A2). While such stresses are unlikely, the mechanism has not been ruled out because of the morphological similarity of the observed trough with the profile predicted for diffusive crack growth.

## FIGURE CAPTIONS

- Fig. 1. Cross section of composite produced by HIPing.
- Fig. 2. Composite tensile test geometry for *in situ* studies in the SEM.
- Fig. 3. a) Fiber strength data: P is the cumulative probability of fracture.  
b) Effect of heat treatment on median strengths and standard deviation.
- Fig. 4. Schematic representations of the surface morphology changes found to occur when coated sapphire fibers are heat treated.
- Fig. 5. Pores observed on the surface of a sapphire fiber.
- Fig. 6. Fiber strength predictions obtained upon assuming that the porous behaviors are penny-cracks. The fracture energy for sapphire was assumed to be  $15 \text{ Jm}^{-2}$ . Typical pore diameters are  $\sim 1 \text{ }\mu\text{m}$ . The stress intensity factor is,  
 $K_I = (2/\sqrt{\pi}) \sigma \sqrt{a} F(a/b)$ .
- Fig. 7. Facets observed on the surfaces of uncoated, heat treated fibers.
- Fig. 8. a) Surface damage was observed on uncoated, heat-treated fibers. A chemical reaction has occurred between the fiber and the contaminant. b) The reaction site examined by EDS, reveals Si and Mg.
- Fig. 9. Localized fiber surface degradation observed when carbon coatings were used.
- Fig. 10. The fiber surface degradation (near the coating edge) for the carbon coated fibers increases with the heat-treatment temperature. a) Surface features of a fiber heated in vacuum for 2 h at  $1250^\circ\text{C}$ . b) Surface features of a fiber heated in vacuum for 2 h at  $1350^\circ\text{C}$ . c) Surface features of a fiber heated in vacuum for 2 h at  $1450^\circ\text{C}$ .
- Fig. 11. Ridges on the sapphire surface observed when Mo coated fibers were heat treated. The coating has been chemically etched from the fiber surface.

- Fig. 12. TEM micrographs reveal that a) 0.7  $\mu\text{m}$  thick Mo coatings do not remain continuous during HIPing . b) 1.4  $\mu\text{m}$  thick Mo coatings are continuous.
- Fig. 13. Bonding between the fiber and the matrix can occur during composite consolidation when thin Mo coatings (0.7  $\mu\text{m}$ ) become morphologically unstable.
- Fig. 14. Matrix grains which sinter to the fiber remain attached upon debonding and pull-out.
- Fig. 15. Surface grooves observed on sapphire fibers in HIPed composites, after fiber pull-out. Also shown are the regions that sintered and then debonded.
- Fig. 16. Sliding between the matrix and fiber during pull-out degrades the fiber surface and can damage the fiber.
- Fig. 17. Extensive bonding between the fiber and matrix led to co-planar fracture of the composite produced with 0.2  $\mu\text{m}$  thick gaps.
- Fig. 18. a) Composites produced with the 0.7  $\mu\text{m}$  thick coatings exhibited moderate fiber pull-out. b) The greatest extent of fiber pull-out was found for the composites produced with 1.4  $\mu\text{m}$  thick coatings.
- Fig. 19. Load-displacement curves for composites produced with 1.4  $\mu\text{m}$  thick interface gaps reveal contributions to crack growth resistance from fiber pull-out. The corresponding energy dissipation is 40  $\text{kJm}^{-2}$ .
- Fig. 20. Shear resistance of interface measurements by fiber push-out.



Figure 1

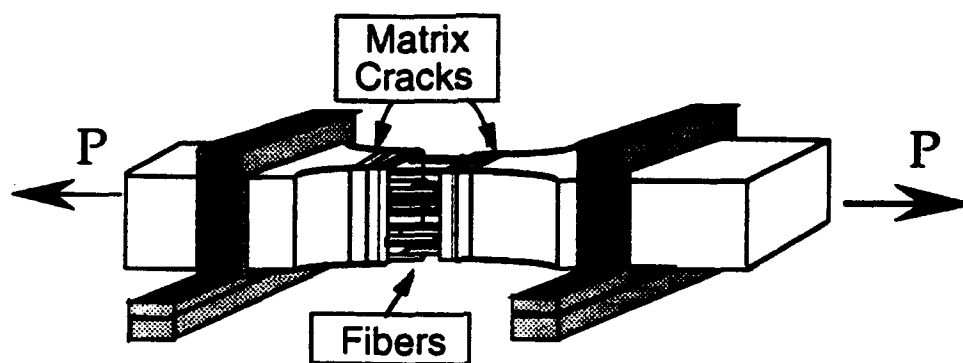


Figure 2

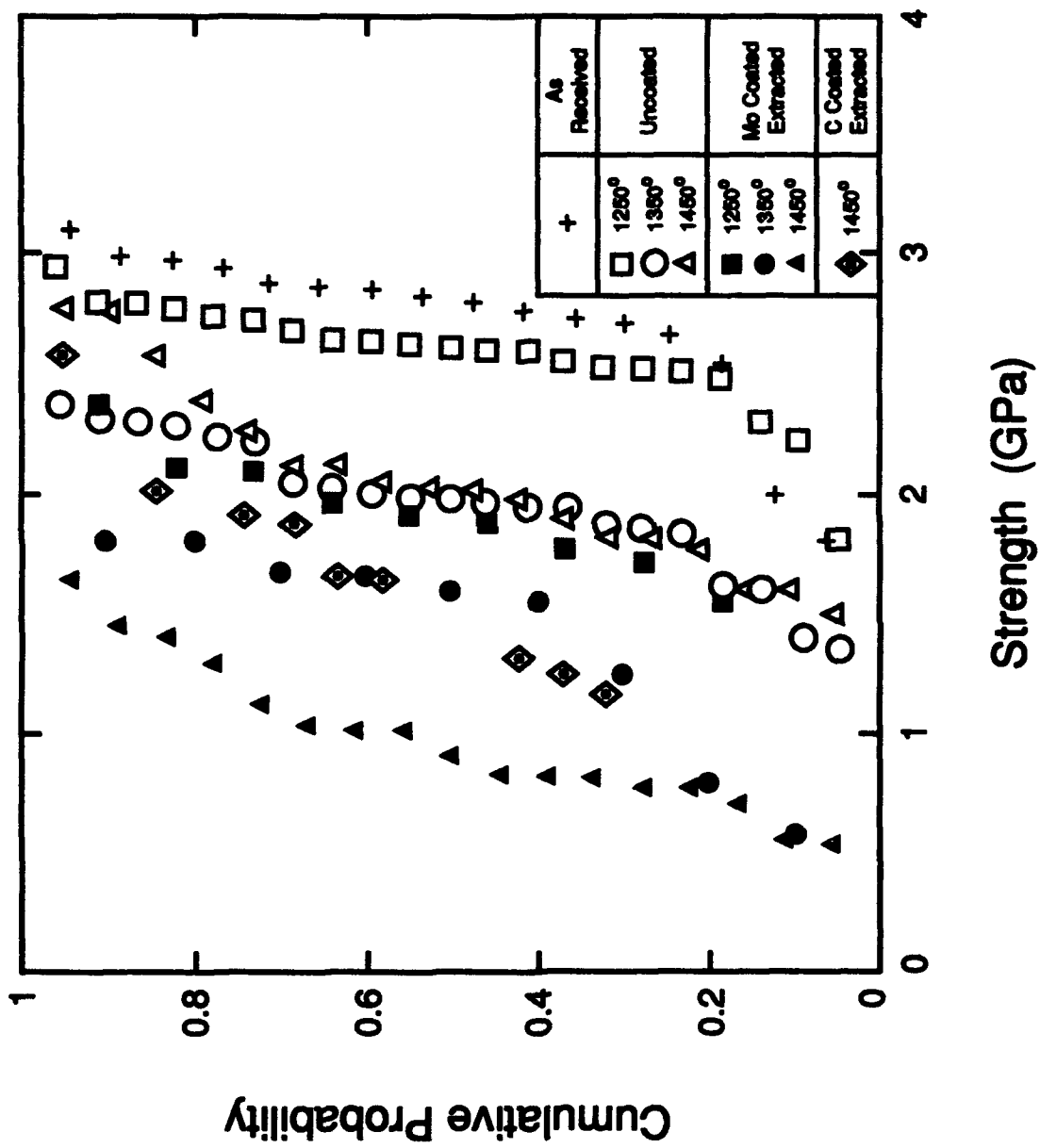


Figure 3a



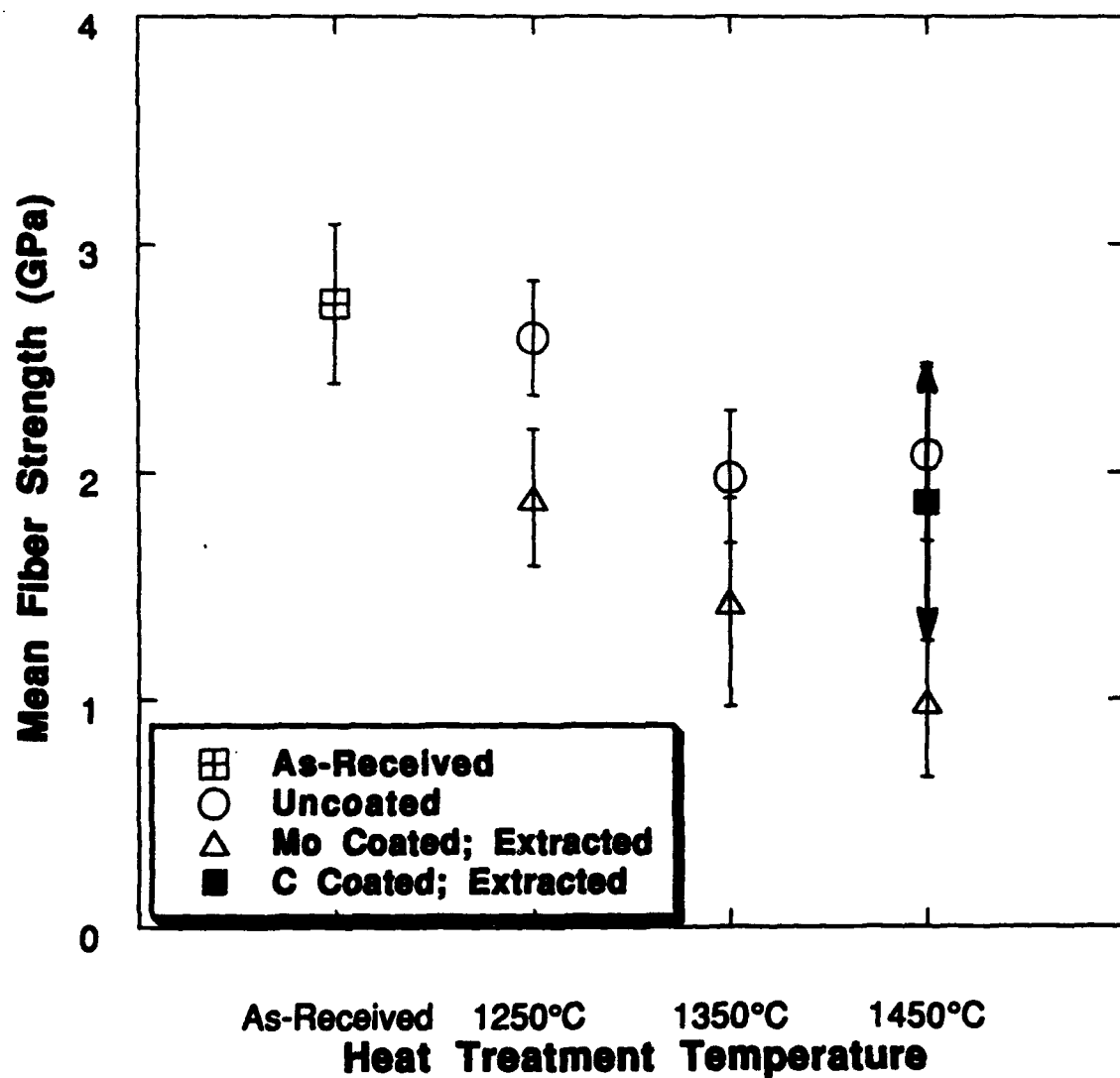


Figure 3b

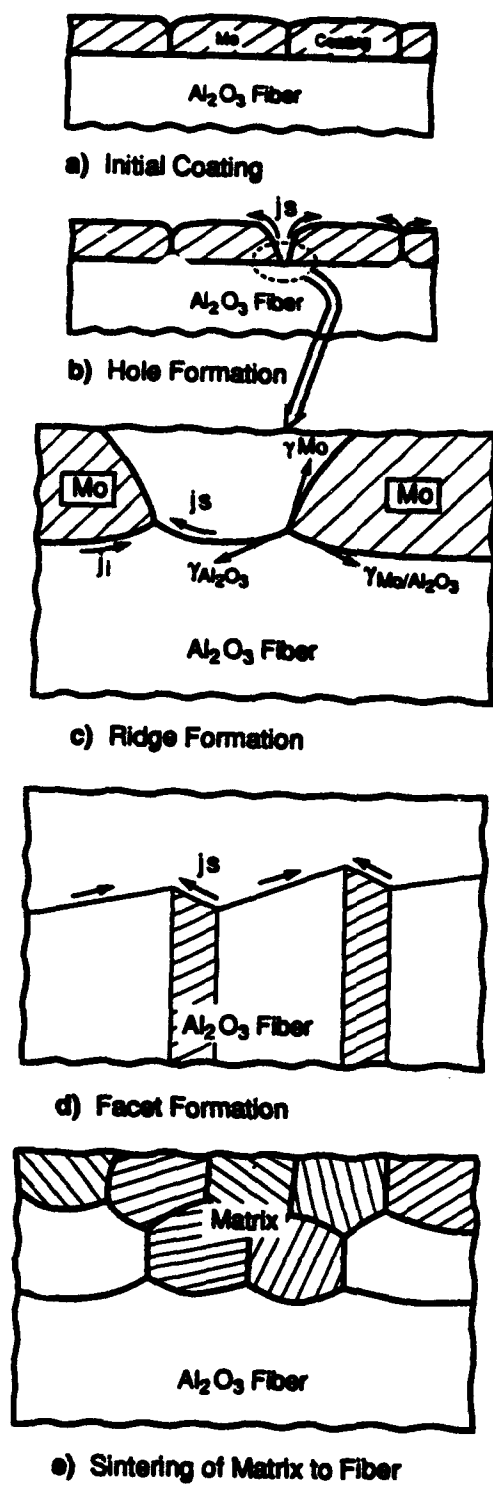


Figure 4



Figure 5

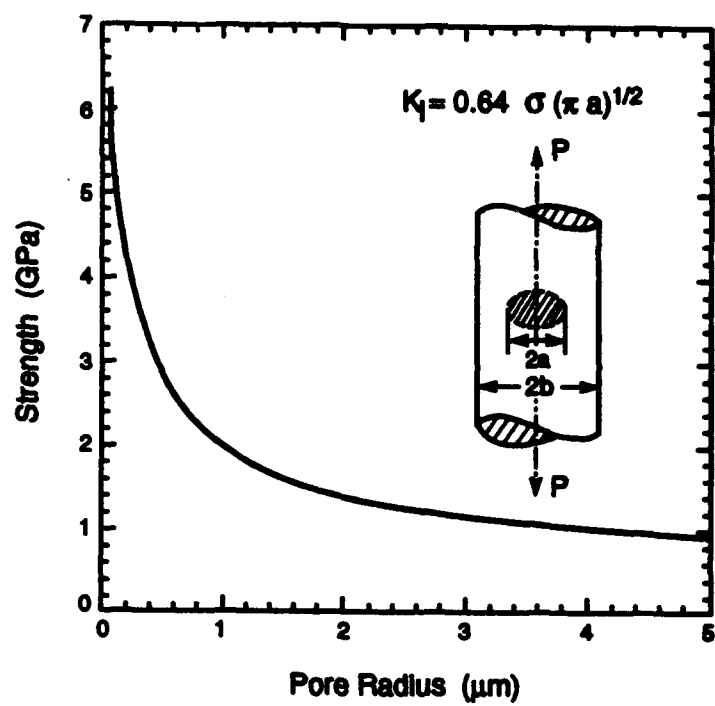
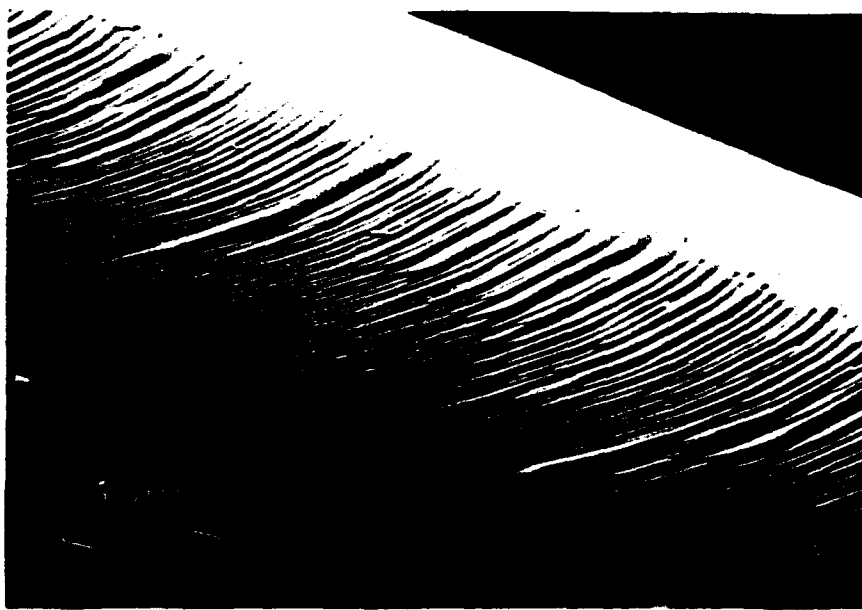


Figure 6



**Figure 7**

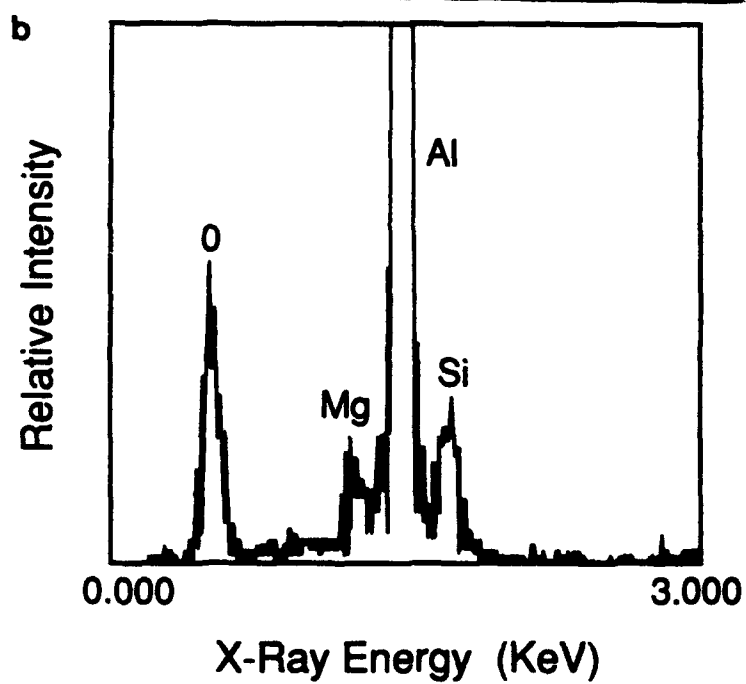
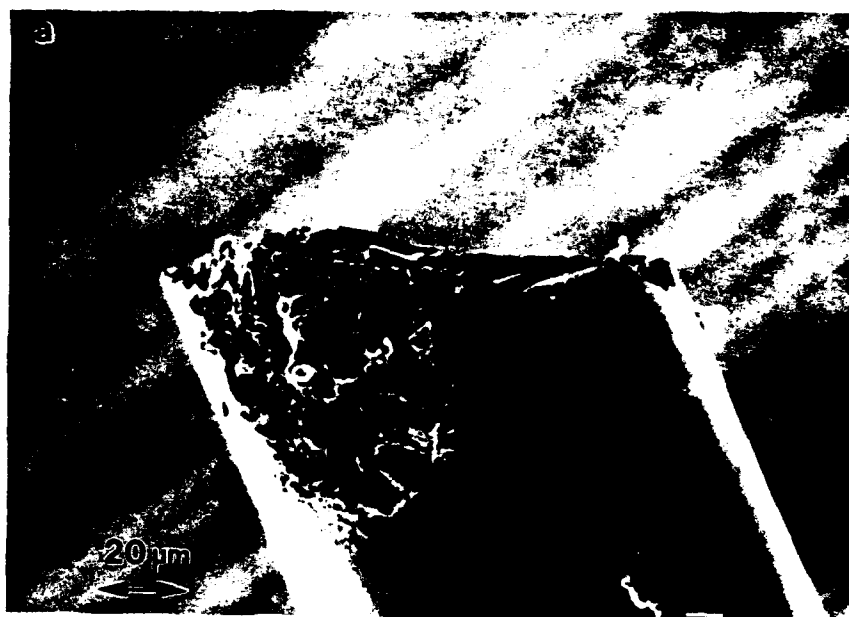


Figure 8



Figure 9

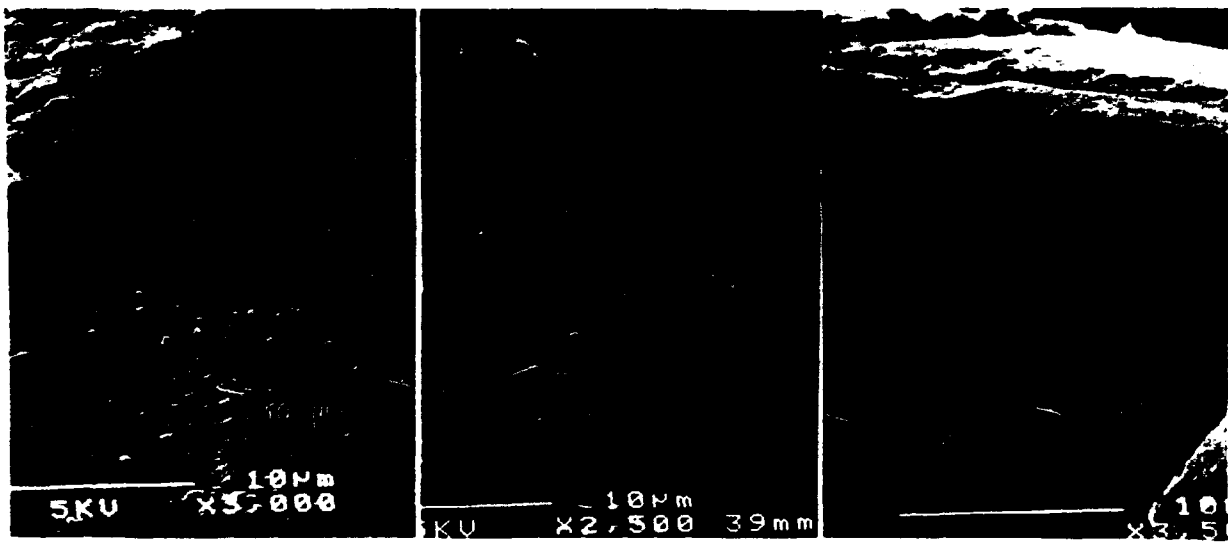


Figure 10



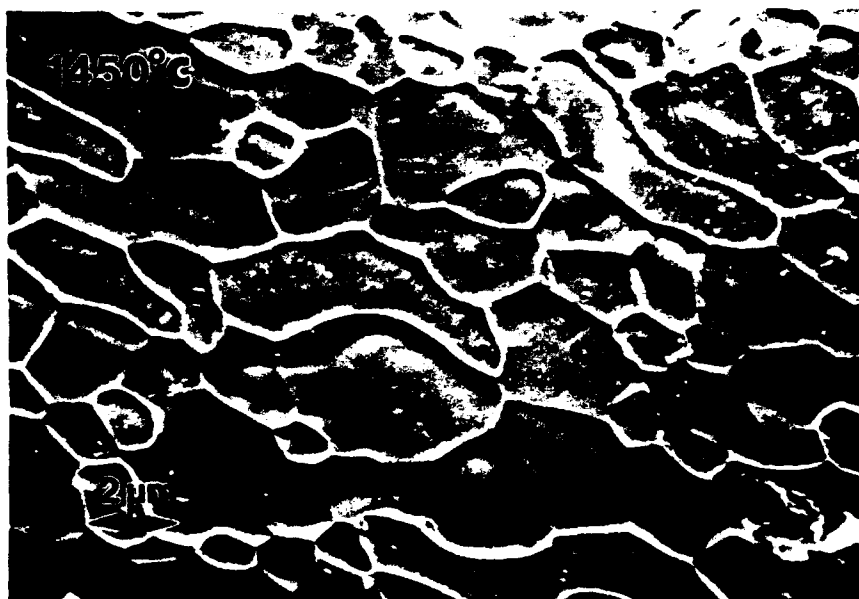


Figure 11

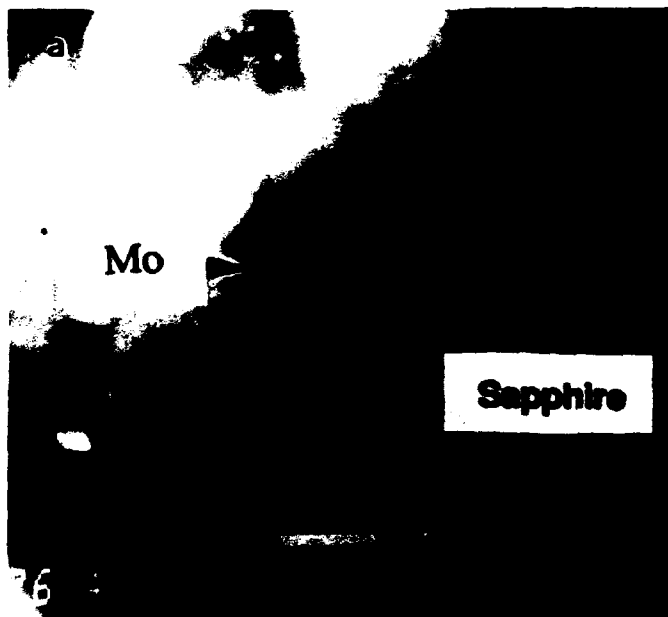


Figure 12

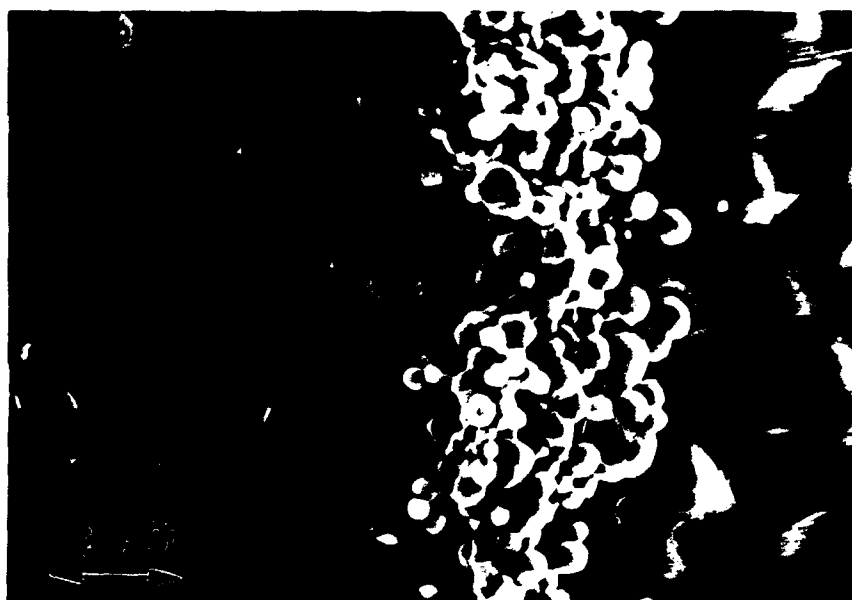


Figure 13

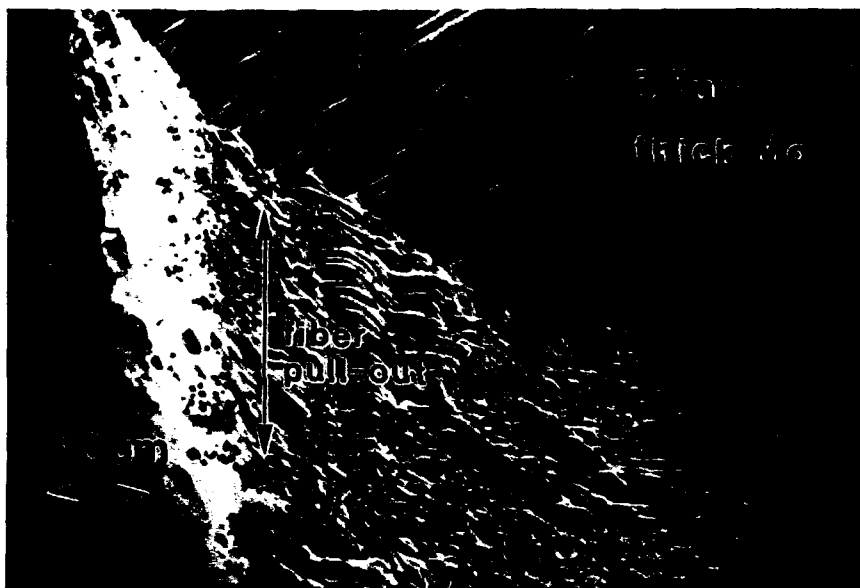


Figure 14

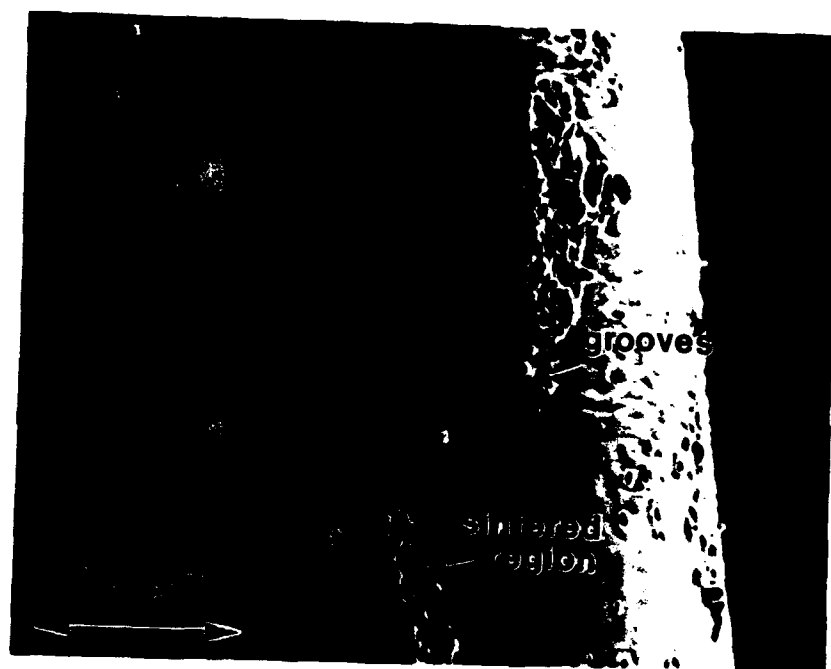


Figure 15



Figure 16



Figure 17

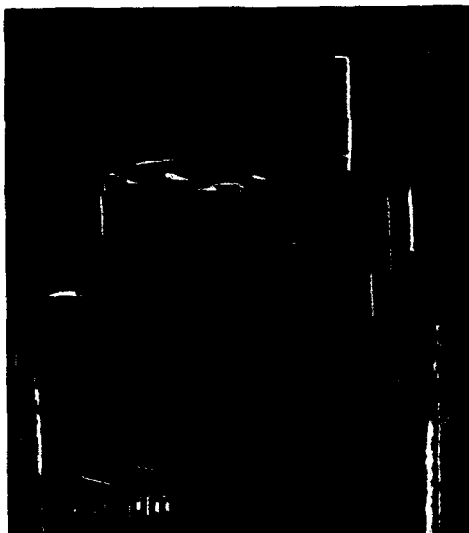


Figure 18



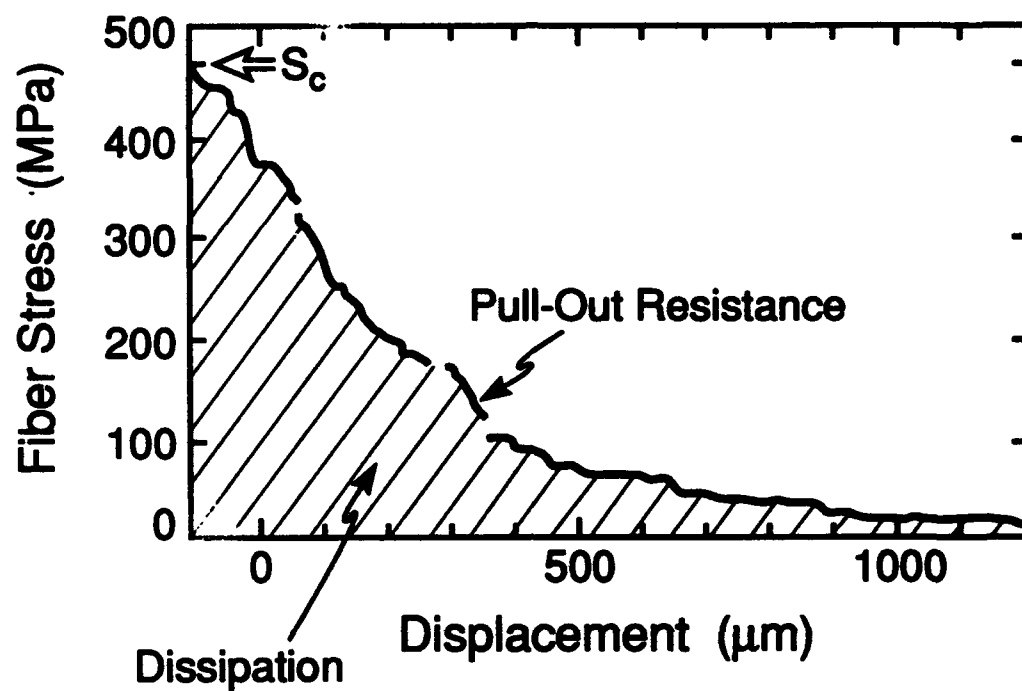


Figure 19

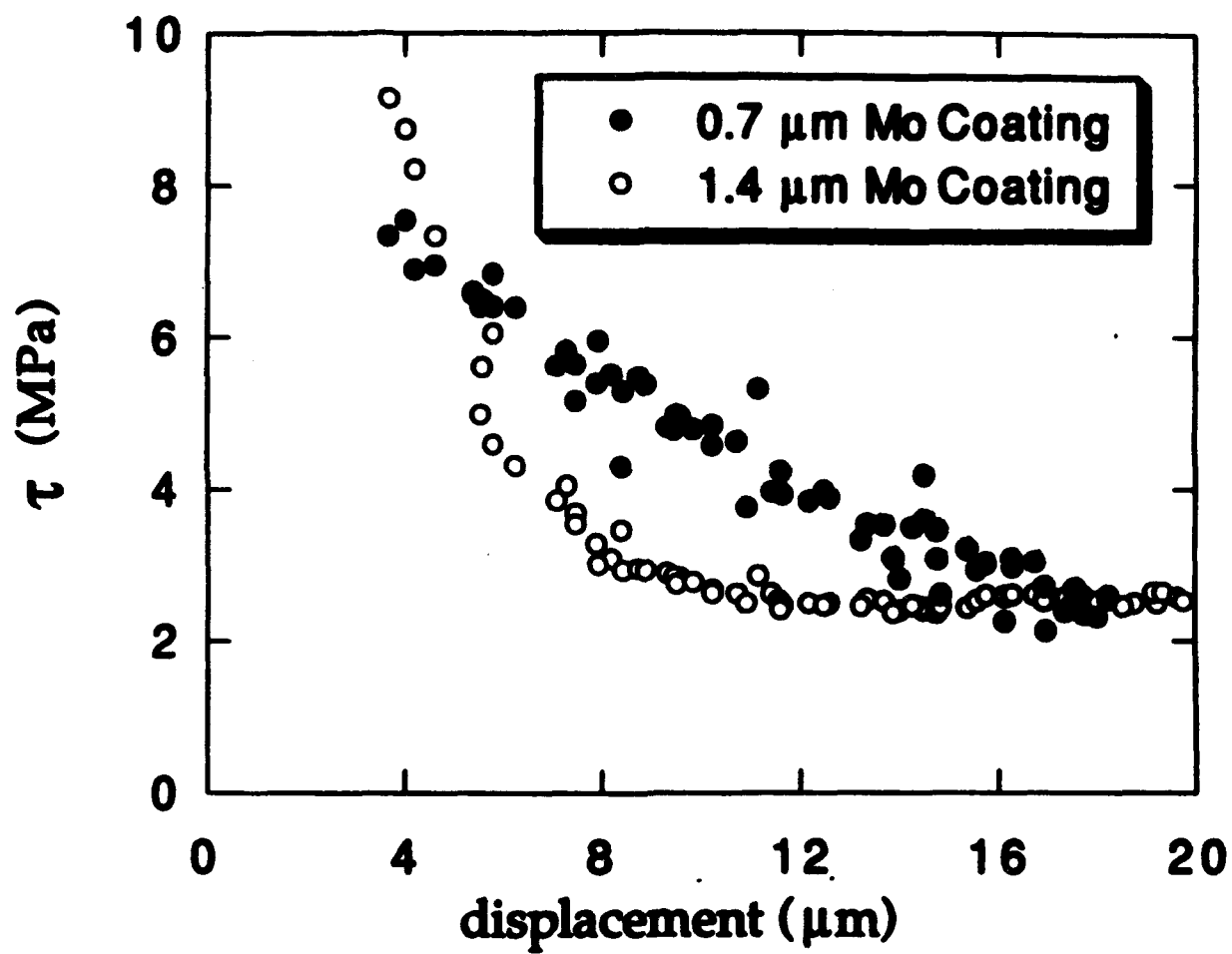


Figure 20